Lateral guidance of all-wheel steered multiple-articulated vehicles

DOI:

[10.6100/IR544960](10.6100/IR544960)

Document status and date:
Published: 01/01/2001

Document Version:
Publisher's PDF, also known as Version of Record (includes final page, issue and volume numbers)

Please check the document version of this publication:

• A submitted manuscript is the version of the article upon submission and before peer-review. There can be important differences between the submitted version and the official published version of record. People interested in the research are advised to contact the author for the final version of the publication, or visit the DOI to the publisher's website.
• The final author version and the galley proof are versions of the publication after peer review.
• The final published version features the final layout of the paper including the volume, issue and page numbers.

Link to publication

Lateral Guidance of All-Wheel Steered Multiple-Articulated Vehicles

PROEFSCHRIFT

ter verkrijging van de graad van doctor aan de
Technische Universiteit Eindhoven,
op gezag van de Rector Magnificus, prof. dr. M. Rem,
voor een commissie aangewezen door het College voor
Promoties in het openbaar te verdedigen op
woensdag 6 juni 2001 om 16.00 uur

door

Dirk de Bruin

geboren te Geldermalsen

Eerste promotor: prof.dr.ir. P.P.J. van den Bosch

Tweede promotor: prof.dr.ir J.P. Pauwelussen

Copromotor: dr.ir. A.A.H. Damen

Kerncommissie:

prof.dr.ir. M. Steinbuch
dr.ir. F.E. Veldpaus

Abstract

Nowadays, roads are becoming more and more congested, resulting in increasing economic losses due to delays. One way to solve this problem is to persuade people use public transportation more frequently. To achieve this, public transportation has to be improved. One way to improve public transportation is to construct a new kind of vehicle that combines the advantages of both commuter busses and railroad vehicles. Such a vehicle could be an all-wheel steered multiple-articulated vehicle.

In the city of Eindhoven in The Netherlands, a new kind of transportation system will be operational in the year 2003, which is based on such vehicles. To achieve a track following behaviour similar to railroad vehicles, these vehicles have to be equipped with a lateral guidance system for steering them along a predefined path. This thesis deals with the design of such a guidance system.

To achieve good tracking performance, the guidance system has to be model-based. Therefore, a dynamic vehicle model has been derived. This model describes the nonlinear planar dynamics of an all-wheel steered n-carriage multiple-articulated vehicle. To validate this model, its frequency responses have been compared with the frequency responses of a 125 degrees of freedom multi-body model. This comparison shows good performance between both models. In order to show that a dynamic vehicle model is required, a comparison has been made between the dynamic vehicle model and a model describing only the kinematics of the vehicle.

The position of the vehicle with respect to the path to be followed is crucial for proper control and therefore a measurement method based on the utilization of rotation symmetric bar magnets is presented. These magnets are buried in the road. By utilizing the rotation symmetry, the position to the magnet can be determined independently of the measurement height and the strength of the magnet. One requirement is that two field components are measured. It is shown that the sensitivity of this method to slant of the magnet and/or vehicle can be reduced by using a second dual-axes field sensor instead of one. Validation measurements show that the distance to the magnet can be determined with about $2\,cm$ accuracy with 9^0 slant of the magnet.

The permanent magnets yield position information exclusively and only at discrete instances. For controller design, knowledge of the complete state of the vehicle is desirable. An extended Kalman filter has been designed to obtain continuous estimates of this state. To keep the influence of varying vehicle parameters small, accelerometers are used as input of the Kalman filter. The accelerometer offsets, road banking angle and vehicle roll angle are estimated online, to reduce the effect of these parameters. The position information obtained from the permanent magnets is used to apply corrections to

state predictions that are based on the accelerometer outputs. The discrete and asynchronous character of this position information has been dealt with by implementing the Kalman filter in a multi-rate fashion. Articulation angle sensors, wheel encoders and rate gyros are added to the Kalman filter to improve the performance and to obtain redundancy of sensors.

The vehicles that will be used in the public transportation system in Eindhoven have, apart from all-wheel steering, also independent electrical drives on each of the wheels, except the two wheels at the front. This independent drive can in principle also be used for steering the vehicle, by using the drives on one axle in a differential way. A singular value analysis shows that steering with normal steering angles is much more influential than using these differential torques. It has also been analyzed that both at low and high speed all-wheel steering is beneficial to reduce off-tracking of the rear axles and to improve the yaw dynamics of the vehicle.

Two different controllers have been designed for steering the vehicle, based on the outputs of the Kalman filter, along the path to be followed. The first of these controllers is a feedback linearizing controller. This controller can be considered to consist of two control loops. The inner loop linearizes the planar vehicle dynamics, under the assumption that the steering system dynamics can be neglected. The outer control loop is used to counteract parameter uncertainty and disturbances. For this outer loop, a PID controller has been used.

The second controller is a so-called backstepping controller. With this controller, also the steering actuator dynamics are taken into account.

To simulate the behavior of the lateral guidance system, a more complex vehicle model has been used. This model describes besides the planar vehicle dynamics also the dynamics of the suspension system. A nonlinear tire model has been used in this model.

Simulations with this 3D simulation model show good tracking performance for both the feedback linearizing controller and the backstepping controller. The backstepping controller shows improved tracking performance compared to the feedback linearizing controller. However, this goes at the cost of increased high frequent behavior or the lateral acceleration.

Contents

1

Introduction

1.1   Motivation

Nowadays, roads are becoming more and more congested, with increasing economic losses due to delays as a consequence. This problem can be reduced by by making public transportation a more favorable way of transportation than passenger cars. To make public transportation attractive, it has amongst others to be cheap, fast, predictable and reliable.

In cities, different types of public transportation are in use. The most common types are subways, trams and commuter busses, which may or may not drive on dedicated bus lanes. All these types have their own inherent advantages and disadvantages.

A subway for example occupies relatively few expensive road space, since the tracks can be constructed underneath or above street level. Constructing the track in this way has as advantage that the tracks cannot be obstructed by other vehicles and/or pedestrians, which makes the traveling time between stations short and predictable. The main disadvantage of the subway is that the construction and the maintenance of the required infrastructure is expensive. This makes the subway only profitable in large, crowded cities. Moreover, the subway is very inflexible when a detour is required for example in case of an obstruction of the track due to an accident.

Compared to subways, the infrastructure required for trams is cheaper (though still more expensive compared to busses), since trams mainly drive on street level. This makes the tram profitable for medium large cities. Often the track is not separated from the normal road, so that other vehicles and passengers can cross the track, which can result in delays, so that the traveling time becomes less predictable. Since the tram also requires a track and electric power supply, it is also inflexible when a detour is required.

An inherent advantage of vehicle on tracks is that it is possible to make accurate stops at the stations, so that the gap between vehicle floor and platform is small. In this way, the boarding time of passengers is much shorter compared to commuter busses.

Compared to subways and trams, the capacity of normal commuter busses is limited. Moreover, due to off-tracking of the rear axles, commuter busses occupy more road space than trams. Especially in densely populated city centers this might be a problem. Advantage of commuter busses is that they don't require expensive infrastructure. Since busses can drive on normal roads, it is relatively easy to make a detour if necessary.

The comparison of the different types of public transportation shows that some of the advantages of one type are complementary with the disadvantages of the other types. This indicates that public transportation can be improved by combining the advantages of all types into a new kind of vehicle for public transportation. Basis for such a vehicle could be a commuter bus. In this way, no track or electric power supply is required, which reduces the construction and maintenance costs. The capacity of these busses can be increased by using multiple-articulated busses and/or by operating vehicles in a platoon. To avoid time delays due to obstructions and congestion, the vehicle should drive on dedicated bus lanes.

Such a type of vehicle is in development to be used in a new kind of transportation system that will be in operation in the year 2003 in and around the city Eindhoven in the Netherlands. For this transportation system, single and double articulated vehicles will be used. To reduce environmental pollution, these vehicles will be equipped with an hybrid drive, consisting of an LPG engine and electric motors. To reduce the space occupied by drive shafts, separate electric motors will be used for each wheel except the front wheels. To be able to imitate the behavior of a tram, the vehicles will be equipped with independently steerable axles, so that accurate stops at the bus stop are possible and the off-tracking of the rear axles can be reduced. In this way, the dedicated bus lanes can be made as small as possible. Figure shows a picture of a scale model of the vehicles that will be used in Eindhoven.

1.2   Goal and global lines of solution

The vehicles as discussed in the previous section are too difficult to operate manually. Therefore, they will be equipped with a lateral guidance system. The goal of this guidance system is to steer the vehicles along the bus lanes in a 'tram-like' way. This means that all axles of the vehicle have to be automatically steered along a predefined path, while the driver controls the throttle and brakes. To provide the guidance system with position information, the bus lanes will be marked with permanent magnets that are buried in the road, as illustrated in figure 1.2 for a single articulated vehicle.

Figure 1.1: Scale model of double articulated vehicle as is going to be used in Eindhoven

This thesis discusses the design of a guidance system that can achieve these goals. To obtain a more general description of this guidance system, n-carriage multiple articulated vehicles are considered, with independent electric drive on all wheels, including the front ones, and independent steering on all axles.

To achieve good performance, the guidance system contains a model of the planar vehicle dynamics and a description of the path to be followed. Therefore, the path is assumed to be (mathematically) known. The nonlinear dynamic vehicle model, that is used for the guidance system, has been derived by means of Lagrange's equation. A dynamic model is used, since analysis shows that a kinematic vehicle model does not suffice to describe the motion of articulated vehicles at high speed. To validate the dynamic model, it is compared with an 125 degrees of freedom multi-body model.

A new kind of measurement method is developed to determine the position of the vehicle by measuring the magnetic field produced by the magnets of the magnetic referencing system that is used to mark the buslanes. This measurement method uses the rotation symmetry of the bar magnets to cancel out the influence of the measurement height and the strength of the magnet.

Due to the discrete character of the magnetic referencing system, the measurement system yields position information at discrete time instances only. An extended Kalman filter has been designed to estimate position and velocity with respect to the path to be followed also in between the magnets. The influence of parameter uncertainty is kept small by using accelerometers as input of the Kalman filter to obtain a prediction of position and velocity. The position information obtained from the magnetic referencing system is used to apply corrections to this prediction. Other sensors like rate-gyro's, wheel encoders and articulation angle sensors are proposed to improve the performance
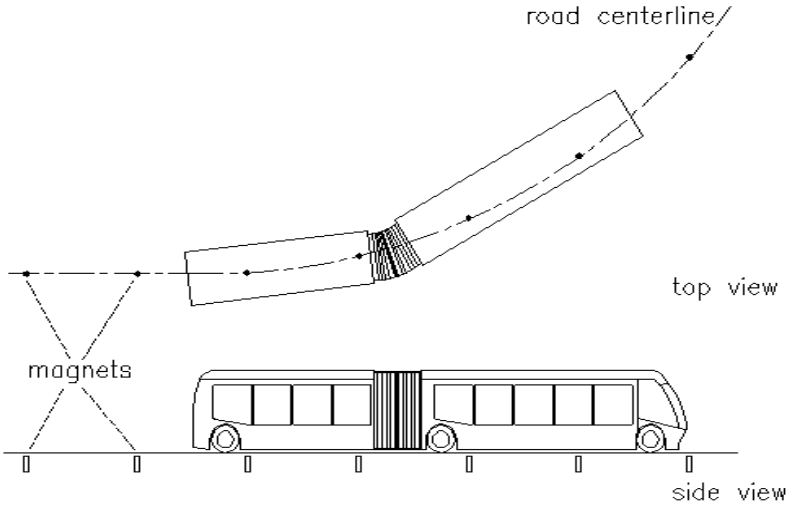
Figure 1.2: Illustration of by permanent magnet marked bus lane

in between the magnets and to introduce redundancy of sensors.

The vehicle can be steered in different ways. Besides independently controllable steering angles of all axles, also the drive torques can be used for steering the vehicle, by using the drive torques in a differential way for the wheels on one axle. A singular value analysis has been carried out to show that the steering angles have the most influence on the outputs to be controlled.

To control these steering angels, two controllers have been designed. The first is a feedback linearizing controller. This controller linearizes and decouples all degrees of freedom in of the vehicle model, leaving a double integrator for each degree of freedom. These double integrators are controlled by simple SISO PID controllers, which also serve to counteract the influence of model uncertainty and disturbances.

This feedback linearizing controller neglects the dynamics of the steering actuators. Therefore, a backstepping controller has been designed. With this controller, the steering actuators dynamics are dealt with in a more formal way.

To simulate the closed loop behavior of the guidance system, a 3D simulation model has been used. This model describes besides the planar motion also the suspension system and the nonlinear characteristic of the lateral tire forces.

1.3 Related work

During the last few decades, many papers have been published on guidance of vehicles. A large part of these papers deals with vehicle guidance for highway automation [46, 56, 70, 71, 78, 85, 90, 94]. A distinction can be made between longitudinal guidance and lateral guidance. Longitudinal guidance is mainly meant to control the distance of vehicles to their predecessor in an automated highway scenario [56, 94] or for adaptive cruise control applications. For the work presented in this thesis, longitudinal guidance is of less importance, since in case of the project in Eindhoven, the bus driver will control the longitudinal speed. Most of the work presented on lateral vehicle guidance deals with passenger vehicles [46, 70, 71, 78]. Both theoretical and experimental results have been reported in literature on this topic.

For lateral guidance of articulated vehicles, a distinction can be made between lateral guidance of robotic like vehicles that mainly drive at low speed [14, 50, 77] and lateral guidance of heavy duty vehicles for automated highway systems [28, 47, 84, 85, 86, 90]. The work on lateral guidance of robotic like articulated vehicles is mainly based on kinematic vehicle models. Due to the low velocity, the vehicle dynamics can be neglected. Since commuter busses will also drive at high speed, the work based on kinematic vehicle models is only of restricted use for this thesis.

Both theoretical and experimental results have been reported about the lateral guidance of heavy duty vehicles for automated highway systems. Dynamic vehicle models suitable for controller design for this application have been presented in [28, 86]. In [47] experimental open loop results have been presented to validate this type of model. The model as presented in [86] has been used to develop different control strategies [84, 85, 90]. Some of these strategies have been tested in full scale experiments [47].

Most of the work presented on lateral vehicle guidance considers front wheel steering only. The work presented on four wheel steering of passenger cars mostly discuss four wheel steering applied for the stabilization of the vehicle yaw dynamics in case of manual steering [3, 59, 96]. This type of four wheel steering is now commercially available for the more expensive cars. For commercial articulated vehicles, rear axle steering is mostly considered to reduce the off-tracking of the rear axle in case of manual steering. This type of rear axle steering is commercially available. This off-tracking reduction is mostly used at low speeds only, so that the steering angle for the rear axle can be derived from the kinematic relation ship between articulation angle and off-tracking at low speed. At high speed the steering possibility of the rear axle is mostly switched off.

In [28], a control strategy is presented for lateral guidance of an articulated vehicle by means of front wheel steering and differential braking applied to the rear axles of the vehicle. This comes close to the goal of the lateral guidance

system that will be presented in this thesis. Lateral guidance of articulated vehicles at high speed by means of all-wheel steering has not be found in literature before.

1.4 Organization of thesis

The organization of this thesis is as follows. The problem of steering an all-wheel steered multiple-articulated vehicle along a path in a 'tram-like' way will be stated more formally in chapter 2, where also a description of the path will be given, as well as some properties of the path.

The derivation of the planar vehicle model will be presented in chapter 3. This model will initially be expressed in inertial coordinates. For some analysis, it is more convenient to have a model expressed in vehicle-fixed coordinates. For this reason, a coordinate transformation will be applied to the model. This transformed model is compared to a multi-body model to validate the model. Finally, the model will be expressed in the dynamics of the tracking error of the vehicle with respect to the path to facilitate controller design.

Chapter 4 will be dedicated to give an overview of a 3D simulation model that has been found in the literature and has been used to obtain the simulation results presented in this thesis.

The magnet based measurement method, that will be used to measure the position of the vehicle, is presented in chapter 5. The performance of this measurement method will be illustrated in the same chapter by measurement results that are obtained from a static measurement setup.

The design of the Kalman filter is presented in chapter 6, where also open loop simulation results of the Kalman filter are presented.

The model derived in chapter 3 will be used in chapter 7 to choose the outputs to be controlled. The same model will be used to show that steering angles are more influential on the lateral behavior of the vehicle considered in this thesis than differential torques. The same chapter will discuss the advantages of all-wheel steering compared to front-wheel steering.

In chapter 8 the design of a feedback linearizing controller and a backstepping controller will be discussed. Simulation results will be presented to demonstrate that the controllers show good performance and are robust against a large range of vehicle parameter variations.

The final conclusions of this thesis and some recomendations will be presented in chapter 9.

2

Preliminaries

2.1 Introduction

In the previous chapter, the goal of the lateral guidance system has been introduced as steering a multiple articulated along a path in a 'tram-like' way. This chapter will be used to formalize this control goal, expressed in a coordinate system linked to the path. In order to arrive at this path linked description, section 2.2 provides an overview of the notation and the most frequently used coordinate frames. Section 2.3 describes the formal measure of the deviation from the path. Conditions on the shape of this path will be discussed in section 2.4. In section 2.5, a transformation matrix will be derived to project the absolute velocity of a point on the vehicle onto the axes of a coordinate frame that moves along the path. In section 2.6, the desired orientation of the carriages and desired distance from the tractors center of gravity (cg) to the path to be followed will be defined, together with the orientation error and the error in the distance between the tractor's center of gravity (cg) and the path. A relation will be derived between these errors and the tracking errors that will be defined in 2.3. This chapter will be closed by section 2.7, where the conclusions of this chapter are presented.

2.2 Notation

Throughout this thesis, vectors and matrices will be denoted in boldfont. Entry i, j of matrix $\mathbf{a}$ will be denoted by $\mathbf{a}_{[i,j]}$, whereas entry i of vector $\mathbf{b}$ will be denoted by $\mathbf{b}_{[i]}$. The ith row of matrix $\mathbf{a}$ will be denoted by $\mathbf{a}_{[i,:]}$, whereas the jth column will be denoted by $\mathbf{a}_{[:,j]}$.

Throughout this thesis, the following coordinate systems (amongst others) will frequently be used (see figure 2.1):
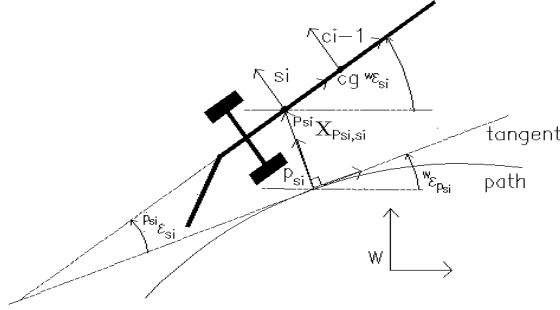
Figure 2.1: Illustration of coordinate frames

World fixed coordinate frame w

The right handed coordinate frame w is fixed to the world and considered to be an inertial frame[1]. For this reason, coordinate frame w will also be referred to as the inertial frame.

Vehicle fixed coordinate frame cj

The origin of the right handed coordinate frame cj, $j = 1, .., n$ with n the number of carriages of the vehicle, is assumed to be fixed to the center of gravity of carriage j of the multiple-articulated vehicle. The x-axis of coordinate frame cj is parallel to the longitudinal axis and points in the driving direction of carriage j.

Vehicle fixed coordinate frame si

The origin of the right handed coordinate frame si, $i = 1, .., n + 1$ is assumed to be fixed to the points $\mathbf{s}_i$ that will be introduced in this chapter. The direction of frame $s1$ is the same as the direction of frame $c1$, and the direction of frame si, $i = 2, .., n + 1$ is equal to the direction of frame $ci - 1$.

Path fixed frame p_{si}

The origin of the righthanded coordinate frame p_{si} is assumed to move along the path, such that the origin of this frame is the orthogonal projection of point $\mathbf{s}_i$ onto the path. The orientation of frame p_{si} is such that its y-axis coincides with the line through $\mathbf{s}_i$ and $\mathbf{p}_{si}$ and the angle $^{p_{si}}\epsilon_{si}$ between the x-axis of frame p_{si} and si is less than or equal to 90^0, as illustrated in figure 2.1.

---

[1]Since the rotational speed of the earth is small ($7.10^{-5}\ rad/s$), it is valid to consider w as an inertial coordinate frame [76]
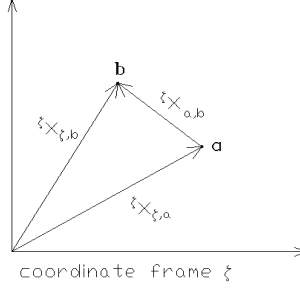
Figure 2.2: Definition of position vectors

All these coordinate frames will be considered in the horizontal plane. In general, the origin of coordinate frame $\xi \in \{w, cj, si, p_{si}, \ldots\}$ will be referred to as point $\boldsymbol{\xi}$.

The position vector of point **a** with respect to the origin and expressed in the directions of coordinate frame ξ will be denoted by ${}^{\xi}\mathbf{x}_{\xi,a}$. The first and second component of ${}^{\xi}\mathbf{x}_{\xi,a}$ will be denoted by ${}^{\xi}x_{\xi,a}$ and ${}^{\xi}y_{\xi,a}$ respectively. The difference between the position vectors ${}^{\xi}\mathbf{x}_{\xi,b}$ and ${}^{\xi}\mathbf{x}_{\xi,a}$, i.e. the vector pointing from point **a** towards the point **b**, as illustrated in figure 2.2, will be denoted by

$$
{}^{\xi}\mathbf{x}_{a,b} = {}^{\xi}\mathbf{x}_{\xi,b} - {}^{\xi}\mathbf{x}_{\xi,a} \tag{2.1}
$$

For example, the position of the origin of the vehicle fixed coordinate frame si with respect to the origin of path fixed coordinate frame p_{si} expressed in the direction of the world fixed frame w will be denoted as ${}^{w}\mathbf{x}_{p_{si},si}$, as elucidated in figure 2.1.

The orientation of a general coordinate frame $\chi_2 \in \{w, cj, si, p_{si}, \ldots\}$ with respect to coordinate frame $\chi_1 \in \{w, cj, si, p_{si}, \ldots\}$ in the two dimensional space will be denoted by ${}^{\chi_1}\epsilon_{\chi_2}$, so that

$$
{}^{\chi_1}\epsilon_{\chi_2} = {}^{\xi}\epsilon_{\chi_2} - {}^{\xi}\epsilon_{\chi_1}, \tag{2.2}
$$

as illustrated in figure 2.3. For example, the angle between the vehicle fixed frame ${}^{w}\epsilon_{si}$ and the path fixed frame ${}^{w}\epsilon_{p_{si}}$ will be denoted by ${}^{p_{si}}\epsilon_{p_{si}}$, as elucidated in figure 2.1.

The rotation matrix that projects a vector expressed in frame χ_1 onto the axes of frame χ_2 will denoted as ${}^{\chi_2}\mathbf{Rot}_{\chi_1}$, so that

$$
{}^{\chi_2}\mathbf{x}_{a,b} = {}^{\chi_2}\mathbf{Rot}_{\chi_1}{}^{\chi_1}\mathbf{x}_{a,b}. \tag{2.3}
$$
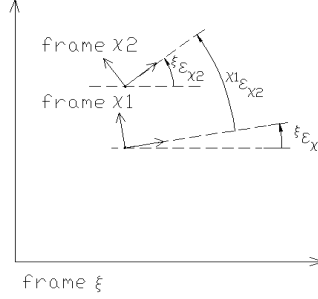
Figure 2.3: Definition of orientation angles

In $\mathbb{R}^2$, $^{\chi_2}\mathbf{Rot}_{\chi_1}$ equals

$$^{\chi_2}\mathbf{Rot}_{\chi_1} = \left[\begin{array}{cc} \cos\,^{\chi_2}\epsilon_{\chi_1} & -\sin\,^{\chi_2}\epsilon_{\chi_1} \\ \sin\,^{\chi_2}\epsilon_{\chi_1} & \cos\,^{\chi_2}\epsilon_{\chi_1} \end{array} \right] \tag{2.4}$$

According to this definition,

$$^{\chi_2}\mathbf{Rot}_{\chi_1} = \,^{\chi_1}\mathbf{Rot}_{\chi_2}^{-1} = \,^{\chi_1}\mathbf{Rot}_{\chi_2}^{T} \tag{2.5}$$

Forces acting on a body at the origin of coordinate frame ζ_1 and expressed in the directions of coordinate frame ζ_2 will be denoted by $^{\zeta_2}\mathbf{F}_{\zeta_2}$.

The superscript χ of the generalized position vector $^{\chi}\mathbf{q}$ and generalized torque vector $^{\chi}\boldsymbol{\tau}$ denotes that the first two elements of $^{\chi}\mathbf{q}$ and $^{\chi}\boldsymbol{\tau}$ are expressed in the directions of coordinate frame χ (see chapter 3).

2.3 Problem formalization

As mentioned in the introduction, this thesis deals with the design of a lateral guidance system to guide all-wheel steered single and double articulated commuter busses along a path. To generalize the design of such a guidance system, n-carriage all wheel steered multiple-articulated vehicles will be considered. These vehicles consist of a four wheeled tractor pulling $n-1$ two wheeled semi-trailers as depicted in figure 2.4. In total, these n-carriage vehicles have $n+1$ axles. All these axles are assumed to be independently steerable. The single and double articulated vehicles mentioned in the introduction are equipped with independent electric drives on each of the wheels, except the tractor's front wheels. To generalize the result, independent all-wheel drive will be considered initially.
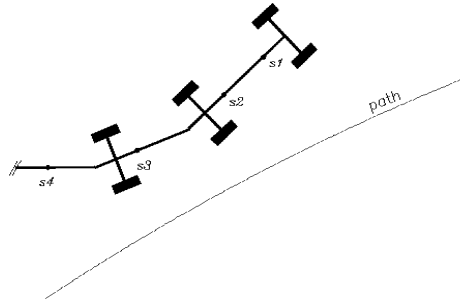
Figure 2.4: definition of control points

The goal of the guidance system is to steer such a vehicle along the path in a tram-like way. In case of trams, or railroad vehicles in general, all axles are forced to follow the same track by means of the railroad. This track following behavior can be imitated by all-axle steered multiple articulated vehicles. Instead of letting the centers of the $n+1$ axles follow the same track, $n+1$ arbitrary points can be chosen to follow the same track, to allow for more freedom. The only condition on these points is that the motion of these points describe the complete motion of the vehicle. These points will be denoted by $\mathbf{s}_i$, $i = 1,..,n+1$. The points $\mathbf{s}_{i+1}$, $i = 1,..,n$ will be each attached to a known location at carriage i and in addition the point $\mathbf{s}_1$ will be attached to a second location at the tractor, such that the points do not coincide, as illustrated in figure 2.4. The goal of the lateral guidance system is to let the points $\mathbf{s}_i$ follow the same path.

This problem can be formalized in different ways. For example, when the shape of the path is given, desired orientations ${}^w\epsilon_{ci_{\mathrm{des}}}$ can be derived for each carriage, such that when one of the points, for example $\mathbf{s}_1$, is on the path and the orientation ${}^w\epsilon_{ci}$ of carriage i equals the desired orientation ${}^w\epsilon_{ci_{\mathrm{des}}}$ for $i = 1,..,n$, all points $\mathbf{s}_i$ are automatically on the path. The control problem can be formulated then as minimizing the difference between between ${}^w\epsilon_{ci}$ and ${}^w\epsilon_{ci_{\mathrm{des}}}$ for $i = 1,..,n$ and the distance from $\mathbf{s}_1$ to the path. One of the disadvantages of formalizing the control problem in this way is that small errors in the orientations ${}^w\epsilon_{ci}$ might result in an unacceptably large tracking error of the points $\mathbf{s}_i$. For example, a double articulated bus might be as long as $25\,m$. With an error of only 1 deg in all orientations, the tracking error of $\mathbf{s}_{n+1}$ can be as large as $0.5\,m$, which is unacceptable large. Other similar ways to formalize the control problem are possible.

A better method to formalize the control problem is to directly minimize the distance from all points $\mathbf{s}_i$ to the path. In this way, all outputs to be controlled are of equal importance, so that an error in one of the outputs does

not automatically result in large tracking errors of the remaining points $\mathbf{s}_i$. Moreover, controlling directly the tracking errors of the points $\mathbf{s}_i$ is intuitively easy to interpret. For these reasons amongst others, the control problem will be formalized according to this last method.

The shortest distance from $\mathbf{s}_i$ to the path to be followed equals the distance between $\mathbf{s}_i$ and point $\mathbf{p}_{si}$, where $\mathbf{p}_{si}$ lies on the path, such that the line connecting $\mathbf{p}_{si}$ and $\mathbf{s}_i$ is perpendicular to the tangent to the path at $\mathbf{p_{si}}$[2]. The point $\mathbf{p}_{si}$ will be referred to as the orthogonal projection of $\mathbf{s}_i$ onto the path [3]. According to these definitions, the distance from $\mathbf{s}_i$ to the path is given by

$$\|{}^{\varsigma}\mathbf{x}_{\varsigma,si} - {}^{\varsigma}\mathbf{x}_{\varsigma,p_{si}}\|_2 = \|{}^{\varsigma}\mathbf{x}_{p_{si},si}\|_2, \tag{2.6}$$

where ς denotes an arbitrary coordinate frame. This expression can be written in a more convenient way by using the coordinate frame p_{si} as introduced in the previous chapter for coordinate frame ς. Then, since according to the definition of coordinate frame p_{si}

$$ {}^{p_{si}}\mathbf{x}_{p_{si},si} = \left[\begin{array}{c} 0 \\ {}^{p_{si}}y_{p_{si},si} \end{array} \right], \tag{2.7}$$

the distance to the path can be written as

$$\|{}^{p_{si}}\mathbf{x}_{p_{si},si}\|_2 = |{}^{p_{si}}y_{p_{si},si}|. \tag{2.8}$$

The vector component ${}^{p_{si}}y_{p_{si},si}$ will be referred to as the tracking error in this thesis. Letting an n-carriage all-wheel steered multiple-articulated vehicle follow a path in a 'tram-like' way boils down to putting $n + 1$ constrains:

$$ {}^{p_{si}}y_{p_{si},si} = 0. \tag{2.9}$$

In this thesis, a weakened version of this will be applied. In stead of putting the constrains ${}^{p_{si}}y_{p_{si},si} = 0$, the magnitudes of the tracking errors ${}^{p_{si}}y_{p_{si},si}$ will be minimized.

Note that for this minimization the exact position of the points $\mathbf{p}_{si}$ is not important. When $\mathbf{s}_i$ is controlled towards $\mathbf{p}_{si}$, $\mathbf{p}_{si}$ will in general even shift over the path.

---

[2]A prove of this statement is given in appendix B

[3]Sufficient condition for existence and uniqueness of the orthogonal projection is guaranteed as the path is twicely differentiable and the distance between $\mathbf{s}_i$ and $\mathbf{p}_{si}$ is less than the minimum turning radius of the path, as proven in appendix B and C. The last requirement yields no practical implications, since the minimum turning circle of the articulated commuter busses is larger than $10\,m$. For a good lateral guidance system, the tracking errors are less than $0.2\,m$

2.4 Shape of path

The shape of the path to be followed is an important factor for the lateral guidance system of a vehicle. In the vehicle guidance literature, often abrupt transitions from straight to circular road segments are assumed, in accordance with typical highways in the United States [72]. Following such a path with zero tracking errors would result in discontinuous changes in the lateral accelerations of the carriages, in turn resulting in to high jerks. For passenger comfort, this is undesirable.

In the Netherlands, a number of guidelines are given for the design of roads [74, 75]. These guidelines suggest to use a clothoide as transition between straight and circular road segments. In this way, the transition from straight to circular road segments is smoother compared to the case of an abrupt transition. Since no analytic expression exists for a clothoide, it is suggested in [52] to use a third-order polynomial as an approximation for a clothoide. Such a polynomial has 4 coefficients to adjust.

Let the position of a point $\mathbf{p}$ on the path be described by $\mathbf{P}(\sigma_p)$, where σ_p denotes the length of the path between a fixed reference point on the path, for example the beginning of the path, and the point $\mathbf{p}$ on the path. Two coefficients of the third-order polynomial can be used to make $\mathbf{P}(\sigma_p)$ continuous on both ends of the polynomial, whereas the remaining two coefficients can be used to make $\frac{d\mathbf{P}(\sigma_p)}{d\sigma_p}$ continues.

The guidance system presented in this thesis depends on the orientation of the tangent to the path ${}^w\epsilon_p$ at point p and its derivative with respect to time. This derivative can be calculated with

$$ {}^w\dot{\epsilon}_p = \frac{d^w\epsilon_p}{d\sigma_p}\dot{\sigma}_p. \tag{2.10} $$

The derivative $\frac{d^w\epsilon_p}{d\sigma_p}$ can be obtained with [40]

$$ \frac{d^2\mathbf{P}}{d\sigma_p^2} = \begin{bmatrix} -\sin{}^w\epsilon_p \\ \cos{}^w\epsilon_p \end{bmatrix} \frac{d^w\epsilon_p}{d\sigma_p}. \tag{2.11} $$

Premultiplication with $\begin{bmatrix} -\sin{}^w\epsilon_p & \cos{}^w\epsilon_p \end{bmatrix}$ yields

$$ \frac{d^w\epsilon_p}{d\sigma_p} = \begin{bmatrix} -\sin{}^w\epsilon_p & \cos{}^w\epsilon_p \end{bmatrix} \frac{d^2\mathbf{P}}{d\sigma_p^2}. \tag{2.12} $$

This shows that the $\mathbf{P}(\sigma_p)$ has to be at least 2 times differentiable, to guarantee existence of ${}^w\dot{\epsilon}_p$. With a third-order polynomial as transition from straight to circular path segments it can be guaranteed that the second derivative of $\mathbf{P}(\sigma_p)$ exists.

One of the controllers as will be presented in chapter 8 also assumes knowledge of the second derivative of ${}^w\epsilon_p$ with respect to time. This second derivative can be calculated with

$$
{}^w\ddot{\epsilon}_p = \frac{d\,{}^w\epsilon_p}{d\sigma_p}\ddot{\sigma}_p + \frac{d^2\,{}^w\epsilon_p}{d\sigma_p^2}\dot{\sigma}_p^2.
\tag{2.13}
$$

It can be derived from equation (2.12) that the derivative $\frac{d^2\,{}^w\epsilon_p}{d\sigma_p^2}$ depends on $\frac{d^3\mathbf{P}(\sigma_p)}{d\sigma_p^3}$, which shows that in order to let ${}^w\ddot{\epsilon}_p$ exist, $\mathbf{P}(\sigma_p)$ has to be at least three times differentiable. With a third-order transition polynomial, this can not be guaranteed. Therefore, a fifth-order polynomial will be used as transition from straight to circular path segments throughout this thesis. With a fifth-order polynomial, $\mathbf{P}(\sigma_p)$, its first and second derivative can be made continuous at both the transition from straight path segment to polynomial and from polynomial to circular path segment.

2.5 Velocity with respect to path

For the derivation of the vehicle model in chapter 3 and for the design of the measurement system as described in chapter 6, it will appear to be convenient to express the absolute velocities of the points $\mathbf{s}_i$ in the frames p_{si}. Therefore, a relation will be derived between the velocity of the point $\mathbf{s}_i$ and the point $\mathbf{p}_{si}$. This relation can easily derived by decomposing the position vector ${}^w\mathbf{x}_{w,si}$ as

$$
\begin{aligned}
{}^w\mathbf{x}_{w,si} &= {}^w\mathbf{x}_{w,p_{si}} + {}^w\mathbf{x}_{p_{si},si} &\qquad (2.14)\\
&= {}^w\mathbf{x}_{w,p_{si}} + {}^w\mathbf{Rot}_{p_{si}}\,{}^{p_{si}}\mathbf{x}_{p_{si},si}. &\qquad (2.15)
\end{aligned}
$$

Differentiating this with respect to time yields

$$
{}^w\dot{\mathbf{x}}_{w,si} = {}^w\dot{\mathbf{x}}_{w,p_{si}} + {}^w\mathbf{Rot}_{p_{si}}\,{}^{p_{si}}\dot{\mathbf{x}}_{p_{si},si} + {}^w\dot{\mathbf{Rot}}_{p_{si}}\,{}^{p_{si}}\mathbf{x}_{p_{si},si}.
\tag{2.16}
$$

This equation relates the absolute velocity of the point **si** to the absolute velocity at which point $\mathbf{p}_{si}$ is moving along the path.

The absolute velocity at which the point $\mathbf{p}_{si}$ is moving along the path can easily be expressed in the direction of coordinate frame p_{si} as

$$
{}^{p_{si}}\dot{\mathbf{x}}_{w,p_{si}} = \begin{bmatrix} \dot{\sigma}_{p_{si}} \\ 0 \end{bmatrix},
\tag{2.17}
$$

where $\sigma_{p_{si}}$ denotes the path length between the point p_{si} and a fixed reference point. With this equation, ${}^w\dot{\mathbf{x}}_{w,p_{si}}$ becomes

$$
{}^w\dot{\mathbf{x}}_{w,p_{si}} = {}^w\mathbf{Rot}_{p_{si}}\begin{bmatrix} \dot{\sigma}_{p_{si}} \\ 0 \end{bmatrix},
\tag{2.18}
$$

According to the definition of coordinate frame p_{si},

$$^{p_{si}}\dot{\mathbf{x}}_{p_{si},si} = \begin{bmatrix} 0 \\ ^{p_{si}}\dot{y}_{p_{si},si} \end{bmatrix} \tag{2.19}$$

Furthermore,

$$
\begin{aligned}
^{w}\dot{\mathbf{Rot}}_{p_{si}}{}^{p_{si}}\mathbf{x}_{p_{si},si} &= {}^{w}\dot{\epsilon}_{p_{si}} \begin{bmatrix} -\sin {}^{w}\epsilon_{p_{si}} & -\cos {}^{w}\epsilon_{p_{si}} \\ \cos {}^{w}\epsilon_{p_{si}} & -\sin {}^{w}\epsilon_{p_{si}} \end{bmatrix} \begin{bmatrix} 0 \\ {}^{p_{si}}y_{p_{si},si} \end{bmatrix} \\
&= {}^{w}\dot{\epsilon}_{p_{si}} \begin{bmatrix} \cos {}^{w}\epsilon_{p_{si}} & -\sin {}^{w}\epsilon_{p_{si}} \\ \sin {}^{w}\epsilon_{p_{si}} & \cos {}^{w}\epsilon_{p_{si}} \end{bmatrix} \begin{bmatrix} {}^{p_{si}}y_{p_{si},si} \\ 0 \end{bmatrix} \\
&= -{}^{w}\dot{\epsilon}_{p_{si}}{}^{w}\mathbf{Rot}_{p_{si}} \begin{bmatrix} {}^{p_{si}}y_{p_{si},si} \\ 0 \end{bmatrix}
\end{aligned} \tag{2.20}
$$

The time derivative $^{w}\dot{\epsilon}_{p_{si}} = \rho_{p_{si}}\dot{\sigma}_{p_{si}}$ can be written as

$$^{w}\dot{\epsilon}_{p_{si}} = \frac{d^{w}\epsilon_{p_{si}}}{\sigma_{p_{si}}}\dot{\sigma}_{p_{si}} = \frac{1}{\rho_{p_{si}}}\dot{\sigma}_{p_{si}}, \tag{2.21}$$

where $\rho_{p_{si}}$ denotes the turning radius of the path. Substituting this into equation 2.21 yields

$$^{w}\dot{\mathbf{Rot}}_{p_{si}}{}^{p_{si}}\mathbf{x}_{p_{si},si} = -\frac{\dot{\sigma}_{p_{si}}}{\rho_{p_{si}}}{}^{w}\mathbf{Rot}_{p_{si}} \begin{bmatrix} {}^{p_{si}}y_{p_{si},si} \\ 0 \end{bmatrix}. \tag{2.22}$$

Substituting equations(2.18), 2.19 and 2.22 into (2.16) yields

$$^{w}\dot{\mathbf{x}}_{w,si} = {}^{w}\mathbf{Rot}_{p_{si}} \begin{bmatrix} (1 - {}^{p_{si}}y_{p_{si},si}/\rho_{p_{si}})\dot{\sigma}_{p_{si}} \\ {}^{p_{si}}\dot{y}_{p_{si},si} \end{bmatrix}. \tag{2.23}$$

In general, the minimum turning circle of articulated busses is larger than $10\,m$, which implies that the turning radius of the path should be larger than $10\,m$. With a good lateral guidance system $^{p_{si}}y_{p_{si},si}$ is small, so that $^{p_{si}}y_{p_{si},si}/\rho_{p_{si}} << 1$. Under this assumption, equation (2.23) can be approximated with

$$\begin{bmatrix} ^{w}\dot{x}_{w,si} \\ ^{w}\dot{y}_{w,si} \end{bmatrix} \approx {}^{w}\mathbf{Rot}_{p_{si}} \begin{bmatrix} \dot{\sigma}_{p_{si}} \\ ^{p_{si}}\dot{y}_{p_{si},si} \end{bmatrix}, \tag{2.24}$$

so that

$$\begin{bmatrix} \dot{\sigma}_{p_{si}} \\ ^{p_{si}}\dot{y}_{p_{si},si} \end{bmatrix} \approx {}^{w}\mathbf{Rot}_{p_{si}}^{-1} \begin{bmatrix} ^{w}\dot{x}_{w,si} \\ ^{w}\dot{y}_{w,si} \end{bmatrix}. \tag{2.25}$$

This equation expresses $\dot{\sigma}_{p_{si}}$ and $^{p_{si}}\dot{y}_{p_{si},si}$ in $^{w}\dot{\mathbf{x}}_{w,si}$. However it is more convenient to express $\dot{\sigma}_{p_{si}}$ and $^{p_{si}}\dot{y}_{p_{si},si}$ in $^{si}\dot{\mathbf{x}}_{w,si}$, which can be estimated out
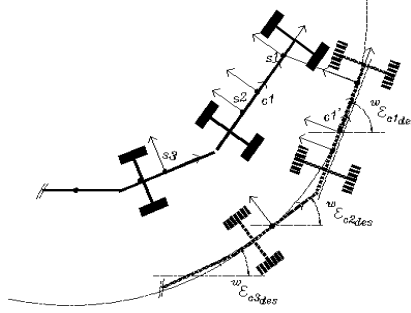
Figure 2.5: Illustration of desired generalized position

of local sensor readings. Treating equation 2.25 as an equality, it can be written as

$$\begin{bmatrix} \dot{\sigma}_{p_{si}} \\ {}^{p_{si}}\dot{y}_{p_{si},si} \end{bmatrix} = {}^{w}\mathbf{Rot}_{p_{si}}^{-1}{}^{w}\mathbf{Rot}_{si}{}^{si}\dot{\mathbf{x}}_{w,si} \tag{2.26}$$

$$= {}^{p_{si}}\mathbf{Rot}_{si}{}^{si}\dot{\mathbf{x}}_{w,si} \tag{2.27}$$

The transformation matrix ${}^{p_{si}}\mathbf{Rot}_{si}$ depends on the angle

$$^{p_{si}}\epsilon_{si} = {}^{w}\epsilon_{si} - {}^{w}\epsilon_{p_{si}}. \tag{2.28}$$

This implies that the orientations of the coordinate frames p_{si} and si have to be known in order to calculate ${}^{p_{si}}\mathbf{Rot}_{si}$. In the next section it will be discussed how ${}^{w}\epsilon_{si}$ can be determined from the tracking errors. How to determine ${}^{w}\epsilon_{p_{si}}$ online will be discussed in chapter 6.

2.6 Desired orientations

For the guidance system as presented in this thesis, it will be required to calculate the articulation angles ${}^{cj-1}\epsilon_{cj} = {}^{w}\epsilon_{cj} - {}^{w}\epsilon_{cj-1}$ of the carriages out of the tracking errors ${}^{p_{si}}y_{p_{si},si}$. Therefore, this section will be used to derive a relation between the tracking errors and the orientations ${}^{w}\epsilon_{cj}$ of the carriages. To obtain this relation, the orientations will be split in a desired part and an error part. The position vector of the points si will be expressed in the desired orientation and orientation errors. Subsequently this position vector will be linearized at the desired orientations, to arrive at a linear relation between the tracking errors and the orientation errors.
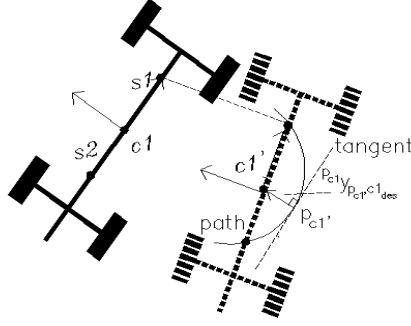
Figure 2.6: Illustration of desired position of tractor's center of gravity

For zero tracking errors, the orientation $^w\epsilon_{cj}$ of carriage j is completely determined by the shape of the path and the position of the points **si**. For nonzero tracking errors, the vehicle can be projected onto the path such that $\sigma_{p_{s1}}$ stays constant and all tracking errors equal zero. This projection is illustrated in figure 2.5. Given this projection, the desired orientation $^w\epsilon_{cj_{\mathrm{des}}}(\sigma_{p_{s1}})$ will be defined as the orientation of carriage j of the projected vehicle. With this definition, the orientation errors $^w\epsilon_{cj_{\mathrm{err}}}$ can be defined as

$$^w\epsilon_{cj_{\mathrm{err}}} = {}^w\epsilon_{cj} - {}^w\epsilon_{cj_{\mathrm{des}}}. \tag{2.29}$$

In a similar way, the desired position of the projected tractor's center of gravity will be defined. Let the projected tractor's center of gravity be denoted by $\mathbf{c}_1'$. Let it's orthogonal projection be denoted by $\mathbf{p}_{c1'}$ and let a coordinate frame $p_{c1'}$ be assigned to $\mathbf{p}_{c1'}$, with a similar orientation as the coordinate frames p_{si}. The desired position of the tractor's center of gravity $^{p_{c1}}\mathbf{x}_{p_{c1},c1_{\mathrm{des}}}$ will be defined as

$$^{p_{c1}}\mathbf{x}_{p_{c1},c1_{\mathrm{des}}} = {}^{p_{c1'}}\mathbf{x}_{p_{c1'},c1'} = \left[\begin{array}{c} 0 \\ {}^{p_{c1'}}y_{p_{c1'},c1'} \end{array} \right]. \tag{2.30}$$

One and another is illustrated in figure 2.6[4]. The error vector $^{p_{c1}}\mathbf{x}_{p_{c1},c1_{\mathrm{err}}}$ will be defined as

$$^{p_{c1}}\mathbf{x}_{p_{c1},c1_{\mathrm{err}}} = {}^{p_{c1}}\mathbf{x}_{p_{c1},c1} - {}^{p_{c1}}\mathbf{x}_{p_{c1},c1_{\mathrm{des}}} \tag{2.31}$$

The position of the points si can easily be expressed in the desired orientations and orientation errors of the frames si and in $^{p_{c1}}\mathbf{x}_{p_{c1},c1_{\mathrm{err}}}$ and $^{p_{c1}}\mathbf{x}_{p_{c1},c1_{\mathrm{des}}}$.

---

[4]Note that the curvature of the path has been exaggerated in this picture to make things visible

Note for convenience that

$$
{}^{w}\epsilon_{sj} = \begin{cases} {}^{w}\epsilon_{c1} & \text{if } j = 1 \\ {}^{w}\epsilon_{cj-1} & \text{if } 1 < j \leq n+1 \end{cases}, \tag{2.32}
$$

so that the desired orientations ${}^{w}\epsilon_{sj_{\text{des}}}$ of the coordinate frames sj can be defined as

$$
{}^{w}\epsilon_{sj_{\text{des}}}(\sigma_{p_{s1}}) = \begin{cases} {}^{w}\epsilon_{c1_{\text{des}}}(\sigma_{p_{s1}}) & \text{if } j = 1 \\ {}^{w}\epsilon_{cj-1_{\text{des}}}(\sigma_{p_{s1}}) & \text{if } 1 < j \leq n+1 \end{cases}, \tag{2.33}
$$

and the orientation errors ${}^{w}\epsilon_{sj_{\text{err}}}$ can be defined as

$$
{}^{w}\epsilon_{sj_{\text{err}}}(\sigma_{p_{s1}}) = \begin{cases} {}^{w}\epsilon_{c1_{\text{err}}}(\sigma_{p_{s1}}) & \text{if } j = 1 \\ {}^{w}\epsilon_{cj-1_{\text{err}}}(\sigma_{p_{s1}}) & \text{if } 1 < j \leq n+1 \end{cases}. \tag{2.34}
$$

The position of frame si with respect to the world can be written as

$$
{}^{w}\mathbf{x}_{w,si} = {}^{w}\mathbf{x}_{w,c1} - \sum_{j=1}^{i} d_{s_{ij}} \begin{bmatrix} \cos {}^{w}\epsilon_{sj} \\ \sin {}^{w}\epsilon_{sj} \end{bmatrix} \tag{2.35}
$$

$$
= {}^{w}\mathbf{x}_{w,c1} - \sum_{j=1}^{i} d_{s_{ij}} \begin{bmatrix} \cos\left({}^{w}\epsilon_{sj_{\text{des}}} + {}^{w}\epsilon_{sj_{\text{err}}}\right) \\ \sin\left({}^{w}\epsilon_{sj_{\text{des}}} + {}^{w}\epsilon_{sj_{\text{err}}}\right) \end{bmatrix}, \tag{2.36}
$$

where

$$
d_{s_{ij}} = \begin{cases} -l_{s1} & \text{if } i = 1, j = 1 \\ 0 & \text{if } i > 1, j = 1 \\ d_{fi} + l_{si} & \text{if } i > 1, j = i \\ d_{r1} & \text{if } i > 2, j = 2 \\ d_{fj} + d_{rj} & \text{if } i > 2, 1 < j < i \\ 0 & \text{if } j > i \end{cases}, \tag{2.37}
$$

with l_{si} the distance from the point $\mathbf{s}_i$ to the center of gravity of the corresponding carriage, d_{ri} the distance from the rear articulation point of carriage i to the center of gravity of carriage i and d_{fi} the distance from the front articulation point of carriage i to the center of gravity of carriage i. One and another is illustrated in figure 2.7.

Using a first-order Taylor expansion at ${}^{w}\epsilon_{si} = {}^{w}\epsilon_{si_{\text{des}}}(\sigma_{p_{s1}})$, (2.35) can be approximated as

$$
{}^{w}\mathbf{x}_{w,si} \approx {}^{w}\mathbf{x}_{w,c1} - \sum_{j=1}^{i} d_{s_{ij}} \begin{bmatrix} \cos\left({}^{w}\epsilon_{sj_{\text{des}}}\right) - \sin\left({}^{w}\epsilon_{sj_{\text{des}}}\right){}^{w}\epsilon_{sj_{\text{err}}} \\ \sin\left({}^{w}\epsilon_{sj_{\text{des}}}\right) + \cos\left({}^{w}\epsilon_{sj_{\text{des}}}\right){}^{w}\epsilon_{sj_{\text{err}}} \end{bmatrix}. \tag{2.38}
$$
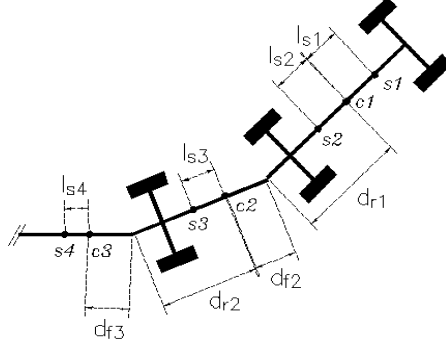
Figure 2.7: Definition of parameters

For small tracking errors, the position of the origin of the frames p_{si} can be written as

$$
{}^w\mathbf{x}_{w,p_{si}} \approx {}^w\mathbf{x}_{w,c1_{\text{des}}} - \sum_{j=1}^{i} d_{s_{ij}} \left[\begin{array}{c} \cos\left({}^w\epsilon_{sj_{\text{des}}}\right) \\ \sin\left({}^w\epsilon_{sj_{\text{des}}}\right) \end{array} \right],
\tag{2.39}
$$

so that,

$$
{}^w\mathbf{x}_{p_{si},si} = {}^w\mathbf{x}_{w,si} - {}^w\mathbf{x}_{w,p_{si}}
\tag{2.40}
$$

$$
\approx {}^w\mathbf{x}_{w,c1_{\text{err}}} - \sum_{j=1}^{i} d_{s_{ij}} \left[\begin{array}{c} -\sin\left({}^w\epsilon_{sj_{\text{des}}}\right) \\ \cos\left({}^w\epsilon_{sj_{\text{des}}}\right) \end{array} \right] {}^w\epsilon_{sj_{\text{err}}}.
\tag{2.41}
$$

This can be expressed in the directions of coordinate frame p_{si} as

$$
{}^{p_{si}}\mathbf{x}_{p_{si},si} \approx {}^{p_{si}}\mathbf{Rot}_{p_{c1}}{}^{p_{c1}}\mathbf{x}_{w,c1_{\text{err}}} - \sum_{j=1}^{i} d_{s_{ij}} \left[\begin{array}{c} -\sin\left({}^{p_{si}}\epsilon_{sj_{\text{des}}}\right){}^w\epsilon_{sj_{\text{err}}} \\ \cos\left({}^{p_{si}}\epsilon_{sj_{\text{des}}}\right){}^w\epsilon_{sj_{\text{err}}} \end{array} \right], \tag{2.42}
$$

where equation 2.2 has been used to calculate ${}^{p_{si}}\epsilon_{sj_{\text{des}}}$ out of ${}^w\epsilon_{sj_{\text{des}}}$ and ${}^w\epsilon_{p_{si}}$.

Using the fact that by definition the first component of ${}^{p_{c1}}\mathbf{x}_{w,c1_{\text{err}}}$ equals zero this yields

$$
{}^{p_{si}}y_{p_{si},si} \approx {}^{p_{c1}}y_{p_{c1},c1_{\text{err}}} \cos{}^{p_{si}}\epsilon_{p_{c1}} - \sum_{j=1}^{i} d_{s_{ij}} \cos({}^{p_{si}}\epsilon_{cj_{\text{des}}}){}^w\epsilon_{cj_{\text{err}}}.
\tag{2.43}
$$

This equation gives a relation between the orientation errors and the error in the distance from the tractor's center of gravity to the path on the one hand

and the tracking errors $^{p_{si}}y_{p_{si},si}$ on the other hand. Equation (2.43) can be written more compactly as

$$\mathbf{y}_s \approx {}^{y}\mathbf{T}_{c1_{q'}}{}^{c1}\mathbf{q}'_{\mathrm{err}}, \tag{2.44}$$

where

$$\mathbf{y}_s = \begin{bmatrix} {}^{p_{s1}}y_{p_{s1},s1} \\ \vdots \\ {}^{p_{sn+1}}y_{p_{sn+1},sn+1} \end{bmatrix}, \tag{2.45}$$

$$^{c1}\mathbf{q}'_{\mathrm{err}} = \begin{bmatrix} {}^{p_{c1}}y_{p_{c1},c1_{\mathrm{err}}} \\ {}^{w}\epsilon_{c1_{\mathrm{err}}} \\ \vdots \\ {}^{w}\epsilon_{cn_{\mathrm{err}}} \end{bmatrix} \tag{2.46}$$

and the $(n+1)$ by $(n+1)$ matrix $^{y}\mathbf{T}_{c1_{q'}}$

$$^{y}\mathbf{T}_{c1_{q'}} = \begin{bmatrix} \cos{}^{p_{s1}}\epsilon_{p_{c1}} & d_{s_{11}}\cos{}^{p_{s1}}\epsilon_{c1_{\mathrm{des}}} & \cdots & d_{s_{1n}}\cos{}^{p_{s1}}\epsilon_{cn_{\mathrm{des}}} \\ \cos{}^{p_{s2}}\epsilon_{p_{c1}} & d_{s_{22}}\cos{}^{p_{s2}}\epsilon_{c1_{\mathrm{des}}} & \cdots & d_{s_{2n+1}}\cos{}^{p_{s2}}\epsilon_{cn_{\mathrm{des}}} \\ \vdots & \vdots & \ddots & \vdots \\ \cos{}^{p_{sn+1}}\epsilon_{p_{c1}} & d_{s_{n2}}\cos{}^{p_{sn+1}}\epsilon_{c1_{\mathrm{des}}} & \cdots & d_{s_{n+1n+1}}\cos{}^{p_{sn+1}}\epsilon_{cn_{\mathrm{des}}} \end{bmatrix} \tag{2.47}$$

Given the tracking errors $^{p_{si}}y_{p_{si},si}$, which can be measured or estimated online, the orientation errors $^{w}\epsilon_{cj_{\mathrm{err}}}$ can be calculated by using the inverse of (2.44). By using (2.29) and the desired orientations $^{w}\epsilon_{cj_{\mathrm{des}}}$, the orientation of the carriage with respect to the to the inertial frame w can be calculated from

$$^{w}\epsilon_{cj} = {}^{w}\epsilon_{cj_{\mathrm{err}}} + {}^{w}\epsilon_{cj_{\mathrm{des}}} \tag{2.48}$$

2.7 Summary

In this chapter the control problem has been stated as keeping the distances of $n+1$ points on the n-carriage vehicle to the path small. To get a convenient expression for these distances, this statement has been formalized as keeping the distance between each of these points and its orthogonal projection onto the path small.

A relation has been derived between the absolute velocity of these points and the absolute velocities of their respective orthogonal projections onto the path. This relation is valid as long as the distance to the path is small compared to the turning radius of the path.

The use of fifth-order polynomials as transition from straight to circular path sections has been discussed. In this way, the second derivative of the orientation of the tangent to the path exists, which reduces the lateral acceleration required to follow the path.

Finally, the desired orientations of the carriages are discussed. A relationship has been derived to express the tracking errors in the orientation errors of the carriages.

3

Control model

3.1 Introduction

In literature, different types of control models for articulated vehicles can be found. For example, vehicle models are used to design controllers for robot like vehicles driving mainly at low speed [14, 50, 77]. Due to the low speed, the dynamics of the vehicle play only a minor role. For this reason, the dynamics of the vehicle can be neglected most of the time, so that a kinematic vehicle model suffices to describe the vehicle motion. For highway automation applications of heavy duty vehicles on the other hand, the longitudinal vehicle velocity will in general be relatively high, so that the vehicle dynamics do play a role. With these applications, dynamic models are usually used to describe the motion of articulated vehicles [28, 84, 86].

In this section, a nonlinear dynamic planar model of an all-wheel steered multiple-articulated vehicle will be derived. A dynamic model will be used since commuter busses will also operate at high speed. Only the planar vehicle motions are considered, in order to keep the model for controller design as simple as possible.

The derivation of the model partially follows the same line as the derivation of an n-carriage model as presented in [86, 84]. In [86, 84], however, Newton's law has been used to derive the tractor's longitudinal and lateral equations of motion. The derivation presented in this chapter is completely based on Lagrange's equation, resulting in a more straight forward derivation. Moreover, the derivation of the model in this section is, contrary to the derivation in [86, 84], elaborated completely, so that the result can be used directly.

The vehicle model that will be derived in this section can be written as

$$^w\mathbf{M}(^w\mathbf{q})^w\ddot{\mathbf{q}} + {}^w\mathbf{C}(^w\dot{\mathbf{q}}, {}^w\mathbf{q})^w\dot{\mathbf{q}} = {}^w\boldsymbol{\tau}_{\text{damp}}(^w\dot{\mathbf{q}}) + {}^w\boldsymbol{\tau}_{\text{tire}}(^w\dot{\mathbf{q}}, {}^w\mathbf{q}) + {}^w\boldsymbol{\tau}_{\text{dist}}. \quad (3.1)$$

An expression for the mass matrix $^w\mathbf{M}$ and the Coriolis and centrifugal force matrix $^w\mathbf{C}(^w\dot{\mathbf{q}}, {}^w\mathbf{q})$ will be derived in section 3.2, where also the generalized position vector $^w\mathbf{q}$ will be introduced. The term $^w\boldsymbol{\tau}_{\text{dist}}$ models the external disturbance forces like rolling resistance, road banking and wind forces. An expression for the articulation angle damping force term $^w\boldsymbol{\tau}_{\text{damp}}(^w\dot{\mathbf{q}})$ will be derived in 3.3. In section 3.4, an expression for the generalized forces $^w\boldsymbol{\tau}_{\text{tire}}(^w\dot{\mathbf{q}}, {}^w\mathbf{q})$ due to the tire-road interaction will be presented. Section 3.5 will be used to combine the results of section 3.2, 3.3 and 3.4. In section 3.7 the planar vehicle model is validated against a double articulated vehicle model modeled in a multi-body software package. Since the tractor's longitudinal and lateral dynamics of the multi-body package model are expressed in body fixed coordinates, a change of coordinates will be performed on the model, in order to make a comparison possible. This coordinate transformation will be discussed in section 3.6. Section 3.8 will be used to make a comparison between a dynamic and a kinematic vehicle model. Since the control problem is posed in the tracking errors $^{p_{si}}y_{p_{si},si}$. Therefore another change of coordinates is performed in section 3.9 in order to express the model in the tracking errors dynamics. This chapter will be closed by section 3.11, where the conclusions of this chapter are presented.

3.2 Lagrange's equation

To derive the inertial term and the centrifugal and Coriolis term of (3.1), Lagrange's equation has been used. Prior to the use of Lagrange's equation, a set of generalized coordinates has to be selected. Since only the planar motion will be considered in this chapter, $n + 2$ generalized coordinates suffice to describe the motion of the vehicle. The two dimensional position vector $^w\mathbf{x}_{w,c1}$ of the tractor's center of gravity and the orientations $^w\epsilon_{cj}$ of each carriage will be used as generalized coordinates.

For the derivation in this section, a multiple-articulated vehicle configuration as depicted in figure 3.1 will be considered. The position vector $^w\mathbf{x}_{w,cj}$ of the center of gravity of carriage j can be expressed in the generalized coordinates as

$$^w\mathbf{x}_{w,cj} = {}^w\mathbf{x}_{w,c1} - \sum_{i=1}^{j} l_{ij} \begin{bmatrix} \cos {}^w\epsilon_{cj} \\ \sin {}^w\epsilon_{cj} \end{bmatrix}, \quad (3.2)$$
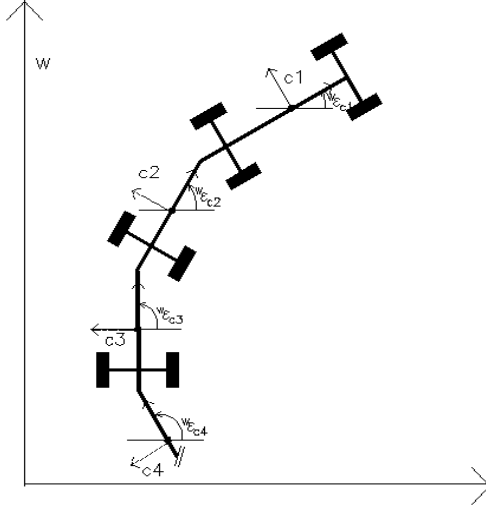
Figure 3.1: Vehicle configuration

where

$$
l_{ij} = \begin{cases}
0 & \text{if } j = 1 \\
d_{r1} & \text{if } j > 1 \text{ and } i = 1 \\
d_{fi} + d_{ri} & \text{if } j > 1 \text{ and } 1 < i < j \\
d_{fj} & \text{if } j > 1 \text{ and } i = j \\
0 & \text{if } j > 1 \text{ and } i > j
\end{cases} \tag{3.3}
$$

Differentiating (3.2) yields for the absolute velocity of the jth carriage

$$
{}^w\dot{\mathbf{x}}_{w,cj} = {}^w\dot{\mathbf{x}}_{w,c1} - \sum_{i=1}^{j} l_{ij} \begin{bmatrix} -\sin {}^w\epsilon_{cj} \\ \cos {}^w\epsilon_{cj} \end{bmatrix} {}^w\dot{\epsilon}_{cj}. \tag{3.4}
$$

The kinetic energy of the planar vehicle motion can be written as

$$
T = \frac{1}{2} \sum_{j=1}^{n} \begin{bmatrix} {}^w\dot{\mathbf{x}}_{w,cj}^T & {}^w\dot{\epsilon}_{cj} \end{bmatrix} \boldsymbol{\mathcal{M}}_j \begin{bmatrix} {}^w\dot{\mathbf{x}}_{w,cj}^T & {}^w\dot{\epsilon}_{cj} \end{bmatrix}^T, \tag{3.5}
$$

where the generalized mass matrix $\boldsymbol{\mathcal{M}}_j$ [63] of the jth carriage is given by

$$
\boldsymbol{\mathcal{M}}_j = \begin{bmatrix} m_j & 0 & 0 \\ 0 & m_j & 0 \\ 0 & 0 & I_{z_j} \end{bmatrix}, \tag{3.6}
$$

with m_j and I_{zj} the mass resp. central moment of inertia of the jth carriage. The vector $\begin{bmatrix} {}^w\dot{\mathbf{x}}^T_{w,cj} & {}^w\dot{\epsilon}_{cj} \end{bmatrix}^T$ can be written as

$$\begin{bmatrix} {}^w\dot{\mathbf{x}}_{w,cj} \\ {}^w\dot{\epsilon}_{cj} \end{bmatrix} = \mathbf{J}_{cj}({}^w\mathbf{q}){}^w\dot{\mathbf{q}}, \tag{3.7}$$

where

$$ {}^w\mathbf{q} = \begin{bmatrix} {}^w x_{w,c1} & {}^w y_{w,c1} & {}^w\epsilon_{c1} & \cdots & {}^w\epsilon_{cn} \end{bmatrix}^T \tag{3.8}$$

is the generalized position vector and

$$\mathbf{J}_{cj}({}^w\mathbf{q}) = \begin{bmatrix} 1 & 0 & l_{1j}\sin{}^w\epsilon_{c1} & \cdots & l_{nj}\sin{}^w\epsilon_{cn} \\ 0 & 1 & -l_{1j}\cos{}^w\epsilon_{c1} & \cdots & -l_{nj}\cos{}^w\epsilon_{cn} \\ 0 & 0 & \delta_{[1j]} & \cdots & \delta_{[1n]} \end{bmatrix}, \tag{3.9}$$

where $\delta_{[ij]}$ is the Kronecker delta function.

Substituting (3.7) into (3.5) yields

$$T({}^w\dot{\mathbf{q}}, {}^w\mathbf{q}) = \frac{1}{2}{}^w\dot{\mathbf{q}}^T{}^w\mathbf{M}({}^w\mathbf{q}){}^w\dot{\mathbf{q}}, \tag{3.10}$$

where,

$$ {}^w\mathbf{M}({}^w\mathbf{q}) = \sum_{j=1}^{n} \mathbf{J}^T_{cj}({}^w\mathbf{q})\mathcal{M}_j\mathbf{J}_{cj}({}^w\mathbf{q}) \tag{3.11}$$

is the mass matrix of the vehicle.

Application of Lagrange's equation yields

$$\frac{d}{dt}\frac{\partial T({}^w\dot{\mathbf{q}}, {}^w\mathbf{q})}{\partial{}^w\dot{\mathbf{q}}} - \frac{\partial T({}^w\dot{\mathbf{q}}, {}^w\mathbf{q})}{\partial{}^w\mathbf{q}} = {}^w\boldsymbol{\tau}, \tag{3.12}$$

where ${}^w\boldsymbol{\tau}$ denotes the total generalized force acting on the vehicle. To solve this equation, the kinetic energy can be written as

$$T({}^w\dot{\mathbf{q}}, {}^w\mathbf{q}) = \frac{1}{2}\sum_{k=1}^{n+2}\sum_{l=1}^{n+2} {}^w M_{[k,l]}{}^w\dot{q}_{[k]}{}^w\dot{q}_{[l]}. \tag{3.13}$$

Substituting this into Lagrange's equation (3.12) yields, after some calculation, for the equation of motion for the ith generalized coordinate

$$\sum_{l=1}^{n+2} {}^w M_{[i,l]}{}^w\ddot{q}_{[l]} + \sum_{l=1}^{n+2}\sum_{k=1}^{n+2}\left\{\frac{\partial{}^w M_{[i,l]}}{\partial{}^w q_{[k]}} - \frac{1}{2}\frac{\partial{}^w M_{[k,l]}}{\partial{}^w q_{[i]}}\right\}{}^w\dot{q}_{[k]}{}^w\dot{q}_{[l]} = {}^w\tau_{[i]}, \quad (3.14)$$

This can be written in matrix form as

$$ {}^w\mathbf{M}({}^w\mathbf{q}){}^w\ddot{\mathbf{q}} + {}^w\mathbf{C}({}^w\mathbf{q}, {}^w\dot{\mathbf{q}}){}^w\dot{\mathbf{q}} = {}^w\boldsymbol{\tau}, \tag{3.15}$$

where the entries of ${}^{w}\mathbf{C}({}^{w}\dot{\mathbf{q}}, {}^{w}\mathbf{q})$ can be written as

$$\sum_{k=1}^{n+2} \left\{ \frac{\partial {}^{w}M_{[i,l]}}{\partial {}^{w}q_{[k]}} - \frac{1}{2} \frac{\partial {}^{w}M_{[k,l]}}{\partial {}^{w}q_{[i]}} \right\} {}^{w}\dot{q}_{[k]} \tag{3.16}$$

The matrices ${}^{w}\mathbf{M}({}^{w}\mathbf{q})$ and ${}^{w}\mathbf{C}({}^{w}\dot{\mathbf{q}}, {}^{w}\mathbf{q})$ are written out in appendix D.

3.3 Articulation angle dampers

Most of the articulated commuter busses are equipped with a mechanism in between the carriages to damp the articulation angle rates. These mechanisms will be modeled as linear viscous dampers . The torque exerted on the jth carriage by the damper in between the jth and the $(j+1)^{th}$ carriage equals $d_j({}^{w}\dot{\epsilon}_{cj+1} - {}^{w}\dot{\epsilon}_{cj})$, where d_j is the damping constant of the corresponding damper. The total torque exerted on the jth carriage by the articulation angle dampers is due to the damper at the front end of the carriage, if present, and the damper at the rear end of the carriage, if present, so that

$${}^{w}\tau_{\text{damp}[j+2]} = \gamma_{[nj]} d_j({}^{w}\dot{\epsilon}_{cj+1} - {}^{w}\dot{\epsilon}_{cj}) - \gamma_{[1j]} d_{j-1}({}^{w}\dot{\epsilon}_{cj} - {}^{w}\dot{\epsilon}_{cj-1}), \tag{3.17}$$

where

$$\gamma_{[ij]} = 1 - \delta_{[ij]}, \tag{3.18}$$

so that in vector notation

$${}^{w}\boldsymbol{\tau}_{\text{damp}} = -{}^{w}\mathbf{D}_{\text{art}} {}^{w}\dot{\mathbf{q}}, \tag{3.19}$$

where

$$D_{\text{art}[1,j]} = 0 \tag{3.20a}$$
$$D_{\text{art}[2,j]} = 0 \tag{3.20b}$$
$$D_{\text{art}[j,1]} = 0 \tag{3.20c}$$
$$D_{\text{art}[j,2]} = 0 \tag{3.20d}$$
$$D_{\text{art}[2+k,2+l]} = \begin{cases} \gamma_{[1k]} d_{k-1} + \gamma_{[nk]} d_k & \text{if } l = k \\ -\gamma_{[1k]} d_{k-1} & \text{if } l = k-1 \\ -\gamma_{[nk]} d_k & \text{if } l = k+1 \\ 0 & \text{otherwise} \end{cases}. \tag{3.20e}$$

3.4 Tire forces

In this section, the method of virtual work [39] will be used to calculate the vector of generalized tire forces ${}^{w}\tau_{\text{tire}}$. To simplify notation, the axles will be

numbered from $j = 1$ to $j = n + 1$, starting with the tractor's front axle and finishing with the rear axle of the last semi-trailer. The wheel on each axle will be numbered as $i = 1$ for the left wheels and $i = 2$ for the right wheels. According to these definitions, a coordinate frame will be assigned to each wheel. The x-axis of these coordinate frames are horizontal and parallel to the wheel plane and the origin is fixed at the center of gravity of the corresponding wheel. The position vector of these coordinate frames ${}^w\mathbf{x}_{w,wij}$ can be expressed in the generalized position vector ${}^w\mathbf{q}$ as

$$
{}^w\mathbf{x}_{w,wi1} = {}^w\mathbf{x}_{w,c1} - d_{w11} \begin{bmatrix} \cos {}^w\epsilon_{c1} \\ \sin {}^w\epsilon_{c1} \end{bmatrix} + (-1)^i\, b_1 \begin{bmatrix} \sin {}^w\epsilon_{c1} \\ -\cos {}^w\epsilon_{c1} \end{bmatrix}, \qquad (3.21)
$$

and

$$
{}^w\mathbf{x}_{w,wij} = {}^w\mathbf{x}_{w,c1} - \sum_{l=1}^{j-1} d_{wlj} \begin{bmatrix} \cos {}^w\epsilon_{cl} \\ \sin {}^w\epsilon_{cl} \end{bmatrix} + (-1)^i\, b_j \begin{bmatrix} \sin {}^w\epsilon_{cj} \\ -\cos {}^w\epsilon_{cj} \end{bmatrix}, \qquad (3.22)
$$

for $j > 1$, where b_j denotes half the width of axle j and

$$
d_{wlj} = \begin{cases} -l_{f1} & \text{if } j = 1, l = 1 \\ l_{r1} & \text{if } j = 2, l = 1 \\ d_{r1} & \text{if } j > 2, l = 1 \\ d_{rl} + d_{fl} & \text{if } j > 2, 2 < l < j - 1 \\ d_{rl} + l_{rl} & \text{if } j > 2, l = j - 1 \\ 0 & \text{if } l \geq j \end{cases}, \qquad (3.23)
$$

where l_{f1} denotes the distance between the tractors's center of gravity and front axle and l_{ri} denotes the distance between the center of gravity and the rear axle of carriage i.

The generalized tire force vector can be calculated with [39]

$$
{}^w\tau_{\text{tire}} = \sum_{i=1}^{2} \sum_{j=1}^{n+1} \left(\frac{\partial {}^w\mathbf{x}_{w,wij}}{\partial {}^w\mathbf{q}} \right)^T {}^w\mathbf{F}_{wij}, \qquad (3.24)
$$

where ${}^w\mathbf{F}_{wij}$ denotes the forces exerted on wheel w_{ij} in the direction of coordinate frame w by means of the tire-road interaction. These forces are easiest expressed in the wheel fixed coordinate frames w_{ij}. Therefore, equation (3.24) will be written as

$$
{}^w\tau_{\text{tire}} = \sum_{i=1}^{2} \sum_{j=1}^{n+1} \left(\frac{\partial {}^w\mathbf{x}_{w,wij}}{\partial {}^w\mathbf{q}} \right)^T {}^w\mathbf{Rot}_{wij}\, {}^{wij}\mathbf{F}_{wij}, \qquad (3.25)
$$

The rotation matrices ${}^w\mathbf{Rot}_{wij}$ depend on the sine and cosine of the steering angles. For controller design, it is desirable to arrive at a model that is linear
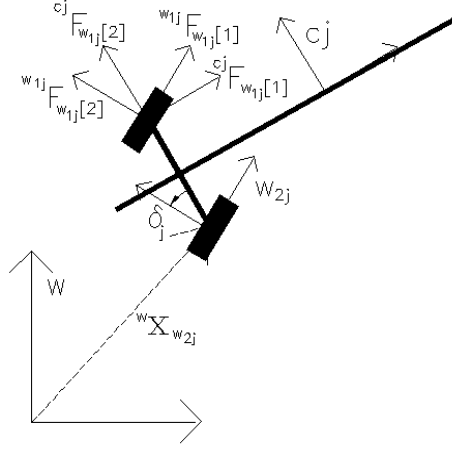
Figure 3.2: Definition of forces

in the steering angles. Since the steering angles are in general small, second and higher order terms of the steering angles can be neglected. Under this assumption,

$$
{}^{w}\mathbf{Rot}_{w_{ij}} = \begin{cases} {}^{w}\mathbf{Rot}_{c1} \begin{bmatrix} \delta_1 & 0 \\ 0 & \delta_1 \end{bmatrix} & \text{if } j = 1 \\ {}^{w}\mathbf{Rot}_{cj-1} \begin{bmatrix} \delta_j & 0 \\ 0 & \delta_j \end{bmatrix} & \text{if } j > 1 \end{cases}, \quad (3.26)
$$

where δ_j denotes the steering angle of axle j. In this way, equation (3.25) can be written as

$$
{}^{w}\boldsymbol{\tau}_{\text{tire}} = \sum_{i=1}^{2} \left\{ {}^{w}\mathbf{L}_{\text{long}_i}(\mathbf{F}_{\text{dr}_i} - \boldsymbol{\Delta}_t \mathbf{F}_{\text{cor}_i}) + {}^{w}\mathbf{L}_{\text{lat}_i}(\boldsymbol{\Delta}_t \mathbf{F}_{\text{dr}_i} + \mathbf{F}_{\text{cor}_i}) \right\}, \quad (3.27)
$$

where $\boldsymbol{\Delta}_t = \text{diag}(\delta_1, \cdots, \delta_{n+1})$. The vectors $\mathbf{F}_{\text{dr}_i}$ and $\mathbf{F}_{\text{cor}_i}$ are given by

$$
\begin{align}
F_{\text{dr}_i[j]} &= {}^{w_{ij}}F_{w_{ij}[1]} \tag{3.28} \\
F_{\text{cor}_i[j]} &= {}^{w_{ij}}F_{w_{ij}[2]} \tag{3.29}
\end{align}
$$

Furthermore,

$$
{}^{w}L_{\mathrm{long}_i[j,:]} = \begin{cases} \left(\dfrac{\partial^{w}\mathbf{x}_{w,w_{i1}}}{\partial^{w}\mathbf{q}}\right)^{T}{}^{w}\mathbf{Rot}_{c1[:,1]} & \text{if } j = 1 \\ \left(\dfrac{\partial^{w}\mathbf{x}_{w,w_{ij}}}{\partial^{w}\mathbf{q}}\right)^{T}{}^{w}\mathbf{Rot}_{cj-1[:,1]} & \text{if } j > 1 \end{cases} \tag{3.30}
$$

$$
{}^{w}L_{\mathrm{lat}_i[j,:]} = \begin{cases} \left(\dfrac{\partial^{w}\mathbf{x}_{w,w_{i1}}}{\partial^{w}\mathbf{q}}\right)^{T}{}^{w}\mathbf{Rot}_{c1[:,2]} & \text{if } j = 1 \\ \left(\dfrac{\partial^{w}\mathbf{x}_{w,w_{ij}}}{\partial^{w}\mathbf{q}}\right)^{T}{}^{w}\mathbf{Rot}_{cj-1[:,2]} & \text{if } j > 1 \end{cases}. \tag{3.31}
$$

The matrices ${}^{w}\mathbf{L}_{\mathrm{lat}}$ and ${}^{w}\mathbf{L}_{\mathrm{long}}$ are elaborated in appendix D.

The longitudinal tire forces $F_{\mathrm{dr}_i[j]} = {}^{w_{ij}}F_{w_{ij}[1]}$ are the result of the drive torques exerted on the wheels by means of the electric drive. Therefore, it is more convenient to work with torques instead of these forces. For the lateral guidance system in this thesis, the longitudinal dynamics of the vehicle are of less importance. Therefore, the longitudinal wheel slip and the inertia of the wheels will be neglected. Under this assumption, the wheel forces can be expressed in the drive torques $T_{\mathrm{dr}_{ij}}$

$$
T_{\mathrm{dr}_{ij}} = r_{w_{ij}}{}^{w_{ij}}F_{w_{ij}[1]}, \tag{3.32}
$$

where $r_{w_{ij}}$ denotes the wheel radius of the corresponding wheel. Substituting equation (3.32) into equation (3.27), (3.27) can be written as

$$
{}^{w}\boldsymbol{\tau}_{\mathrm{tire}} = \sum_{i=1}^{2}\left\{{}^{w}\mathbf{L}_{\mathrm{long}_i}(\mathbf{R}_{wi}^{-1}\mathbf{T}_{\mathrm{dr}_i} - \boldsymbol{\Delta}_t\mathbf{F}_{\mathrm{cor}_i}) + {}^{w}\mathbf{L}_{\mathrm{lat}_i}(\boldsymbol{\Delta}_t\mathbf{R}_{wi}^{-1}\mathbf{T}_{\mathrm{dr}_i} + \mathbf{F}_{\mathrm{cor}_i})\right\}, \tag{3.33}
$$

where $\mathbf{R}_{wi}$ is a diagonal matrix with $r_{w_{ij}}$ at the jth diagonal element and

$$
T_{\mathrm{dr}_i[j]} = T_{\mathrm{dr}_{ij}} \tag{3.34}
$$

To keep the model general, it will be assumed that drive torques can be applied to all wheels, including the tractor's front wheels.

The lateral wheel forces ${}^{w_{ij}}F_{w_{ij}[2]}$ are due to the cornering behavior of the tires. When a force is exerted on the tire of wheel w_{ij}, perpendicular to the wheel plane, the tire will move in a direction at a tire slip angle $\alpha_{w_{ij}}$ with respect to the wheel plane as elucidated in figure 3.3. This due to the deformation of the tires [33, 93]. This will cause a cornering force ${}^{w_{ij}}F_{w_{ij}[2]}$ in the contact patch of the tire. The relation between tire slip angle $\alpha_{w_{ij}}$ and cornering force is in general nonlinear and depends on road surface, tire pressure, weather condition, load etc..
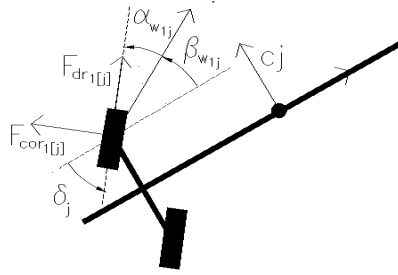
Figure 3.3: Definition of slipangles
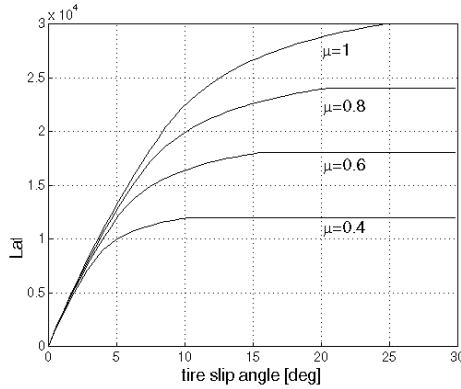
Figure 3.4: Relation between the lateral tire force and the tire slip angles, for different values of the road adhesion coefficient μ

The interaction between the road surface and the tire contact patch is usually modeled by the road adhesion coefficient μ [33, 93, 9]. Figure 3.4 shows a plot of the lateral tire force as function of the tire slip angle for different road adhesion coefficients[1]. As this plot shows, the cornering force is linear in the tire slip angle for low values of the slip angle. At high slip angles, the tire force saturates[2]. The saturation value strongly depends on the road adhesion coefficient. Under normal driving conditions, the tire slip angles are small, so that the relation between the tire force and slip angle can be approximated to be linear. In some of the vehicle guidance literature [1, 42, 41, 69, 88], the tire force is approximated with

$$^{w_{ij}}F_{w_{ij}[2]} = \mu C_{w_j}\alpha_{w_{ij}}, \tag{3.35}$$

[1]The tire model as described in [9] has been used to produce this plot
[2]In the saturation region the slope of the tire force characteristic actually is negative. This is not shown in figure 3.4

where C_{w_j} is the cornering stiffness of the tire [33, 93] and is defined as being the slope of the slip angle-lateral force characteristic around zero slip angle. However, the plot in figure 3.4 shows that the slope of the lateral tire force characteristic at small slip angles is almost independent on the road adhesion coefficient. Therefore, a better approximation is

$$^{w_{ij}}F_{w_{ij}[2]} = C_{w_j}\alpha_{w_{ij}} \tag{3.36}$$

This approximation of the tire lateral tire force will be used in this thesis.

The cornering stiffness C_{w_j} of a tire in general depends amongst others on the vertical load exerted on the tire. To illustrate this effect, figure 3.5 shows a plot of the lateral tire force as function of the tire slip angle with the vertical tire load as parameter[3]. In general, the relation between the cornering stiffness and the tire load is nonlinear. This especially has effect on the vehicle dynamics when the vehicle experiences a lateral acceleration. If this happens, a load transfer takes place from the tires on one side of the vehicle to the tires on the other side. Due to the nonlinear dependence of the cornering stiffness on the tire load, the total cornering stiffness of the tires on one axle of the vehicle will change in this condition, so that the dynamic behavior of the vehicle changes. Moreover, the rate of change of the cornering stiffnesses might be in the same dynamic range as the lateral vehicle dynamics. For bus and truck tires however, the dependence of the cornering stiffness on the tire load is only slightly nonlinear [93], so that this effect is negligible for the type of vehicle considered here. For this reason, the change in the cornering stiffness due to load transfer will be neglected. The cornering stiffnesses will also vary with changing load condition of the vehicle. However, this will be treated as model uncertainty. In this way, the cornering stiffnesses can be kept constant in the control model.

As illustrated in figure 3.3, the tire slip angle $\alpha_{w_{ij}}$ depends on the difference between the steering angle δ_j and the body side slip angle $\beta_{w_{ij}}$, which denotes the direction of the velocity of wheel w_{ij} with respect to the corresponding carriage's longitudinal axis. So,

$$\alpha_{w_{ij}} = \delta_j - \beta_{w_{ij}}, \tag{3.37}$$

The body slip angles $\beta_{w_{ij}}$ can be calculated with

$$\beta_{w_{ij}} = \begin{cases} \arctan \frac{^{c1}\dot{y}_{w,w_{ij}}(^{\chi}\mathbf{q})}{^{c1}\dot{x}_{w,w_{ij}}(^{\chi}\mathbf{q})} & \text{if } j = 1 \\ \arctan \frac{^{cj-1}\dot{y}_{w,w_{ij}}(^{\chi}\mathbf{q})}{^{cj-1}\dot{x}_{w,w_{ij}}(^{\chi}\mathbf{q})} & \text{if } j > 1 \end{cases}, \tag{3.38}$$

where χ denotes an arbitrary coordinate frame.

---

[3]The tire model as described in [9] has been used to produce this plot
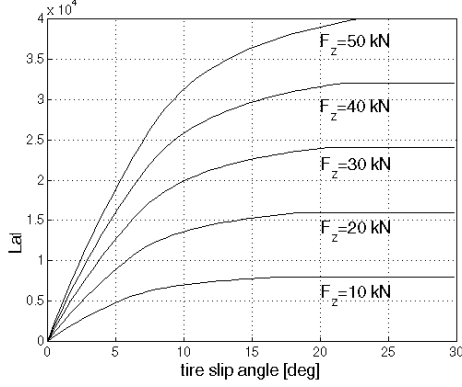
Figure 3.5: Relation between the lateral tire force and the tire slip angles, for different values of the vertical tire load

Substituting (3.37) in (3.36) yields

$$^{w_{ij}}F_{w_{ij[2]}} = C_{w_j}(\delta_j - \beta_{w_{ij}}). \tag{3.39}$$

Substituting (3.39) in turn into (3.33) yields

$$
\begin{aligned}
^w\boldsymbol{\tau}_{\text{tire}} = & \sum_{i=1}^2 {}^w\mathbf{L}_{\text{long}_i}(\mathbf{R}_{wi}^{-1}\mathbf{T}_{\text{dr}_i} + \boldsymbol{\Delta}_t\mathbf{C}_t(\boldsymbol{\delta}_t - \boldsymbol{\beta}_{ti})) + \\
& \sum_{i=1}^2 {}^w\mathbf{L}_{\text{lat}_i}(\boldsymbol{\Delta}_t\mathbf{R}_{wi}^{-1}\mathbf{T}_{\text{dr}_i} + \mathbf{C}_t(\boldsymbol{\delta}_t - \boldsymbol{\beta}_{ti})),
\end{aligned} \tag{3.40}
$$

where

$$\boldsymbol{\delta}_t = \begin{bmatrix} \delta_1 & \dots & \delta_{n+1} \end{bmatrix}^T \tag{3.41}$$

$$\mathbf{C}_t = \text{diag}(C_{w_1}, \dots, C_{w_{n+1}}). \tag{3.42}$$

and

$$\boldsymbol{\beta}_{t_j} = \begin{bmatrix} \beta_{w_{i1}} & \dots & \beta_{w_{in+1}} \end{bmatrix}^T \tag{3.43}$$

Equation (3.40) is still quadratic in the steering angles. For controller design it is desirable that the model is linear in the steering angles. However, the term $^w\mathbf{L}_{\text{long}_i}\boldsymbol{\Delta}_t\mathbf{C}_t(\boldsymbol{\delta}_t - \boldsymbol{\beta}_{ti})$ is one order of magnitude smaller than the term $\sum_{i=1}^2 {}^w\mathbf{L}_{\text{lat}_i}\mathbf{C}_t(\boldsymbol{\delta}_t - \boldsymbol{\beta}_{ti})$ and can therefore be neglected. With this omission, equation (3.40) can be written as

$$^w\boldsymbol{\tau}_{\text{tire}} = \sum_{i=1}^2 {}^w\mathbf{L}_{\text{long}_i}\mathbf{R}_{wi}^{-1}\mathbf{T}_{\text{dr}_i} + {}^w\mathbf{L}_{\text{lat}_i}(\mathbf{R}_{wi}^{-1}\boldsymbol{\mathcal{D}}(\mathbf{T}_{\text{dr}_i})\boldsymbol{\delta}_t + \mathbf{C}_t(\boldsymbol{\delta}_t - \boldsymbol{\beta}_{ti})), \tag{3.44}$$

where the equality

$$\boldsymbol{\Delta}_t\mathbf{R}_{wi}^{-1}\mathbf{T}_{\text{dr}_i} = \mathbf{R}_{wi}^{-1}\boldsymbol{\mathcal{D}}(\mathbf{T}_{\text{dr}_i})\boldsymbol{\delta}_t \tag{3.45}$$

has been used, with $\mathcal{D}(\mathbf{T}_{\mathrm{dr}_i})$ denoting a diagonal matrix with the elements of the vector $\mathbf{T}_{\mathrm{dr}_i}$ on its diagonal. In this way, the generalized tire force term of the model is linear in the steering angles.

3.5 Model overview

The total equation of motion of the all-wheel steered multiple-articulated vehicle can be obtained by substituting (3.40) and (3.17) into (3.1), yielding

$${}^w\mathbf{M}({}^w\mathbf{q}){}^w\ddot{\mathbf{q}} + {}^w\mathbf{C}({}^w\dot{\mathbf{q}}, {}^w\mathbf{q}){}^w\dot{\mathbf{q}} + {}^w\mathbf{D}_{\mathrm{art}}{}^w\dot{\mathbf{q}} =$$
$${}^w\boldsymbol{\tau}_{\mathrm{dist}} + \sum_{i=1}^{2} {}^w\mathbf{L}_{\mathrm{long}_i}\mathbf{R}_{wi}^{-1}\mathbf{T}_{\mathrm{dr}_i} + {}^w\mathbf{L}_{\mathrm{lat}_i}(\mathbf{R}_{wi}^{-1}\mathcal{D}(\mathbf{T}_{\mathrm{dr}_i})\boldsymbol{\delta}_t + \mathbf{C}_t(\boldsymbol{\delta}_t - \boldsymbol{\beta}_{ti})), \tag{3.46}$$

In this equation, the term ${}^w\mathbf{M}({}^w\mathbf{q}){}^w\ddot{\mathbf{q}}$ models the inertial forces acting on the vehicle. The term ${}^w\mathbf{C}({}^w\dot{\mathbf{q}}, {}^w\mathbf{q}){}^w\dot{\mathbf{q}}$ models the Coriolis and centrifugal forces acting on the vehicle, whereas the term ${}^w\mathbf{D}_{\mathrm{art}}{}^w\dot{\mathbf{q}}$ models the articulation angle dampers. The right hand side of (3.46) models the forces acting on the vehicle due to the tire-road interaction. In this right hand side, the term

$$\sum_{i=1}^{2} {}^w\mathbf{L}_{\mathrm{long}_i}\mathbf{R}_{wi}^{-1}\mathbf{T}_{dr_i} \tag{3.47}$$

models the forces acting on the vehicle in the longitudinal direction of the carriages, where $\mathbf{T}_{dr_i}$ is a vector with the driving torque inputs. The subscript i equals 1 for the torques on the left side and $i = 2$ for the torques on the right side. The matrix $\mathbf{R}_{wi}^{-1}$ is a diagonal matrix with the wheel diameters at the diagonal. Furthermore, $\boldsymbol{\delta}_t$ is a vector with steering angles, $\mathbf{C}_t$ is a diagonal matrix with the tire cornering stiffnesses on the diagonal and $\boldsymbol{\beta}_{ti}$ is a vector with the body slip angles of the vehicle at the connection of the wheels. Furthermore in (3.46), the term

$$\sum_{i=1}^{2} {}^w\mathbf{L}_{\mathrm{lat}_i}(\mathbf{R}_{wi}^{-1}\mathcal{D}(\mathbf{T}_{\mathrm{dr}_i})\boldsymbol{\delta}_t + \mathbf{C}_t(\boldsymbol{\delta}_t - \boldsymbol{\beta}_{ti})) \tag{3.48}$$

models the lateral forces acting on the carriages by means of the tires. In this term,

$$\sum_{i=1}^{2} -{}^w\mathbf{L}_{\mathrm{lat}_i}\mathbf{C}_t\boldsymbol{\beta}_{ti} \tag{3.49}$$

is a damping force that is caused by the tires. Due to the dependency of $\boldsymbol{\beta}_{ti}$ on the longitudinal velocity of the vehicle, this damping force decreases with increasing velocity.

3.6 Vehicle fixed coordinates

The generalized coordinate vector ${}^{w}\mathbf{q}$ contains the position of the centre of gravity of the tractor expressed in the inertial frame ${}^{w}\mathbf{x}_{w,c1}$. This means that the model (3.46) depends amongst others on the velocity of the tractor's center of gravity expressed in the inertial frame. For model analysis purposes however, it is more convenient to have a model expressed in the directions of the vehicle fixed coordinate frame $c1$. Therefore, a change of coordinates will be applied to equation (3.46).

Projecting the velocity of the tractor's centre of gravity ${}^{w}\dot{\mathbf{x}}_{w,c1}$ onto the tractor fixed frame $c1$ yields

$$
{}^{c1}\dot{\mathbf{x}}_{w,c1} = {}^{c1}\mathbf{Rot}_w\,{}^{w}\dot{\mathbf{x}}_{w,c1}. \tag{3.50}
$$

With this transformation, a new generalized coordinate vector

$$
{}^{c1}\mathbf{q} = \begin{bmatrix} {}^{c1}x_{w,c1} & {}^{c1}y_{w,c1} & {}^{w}\epsilon_{c1} & \cdots & {}^{w}\epsilon_{cn} \end{bmatrix}^T, \tag{3.51}
$$

can be defined, such that

$$
{}^{w}\dot{\mathbf{q}} = {}^{w}\mathbf{T}_{c1}\,{}^{c1}\dot{\mathbf{q}}, \tag{3.52}
$$

where

$$
{}^{w}\mathbf{T}_{c1} = \begin{bmatrix} {}^{w}\mathbf{Rot}_{c1} & \mathbf{0} \\ \mathbf{0} & \mathbf{I} \end{bmatrix}. \tag{3.53}
$$

Differentiating (3.52) with respect to time yields

$$
{}^{w}\ddot{\mathbf{q}} = {}^{w}\mathbf{T}_{c1}\,{}^{c1}\ddot{\mathbf{q}} + {}^{w}\dot{\mathbf{T}}_{c1}\,{}^{c1}\dot{\mathbf{q}}. \tag{3.54}
$$

Substituting (3.52) and (3.54) into (3.46) and premultiplying (3.46) with ${}^{w}\mathbf{T}_{c1}^{T}$ yields

$$
\begin{gathered}
{}^{c1}\mathbf{M}\,{}^{c1}\ddot{\mathbf{q}} + {}^{c1}\mathbf{C}\,{}^{c1}\dot{\mathbf{q}} + {}^{c1}\mathbf{D}_{\mathrm{art}}\,{}^{c1}\dot{\mathbf{q}} = {}^{c1}\boldsymbol{\tau}_{\mathrm{dist}} \\
\sum_{i=1}^{2}{}^{c1}\mathbf{L}_{\mathrm{long}_i}\mathbf{R}_{wi}^{-1}\mathbf{T}_{\mathrm{dr}_i} + {}^{c1}\mathbf{L}_{\mathrm{lat}_i}(\mathbf{R}_{\boldsymbol{wi}}^{-1}\boldsymbol{\mathcal{D}}(\mathbf{T}_{\mathrm{dr}_i})\boldsymbol{\delta}_t + \mathbf{C}_t(\boldsymbol{\delta}_t - \boldsymbol{\beta}_{ti}))
\end{gathered} \tag{3.55}
$$

where

$$
\begin{aligned}
{}^{c1}\mathbf{M}({}^{c1}\mathbf{q}) &= {}^{w}\mathbf{T}_{c1}^{T}\,{}^{w}\mathbf{M}({}^{c1}\mathbf{q}){}^{w}\mathbf{T}_{c1} & \text{(3.56a)} \\
{}^{c1}\mathbf{C}({}^{c1}\mathbf{q}, {}^{c1}\dot{\mathbf{q}}) &= {}^{w}\mathbf{T}_{c1}^{T}\,{}^{w}\mathbf{C}({}^{c1}\mathbf{q}, {}^{c1}\dot{\mathbf{q}}){}^{w}\mathbf{T}_{c1} + {}^{w}\mathbf{T}_{c1}^{T}\,{}^{w}\mathbf{M}({}^{c1}\mathbf{q}){}^{w}\dot{\mathbf{T}}_{c1} & \text{(3.56b)} \\
{}^{c1}\mathbf{D}_{\mathrm{art}} &= {}^{w}\mathbf{T}_{c1}^{T}\,{}^{w}\mathbf{D}_{\mathrm{art}} & \text{(3.56c)} \\
{}^{c1}\mathbf{L}_{\mathrm{long}_i}({}^{c1}\mathbf{q}) &= {}^{w}\mathbf{T}_{c1}^{T}\,{}^{c1}\mathbf{L}_{\mathrm{long}_i}({}^{c1}\mathbf{q}) & \text{(3.56d)} \\
{}^{c1}\mathbf{L}_{\mathrm{lat}_i}({}^{c1}\mathbf{q}) &= {}^{w}\mathbf{T}_{c1}^{T}\,{}^{c1}\mathbf{L}_{\mathrm{lat}_i}({}^{c1}\mathbf{q}) & \text{(3.56e)} \\
{}^{c1}\boldsymbol{\tau}_{\mathrm{dist}} &= {}^{w}\mathbf{T}_{c1}^{T}\,{}^{w}\boldsymbol{\tau}_{\mathrm{dist}}. & \text{(3.56f)}
\end{aligned}
$$

Equation (3.55) expresses the vehicle dynamics in the directions of the body fixed coordinate frame $c1$.
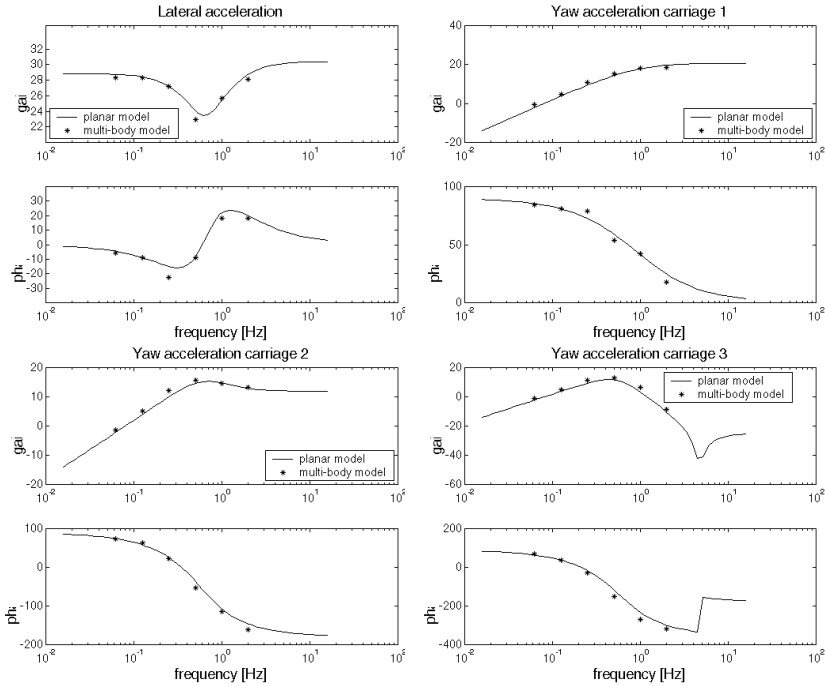
Figure 3.6: Comparison of planar model and multi-body model

3.7 Model validation

To validate the model (3.55), it has been compared with a 3D model of a double articulated commuter bus that has been programmed in a multi-body package. This multi-body model describes about 125 degrees of freedom of this bus, including the degrees of freedom of the suspension system of the vehicle. The comparison of both models has been carried out in the frequency domain. Therefore, (3.55) has been linearized numerically around a fixed longitudinal speed and zero articulation angles, to be able to produce Bode plots. The multi-body model has been excited with sinusoidal inputs at discrete frequency points. The transfer functions from front wheel steering input to the lateral acceleration of the tractor's center of gravity and the yaw accelerations of each carriage have been considered. The frequency domain analysis has been carried out at different constant speeds. As an example, figure 3.6 shows the Bode plots of the analysis at $50\,km/h$ longitudinal speed. As these plots show, the Bode plots of the planar model correspond to the body plots of the multi-body model very well.

3.8   Dynamic versus kinematic model

As already mentioned in the introduction of this chapter, a distinction can be made between dynamic and kinematic vehicle models. This section will be used to make a comparison between these two types of model. For convenience, the influence of the drive torques and the width of the vehicle will be neglected, so that

$$
\begin{array}{rcl}
\mathbf{T}_{\mathrm{dr}_i} & = & \mathbf{0} \\[4pt]
{}^{c1}\mathbf{L}_{\mathrm{lat}} & = & {}^{c1}\mathbf{L}_{\mathrm{lat}_1} = {}^{c1}\mathbf{L}_{\mathrm{lat}_2} \\[4pt]
{}^{c1}\mathbf{L}_{\mathrm{long}} & = & {}^{c1}\mathbf{L}_{\mathrm{long}_1} = {}^{c1}\mathbf{L}_{\mathrm{long}_2} \\[4pt]
\boldsymbol{\beta}_t & = & \boldsymbol{\beta}_{t1} = \boldsymbol{\beta}_{t2}
\end{array}
$$

(3.57)
(3.58)
(3.59)
(3.60)

Under these assumptions, the dynamic vehicle model (3.55) reduces to

$$
{}^{c1}\mathbf{M}({}^{c1}\mathbf{q}){}^{c1}\ddot{\mathbf{q}} + {}^{c1}\mathbf{C}({}^{c1}\dot{\mathbf{q}}, {}^{c1}\mathbf{q}){}^{c1}\dot{\mathbf{q}} + {}^{c1}\mathbf{D}_{\mathrm{art}}\,{}^{c1}\dot{\mathbf{q}} = 2\,{}^{c1}\mathbf{L}_{\mathrm{lat}}\,\mathbf{C}_t(\boldsymbol{\delta}_t - \boldsymbol{\beta}_t),
\quad (3.61)
$$

The main assumption made for the kinematic vehicle model is that there are no forces acting on the vehicle. This implies that there is no tire slip [14, 50, 77], so that the tire slip angles $\alpha_{w_{ij}}$ equal zero. Under this assumption, the equations of motion of the kinematic model can simply be derived from figure 3.3 as

$$
\boldsymbol{\beta}_t({}^{c1}\mathbf{q}) = \boldsymbol{\delta}_t.
\quad (3.62)
$$

Comparing equation (3.61) and (3.62) it is clear that the kinematic (3.62) model is a subset of the dynamic model (3.61). The kinematic model completely neglects the transient dynamics and the centrifugal- and Coriolis forces acting on the vehicle in steady state. To investigate the effect of neglecting the centrifugal- and Coriolis forces, the steering angles necessary to negotiate an ideal circular curve with radius R will be calculated for both the dynamic and kinematic model.

To facilitate this calculation, a single articulated vehicle will be considered, driving at a constant longitudinal speed v_x. Second and higher order terms of the components of the body slip angle vector $\boldsymbol{\beta}_t$ and the articulation angles will be neglected and it will be assumed that the points **s1** and **s2** are equally spaced around the tractor's center of gravity. Due to this last assumption, the lateral velocity of the tractor's center of gravity equals zero in steady state. When a single articulated vehicle negotiates a circular shaped curve with radius R, while the tracking errors equal zero, the yaw rates of both carriages equal $\frac{v_x}{R}$, so that the generalized velocity vector ${}^{c1}\dot{\mathbf{q}}$ becomes

$$
{}^{c1}\dot{\mathbf{q}} = \begin{bmatrix} v_x \\ 0 \\ \frac{v_x}{R} \\ \frac{v_x}{R} \end{bmatrix}
\quad (3.63)
$$

and the generalized acceleration equals

$$^{c1}\ddot{\mathbf{q}} = \mathbf{0}. \tag{3.64}$$

To obtain the steady state solution of the dynamic model, equations (3.63) and (3.64) have been substituted into (3.61). Solving the result for $\boldsymbol{\delta}_t$ yields

$$\delta_1 = \frac{l_{f1}}{R} + \left(\frac{(m_1 + m_2)l_{r1}}{2C_{w1}(l_{r1} + l_{f1})} - \frac{m_2(d_{r1}l_{w2} + d_{f2}l_{r1} - d_{r1}l_{f2})}{2C_{w1}(d_{f2} + l_{r2})(l_{r1} + l_{f1})} \right) \frac{v_x^2}{R} \tag{3.65a}$$

$$\delta_2 = -\frac{l_{r1}}{R} + \left(\frac{(m_1 + m_2)l_{f1}}{2C_{w2}(l_{r1} + l_{f1})} + \frac{m_2(d_{r1}l_{w2} + d_{f2}l_{f1} - d_{r1}d_{f2})}{2C_{w2}(d_{f2} + l_{r2})(l_{r1} + l_{f1})} \right) \frac{v_x^2}{R} \tag{3.65b}$$

$$\delta_3 = -\frac{d_{f2} + l_{r2} + d_{r1}}{R} + \frac{m_2 d_{f2}}{2C_{w3}l_{w2}} \frac{v_x^2}{R} + \epsilon_{fd}, \tag{3.65c}$$

where ϵ_{fd} is the articulation angle when the vehicle follows a circular curve with radius R and zero tracking error.

To calculate the steady state solution of the kinematic model, the components of the body slip angle vector $\boldsymbol{\beta}_t(^{c1}\mathbf{q})$ have been calculated with equation 3.38 at the steady state values $^w\dot{\epsilon}_{c1} = {}^w\dot{\epsilon}_{c2} = \frac{v_x}{R}$ and $v_y = 0$. Using the small angle approximation as already discussed equation (3.62) than yields

$$\delta_1 = \frac{l_{f1}}{R} \tag{3.66a}$$

$$\delta_2 = -\frac{l_{r1}}{R} \tag{3.66b}$$

$$\delta_3 = -\frac{l_{w2} + d_{r1}}{R} + \epsilon_{fd}. \tag{3.66c}$$

Comparing (3.66) and (3.65), it can be concluded that the solution for the steering angles of the dynamic model consists of the steering angles predicted by the kinematic model plus a term proportional to the square of the longitudinal velocity. So, at low velocity and for a given curvature, the solutions for the steering angles predicted by the dynamic model are approximately equal to the solutions for the steering angles predicted by the kinematic model. At high velocity, however, the steering angles predicted by the dynamic model may deviate considerably from the steering angles predicted by the kinematic model. To illustrate this, figure 3.7 shows a plot of the steering angles predicted by the dynamic and kinematic model for increasing longitudinal velocity and radius $R = 300\,m$. As the figure shows, the steering angles predicted by the dynamic model deviate considerably from the steering angles predicted by the kinematic model. At high velocity, the steering angles of the two rear axles might even change sign. The difference between the two solutions is due to the fact that for a given radius R, the centrifugal forces acting on the vehicle increase with increasing velocity. For this reason, amongst others, a dynamic vehicle model has to and will be used for controller design in this thesis.
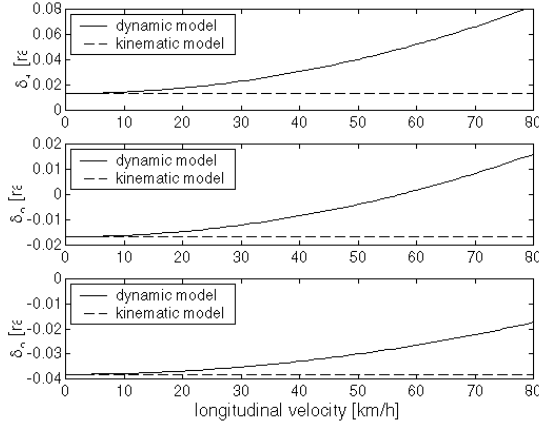
Figure 3.7: Steering angles based on dynamic model and kinematic model as function of longitudinal velocity

3.9   Output dynamics

Till so far, the vehicle dynamics have been expressed in the generalized position vector $^{c1}\mathbf{q}$. However, in chapter 2 the lateral guidance problem was formalized as a minimization problem of the tracking errors $^{psi}y_{p_{si},si}$. Therefore, a change of coordinates will be applied to equation (3.55) in order to express the vehicle dynamics in the deviations $^{psi}y_{p_{si},si}$. To change coordinates from $^{c1}\mathbf{q}$, to the tracking errors $^{psi}y_{p_{si},si}$, the following transformation will be used

$$\dot{\mathbf{Y}}_s = \mathbf{J}_{\text{path}}(^{c1}\mathbf{q})^{c1}\dot{\mathbf{q}}, \qquad (3.67)$$

where

$$\dot{\mathbf{Y}}_s = \begin{bmatrix} v_x \\ ^{ps1}\dot{y}_{p_{s1},s1} \\ \vdots \\ ^{psn+1}\dot{y}_{p_{sn+1},sn+1} \end{bmatrix}. \qquad (3.68)$$

The derivation of equation (3.67) is outlined in appendix E. This derivation uses equation 2.25, therefore, it is assumed that the tracking errors are small compared to the turning radius of the path. Note that the vector $\dot{\mathbf{Y}}_s$ contains besides the velocities $^{psi}\dot{y}_{p_{si},si}$ also the longitudinal velocity of the tractor v_x. This is done to let both $\dot{\mathbf{Y}}_s$ and $\dot{\mathbf{q}}$ have the same dimension, so that the transformation (3.67) is invertible. For the lateral guidance problem, only the lateral deviations are of interest. Therefore, the longitudinal degree of freedom will be eliminated from the vehicle model later on.

Differentiating equation (3.67) with respect to time yields

$$\ddot{\mathbf{Y}}_s = \dot{\mathbf{J}}_{\text{path}}(^{c1}\mathbf{q}, {}^{c1}\dot{\mathbf{q}})^{c1}\dot{\mathbf{q}} + \mathbf{J}_{\text{path}}(^{c1}\mathbf{q})^{c1}\ddot{\mathbf{q}}. \tag{3.69}$$

Rewriting (3.67) as

$$^{c1}\dot{\mathbf{q}} = \mathbf{J}_{\text{path}}^{-1}(^{c1}\mathbf{q})\dot{\mathbf{Y}}_s \tag{3.70}$$

and substituting this in (3.69) yields after rearranging terms

$$^{c1}\ddot{\mathbf{q}} = \mathbf{J}_{\text{path}}^{-1}(^{c1}\mathbf{q})\ddot{\mathbf{Y}}_s - \mathbf{J}_{\text{path}}^{-1}(^{c1}\mathbf{q})\dot{\mathbf{J}}_{\text{path}}(^{c1}\mathbf{q}, {}^{c1}\dot{\mathbf{q}})\,\mathbf{J}_{\text{path}}^{-1}(^{c1}\mathbf{q})\dot{\mathbf{Y}}_s. \tag{3.71}$$

Substituting (3.70) and (3.71) into (3.55) and premultiplying the result with $\mathbf{J}_{\text{path}}^{-T}(\mathbf{q})$ yields

$$\begin{aligned}
{}^Y\mathbf{M}(^{c1}\mathbf{q})\ddot{\mathbf{Y}}_s + {}^Y\mathbf{C}(^{c1}\dot{\mathbf{q}}, {}^{c1}\mathbf{q})\dot{\mathbf{Y}}_s + {}^Y\mathbf{D}(^{c1}\dot{\mathbf{q}}, {}^{c1}\mathbf{q}) = \\
{}^Y\mathbf{B}_{\text{lat}}(^{c1}\dot{\mathbf{q}}, {}^{c1}\mathbf{q}, \mathbf{T}_{\text{dr}})\boldsymbol{\delta}_t + {}^Y\mathbf{B}_{\text{long}}(^{c1}\mathbf{q})\boldsymbol{T}_{\text{dr}} + {}^Y\boldsymbol{\tau}_{\text{dist}}
\end{aligned} \tag{3.72}$$

where

$$^Y\mathbf{M}(^{c1}\mathbf{q}) = \mathbf{J}_{\text{path}}^{-T}\,{}^{c1}\mathbf{M}(^{c1}\mathbf{q})\mathbf{J}_{\text{path}}^{-1} \tag{3.73a}$$

$$^Y\mathbf{C}(^{c1}\dot{\mathbf{q}}, {}^{c1}\mathbf{q}) = \mathbf{J}_{\text{path}}^{-T}\,{}^{c1}\mathbf{C}(^{c1}\dot{\mathbf{q}}, {}^{c1}\mathbf{q})\mathbf{J}_{\text{path}}^{-1} - \mathbf{J}_{\text{path}}^{-T}\,{}^{c1}\mathbf{M}(^{c1}\mathbf{q})\mathbf{J}_{\text{path}}^{-1}\dot{\mathbf{J}}_{\text{path}}\mathbf{J}_{\text{path}}^{-1}$$

$$^Y\mathbf{D}(^{c1}\dot{\mathbf{q}}, {}^{c1}\mathbf{q}) = \mathbf{J}_{\text{path}}^{-T}\sum_{i=1}^{2}{}^{c1}\mathbf{L}_{\text{lat}_i}(^{c1}\mathbf{q})\mathbf{C}_t\boldsymbol{\beta}_{ti} + \mathbf{J}_{\text{path}}^{-T}\,{}^{c1}\mathbf{D}_{\text{art}}{}^{c1}\dot{\mathbf{q}} \tag{3.73c}$$

$$^Y\mathbf{B}_{\text{lat}}(^{c1}\dot{\mathbf{q}}, {}^{c1}\mathbf{q}, \mathbf{T}_{\text{dr}}) = \mathbf{J}_{\text{path}}^{-T}\sum_{i=1}^{2}{}^{c1}\mathbf{L}_{\text{lat}_i}(^{c1}\mathbf{q})(\mathbf{R}_{\boldsymbol{wi}}^{-1}\boldsymbol{\mathcal{D}}(\mathbf{T}_{\text{dr}_i}) + \mathbf{C}_t) \tag{3.73d}$$

$$^Y\mathbf{B}_{\text{long}}(^{c1}\mathbf{q}) = \mathbf{J}_{\text{path}}^{-T}\begin{bmatrix} {}^{c1}\mathbf{L}_{\text{long}_1}(^{c1}\mathbf{q}) & {}^{c1}\mathbf{L}_{\text{long}_2}(^{c1}\mathbf{q}) \end{bmatrix} \tag{3.73e}$$

$$\mathbf{T}_{dr} = \begin{bmatrix} \mathbf{T}_{dr_1} \\ \mathbf{T}_{dr_2} \end{bmatrix} \tag{3.73f}$$

$$^Y\boldsymbol{\tau}_{\text{dist}} = {}^{c1}\boldsymbol{\tau}_{\text{dist}}\mathbf{J}_{\text{path}}^{-T} \tag{3.73g}$$

For brevity, the dependency of $\mathbf{J}_{\text{path}}$ on $^{c1}\mathbf{q}$ and $\dot{\mathbf{J}}_{\text{path}}$ on $^{c1}\mathbf{q}$ and $^{c1}\dot{\mathbf{q}}$ has been omitted. Note that in (3.72) the damping due to the tires and the damping of the articulation angle dampers has been modeled by the term $^Y\mathbf{D}(^{c1}\dot{\mathbf{q}}, {}^{c1}\mathbf{q})$. All matrices in equation (3.72) still show dependence on $^{c1}\mathbf{q}$ and $^{c1}\dot{\mathbf{q}}$. Using equation (3.67), $^{c1}\dot{\mathbf{q}}$ can easily be transformed into $\dot{\mathbf{Y}}_s$. The matrices depend only on the last n components of $^{c1}\mathbf{q}$, representing the orientations of the carriages. Using equations (2.29), (2.31) and (2.44), these orientations can be transformed in $\mathbf{Y}_s$ and the desired generalized coordinates as defined in chapter 2.

The model (3.72) contains, besides dynamics of the outputs, also the longitudinal vehicle dynamics. For the design of the controller, it is more convenient to

extract the longitudinal dynamics from (3.72) [92]. To extract the longitudinal dynamics, it is convenient to factorize (3.72) as

$$
\begin{bmatrix} \mathbf{M}_{xx} & \mathbf{M}_{xy} \\ \mathbf{M}_{xy}^T & \mathbf{M}_{yy} \end{bmatrix} \begin{bmatrix} \dot{v}_x \\ \ddot{\mathbf{y}}_s \end{bmatrix} + \begin{bmatrix} \mathbf{C}_{xx} & \mathbf{C}_{xy} \\ \mathbf{C}_{yx} & \mathbf{C}_{yy} \end{bmatrix} \begin{bmatrix} v_x \\ \dot{\mathbf{y}}_s \end{bmatrix} + \begin{bmatrix} \mathbf{D}_x \\ \mathbf{D}_y \end{bmatrix} =
$$
$$
\begin{bmatrix} \mathbf{B}_{\mathrm{lat}_x} \\ \mathbf{B}_{\mathrm{lat}_y} \end{bmatrix} \boldsymbol{\delta}_t + \begin{bmatrix} \mathbf{B}_{\mathrm{long}_x} \\ \mathbf{B}_{\mathrm{long}_y} \end{bmatrix} \mathbf{T}_{dr} + \begin{bmatrix} \boldsymbol{\tau}_{\mathrm{dist}_x} \\ \boldsymbol{\tau}_{\mathrm{dist}_y} \end{bmatrix}, \tag{3.74}
$$

where $\mathbf{y}_s = \begin{bmatrix} {}^{p_{s1}}y_{p_{s1},s1} & \cdots & {}^{p_{sn+1}}y_{p_{sn+1},sn+1} \end{bmatrix}^T$. The superscripts Y have been omitted for brevity. Solving 3.74 for $\dot{v}_x$ yields

$$
\dot{v}_x = \mathbf{M}_{xx}^{-1}(\mathbf{B}_{\mathrm{lat}_x}\boldsymbol{\delta}_t + \mathbf{B}_{\mathrm{long}_y}\mathbf{T}_{dr} - \mathbf{M}_{xy}\ddot{\mathbf{y}}_s - \mathbf{C}_{xx}v_x - \mathbf{C}_{xy}\ddot{\mathbf{y}}_s - \mathbf{D}_x + \boldsymbol{\tau}_{\mathrm{dist}_x}) \tag{3.75}
$$

This equation describes the zero dynamics for the final closed loop system. It is assumed that the zero dynamics are stabilized either by the driver of the vehicle or a cruise control system. Substituting (3.75) in (3.74) yields

$$
{}^{y}\mathbf{M}({}^{c1}\mathbf{q})\ddot{\mathbf{y}}_s + {}^{y}\mathbf{C}_{\dot{y}}({}^{c1}\dot{\mathbf{q}}, {}^{c1}\mathbf{q})\dot{\mathbf{y}}_s + {}^{y}\mathbf{C}_{v_x}({}^{c1}\dot{\mathbf{q}}, {}^{c1}\mathbf{q})v_x + {}^{y}\mathbf{D}({}^{c1}\dot{\mathbf{q}}, {}^{c1}\mathbf{q}) =
$$
$$
{}^{y}\mathbf{B}_{\mathrm{lat}}({}^{c1}\dot{\mathbf{q}}, {}^{c1}\mathbf{q}, \mathbf{T}_{\mathrm{dr}})\boldsymbol{\delta}_t + {}^{y}\mathbf{B}_{\mathrm{long}}({}^{c1}\mathbf{q})\boldsymbol{T}_{dr} + {}^{y}\boldsymbol{\tau}_{\mathrm{dist}} \tag{3.76}
$$

with

$$
{}^{y}\mathbf{M}({}^{c1}\mathbf{q}) = {}^{Y}\mathbf{M}_{yy} - {}^{Y}\mathbf{M}_{xy}^{T}\,{}^{Y}\mathbf{M}_{xx}^{-1}\,{}^{Y}\mathbf{M}_{xy} \tag{3.77a}
$$

$$
{}^{y}\mathbf{C}({}^{c1}\dot{\mathbf{q}}, {}^{c1}\mathbf{q}) = {}^{Y}\mathbf{C}_{yy} - {}^{Y}\mathbf{M}_{xy}^{T}\,{}^{Y}\mathbf{M}_{xx}^{-1}\,{}^{Y}\mathbf{C}_{xy} \tag{3.77b}
$$

$$
{}^{y}\mathbf{C}_{v_x}({}^{c1}\dot{\mathbf{q}}, {}^{c1}\mathbf{q}) = {}^{Y}\mathbf{C}_{yx} \tag{3.77c}
$$

$$
{}^{y}\mathbf{D}({}^{c1}\dot{\mathbf{q}}, {}^{c1}\mathbf{q}) = {}^{Y}\mathbf{D}_y - {}^{Y}\mathbf{M}_{xy}^{T}\,{}^{Y}\mathbf{M}_{xx}^{-1}\,{}^{Y}\mathbf{D}_x \tag{3.77d}
$$

$$
{}^{y}\mathbf{B}_{\mathrm{lat}}({}^{c1}\dot{\mathbf{q}}, {}^{c1}\mathbf{q}, \mathbf{T}_{\mathrm{dr}}) = {}^{Y}\mathbf{B}_{\mathrm{lat}_y} - {}^{Y}\mathbf{M}_{xy}^{T}\,{}^{Y}\mathbf{M}_{xx}^{-1}\,{}^{Y}\mathbf{B}_{\mathrm{lat}_x} \tag{3.77e}
$$

$$
{}^{y}\mathbf{B}_{\mathrm{long}}({}^{c1}\mathbf{q}) = {}^{Y}\mathbf{B}_{\mathrm{long}_y} - {}^{Y}\mathbf{M}_{xy}^{T}\,{}^{Y}\mathbf{M}_{xx}^{-1}\,{}^{Y}\mathbf{B}_{\mathrm{long}_x} \tag{3.77f}
$$

$$
{}^{y}\boldsymbol{\tau}_{\mathrm{dist}} = {}^{Y}\boldsymbol{\tau}_{\mathrm{dist}_y} - {}^{Y}\mathbf{M}_{xy}^{T}\,{}^{Y}\mathbf{M}_{xx}^{-1}\,{}^{Y}\boldsymbol{\tau}_{\mathrm{dist}_y}. \tag{3.77g}
$$

The arguments on the right hand side of (3.77) have been omitted for brevity.

3.10 Actuator dynamics

The model as developed so far has the actual steering angles and drive torques of the vehicle as inputs. In reality however, both the steering angles and the drive torques have to be produced by electro-mechanic or electro-hydraulic actuators. These actuators generally have their own dynamics, that might influence the closed loop behavior. Therefore, a model of the actuators has to be included in

the control model. The steering actuators will be modeled as first order systems, so that

$$\dot{\boldsymbol{\delta}}_t = \boldsymbol{\tau}_{\mathrm{st}}^{-1}(\mathbf{u}_{\mathrm{st}} - \boldsymbol{\delta}_t), \tag{3.78}$$

where the $n + 1$ vector $\mathbf{u}_{\mathrm{st}}$ denotes the steering actuator inputs, whereas $\boldsymbol{\tau}_{\mathrm{st}}$ is a $(n + 1) \times (n + 1)$ diagonal matrix with the time constants of the steering actuators at the diagonal.

In a similar way, the drive torque actuators will modeled as

$$\dot{\boldsymbol{T}}_{\mathrm{dr}} = \boldsymbol{\tau}_{\mathrm{dr}}^{-1}(\mathbf{u}_{\mathrm{dr}} - \boldsymbol{T}_{\mathrm{dr}}), \tag{3.79}$$

where the $2(n + 1)$ vector $\mathbf{u}_{\mathrm{dr}}$ denotes the driving actuator inputs and the $2(n + 1) \times 2(n + 1)$ matrix $\boldsymbol{\tau}_{\mathrm{dr}}$ is a diagonal matrix with the time constants of the torque actuators at the diagonal.

3.11   Summary

In this chapter, the derivation of a model, meant for controller design, of an all-wheel steered multiple-articulated vehicle has been presented. The main assumptions made for this model are:

- only planar motion

- small steering angles

- small tire slip angles and consequently a linear tire-force characteristic

- constant cornering stiffness

- wheel dynamics can be neglected

- non-zero longitudinal speed

This control model, has been validated by comparing it with a 125 degrees of freedom multi-body model. This comparison showed that the planar dynamics described by the control model correspond reasonably well to the planar dynamics as described by the multi-body model.

The control model has been used to show that a dynamic vehicle model is required to describe the planar vehicle dynamics, especially at high speed.

A change of coordinates has been applied to express the vehicle model in the tracking error dynamics. For this transformation, it has been assumed that the tracking errors are small compared to the turning radius of the path.

4

Simulation model

4.1   Introduction

The nonlinear planar vehicle model as discussed in the previous chapter is mainly meant for controller design purposes and is for this reason kept as simple as possible. To simulate the behavior of the lateral guidance system, a more complex vehicle model will be used, including a suspension system to simulate the vehicle's roll and pitch motion. Moreover, a more complex tire model will be used that also describes the load dependence of the cornering stiffnesses and the nonlinear tire force characteristic. The dynamic part of the model is mainly taken from [86]. Therefore, only the features of the model and the modifications made to the model as described in [86] will be discussed in section 4.2. The tire model as proposed by [86] is described in [9]. In this thesis, a simplified version of this model will be used. This simplified tire model will be discussed in section 4.3. The model as described in [86] has been extended with a wind disturbance model, that will be discussed in section 4.5. The path to be followed is added to the model in order to be able to calculate the deviations from the track, as described in more detail in section 4.6. The contribution of this chapter has been summarized in section 4.7

4.2   Body dynamics

In [86], the body of the n-carriage multiple articulated vehicle has been modeled as a system of n free rigid bodies, actuated by means of external forces and constraint forces, as illustrated in figure 4.1. The external forces are given by the tire forces and the forces acting on the body by means of the suspension system. Besides these forces, also a wind disturbance force and a wind disturbance moment are added to the model. The suspension forces acting on the carriages
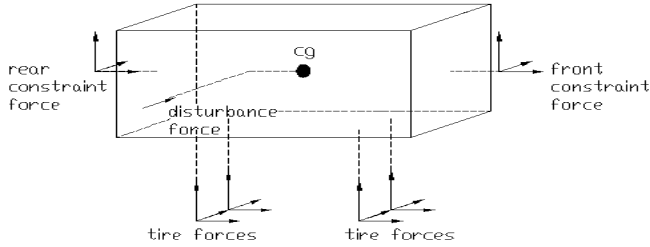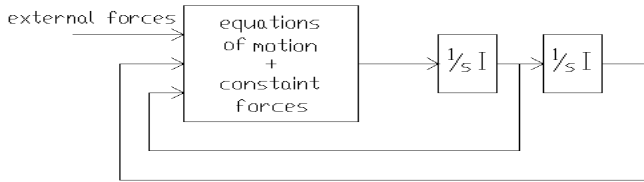
Figure 4.1: Forces acting on each carriage

Figure 4.2: Structure of simulation model

are modeled by a simple suspension system, formed by a linear damper and a linear spring, connecting each wheel to the vehicle.

Each unconstrained rigid body has 6 degrees of freedom. Each degree of freedom is associated with 2 states, which represent a generalized position and a generalized velocity. The constraint forces connect the free bodies to each other. Each constraint force is associated with one eliminated degree of freedom. In the model as described in [86], constraint forces are used to constrain the vertical, longitudinal and lateral motion of the carriages. Furthermore, the roll motions of the carriages are coupled, as will be described later on. All together there are $4n - 4$ constraint forces, so that in total $2n + 4$ degrees of freedom or $4n + 8$ states remain. The generalized accelerations of these remaining degrees of freedom can be solved numerically from the equations of motion of the carriages and the constraint force equations and can can be solved from these equations numerically. The accelerations can subsequently be integrated to obtain the states of the simulation model, as illustrated in figure 4.2.

In the model as described in [86], the hitching mechanism connecting the carriages is a so called fifth-wheel connection. Figure 4.3 shows a simplified picture of the hitching mechanism used for articulated busses. Though the construction differs from the construction of a fifth-wheel connection, the hitching mechanism as depicted in figure 4.3 has the same effect. There is one axis of
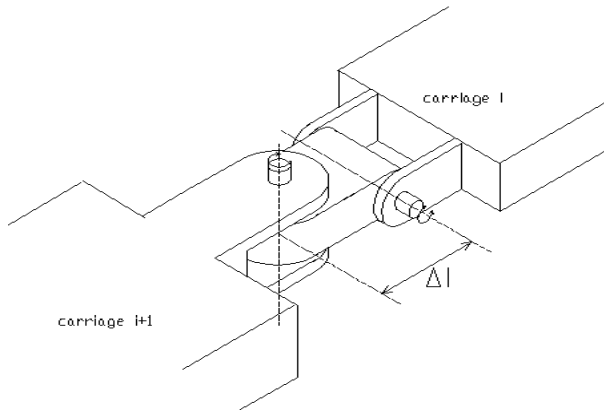
Figure 4.3: Hitching mechanism connecting the carriages

rotation in the z-direction of carriage $i + 1$ and one axis of rotation in the y-direction of carriage i. This type of construction couples the roll motions of the carriages when the articulation angles are small. When the articulation angles are 90^0, the roll motion of carriage i is completely coupled with the pitch motion of carriage $i + 1$. The axes of rotation, as depicted in figure 4.3, in general do not intersect, but have a small offset. In the model of the hitching mechanism as used in the simulation model, this offset has been neglected. The friction in the hitching mechanism has completely be neglected in the simulation model.

4.3   Tire model

The tire model used in the vehicle simulation model is a simplified version of the tire model as presented in [9]. The main simplification the omission of the friction model. This friction model calculates, given a number of parameters like tire groove depth, road texture and tire wear, the road adhesion coefficient μ of the tire [33, 93]. For the vehicle simulation model as described in this chapter, it is of less importance how this road adhesion coefficient is determined. For this reason, the friction model is completely omitted. The most important characteristics of the tire model as presented in [9] are the nonlinear relation between the lateral force and tire slip angle and the load dependence of the cornering stiffness (see also section 3.4). These characteristics are completely maintained in the tire model used for the simulation model. For the simulation model, type $385/65R.22$ tires were used. For these tires, a number of values of the cornering stiffness for different values of the tire load were obtained. A second order-polynomial was fitted through these points to model the load
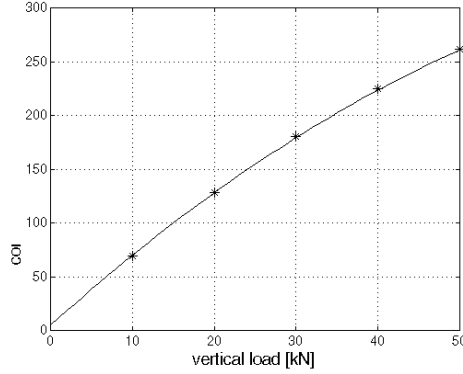
Figure 4.4: Relation between the cornering stiffness and the vertical tire load

dependence of the cornering stiffness. Figure 4.4 shows a plot of the cornering stiffness, that was obtained in this way. The plot also shows the data points that where used. It can be seen that the second-order polynomial is a good fit through these points. For the vehicle considered in this thesis, the cornering stiffnesses range from $10.000\,N/rad$ for the tractor's front axle in case of an empty vehicle to $26000N/rad$ for the wheels of the semi-trailers in case of a full vehicle

4.4   Actuator models

The steering system of a real vehicle consists of a difficult to model hydraulic and mechanical and/or electro- mechanical part. For the simulation model, this steering system is approximated with a first order model, for small steering angles and small steering angle rates. In a real steering system, the steering angles are bounded to a maximum $\delta_{t_{[i]\mathrm{max}}}$ due to the construction of the steering mechanisms, where $\delta_{t_{[i]}}$ denotes the ith component of the steering input vector $\boldsymbol{\delta}_t$ as defined in the previous chapter. Moreover, the rate of change of the steering angles is bounded by an upper bound $\dot{\delta}_{t_{[i]\mathrm{max}}}$. In the simulation model, these effects have been approximated by a saturation on the steering angles and a saturation on the rate of change of the steering angles. Figure 4.5 shows a block scheme of the actuator model as used in the simulations. In this figure, $\tau_{\mathrm{st}[i]}$ denotes the time constants of the steering actuator corresponding with steering input $\delta_{t_{[i]}}$. In the simulation model, these time constants are set to $0.032\,s$, representing a bandwidth of $5\,Hz$. The maximum steering angles $\delta_{t_{[i]\mathrm{max}}}$ are set to $0.5\,rad$, whereas the maximum rate of change of the steering angles $\dot{\delta}_{t_{[i]\mathrm{max}}}$ is set to $0.35\,rad/s$.
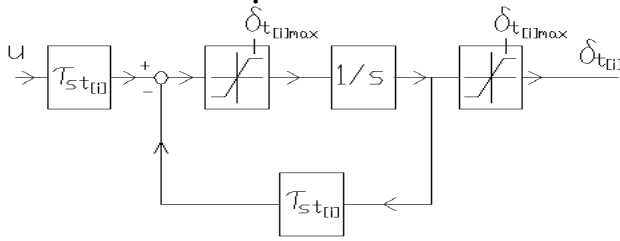
Figure 4.5: Block scheme of actuator

For the simulation results in this thesis, the drive torque actuators are of less importance. and therefore not included in the simulation model.

4.5 Wind disturbance model

When a vehicle is exposed to wind, it experiences a force due to this wind [61, 83]. This section will be dedicated to the modeling of this wind force. For lateral guidance, only lateral disturbances and disturbing yaw moments are of importance. Therefore only the wind forces acting on the vehicle in the lateral direction will be modeled.

The physics behind an airflow over a vehicle are hard to express in mathematical equations. Therefore, the semi empirical wind force model as discussed in [61] and [83] will be used. This model can be written as

$$F_{wy} = \frac{1}{2}\rho_a C_{wd} A_c v_{\text{rwind}_y}|v_{\text{rwind}_y}|, \tag{4.1}$$

where ρ_a is the mass density of the air surrounding the vehicle, C_{wd} the aerodynamic drag coefficient, A_c the total area of the vehicle that is exposed to the wind and v_{rwind_y} is the effective relative velocity of the wind towards the side of the vehicle. For the simulations including wind disturbances, only strong wind disturbances are of interest. Therefore, the lateral velocity of the vehicle will be low compared to the wind velocity, and can be neglected. Then

$$v_{\text{rwind}_y} = v_{\text{wind}_y}, \tag{4.2}$$

where v_{wind_y} is the velocity of the wind with respect to the world and directed perpendicular to the vehicle.

The mass density of the air depends amongst others on temperature, pressure and humidity conditions. However, a good value for ρ_a at sea level is $1.225\,kgm^{-3}$ [83]. The dynamic drag coefficient C_{wd} depends on the shape of

the vehicle and has actually to be determined empirically for each vehicle. For commuter busses however, a good approximation for the shape of the side will be a flat plate, of which the drag coefficient equals 1.28.

In the simulation model, it is assumed that a separate disturbance force acts on each carriage, at a distance x_{wind} in front of the center of gravity, resulting in a force ${}^{cj}F_{cj_{wy}}$ in the center of gravity of each carriage and a resulting yaw moment $M_{j_{wy}}$ acts around the center of gravity of the tractor and around each articulation point.

4.6 Tracking errors

The simulation model as described so far, only describes the dynamics of the vehicle. To validate the lateral guidance system and to simulate the magnetic referencing system that will be discussed in the next chapter, it is necessary to calculate the true tracking errors from these vehicle dynamics and the path to be followed.

At straight and circular path sections, the tracking errors can easily be expressed in the position vector ${}^{w}\mathbf{x}_{w,si}$ by means of local analytic expressions. To obtain ${}^{w}\mathbf{x}_{w,si}$, the velocity ${}^{w}\dot{\mathbf{x}}_{w,si}$ has been calculated with

$$
{}^{w}\dot{\mathbf{x}}_{w,si} = {}^{si}\mathbf{Rot}_{si}\,{}^{si}\dot{\mathbf{x}}_{w,si} \tag{4.3}
$$

and integrated to arrive at ${}^{w}\mathbf{x}_{w,si}$.

For the fifth-order polynomial path segments, as discussed in chapter 2, it is difficult to find an analytic relation between the tracking errors and ${}^{w}\mathbf{x}_{w,si}$. Therefore, the tracking errors have been calculated numerically for these path segments. To do this, ${}^{psi}y_{psi,si}$ has been written as

$$
{}^{psi}y_{psi,si} = sgn({}^{psi}y_{psi,si})|{}^{psi}y_{psi,si}|, \tag{4.4}
$$

where

$$
sgn({}^{psi}y_{psi,si}) = \begin{cases} 1 & \text{if } {}^{psi}y_{psi,si} \geq 0 \\ -1 & \text{if } {}^{psi}y_{psi,si} < 0 \end{cases}. \tag{4.5}
$$

Since, according to the definition of the coordinate frames p_{si} as given in chapter 2, the magnitude of ${}^{psi}y_{psi,si}$ equals the minimum distance from the point **si** to the path, $|{}^{psi}y_{psi,si}|$ can be calculated by solving

$$
|{}^{psi}y_{psi,si}| = \min_{{}^{w}x_{w,p}} \sqrt{({}^{w}x_{w,si} - {}^{w}x_{w,p})^2 + ({}^{w}y_{w,si} - {}^{w}y_{w,p})^2}, \tag{4.6}
$$

where

$$
{}^{w}\mathbf{x}_{w,p} = \begin{bmatrix} {}^{w}x_{w,p} \\ {}^{w}y_{w,p} \end{bmatrix}. \tag{4.7}
$$

denotes the position vector of a point on the path, expressed in and with respect to the world fixed frame w. To calculated $^w y_{w,p}$, the path has locally been described by

$$^w y_{w,p} = f(^w x_{w,p}), \tag{4.8}$$

where f is a fifth-order polynomial in $^w x_{w,p}$. The value of $^w x_{w,p_{si}}$ is the value of $^w x_{w,p}$ for which equation (4.6) attains its minimum.

The sign of $^{p_{si}} y_{p_{si},si}$ can be determined by calculating the cross product of the direction vector

$$\begin{bmatrix} \cos {}^w\epsilon_{si} \\ \sin {}^w\epsilon_{si} \\ 0 \end{bmatrix} \tag{4.9}$$

of coordinate frame si and the vector

$$\begin{bmatrix} {}^w x_{w,si} - {}^w x_{w,p_{si}} \\ {}^w y_{w,si} - {}^w y_{w,p_{si}} \\ 0 \end{bmatrix} \tag{4.10}$$

The sign of the third component of the resulting vector equals the sign of $^{p_{si}} y_{p_{si},si}$, so

$$sgn(^{p_{si}} y_{p_{si},si}) = sgn \left(\begin{bmatrix} 0 & 0 & 1 \end{bmatrix} \left\{ \begin{bmatrix} \cos {}^w\epsilon_{si} \\ \sin {}^w\epsilon_{si} \\ 0 \end{bmatrix} \times \begin{bmatrix} {}^w x_{w,si} - {}^w x_{w,p_{si}} \\ {}^w y_{w,si} - {}^w y_{w,p_{si}} \\ 0 \end{bmatrix} \right\} \right). \tag{4.11}$$

In this way, the sign of $^{p_{si}} y_{p_{si},si}$ can be determined independently of the driving direction of the vehicle, i.e it doesn't matter whether the path is driven in clockwise or counter clockwise direction.

4.7 Summary

A 3D simulation model, to simulate an all-wheel steered multiple-articulated vehicle under lateral guidance has been presented. This 3D model describes, besides the planar dynamics, also the vertical dynamics due to the suspension system. A nonlinear tire model is used for the simulation model. This tire model describes also the saturation and load dependence of the lateral tire force characteristic.

To investigate the influence of lateral wind disturbances, a model of lateral wind forces has been included in the simulation model.

5

Absolute position estimation

5.1   Introduction

For the automated guidance of vehicles, it is necessary to have information about the distance from one or more points on the vehicle to the path to be followed. This chapter is dedicated to discuss a measurement method to determine this distance. This method utilizes a magnetic referencing system which consists of discrete permanent magnets that are buried in the road. The distance to the magnet can be determined from the measurement of the longitudinal and lateral component of the magnetic field around the magnets. To motivate the choice for permanent magnets, section 5.2 will be used to discuss different methods to measure the distance to the path. In section 5.3, the problem of measuring the distance to the path will be restated in determining the position with respect to a magnet. Also the problems involved with determining this position will be discussed in this section. How to obtain the position with respect to the magnet from the readings of a dual-axes magnetic field sensor will be discussed in section 5.4. Since this measurement method, based on one sensor, is too sensitive to slant of magnet and/or vehicle, the use of a second dual-axes sensor to reduce this sensitivity will be discussed in section 5.5. Measurement results obtained with a static measurement setup will be discussed in section 5.6. Final conclusions of this chapter will be presented in 5.7.

5.2   Literature overview

In literature, many methods can be found to determine the distance from a vehicle to a path. These methods utilize amongst others

- vision

- gps

- transponder

- radar beacons

- passive/active wire

- magnetic tape

- permanent magnets

The methods utilizing vision [10, 12, 32, 93] use cameras to detect the road boundaries and/or road markings in order to calculate the distance to the road centerline. Main disadvantage of vision based system is the need for visibility. This might be a problem when for example the road markings are covered with leaves, snow, water or dirt.

With normal gps, the position of a vehicle can be determined within $100\,m$ accuracy. For vehicle guidance, this is far from accurate enough. However, by using dgps, i.e. using a ground station, and using the phase information of the carrier of the gps signal, centimeter accuracy can be achieved [7, 13, 24, 56, 62, 65]. An advantage of this method is that almost no changes have to be made to the existing road infrastructure. The main disadvantage of using gps satellites is that satellites are not always visible in between buildings and underneath bridges and tunnels. Moreover, availability of the gps system is not guaranteed by the owner of the gps satellites.

Passive beacons can also be used to determine the position of a vehicle. The passive beacons are mounted in the road surface. An antenna mounted on a vehicle broadcasts a signal, which can be received by one of the beacons. Once this signal is received, the transponder sends a signal back that contains the position information. The energy required to send a signal back is withdrawn from the received signal. This method of position measurement is commercially available. Disadvantage is that it is only applicable for vehicles traveling at low speed. When the speed is too high, the vehicle travels too far between the time it sends a signal to the transponder and the transponder sends a signal back. This makes this method useless for the guidance system discussed in this thesis.

The last three listed methods use magnetic fields to mark the path to be followed. Advantage of marking a path in this way is that the path is 'visible' under all weather circumstances. The methods relying on wires, that are buried in the road [36, 45, 49], have the disadvantage of requiring relatively expensive changes to the infrastructure. Moreover, the methods using active wires need current supplies along the road, which are also expensive in maintenance. The wires are also sensitive to strokes of lightning and subsiding of the road. Both may cause cracks in the wires.
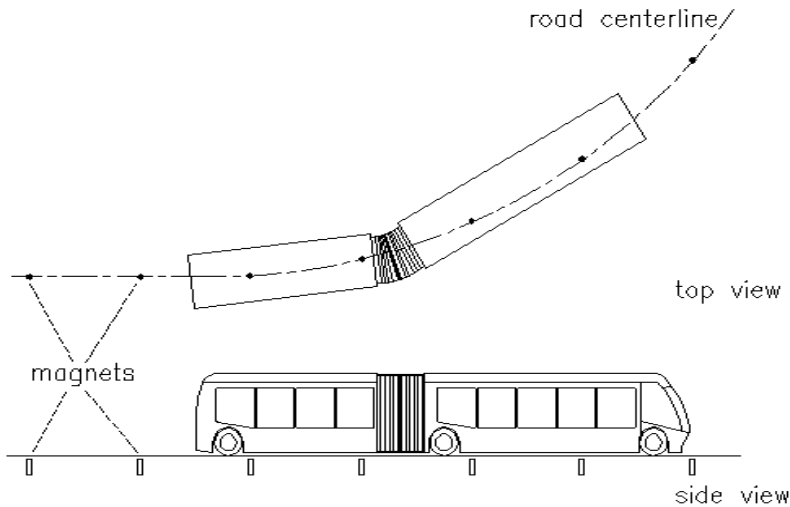
Figure 5.1: Illustration of by permanent magnet marked bus lane

In [82], a marking method based on magnetic tape has been discussed. This tape is made in the same form as normal road markings and is embedded with a magnetizable material. The path to be followed can simply be marked by sticking this tape on the road. Practice still has to show how robust this kind of tape is.

The most promising magnetic field based methods use a magnetic referencing system consisting of discrete permanent magnets that are buried in the road [6, 26, 29, 98, 99]. By measuring the magnetic fields produced by this magnets, the position of the magnet with respect to the vehicle can be determined. This method needs only relatively cheap changes to the infrastructure. Once the magnets are installed, no further maintenance is required for the first 10 years. The magnets are believed to loose their strength only slowly. Moreover, the magnets need no extra power supply to produce the magnetic field. In the remaining of this chapter, a new method for determining the position of the vehicle with respect to the magnets of a magnetic referencing system will be discussed.

5.3   Problem description

The objective of the magnetic referencing system is to provide the lateral guidance system of the vehicle with information about the position of the carriages
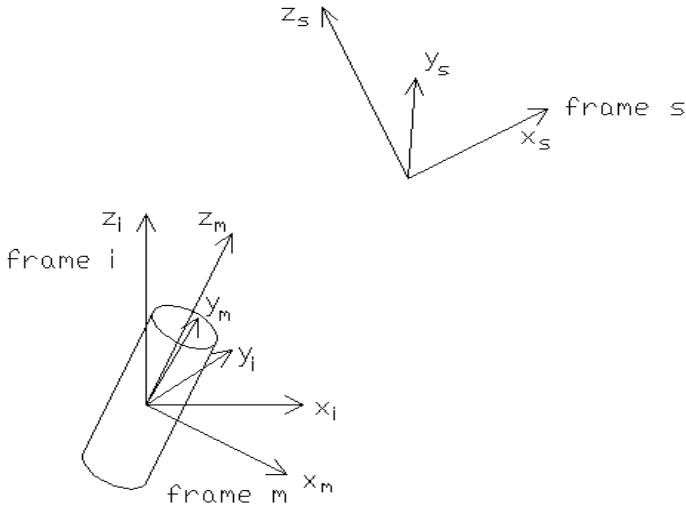
Figure 5.2: Definition of coordinate frames

of the vehicle with respect to the path to be followed. To accomplish this, it is required that a number of permanent rotation symmetric bar magnets are placed at a known position underneath the road surface of the path to be followed, as illustrated in figure 5.1.

Before explaining how the permanent magnets can be used to determine the position, the following coordinate frames, as illustrated in figure 5.2, will be defined

- Sensor-fixed coordinate frame s

  The right-handed coordinate frame s is fixed to the magnetic field sensor measuring the magnetic fields. Since these sensors are assumed to be mounted on the vehicle's sprung mass, coordinate frame s is subjected to the roll and pitch motion of the vehicle. When the vehicle is at rest, the x-axis of frame s points in the forward direction of the vehicle and the z-axis is directed vertical and points upwards.

- Magnet-fixed coordinate frame m

  The origin of the right-handed coordinate frame m is also fixed at the center of gravity of the magnet. The z-axis of this frame is directed along the symmetry axis of the magnet and is pointing upwards. Due to slant of the magnet, this z-axis is not necessarily perpendicular to the road

surface. The x-axis is directed such that its projection on the horizontal plane points in the driving direction of the vehicle.

- Ideal magnet-fixed coordinate frame i

  The origin of the right-handed frame i is fixed to the center of gravity of the magnet. The z-axis of coordinate frame i is directed perpendicular to the road surface and points upwards. When the magnet is placed exactly perpendicular to the road surface, the frames m and i coincide. When this is not the case,the x-axis and y-axis can be found by rotating frame m with

$$
{}^i\mathbf{Rot}_m = \begin{bmatrix} \cos\beta_m & 0 & \sin\beta_m \\ -\sin\alpha_m\sin\beta_m & \cos\alpha_m & \sin\alpha_m\cos\beta_m \\ -\cos\alpha_m\sin\beta_m & -\sin\alpha_m & \cos\alpha_m\cos\beta_m \end{bmatrix}, \quad (5.1)
$$

  where α_m denotes the angle of the rotation of the magnet fixed frame around its x-axis and β_m denotes the angle of the rotation around the rotated y-axis[1]. Since the magnet is rotation symmetric, and due to the definitions of the frames m, i and s rotations around the z-axis of the magnet can be neglected.

According to these definitions, determining the position of the magnet boils down to determining the position vector components ${}^i x_{i,s}$ and ${}^i y_{i,s}$. How to calculate the distance to the path from ${}^i x_{i,s}$ and ${}^i y_{i,s}$ and how to determine the exact position of the magnets with respect to the path online will be discussed in subsection 6.8.1. This chapter will continue with discussing how ${}^i x_{i,s}$ and ${}^i y_{i,s}$ can be determined from measurements of the magnetic fields produced by the permanent magnets.

Using a dipole approximation, the field of a permanent rotation symmetric bar magnet, observed at position ${}^m\mathbf{x}_{m,s}$ and expressed in the directions of frame m, can be expressed as [5, 98]

$$
\begin{array}{rcll}
{}^m B_x({}^m\mathbf{x}_{m,s}) &=& 3f(r){}^m z_{m,s}{}^m x_{m,s} & (5.2a) \\
{}^m B_y({}^m\mathbf{x}_{m,s}) &=& 3f(r){}^m z_{m,s}{}^m y_{m,s} & (5.2b) \\
{}^m B_z({}^m\mathbf{x}_{m,s}) &=& f(r)(2{}^m z_{m,s}{}^2 - {}^m x_{m,s}{}^2 - {}^m y_{m,s}{}^2), & (5.2c)
\end{array}
$$

where

$$
f(r) = \frac{\mu M}{4\pi r^5} \quad (5.3)
$$

and

$$
r = \sqrt{{}^m x_{m,s}{}^2 + {}^m y_{m,s}{}^2 + {}^m z_{m,s}{}^2} \quad (5.4)
$$

[1]The order of rotationis first around the y-axis and subsequently around the rotatedx-axis

In (5.3), M is the strength of the magnet and μ is the permeability of the environment in which the magnet is placed. It is assumed that μ is constant everywhere around the magnet.

The magnetic field components in equation (5.2) are expressed in the directions of the magnet fixed frame m. These field components will however be 'observed' in the directions of the sensor fixed coordinate frame s. The fields

$$
{}^m\mathbf{B} = \left[\begin{array}{c} {}^m B_x \\ {}^m B_y \\ {}^m B_z \end{array} \right] \tag{5.5}
$$

can be expressed in the directions of coordinate frame s with

$$
{}^s\mathbf{B} = {}^s\mathbf{Rot}_m \, {}^m\mathbf{B} = {}^s\mathbf{Rot}_i \, {}^i\mathbf{Rot}_m \, {}^m\mathbf{B}, \tag{5.6}
$$

with

$$
{}^s\mathbf{Rot}_i = \left[\begin{array}{ccc} \cos\beta_s & 0 & -\sin\beta_s \\ -\sin\alpha_s \sin\beta_s & \cos\alpha_s & -\sin\alpha_s \cos\beta_s \\ \cos\alpha_s \sin\beta_s & \sin\alpha_s & \cos\alpha_s \cos\beta_s \end{array} \right], \tag{5.7}
$$

where α_s denotes the angle of rotation of the sensor fixed frame around its x-axis and β_s denotes the angle of rotation of the sensor frame around its y-axis[2].

Equation (5.2) expresses the magnetic fields in the position vector ${}^m\mathbf{x}_{m,s}$. For the lateral guidance system the position vector ${}^i\mathbf{x}_{m,s}$ is however more interesting. The vector ${}^m\mathbf{x}_{m,s}$ can be expressed in ${}^i\mathbf{x}_{m,s}$ with

$$
{}^m\mathbf{x}_{m,s} = {}^i\mathbf{Rot}_m^{-1} \, {}^i\mathbf{x}_{m,s} \tag{5.8}
$$

The equations (5.6) and (5.8) express the magnetic fields in 7 independent variables (3 position vector components and 4 orientations). From these variables, ${}^i x_{i,s}$ and ${}^i y_{i,s}$ have to be determined from the magnetic field components independently from the other variables. To explain how this can be done, it will initially be assumed that the orientations of the frames m, i and s are the same, so that

$$
{}^m\mathbf{x}_{m,s} = {}^i\mathbf{x}_{m,s} = {}^s\mathbf{x}_{m,s} \tag{5.9}
$$

and

$$
{}^m\mathbf{B} = {}^i\mathbf{B} = {}^s\mathbf{B}. \tag{5.10}
$$

In this way, only 3 independent variables are left. This assumption will be relaxed later on to analyze the effect of the rotations.

To give an idea of the shape of the magnetic fields, figure 5.3 shows a plot of ${}^m B_y$ and ${}^m B_z$ as function of ${}^m y_{m,s}$ for different values of ${}^m z_{m,s}$ [3]. For a

---

[2]The order of rotation is first around the y-axis and subsequently around the rotated x-axis
[3]Note that due to the rotation symmetry of the field equations ${}^m B_y$ and ${}^m y_{m,s}$ can be replaced with ${}^m B_x$ and ${}^m x_{m,s}$ respectively to yield the same plot.
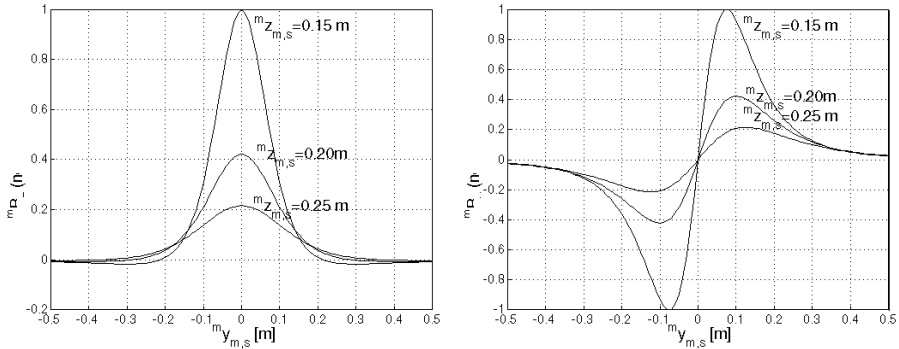
Figure 5.3: Plot of ^mB_z (left figure) and ^mB_y (right figure) as function of $^my_{m,s}$, with $^mz_{m,s}$ as parameter.

fixed and known measurement height $^mz_{m,s}$, the lateral position component $^my_{m,s}$ of the magnet can in principle be determined by measuring the field ^sB_y only. In practice however, the measurement height will not be constant, since the sensors are mounted on the vehicle's sprung mass. As figure 5.3 shows, equation (5.2b) depends strongly on $^mz_{m,s}$. The slope of ^sB_y at $^sy_{m,s} = 0$ varies due to variations in $^mz_{m,s}$. Therefore, it is impossible to obtain accurate position measurements when only the field ^mB_y is used. Moreover, the slope also depends on the strength of the magnet. The strength of the magnets may decrease slowly due to wear of the magnet when the magnets are placed underneath the road surface for several years, so that the slope of the field ^mB_y will also decrease, which makes it cumbersome to obtain an accurate position measurement by measuring ^mB_y only.

This short analysis shows that is difficult to determine $^my_{m,s}$ by measuring one magnetic field component only. Moreover determining $^mx_{m,s}$ was even not considered yet. Therefore, other field components have to be measured to come to a correct determination of $^my_{m,s}$ and $^mx_{m,s}$.

In literature, several methods to determine the lateral deviation independent of the measurement height can be found. For example the method described in [6, 98, 99] combines observations of ^mB_y and ^mB_z by means of a lookup table to come to $^my_{m,s}$. The vector component $^mx_{m,s}$ is determined by detecting when the magnetic field sensor is on top of the magnet, by means of a peak detection of the ^mB_z field. This method however still depends on the strength of the magnet. When for example the strength of the magnet decreases due to wear of the magnet, the lookup table should be corrected for the new strength regularly.

The method presented in [29] is both independent on the strength of the magnet and the measurement height, but is relatively complicated and very

sensitive to slant of the magnet and pitch motions of the vehicle, as can be shown by some simple analysis. The same applies to the method explained in [26]. Though this method is not as complicated as the method in [29], it is still very sensitive to slant of the magnet and pitch motions of the vehicle. In the next sections, a new method is proposed, which avoids all above disadvantages.

5.4   Symmetric measurement method

Using the rotation symmetry of the fields around the bar magnet, the vector component $^{i}y_{m,s}$ can be obtained from measurements of $^{s}B_x$ and $^{s}B_y$ as

$$^{i}y_{m,s} = \frac{^{s}B_y}{^{s}B_x}\,^{i}x_{m,s}, \tag{5.11}$$

under the condition that $^{s}B_x \neq 0$ [4]. In this way, $^{i}y_{m,s}$ can be estimated independent of the magnet strength M and the measurement height $^{i}z_{m,s}$, since both cancel completely out as follows by substituting (5.2a) and (5.2b) into (5.11).

As equation (5.11) shows, it is required that $^{i}x_{m,s}$ is known in order to estimate $^{i}y_{m,s}$. There are several possibilities to determine $^{i}x_{m,s}$. For example, when the signal $^{s}B_x$ crosses zero after a peak or valley at $t = t_0$, the sensor is exactly above the y-axis of coordinate frame m. Assuming the longitudinal acceleration is small, $^{i}x_{m,s}$ can be determined at $t = t_1$ with

$$^{m}x_{m,s} = v_x(t_1 - t_0), \tag{5.12}$$

where v_x is the longitudinal velocity of the vehicle. In this way, $^{i}y_{m,s}$ can in principle be determined continuously for $t > t_0$, till the measured signals disappear in the measurement noise. A disadvantage of this method is that the accuracy of the determination of $^{i}x_{m,s}$ depends on the accuracy with which the velocity v_x can be determined. By using two sensors instead of one, a different approach can be followed, that is independent of the vehicle velocity. Assume that both sensors are placed at a distance d from each other on the vehicle's longitudinal axis, as shown in figure 5.4. $^{i}x_{m,s}$ can be determined in three different ways, by combining both sensors.

1. When the $^{s}B_{x_{\text{front}}}$ field measured by the front sensor crosses zero after a peak or valley, $^{i}x_{m,s} = 0$ for the front sensor. Since the distance between the sensors is given by d, $^{i}x_{m,s}$ equals d for the rear most sensor and $^{i}y_{m,s}$ can be determined with this sensor

2. When the $^{s}B_{x_{\text{rear}}}$ field measured by the rear sensor crosses zero after a peak or valley, the rear sensor is exactly above the magnet. Now $^{i}x_{m,s}$ equals $-d$ for the front sensor and $^{i}y_{m,s}$ can be determined with this sensor

---

[4]Note that still the same orientations of the frames m, i and s is assumed
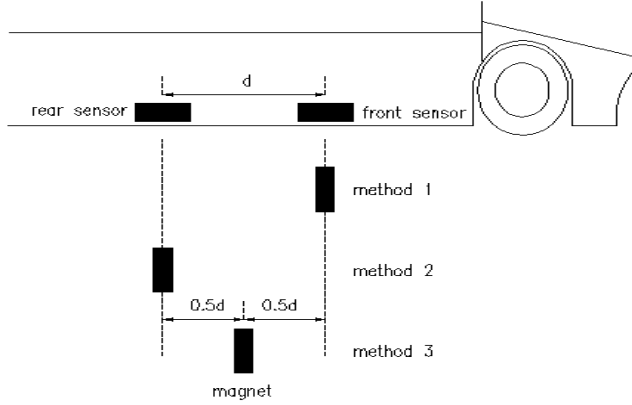
Figure 5.4: Sensor setup for two magnetic field sensors

3. When the signal $^{s}B_{x_{\text{front}}} + {}^{s}B_{x_{\text{rear}}}$ crosses zero after a peak or valley, the magnet is exactly in between the two sensors, so that $^{i}x_{m,s} = \frac{1}{2}d$ for the rear sensor and $^{i}x_{m,s} = -\frac{1}{2}d$ for the front sensor. Both sensors can be used to determine $^{i}y_{m,s}$

One and another is clarified in figure 5.4. The last method has the advantage that both measured deviations can be combined to cancel some of the effects of slant of the magnet and/or vehicle as will be discussed in the next section.

5.5   Corrected symmetric measurement method

In the previous section, it was assumed that the frames m, s and i have the same orientation. In this section, the effect of slant and magnet and/or vehicle will be analyzed.

Figure 5.5 shows the lateral deviation that would be determined in case $\alpha_s = \alpha_m = \beta_s = \beta_m = 5^0$ versus the true lateral deviation $^{i}y_{m,s}$. As this figure shows, there is a small error around $^{i}y_{m,s} = 0$ and an error becoming unacceptably large for $\|^{i}y_{m,s}\| \geq 0.3\,m$. So as long as the measurement range does not need to be larger than $0.3\,m$, the lateral deviation can be estimated with equation (5.11) reasonably well.

To analyze which type of slant has the most influence for $\|^{i}y_{m,s}\| \geq 0.3\,m$, figures 5.6 and 5.7 shows the lateral deviation from the magnet that would be determined in case $\alpha_s = \alpha_m = 0^0\,\beta_s = \beta_m = 5^0$ resp. $\alpha_s = \alpha_m = 5^0\,\beta_s = \beta_m = 0^0$ versus the true lateral deviation $^{i}y_{m,s}$, together with the errors. From these figures it is clear that the major part of the error in figure 5.5 comes from the rotation of the magnet and sensor around their y-axis.   The influence of
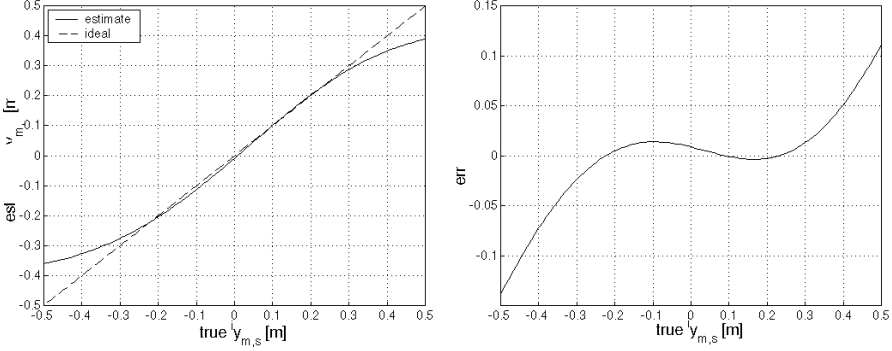
Figure 5.5: Estimated lateral deviation with slant of magnet and vehicle
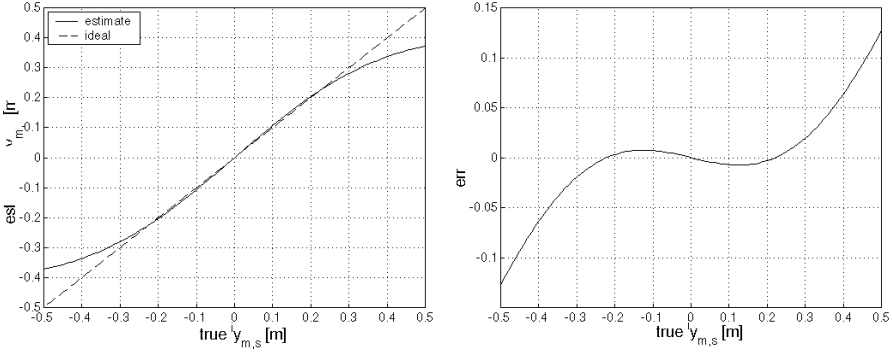
Figure 5.6: Estimated lateral deviation with slant of magnet and vehicle in longitudinal direction

slant in this direction can be reduced considerably by measuring the magnetic fields with two dual-axes sensors that are placed behind each other at distance $2d$ from each other. To explain this, it is the easiest to consider a rotation of magnet and sensor around their y-axes only, so $\alpha_m = \alpha_s = 0$. Calculating $^sB_x(^i\mathbf{x}_{m,s})$ and $^sB_y(^i\mathbf{x}_{m,s})$ yields

$$
\begin{aligned}
^sB_x(^i\mathbf{x}_{m,s}) \;=\; & 3f(r)\{^ix_{m,s}\,^iz_{m,s}(\cos\beta_m\cos\beta_s - \sin\beta_m\sin\beta_s)+ \\
& ^iz_{m,s}^2(\tfrac{1}{3}\sin\beta_m\cos\beta_s - \tfrac{2}{3}\cos\beta_m\sin\beta_s)+ \\
& \tfrac{1}{3}{}^iy_{m,s}^2(\sin\beta_m\cos\beta_s + \cos\beta_m\sin\beta_s)\}+ \\
& ^ix_{m,s}^2(\tfrac{1}{3}\cos\beta_m\sin\beta_s - \tfrac{2}{3}\sin\beta_m\cos\beta_s)
\end{aligned}
\tag{5.13}
$$

and

$$
^sB_y(^i\mathbf{x}_{m,s}) = 3f(r)^iy_{m,s}\{-^ix_{m,s}\sin\beta_m + {}^iz_{m,s}\cos\beta_m\}.
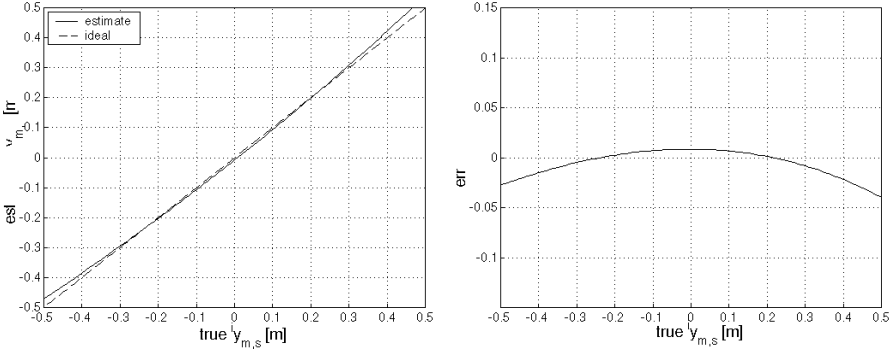\tag{5.14}
$$

Figure 5.7: Estimated lateral deviation with slant of magnet and vehicle in lateral direction

Especially the expression for ${}^sB_x({}^i\mathbf{x}_{m,s})$ looks complicated, but the essence is that there is a term proportional with ${}^ix_{m,s}{}^iz_{m,s}$ and there are terms proportional with the squares of ${}^ix_{m,s}$, ${}^iy_{m,s}$ and ${}^iz_{m,s}$. Assuming for the time being that also $\beta_s = 0$, a better estimate ${}^i\hat{y}_{m,s}$ of ${}^wy_{m,s}$ can be obtained by observing ${}^sB_x$ and ${}^sB_y$ at ${}^ix_{m,s} = d$ and ${}^ix_{m,s} = -d$ at the same time. An estimate of ${}^iy_{m,s}$ can be calculated then by

$$
{}^i\hat{y}_{m,s} \approx \frac{d}{2} \frac{{}^sB_y({}^ix_{m,s}=d, {}^iy_{m,s}, {}^iz_{m,s}) + {}^sB_y({}^ix_{m,s}=-d, {}^iy_{m,s}, {}^iz_{m,s})}{{}^sB_x({}^ix_{m,s}=d, {}^iy_{m,s}, {}^iz_{m,s}) - {}^sB_x({}^ix_{m,s}=-d, {}^iy_{m,s}, {}^iz_{m,s})} \tag{5.15}
$$

Substituting (5.13) and (5.14) in (5.15) yields [5]

$$
{}^i\hat{y}_{m,s} = {}^iy_{m,s}. \tag{5.16}
$$

So for slant of the magnet in the longitudinal direction only, ${}^iy_{m,s}$ can be reconstructed completely with equation (5.15). Considering also slant of the sensor in the longitudinal direction, the field can not be observed at ${}^ix_{m,s} = d$ and ${}^ix_{m,s} = -d$ exactly due to the slant of the sensor. In this case, the fields will be observed at ${}^ix_{m,s} = d\cos\beta_s$ and ${}^ix_{m,s} = -d\cos\beta_s$. Replacing d with $d\cos\beta_s$ in equation (5.15) yields

$$
{}^i\hat{y}_{m,s} \approx \frac{{}^iy_{m,s}}{\cos^2\beta_s - \frac{\sin\beta_m \sin\beta_s \cos\beta_s}{\cos\beta_m}}. \tag{5.17}
$$

For small rotation angles, this still yields a good estimate of ${}^iy_{m,s}$.

---

[5]Note that in equation (5.13) and (5.14) α_m and α_s where assumed to be zero. Therefore, this equation is exact
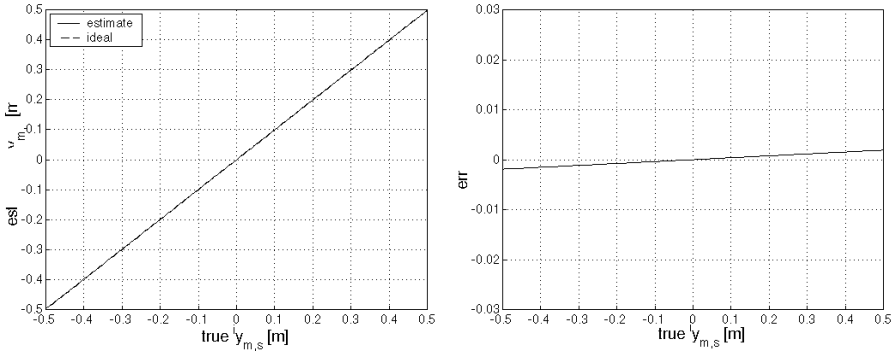
Figure 5.8: Estimated lateral deviation according to equation (5.15), with slant of magnet and vehicle in longitudinal direction
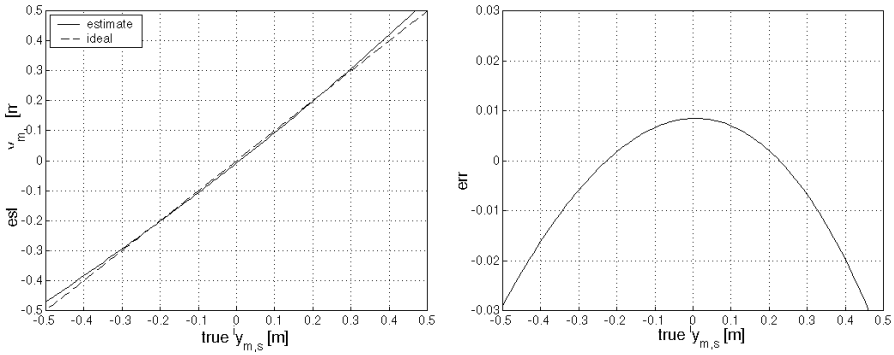
Figure 5.9: Estimated lateral deviation according to equation (5.15), with combined slant of magnet and vehicle in longitudinal and lateral direction

Figure 5.8 shows the estimated $^{i}y_{m,s}$ according to equation (5.15), in case $\beta_s = \beta_m = 5^0$ and $\alpha_s = \alpha_m = 0$. As the figure shows, there is only a very small measurement error in this way. The influence of the slant of vehicle and magnet has been eliminated almost completely. In the analysis above, it was assumed that $\alpha_m = \alpha_s = 0$, to show that slant in the longitudinal direction can be eliminated almost completely. In practice, there will be some cross terms in case $\alpha_m \neq 0$ and $\alpha_s \neq 0$. Figure 5.9 shows the lateral deviation estimated with equation (5.15) in case $\alpha_m = \alpha_s = \beta_m = \beta_s = 5^0$. As the figure shows, also in this case the measurement error is much smaller than in the case the deviation is estimated with equation (5.11), as shown in figure 5.5.

5.6 Validation measurements

Measurements where carried out on a static measurement setup [31]. A $10 \times$ ø1.5 cm AlNiCo bar magnet was used to produce the magnetic field. The magnetic field was measured with two Honeywell HMC2003 magnetoresistive sensors, placed at a distance of 20 cm from each other. To eliminate the influence of the earth magnetic field, which is in the same order of magnitude as the fields of the magnet, the earth magnetic field (and all other dc fields) was measured in the absence of the permanent magnet and subtracted from the measurements with the permanent magnet.

The left plot of figure 5.10 shows the measured lateral deviation from the magnet for different values of the real deviation. The real deviation ranges from $-0.5\,m$ to $0.5\,m$. For the measurements shown in figure 5.10, the magnet was rotated over about 9^0 degrees in the longitudinal direction (rotation over the y-axis of frame m). The plot shows the deviation measured with two sensors separate and with the two sensors combined following equation (5.15). As the plot shows, the measurement error due to slant of the magnet in the longitudinal direction can be reduced considerably by utilizing (5.15). The measurement error of the combination of the two sensors is shown in the right plot of figure 5.10. As this plot shows, the measurement error is less then $1\,cm$ over a real deviation ranging from $-0.5\,m$ to $0.5\,m$ for this type of rotation.

Figure 5.11 shows the measurement results of measurements with the magnet rotated in both the longitudinal and lateral direction. As the left plot of this figure shows, part of the effect of the (longitudinal) slant cancels out when equation (5.15) is used to determine the deviation. The right plot shows that the maximum measurement error is about $2\,cm$ for the combination of both sensors. This maximum error seems quite large, but it has to be noted that also the angles of slant where taken quite large for these experiments, to show that the large effect of longitudinal slant cancels out almost completely.
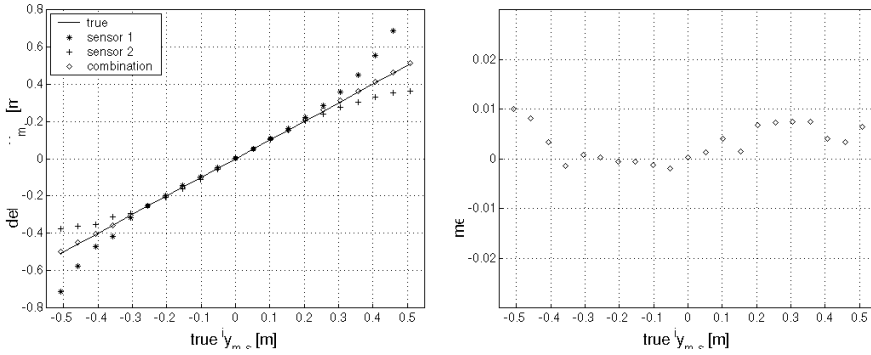
Figure 5.10: Measurement results with slant of magnet in longitudinal direction
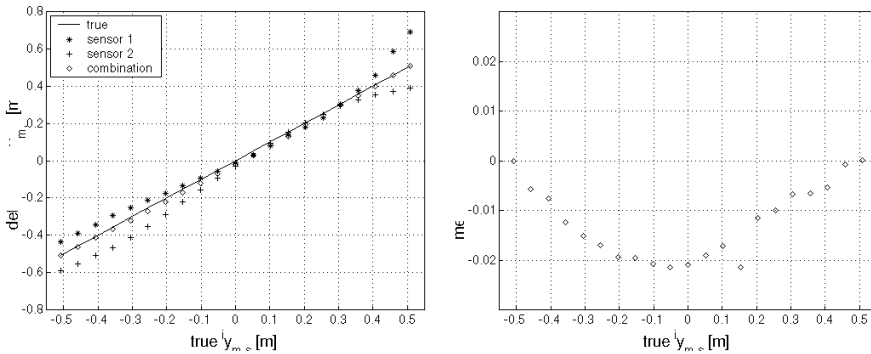
Figure 5.11: Measurement results with combined slant of magnet in lateral and longitudinal direction

5.7   Summary

A method to determine the position of a rotation symmetric bar magnet with respect to a point on a vehicle has been developed. The principle of this measurement method is based on the use of dual-axes magnetic field sensors. By utilizing the rotation symmetry of the field around the magnet, the lateral distance to the magnet can be determined independently of the strength of the magnet and the measurement height.

Analysis shows that that by using one dual-axes sensor only, the measurement method is especially sensitive to slant of magnet and/or vehicle. This sensitivity can be almost completely reduced by a second dual-axes sensor. Measurements show that with 9^0 of slant of the magnet, an accuracy of $2\,cm$ can be achieved in a measurement range of $\pm 0.5\,m$.

6

Observer design

6.1   Introduction

To achieve appropriate performance of the closed loop system, it is desirable that the complete (lateral) state is continuously available for feedback. The measurement method presented in the previous section however, gives position information only, and only at discrete time instances. Therefore, the velocities of the vehicle with respect to the path and the deviations from the path in between the magnets have to be estimated. This chapter deals with the design of an extended Kalman filter to accomplish this. Section 6.2 discusses the choice of the coordinate system in which the states will be estimated. Section 6.3 discusses the different models that can be used for the Kalman filter and what the implications of these models are. In section 6.4, the kinematics involved with the observer design are discussed. The systematic measurement errors involved with accelerometers are discussed in section 6.5. Section 6.6 will be used to derive a state-space equation for the Kalman filter. Next, section 6.7 deals with the prediction equation of the Kalman filter, followed by section 6.8, where the update equations are discussed. How the path orientations can be determined online will be discussed in section 6.9. Section 6.10 will be used to present some simulation results. The conclusions of this chapter are presented in section

6.2   Choice of coordinate system

For the design of the observer, two different approaches can be followed. In one approach, the position and velocity of the origin of each frame si is estimated
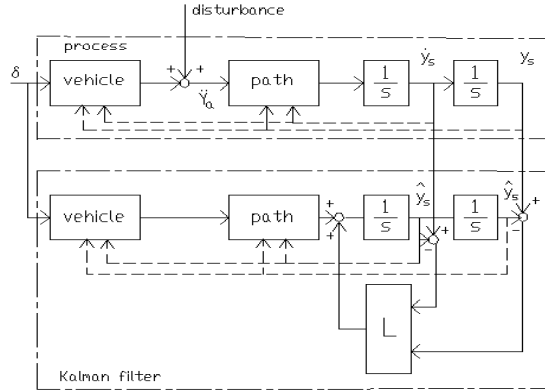
Figure 6.1: Kalman filter scheme based on complete vehicle model

with respect to the world. When a map of the path to be followed is available on-line, the shortest distance between each origin and the path can be calculated, yielding $^{psi}y_{p_{si},si}$ and $^{psi}\dot{y}_{p_{si},si}$. This method requires an on-line minimization routine to calculate the distance to the path, when non-circular or non-straight paths are considered. This can be very (calculation) time consuming. Another approach is to estimate $^{psi}y_{p_{si},si}$ and $^{psi}\dot{y}_{p_{si},si}$ directly. With this approach, only the orientation of the path and the desired state, as introduced in chapter 2 are required to be available on-line. To calculate these quantities, a same kind of optimization routine is necessary. In this way however, this calculation can be done off-line. Disadvantage of this second method is that the model to be used in the observer has to be linearized around the path in order to apply updates of articulation angles and orientation measurements. However, when the deviations from the path remain small, this is not a problem. In this chapter, the observer will be designed using the second approach to avoid problems due to the minimization algorithm.

6.3 Process model

One obvious model to be used in the Kalman filter is the model derived in chapter 3. With this approach, the inputs of the Kalman filter are the steering angles of the vehicle, as illustrated in figure 6.1. This is basically the same approach as discussed in [27, 34, 53, 57, 89]. Disadvantage of this method is that the Kalman filter depends on varying vehicle parameters like masses and cornering stifnesses. Moreover, the effect of disturbances like wind are not directly taken into account in the prediction step of the filter with this approach. Since position updates can only be applied to the filter when the vehicle passes a
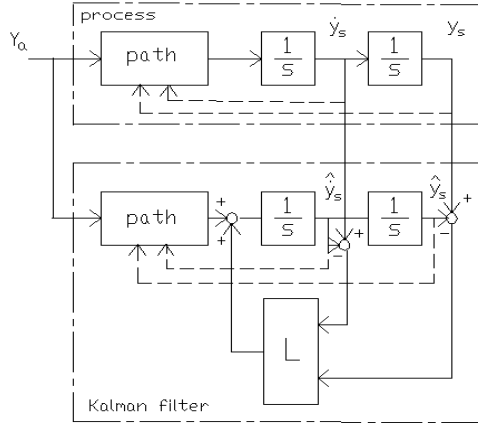
Figure 6.2: Kalman filter scheme based on accelerometers

magnet, both disadvantages may cause unacceptable drift of the state estimates. In figure 6.1, $\ddot{\mathbf{Y}}_a$ denotes a vector of the lateral accelerations of each carriage and the longitudinal acceleration of the tractor. These signals can be measured directly by accelerometers. Looking at figure 6.1, it is clear that also $\ddot{\mathbf{Y}}_a$ can be used as input for the filter, as illustrated in figure 6.2. Advantage of this method is that the Kalman filter is almost independent of varying vehicle parameters. Furthermore, the accelerometers also measure the effect of disturbances like wind, so that the effect of these disturbances is directly taken into account in the prediction step of the filter. This approach is mainly the same as presented in [78] and [48], where it has been used to estimate the distance with respect to the path of a single unit vehicle. In [78], this method is implemented as a multi-rate Kalman filter to deal with the discrete character of the magnetic markers. In this chapter, this approach will be extended to multiple-articulated vehicles. The difference with the filter as presented in [78] is that an extended Kalman filter approach has been followed in order to allow for nonlinearities due to the articulation angles and paths with large curvatures. Furthermore, the systematic errors involved with the use of accelerometers are taken into account. Besides accelerometers and the magnet sensors as discussed in the previous chapter, other sensors will be incorporated in the filter to allow for large distances between the magnets.
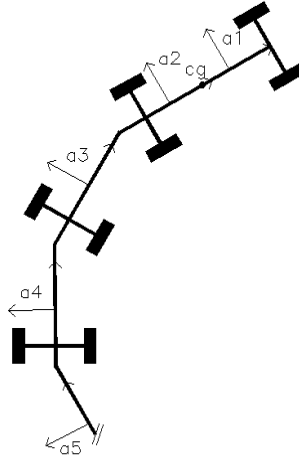
Figure 6.3: Accelerometer configuration

6.4 Kinematics

To explain the kinematics involved with the observer design, a vehicle configuration as shown in figure 6.3, will be considered. In this figure, the coordinate frames ai illustrate two-axes accelerometers, with their sensitive axes corresponding with the orientation of the frames ai. The orientations of the coordinate frames ai is the same as the orientations of the frames si. In this section, it will be assumed that the accelerometers are exactly horizontal. Slant of the accelerometers will be discussed in the next section.

This section deals mainly with the relation between the accelerometer outputs and the accelerations with respect to the path $^{psi}\ddot{y}_{psi,si}$. For the derivation of this relation, both axes of the accelerometers will be considered. Later on, the x-axes of the accelerometers will be omitted.

To simplify the derivation, the generalized acceleration vector $^{c1}\ddot{\mathbf{q}}$ will be used as an intermediate variable. Considering a vehicle configuration as given in figure 6.3, a vector $\mathbf{Y}_a$ can be defined as

$$
\mathbf{Y}_a = \begin{bmatrix}
^{a_1}x_{w,a_1} \\
^{a_1}y_{w,a_1} \\
^{a_2}y_{w,a_2} \\
^{a_3}y_{w,a_3} \\
\vdots \\
^{a_{n+1}}y_{w,a_{n+1}}
\end{bmatrix}. \tag{6.1}
$$

The vector components $^{a_i}y_{w,a_i}$ denote the y-components of the position vectors of the accelerometers with respect to the inertial frame w, expressed in the directions of the frames a_i. The acceleration vector $\dot{\mathbf{Y}}_a$ can be expressed in the generalized velocity $^{c1}\dot{\mathbf{q}}$ as

$$\dot{\mathbf{Y}}_a = \mathbf{J}_{\text{lat}}(^{c1}\mathbf{q})^{c1}\dot{\mathbf{q}}. \tag{6.2}$$

An expression for the matrix $\mathbf{J}_{\text{lat}}(^{c1}\mathbf{q})$ is given in appendix E. Differentiating (6.2) with respect to time yields

$$\ddot{\mathbf{Y}}_a = \dot{\mathbf{J}}_{\text{lat}}(^{c1}\mathbf{q}, {}^{c1}\dot{\mathbf{q}})^{c1}\dot{\mathbf{q}} + \mathbf{J}_{\text{lat}}(^{c1}\mathbf{q})^{c1}\ddot{\mathbf{q}}, \tag{6.3}$$

so that

$$^{c1}\ddot{\mathbf{q}} = \mathbf{J}_{\text{lat}}^{-1}(^{c1}\mathbf{q})\ddot{\mathbf{Y}}_a - \mathbf{J}_{\text{lat}}^{-1}(^{c1}\mathbf{q})\dot{\mathbf{J}}_{\text{lat}}(^{c1}\mathbf{q}, {}^{c1}\dot{\mathbf{q}})^{c1}\dot{\mathbf{q}}. \tag{6.4}$$

This equation relates the generalized acceleration $^{c1}\ddot{\mathbf{q}}$ to the accelerations of the accelerometers. In the next step, $^{c1}\ddot{\mathbf{q}}$ will be expressed in the tracking accelerations $^{p_{si}}\ddot{y}_{p_{si},si}$.

In chapter 3 it was derived that

$$\dot{\mathbf{Y}}_s = \mathbf{J}_{\text{path}}(^{c1}\mathbf{q})^{c1}\dot{\mathbf{q}}, \tag{6.5}$$

so that

$$\ddot{\mathbf{Y}}_s = \dot{\mathbf{J}}_{\text{path}}(^{c1}\mathbf{q})^{c1}\dot{\mathbf{q}} + \mathbf{J}_{\text{path}}(^{c1}\mathbf{q}, {}^{c1}\dot{\mathbf{q}})^{c1}\ddot{\mathbf{q}}. \tag{6.6}$$

Substituting equation (6.4) into equation (6.6) and utilizing (6.5) yields

$$\ddot{\mathbf{Y}}_s = \mathbf{J}_{\text{path}}\mathbf{J}_{\text{lat}}^{-1}\ddot{\mathbf{Y}}_a + (\dot{\mathbf{J}}_{\text{path}} - \mathbf{J}_{\text{path}}\mathbf{J}_{\text{lat}}^{-1}\dot{\mathbf{J}}_{\text{lat}})\mathbf{J}_{\text{path}}^{-1}\dot{\mathbf{Y}}_s. \tag{6.7}$$

For brevity, the arguments $(^{c1}\mathbf{q})$ and $(^{c1}\mathbf{q}, {}^{c1}\dot{\mathbf{q}})$ have been omitted.

Accelerometers measure accelerations with respect to an inertial frame. This means that an accelerometer mounted in the origin of frame ai does not measure $^{ai}\ddot{y}_{w,ai}$ directly, since ai is a rotating frame. $^{ai}\ddot{y}_{w,ai}$ can be derived from the accelerometer readings as follows: The velocity of frame ai with respect to the world and expressed in frame ai can be projected on the inertial frame w with

$$^{w}\dot{\mathbf{x}}_{w,ai} = {}^{w}\mathbf{Rot}_{ai}{}^{ai}\dot{\mathbf{x}}_{w,ai}. \tag{6.8}$$

Differentiating this equation with respect to time yields

$$^{w}\ddot{\mathbf{x}}_{w,ai} = {}^{w}\mathbf{Rot}_{ai}{}^{ai}\ddot{\mathbf{x}}_{w,ai} + {}^{w}\dot{\mathbf{Rot}}_{ai}{}^{ai}\dot{\mathbf{x}}_{w,ai}. \tag{6.9}$$

Considering planar motion only, a two axes accelerometer mounted at the origin of frame ai and with the sensitive axes in the direction of frame ai measures $^{w}\ddot{\mathbf{x}}_{w,ai}$ projected on the axes of frame ai, so

$$\boldsymbol{a}_{ai} = \begin{bmatrix} a_{ai_x} \\ a_{ai_y} \end{bmatrix} \begin{aligned} &= {}^{ai}\mathbf{Rot}_{w}{}^{w}\ddot{\mathbf{x}}_{w,ai} \\ &= {}^{ai}\ddot{\mathbf{x}}_{w,ai} + {}^{ai}\mathbf{Rot}_{w}{}^{w}\dot{\mathbf{Rot}}_{ai}{}^{ai}\dot{\mathbf{x}}_{w,ai} \end{aligned}, \tag{6.10}$$

where $\boldsymbol{a}_{ai}$ denotes the accelerations an accelerometer would measure if it is placed exactly horizontal. The term $^{ai}\mathbf{Rot}_w{}^w\dot{\mathbf{Rot}}_{ai}$ models the centripetal acceleration of the accelerometers. With

$$^w\mathbf{Rot}_{ai} = \begin{bmatrix} \cos{}^w\epsilon_{ai} & -\sin{}^w\epsilon_{ai} \\ \sin{}^w\epsilon_{ai} & \cos{}^w\epsilon_{ai} \end{bmatrix}, \tag{6.11}$$

the term $^{ai}\mathbf{Rot}_w{}^w\dot{\mathbf{Rot}}_{ai}$ becomes

$$^{ai}\mathbf{Rot}_w{}^w\dot{\mathbf{Rot}}_{ai} = \begin{bmatrix} 0 & -1 \\ 1 & 0 \end{bmatrix}{}^w\dot{\epsilon}_{ai}, \tag{6.12}$$

so that, combining (6.10) and (6.12), $^{ai}\ddot{y}_{w,ai}$ can be obtained from the accelerometer readings by

$$^{ai}\ddot{y}_{w,ai} = a_{ai_y} - {}^{ai}\dot{x}_{w,ai}{}^w\dot{\epsilon}_{ai}. \tag{6.13}$$

Substituting this into equation (6.7), equation (6.7) can be rewritten as

$$\ddot{\mathbf{Y}}_s = (\dot{\mathbf{J}}_{\text{path}} - \mathbf{J}_{\text{path}}\mathbf{J}_{\text{lat}}^{-1}\dot{\mathbf{J}}_{\text{lat}})\mathbf{J}_{\text{path}}^{-1}\dot{\mathbf{Y}}_s + \mathbf{J}_{\text{path}}\mathbf{J}_{\text{lat}}^{-1}\left[\boldsymbol{a} - \dot{\boldsymbol{\epsilon}}\mathbf{V}_x\right], \tag{6.14}$$

where

$$\mathbf{V}_x = \begin{bmatrix} 0 \\ {}^{a1}\dot{x}_{w,a1} \\ \vdots \\ {}^{an+1}\dot{x}_{w,an+1} \end{bmatrix}, \tag{6.15}$$

$$\dot{\boldsymbol{\epsilon}} = \text{diag}(0, {}^w\dot{\epsilon}_{c1}, {}^w\dot{\epsilon}_{c1}, {}^w\dot{\epsilon}_{c2}, \ldots, {}^w\dot{\epsilon}_{cn}) \tag{6.16}$$

and

$$\boldsymbol{a} = \begin{bmatrix} {}^{c1}\ddot{x}_{w,c1} \\ a_{a1_y} \\ \vdots \\ a_{an+1_y} \end{bmatrix}. \tag{6.17}$$

$\mathbf{V}_x$ can be written as

$$\mathbf{V}_x = \mathbf{J}_{\text{long}}({}^{c1}\dot{\mathbf{q}}), \tag{6.18}$$

where an expression for $\mathbf{J}_{\text{long}}({}^{c1}\mathbf{q})$ is given in appendix E. Note that according to this expression the first component of $\boldsymbol{a} - \boldsymbol{\epsilon}\mathbf{V}_x$ reads $^{c1}\ddot{x}_{w,c1}$ instead of one of the longitudinal accelerometer readings. To avoid problems when the vehicle drives on a ramp, the longitudinal acceleration of the tractor will be obtained by differentiating the longitudinal speed of the tractor.

Equation (6.14) contains besides the lateral dynamics also the longitudinal dynamics of the tractor. For the lateral guidance system, these dynamics only

are of minor importance. Therefore the longitudinal dynamics will be eliminated. Substituting equation (6.18) into equation (6.14) and utilizing equation (6.5), the vector

$$\ddot{\mathbf{y}}_s = \begin{bmatrix} {}^{p_{s1}}\ddot{y}_{p_{s1},s1} \\ \vdots \\ {}^{p_{sn+1}}\ddot{y}_{p_{sn+1},sn+1} \end{bmatrix} \tag{6.19}$$

can be derived from equation (6.14) as

$$\ddot{\mathbf{y}}_s = \boldsymbol{\nu}\,{}^{y}\mathbf{T}_Y^T \dot{\mathbf{y}}_s + \boldsymbol{\nu}\,{}^{x}\mathbf{T}_Y^T v_x + {}^{y}\mathbf{T}_Y \mathbf{J}_{\text{path}} \mathbf{J}_{\text{lat}}^{-1} \boldsymbol{a}, \tag{6.20}$$

with

$$\begin{align} {}^{y}\mathbf{T}_Y &= \begin{bmatrix} \mathbf{0}^{(\mathbf{n+1}) \times \mathbf{1}} & \mathbf{I}^{(\mathbf{n+1}) \times (\mathbf{n+1})} \end{bmatrix}, \tag{6.21} \\ {}^{x}\mathbf{T}_Y &= \begin{bmatrix} 1 & 0 & \dots & 0 \end{bmatrix} \tag{6.22} \end{align}$$

and

$$\boldsymbol{\nu}(\dot{\mathbf{y}}_s, \mathbf{y}_s) = {}^{y}\mathbf{T}_Y \left((\dot{\mathbf{J}}_{\text{path}} - \mathbf{J}_{\text{path}} \mathbf{J}_{\text{lat}}^{-1} \dot{\mathbf{J}}_{\text{lat}}) \mathbf{J}_{\text{path}}^{-1} - \dot{\boldsymbol{\epsilon}} \mathbf{J}_{\text{long}} \mathbf{J}_{\text{path}}^{-1} \right). \tag{6.23}$$

Equation (6.20) expresses the lateral accelerations ${}^{p_{si}}\ddot{y}_{p_{si},xi}$ in the accelerometer readings and the tractor's longitudinal velocity.

6.5 Error modeling

One of the problems involved with accelerometers is their alignment with respect to the horizontal. In the previous section it was assumed that the accelerometers are exactly parallel to the horizontal. In practice however, the accelerometers will be under a certain angle ϕ with respect to the horizontal, due to amongst others banking of the road and the roll motion of the vehicle. Due to this misalignment angle, the accelerometers will also measure part of the gravitational acceleration g, as is illustrated in figure 6.4. Moreover, the outputs of the accelerometers will also be subjected to offsets.

Incorporating these offsets and the effect of vehicle roll and road banking, the accelerometer outputs α_{ai_y} can be written as

$$\alpha_{ai_y} = a_{ai_y} \cos\phi + g \sin\phi + o_{ai}, \tag{6.24}$$

where a_{ai} denotes the accelerations of the accelerometers in the direction of the sensitive axes of the accelerometer projected on the horizontal plane and expressed with respect to an inertial frame, ϕ denotes the angle between the sensitive axes of accelerometer ai and the horizontal plane and o_{ai} denotes the accelerometer offsets.

The 'disturbing' term $g \sin\phi + o_{ai}$ causes drift of the measurement system, since the accelerometer readings have to be integrated twice in order to obtain
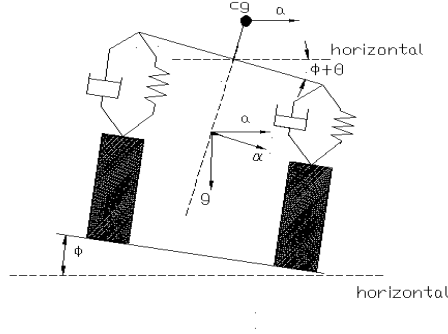
Figure 6.4: Vehicle suspension system under the influence of road banking and lateral acceleration

the lateral deviation from the path to be followed. Especially when the velocity is low, so that the time to the next magnet hit is large, this drift may become unacceptably large. Therefore, the term $g \sin \phi + o_{ai}$ has to be estimated. The misalignment angle ϕ can be split into a part Φ due road banking and a dynamic, lateral acceleration dependent part θ due to the roll motion of the vehicle, so

$$\phi = \Phi + \theta. \tag{6.25}$$

To model the lateral acceleration dependence of θ,the vehicle's suspension system will be taken into account. In figure 6.4 the suspension system of a vehicle has been schematized. The equation of motion of the suspension system of a single carriage can be written as

$$\ddot{\theta} + \frac{D_s}{I_x}\dot{\theta} + \frac{K_s}{I_x}\theta = \frac{ml}{I_x}(a_{c_y}\cos\phi + g\sin\phi) + \frac{T_d}{I_x}, \tag{6.26}$$

where I_x is the vehicle's moment of inertia around the longitudinal vehicle axis, D_s is the total damping constant of the suspension system, K_s the total spring constant, m the mass of the vehicle, a_{c_y} the lateral acceleration acting on the center of gravity and l is the distance from the vehicle's center of gravity to the roll center of the vehicle. The disturbance torque due to wind and bad road quality is modeled by T_d. Considering a multiple-articulated vehicle, a similar expression can be derived. For this expression, it will be assumed that the roll motions of all carriages are completely coupled. This assumption is valid for small articulation angles due to the construction of the hitching mechanism. For large articulation angles, this assumption doesn't hold anymore, but in this case the lateral accelerations are small in general, so that the effect of the roll motion is negligible. Under this assumption the equation of motion of the total
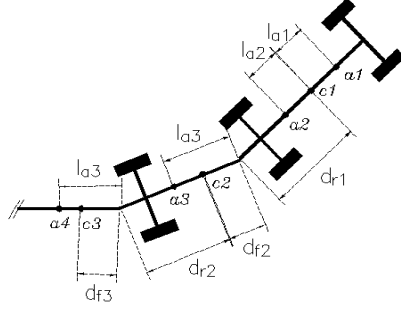
Figure 6.5: Definition of distances

suspension system of the multiple-articulated vehicle can be written as

$$\ddot{\theta} + \frac{D_s}{I_x}\dot{\theta} + \frac{K_s}{I_x}\theta \approx \sum_{i=1}^{n} \frac{m_i l_i}{I_x}(a_{ci_y}\cos\phi + g\sin\phi) + \frac{T_d}{I_x}, \qquad (6.27)$$

where m_i is the mass of the ith carriage, l_i the distance from the ith center of gravity to the ith roll center, a_{ci_y} the lateral acceleration of the center of gravity of the ith carriage and $\phi = \theta + \Phi$ the total angle between the horizontal and the sensitive axes of the accelerometers. It has been assumed that also the road banking angle Φ is the same for all accelerometers. The accelerations of the centers of gravity can be expressed in the accelerometer readings as

$$a_{c1_y} = \frac{l_{a1}a_{a2_y} + l_{a2}a_{a1_y}}{l_{a1} + l_{a2}}$$

$$a_{ci_y} = \frac{(l_{ai+1} - d_{fi})(a_{ai_y}d_{ri-1} - (d_{ri-1} + d_{fi-1} - l_{ai})a_{ci-1_y})\cos\left({}^w\epsilon_{ci} - {}^w\epsilon_{ci-1}\right)}{l_{ai+1_y}(l_{ai} - d_{fi_1})}$$

$$+ \frac{d_{fi}a_{ai+1_y} - (l_{ai+1} - d_{fi})a_{ci-1_y}\sin({}^w\epsilon_{ci} - {}^w\epsilon_{ci-1})}{l_{ai+1}} \quad \text{for } i \geq 2 \qquad (6.28)$$

with l_{ai}, d_{fi} and d_{ri} as defined in figure 6.5.

Assuming small articulation angles, neglecting second and higher order terms of small quantities and using

$$a_{ai_y} = \frac{\alpha_{ai_y} - g\sin\phi - o_{ai}}{\cos\phi}, \qquad (6.29)$$

yields

$$a_{c1_y} \quad = \quad -g\tan\phi + \frac{\eta_{11}(\alpha_{a1_y} - o_{a1}) + \eta_{12}(\alpha_{a2_y} - o_{a2})}{\cos\phi} \tag{6.30}$$

$$a_{ci_y} \quad \approx \quad -g\tan\phi + \frac{1}{\cos\phi}\sum_{j=1}^{i}\eta_{ij}(\alpha_{ai_y} - o_{ai}) \text{ for } i \geq 2, \tag{6.31}$$

where η_{ij} are parameters depending on the accelerometer positions, with as example

$$\eta_{11} \quad = \quad \frac{l_{a2}}{l_{a1} + l_{a2}} \tag{6.32}$$

$$\eta_{12} \quad = \quad \frac{l_{a1}}{l_{a1} + l_{a2}} \tag{6.33}$$

Substituting (6.30) in the equations of motion (6.27), (6.27) can be written as

$$\ddot{\theta} + \frac{D_s}{I_x}\dot{\theta} + \frac{K_s}{I_x}\theta \approx \sum_{i=1}^{n}\eta_i\frac{\alpha_{ai_y} - o_{ai}}{\cos\phi} + \frac{T_d}{I_z}, \tag{6.34}$$

where the parameters η_i depend on η_{ij}, the masses of the carriages, the location of the centers of gravity and the total moment of inertia around the vehicle's longitudinal axes I_x.

6.6 State-space equation

Equations (6.20) and (6.34) can be written in a nonlinear state-space form as

$$\dot{\mathbf{x}} = \mathbf{A}(\mathbf{x})\mathbf{x} + \mathbf{B}(\mathbf{x})\mathbf{u}, \tag{6.35}$$

where

$$\mathbf{u} = \begin{bmatrix} v_x & {}^{c1}\ddot{x}_{w,c1} & \alpha_{a1_y} & \dots & \alpha_{an+1_y} \end{bmatrix}^T \tag{6.36}$$

and

$$\mathbf{x} = \begin{bmatrix} \dot{\mathbf{y}}_{si} & \mathbf{y}_{si} & \boldsymbol{o}_{ai} & \boldsymbol{\eta}_i & \Phi & \dot{\theta} & \theta & \zeta_1 & \zeta_2 \end{bmatrix}^T, \tag{6.37}$$

where

$$\boldsymbol{o}_{ai} \quad = \quad \begin{bmatrix} o_{a1} & \dots & o_{an+1} \end{bmatrix}^T \tag{6.38}$$

$$\boldsymbol{\eta}_i \quad = \quad \begin{bmatrix} \eta_{a1} & \dots & \eta_{an+1} \end{bmatrix}^T \tag{6.39}$$

$$\zeta_1 \quad = \quad \frac{D_s}{I_z} \tag{6.40}$$

$$\zeta_2 \quad = \quad \frac{K_s}{I_z}. \tag{6.41}$$

The parameters $\boldsymbol{o}_{ai}$, $\boldsymbol{\eta}_i$ ζ_1, ζ_2 and the road banking angle Φ are also added to the state vector $\mathbf{x}$ to be able to estimate them online. The nonlinear system matrix $\mathbf{A}(\mathbf{x})$ can be factorized as

$$\mathbf{A}(\mathbf{x}) = \begin{bmatrix} \mathbf{a}_{11} & \mathbf{a}_{12} & \mathbf{a}_{13} \\ \mathbf{0} & \mathbf{0} & \mathbf{0} \\ \mathbf{0} & \mathbf{a}_{32} & \mathbf{a}_{33} \end{bmatrix}, \tag{6.42}$$

where

$$\mathbf{a}_{11} = \begin{bmatrix} \boldsymbol{\nu}(\mathbf{x})^y \mathbf{T}_Y^T & \mathbf{0}^{(n+1)\times(n+1)} \\ \mathbf{I}^{(n+1)\times(n+1)} & \mathbf{0}^{(n+1)\times(n+1)} \end{bmatrix} \tag{6.43}$$

$$\mathbf{a}_{12} = \begin{bmatrix} -{}^y\mathbf{T}_a & \mathbf{0}^{(n+1)\times(n+1)} \\ \mathbf{0}^{(n+1)\times(n+1)} & \mathbf{0}^{(n+1)\times(n+1)} \end{bmatrix} \tag{6.44}$$

$$\mathbf{a}_{13} = \begin{bmatrix} -\mathbf{g}^{(n+1)\times1} & \mathbf{0}^{(n+1)\times1} & -\mathbf{g}^{(n+1)\times1} & \mathbf{0}^{(n+1)\times2} \\ \mathbf{0}^{(n+1)\times1} & \mathbf{0}^{(n+1)\times1} & \mathbf{0}^{(n+1)\times1} & \mathbf{0}^{(n+1)\times2} \end{bmatrix} \tag{6.45}$$

$$\mathbf{a}_{32} = \begin{bmatrix} 0 & \dots & 0 & 0 & \dots & 0 \\ 0 & \dots & 0 & -o_{a1} & \dots & -o_{an+1} \\ 0 & \dots & 0 & 0 & \dots & 0 \\ 0 & \dots & 0 & 0 & \dots & 0 \\ 0 & \dots & 0 & 0 & \dots & 0 \end{bmatrix} \tag{6.46}$$

$$\mathbf{a}_{33} = \begin{bmatrix} 0 & 0 & 0 & 0 & 0 \\ 0 & -\zeta_1 & -\zeta_2 & 0 & 0 \\ 0 & 0 & 0 & 0 & 0 \\ 0 & 0 & 0 & 0 & 0 \\ 0 & 0 & 0 & 0 & 0 \end{bmatrix} \tag{6.47}$$

with

$$^y\mathbf{T}_a = {}^y\mathbf{T}_Y^T \mathbf{J}_{\text{path}} \mathbf{J}_{\text{lat}}^{-1y}\mathbf{T}_Y \tag{6.48}$$

and

$$\mathbf{g} = \begin{bmatrix} g \\ \vdots \\ g \end{bmatrix} \tag{6.49}$$

Furthermore, $\cos\phi$ and $\sin\phi$ have been approximated with a first order approximation. In a similar way, $\mathbf{B}(\mathbf{x})$ can be factorized as

$$\mathbf{B}(\mathbf{x}) = \begin{bmatrix} \mathbf{b}_1 \\ \mathbf{0}^{2(n+1)\times(n+3)} \\ \mathbf{b}_3 \end{bmatrix}, \tag{6.50}$$

with

$$\mathbf{b}_1 = \begin{bmatrix} \boldsymbol{\nu}(\mathbf{x})^x \mathbf{T}_Y^T & {}^y\mathbf{T}_Y \mathbf{J}_{\text{path}} \mathbf{J}_{\text{lat}}^{-1} \\ \mathbf{0}^{(n+1)\times 1)} & \mathbf{0}^{(n+1)\times(n+2)} \end{bmatrix} \tag{6.51}$$

$$\mathbf{b}_3 = \begin{bmatrix} 0 & 0 & 0 & \dots & 0 \\ 0 & 0 & \eta_1 & \dots & \eta_{n+1} \\ 0 & 0 & 0 & \dots & 0 \\ 0 & 0 & 0 & \dots & 0 \\ 0 & 0 & 0 & \dots & 0 \end{bmatrix} \tag{6.52}$$

The roll acceleration disturbance term T_d term in equation (6.34) has not yet been taken into account in equation (6.35). Moreover, the parameters η_i, ζ_1, ζ_2 and the sensor offsets o_i may vary in time, due to for example changing load conditions of the vehicle and changing operating temperature of the accelerometers. These effects will be modeled by a state disturbance term

$$\mathbf{B}_{v1}(\mathbf{x})\mathbf{v_1}, \tag{6.53}$$

with

$$\mathbf{B}_{v1}(\mathbf{x}) = \begin{bmatrix} \mathbf{0}^{2(n+1)\times[2(n+1)+4]} \\ \mathbf{b}_{v1_{[2]}}^{2(n+1)\times[2(n+1)+4]} \\ \mathbf{b}_{v1_{[3]}}^{5\times[2(n+1)+4]} \end{bmatrix}, \tag{6.54}$$

where

$$\mathbf{b}_{v1_{[2]}} = \begin{bmatrix} \mathbf{0}^{2(n+1)\times(n+1)} & \mathbf{I}^{2(n+1)\times 2(n+1)} & \mathbf{0}^{2(n+1)\times 4} \end{bmatrix} \tag{6.55}$$

$$\mathbf{b}_{v1_{[3]}} = \begin{bmatrix} 0 & \dots & 0 & 1 & 0 & 0 & 0 \\ 0 & \dots & 0 & 0 & 1 & 0 & 0 \\ 0 & \dots & 0 & 0 & 0 & 0 & 0 \\ 0 & \dots & 0 & 0 & 0 & 1 & 0 \\ 0 & \dots & 0 & 0 & 0 & 0 & 1 \end{bmatrix} \tag{6.56}$$

Furthermore, the noise vector $\mathbf{v}_1$ is assumed to be white, Gaussian with known covariance $\mathbf{V}_1$.

Besides the disturbances modeled with (6.53), the observer will also be subjected to noise of the sensors measuring v_x, ${}^{cl}\ddot{x}_{w,c1}$ and the accelerometers. These noises will be modeled by a second state disturbance term

$$\mathbf{B}_{v2}(\mathbf{x})\mathbf{v_2}, \tag{6.57}$$

where $\mathbf{v}_2$ models the sensor noise and

$$\mathbf{B}_{v2}(\mathbf{x}) = \begin{bmatrix} \mathbf{b}_{v2_{[1]}}^{(n+1)\times(n+3)} \\ \mathbf{0}^{[3(n+1)+5]\times[(n+3)]} \end{bmatrix}, \tag{6.58}$$
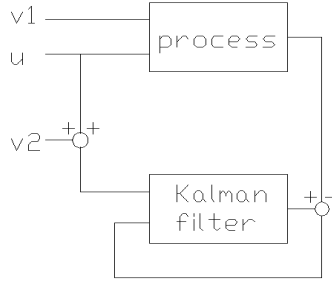
Figure 6.6: Kalman filter scheme with input sensor noise and state disturbance noise

with

$$\mathbf{b}_{v2_{[1]}} = \begin{bmatrix} \boldsymbol{\nu}(\mathbf{x})^x\mathbf{T}_Y^T & {}^y\mathbf{T}_Y\mathbf{J}_{\text{path}}\mathbf{J}_{\text{lat}}^{-1} \end{bmatrix} \tag{6.59}$$

$$\tag{6.60}$$

The sensor noise term (6.57) and the state disturbance term modeled by (6.53) have been modeled separately, because both have a different effect on the observer, as illustrated in figure 6.6. As the figure shows, the sensor noise acts directly on the observer, whereas the noise term modeled with (6.57) acts directly on the process. For this reason, both noise terms have to be treated separately in the calculation of the discrete time state disturbance covariance matrix in section 6.7

With the state disturbance terms, the total nonlinear state-space equation becomes

$$\dot{\mathbf{x}} = \mathbf{A}(\mathbf{x})\mathbf{x} + \mathbf{B}(\mathbf{x})\mathbf{u} + \mathbf{B}_{v1}(\mathbf{x})\boldsymbol{v}_1 + \mathbf{B}_{v2}(\mathbf{x})\boldsymbol{v}_2, \tag{6.61}$$

The observer has to be implemented on a digital computer. Therefore, equation (6.61) has to be discretized. Since (6.61) is a nonlinear equation, discretization is not straightforward in general. However, under some conditions, equation (6.61) can be discretized following the same procedure as for a linear state-space equation. The general solution for the linear state-space equation

$$\dot{\mathbf{x}} = \mathbf{F}\mathbf{x} + \mathbf{G}\mathbf{u} \tag{6.62}$$

is given by [8]

$$x(t+\tau) = e^{\mathbf{F}\tau}x(t) + \int_t^{t+\tau} e^{\mathbf{F}(t+\tau-\xi)}\mathbf{G}\mathbf{u}(\xi)d\xi \tag{6.63}$$

Since $\mathbf{A}(\mathbf{x})$ and $\mathbf{B}(\mathbf{x})$ are smooth functions of $\mathbf{x}$, the solution of (6.61) can also be approximated by

$$\begin{aligned}
x(t+\tau) \approx{} & e^{\mathbf{A}(\mathbf{x}(t))\tau}x(t) + \int_t^{t+\tau}e^{\mathbf{A}(\mathbf{x}(t))(t+\tau-\xi)}(\mathbf{B}(\mathbf{x}(t))\mathbf{u}(\xi))d\xi + \\
& \int_t^{t+\tau}e^{\mathbf{A}(\mathbf{x}(t))(t+\tau-\xi)}(\mathbf{B}_{v1}(\mathbf{x}(t))\mathbf{v_1}(\xi) + \mathbf{B}_{v2}(\mathbf{x}(t))\mathbf{v_2}(\xi))d\xi
\end{aligned} \tag{6.64}$$

if τ is small compared to the time constants of the system (6.61). Note that all nonlinear matrices are kept constant during the integration. Treating (6.64) as an equality, assuming that $\mathbf{u}(t)$ is piecewise-constant and evaluating (6.64) at $t = k\Delta$ and with $\tau = \Delta$, where Δ is the sample period, yields

$$\mathbf{x}_{k+1} = \mathbf{A}_k(\mathbf{x}_k)\mathbf{x}_k + \mathbf{B}_k(\mathbf{x}_k)\mathbf{u}_k + \mathbf{v_{1k}} + \mathbf{v_{2k}}, \tag{6.65}$$

where $\mathbf{x}_k$ is shorthand notation for $\mathbf{x}(k\Delta)$, $\mathbf{u}_k$ is shorthand notation for $\mathbf{u}(k\Delta)$ and

$$\mathbf{A}_k(\mathbf{x}_k) = e^{\mathbf{A}(\mathbf{x}_k)\Delta} \tag{6.66}$$

$$\mathbf{B}_k(\mathbf{x}_k) = \int_{k\Delta}^{(k+1)\Delta} e^{\mathbf{A}(\mathbf{x}_k)((k+1)\Delta - \xi)}\mathbf{B}(\mathbf{x}_k)d\xi = \int_0^\Delta e^{\mathbf{A}(\mathbf{x}_k)\chi}\mathbf{B}(\mathbf{x}_k)d\chi \tag{6.67}$$

$$\mathbf{v}_{1k} = \int_{k\Delta}^{(k+1)\Delta} e^{\mathbf{A}(\mathbf{x}_k)((k+1)\Delta - \xi)}\mathbf{B}_{v1}(\mathbf{x}_k)\boldsymbol{v}_1(\xi)d\xi \tag{6.68}$$

$$\mathbf{v}_{2k} = \int_{k\Delta}^{(k+1)\Delta} e^{\mathbf{A}(\mathbf{x}_k)((k+1)\Delta - \xi)}\mathbf{B}_{v2}(\mathbf{x}_k)\boldsymbol{v}_2(\xi)d\xi \tag{6.69}$$

The noise component $\mathbf{v}_2$ models the accelerometer noises. The outputs of the accelerometers are sampled, so that also $\mathbf{v}_2$ stays constant during one sampling interval. The sampled noise $\mathbf{v}_{2k}$ can then be written as

$$\begin{aligned} \mathbf{v}_{2k} &= \int_{k\Delta}^{(k+1)\Delta} e^{\mathbf{A}(\mathbf{x}_k)((k+1)\Delta - \xi)}\mathbf{B}_{v2}(\mathbf{x}_k)d\xi\boldsymbol{v}_2(k\Delta) \\ &= \mathbf{B}_{v2_k}(\mathbf{x}_k)\boldsymbol{v}_2(k\Delta), \end{aligned} \tag{6.70}$$

where

$$\mathbf{B}_{v2_k}(\mathbf{x}_k) = \int_0^\Delta e^{\mathbf{A}(\mathbf{x}_k)\chi}d\chi\mathbf{B}_{v2}(\mathbf{x}_k) \tag{6.71}$$

To implement the observer, the matrix exponent $e^{\mathbf{A}(\mathbf{x}(k))\Delta}$ has been approximated with a second-order approximation.

6.7 Predictor equations

Before discussing the predictor equation of the Kalman filter, some timing issues have to be discussed. In the deviation of equation (6.65), it was assumed that the sampling interval Δ is small compared with the system dynamics. This means that the prediction equations of the Kalman filter have to be calculated at a high sampling frequency. The measurement updates of the Kalman filter however don't necessarily have to be obtained at the same high sampling frequency. Moreover, the measurement updates may occur asynchronously with the sampling instances, as is the case with the information coming from the magnetic referencing system, as is illustrated in figure 6.7. In this figure k de-
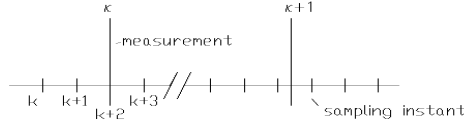
Figure 6.7: Timing diagram for sampling and measurement instances

notes the sampling instances for the prediction steps, whereas κ denotes the sampling instances for the updates of the Kalman filter. The way to deal with the asynchronous behavior of the magnet reference system will be discussed in the next section.

For every k after measurement update κ the following predictor equation will be used for the system (6.65).

$$\hat{\mathbf{x}}_{k+1,\kappa} = \mathbf{A}_k(\hat{\mathbf{x}}_{k,\kappa})\hat{\mathbf{x}}_{k,\kappa} + \mathbf{B}_{k,\kappa}(\hat{\mathbf{x}}_k)\hat{\mathbf{u}}_k, \tag{6.72}$$

where $\hat{\mathbf{x}}_{k,\kappa}$ denotes the estimate of $\mathbf{x}_k$, based on the update information obtained at instant κ. For convenience, equation (6.65) will be rewritten as

$$\mathbf{x}_{k+1} = \mathbf{f}(\mathbf{x}_k, \mathbf{u}_k, \mathbf{v}_k), \tag{6.73}$$

where

$$\mathbf{f}(\mathbf{x}_k, \mathbf{u}_k, \mathbf{v}_k) = \mathbf{A}_k(\mathbf{x}_k)\mathbf{x}_k + \mathbf{B}_k(\mathbf{x}_k)\mathbf{u}_k + \mathbf{v}_k, \tag{6.74}$$

with $\mathbf{v}_k = \mathbf{v}_{1k} + \mathbf{v}_{2k}$. This equation can be linearized around the estimate $\hat{\mathbf{x}}_{k,\kappa}$ as

$$\mathbf{x}_{k+1} \approx \mathbf{f}(\hat{\mathbf{x}}_{k,\kappa}, \mathbf{u}_k, \mathbf{0}) + \left.\frac{\partial \mathbf{f}(\mathbf{x}_k, \mathbf{u}_k, \mathbf{v}_k)}{\partial \mathbf{x}}\right|_{(\hat{\mathbf{x}}_{k,\kappa}, \mathbf{u}_k, \mathbf{0})} (\mathbf{x}_k - \hat{\mathbf{x}}_{k,\kappa}) + \mathbf{v}_k \tag{6.75}$$

$$= \mathbf{f}(\hat{\mathbf{x}}_{k,\kappa}, \mathbf{u}_k, \mathbf{0}) + \mathbf{A}_p(\hat{\mathbf{x}}_{\mathbf{k},\kappa}, \mathbf{u}_k)(\mathbf{x}_k - \hat{\mathbf{x}}_{k,\kappa}) + \mathbf{v}_k, \tag{6.76}$$

where

$$\mathbf{A}_p(\hat{\mathbf{x}}_{\mathbf{k},\kappa}, \mathbf{u}_k) = \left.\frac{\partial \mathbf{f}(\mathbf{x}_k, \mathbf{u}_k, \mathbf{v}_k)}{\partial \mathbf{x}}\right|_{(\hat{\mathbf{x}}_{k,\kappa}, \mathbf{u}_k, \mathbf{0})} \tag{6.77}$$

Now the estimation error $\tilde{\mathbf{x}}_{k+1,\kappa} = \mathbf{x}_{k+1} - \hat{\mathbf{x}}_{k+1,\kappa}$ can be expressed in $\tilde{\mathbf{x}}_{k,\kappa}$ and $\mathbf{v}_k$. Using

$$\mathbf{f}(\hat{\mathbf{x}}_{k,\kappa}, \mathbf{u}_k, \mathbf{0}) = \mathbf{A}_k(\hat{\mathbf{x}}_{k,\kappa})\hat{\mathbf{x}}_{k,\kappa} + \mathbf{B}_k(\hat{\mathbf{x}}_{k,\kappa})\mathbf{u}_k, \tag{6.78}$$

$\tilde{\mathbf{x}}_{k+1,\kappa}$ can be written as

$$\tilde{\mathbf{x}}_{k+1,\kappa} = \mathbf{x}_{k+1} - \hat{\mathbf{x}}_{k+1,\kappa} \approx \mathbf{A}_p(\hat{\mathbf{x}}_{\mathbf{k},\kappa}, \mathbf{u}_k)\tilde{\mathbf{x}}_{k,\kappa} + \mathbf{v}_k. \tag{6.79}$$

With (6.79), the covariance matrix of the estimation error $\tilde{\mathbf{x}}_{k+1,\kappa}$ becomes [91]

$$\mathbf{P}_{k+1,\kappa} = E[\tilde{\mathbf{x}}_{k+1,\kappa}\tilde{\mathbf{x}}_{k+1,\kappa}^T] = \mathbf{A}_p(\hat{\mathbf{x}}_{\mathbf{k},\kappa}, \mathbf{u}_k)\mathbf{P}_{k,\kappa}\mathbf{A}_p(\hat{\mathbf{x}}_{\mathbf{k},\kappa}, \mathbf{u}_k)^T + \mathbf{V}_k, \tag{6.80}$$

where $\mathbf{P}_{k,\kappa}$ denotes the covariance matrix of the error $\tilde{\mathbf{x}}_{k,\kappa}$ on time instant k, based at measurement update κ and $\mathbf{V}_k = \mathbf{V}_{1k} + \mathbf{V}_{2k}$ denotes the covariance matrix of $\mathbf{v}_k$. Using 6.68, $\mathbf{V}_{1k}$ can be calculated with

$$\mathbf{V}_{1k} = E[\int_{k\Delta}^{(k+1)\Delta} \int_{k\Delta}^{(k+1)\Delta} e^{\mathbf{A}((k+1)\Delta - \xi)} \mathbf{B}_{v1}\mathbf{v1}(\xi)\mathbf{v1}^T(\chi)\mathbf{B}_{v1}^T e^{\mathbf{A}^T((k+1)\Delta - \chi)} d\xi d\chi]. \tag{6.81}$$

For brevity, the dependency of $\mathbf{A}(\hat{\mathbf{x}}_{k,\kappa})$ and $\mathbf{B}_{v1}(\hat{\mathbf{x}}_{k,\kappa})$ on $\hat{\mathbf{x}}_{k,\kappa}$ has been omitted. Elaborating this equation by interchanging the expectation and integration in equation (6.81) yields

$$\mathbf{V}_{1k} = \int_0^\Delta e^{\mathbf{A}\chi} \mathbf{B}_{v1} \mathbf{V}_1 \mathbf{B}_{v1}^T e^{\mathbf{A}\chi} d\chi \tag{6.82}$$

To solve this equation, a second order approximation of $e^{\mathbf{A}\chi}$ has been used
   With equation (6.70), $\mathbf{V}_{2k}$ can be written as

$$\begin{aligned} \mathbf{V}_{2k} &= E[\mathbf{B}_{v2_k}(\mathbf{x}_k)\mathbf{v}_2(k\Delta)\mathbf{v}_2^T(k\Delta)\mathbf{B}_{v2_k}^T(\mathbf{x}_k)] \\ &= \mathbf{B}_{v2_k}(\mathbf{x}_k)\mathbf{V}_2\mathbf{B}_{v2_k}^T(\mathbf{x}_k), \end{aligned} \tag{6.83}$$

where $\mathbf{V}_2$ is the covariance matrix of $\mathbf{v}_2$.

6.8   Measurements updates

In this section, the measurement updates for the Kalman filter will be discussed. The most important measurement to update the Kalman filter is the measurement coming from the magnet reference system as discussed in the previous chapter. A problem of these measurements is that they are available only at discrete time instances, i.e. only when one of the magnet sensors on the vehicle passes a magnet. Moreover, the lower the vehicle speed (or the larger the distance between the magnets), the less frequent in time a measurement becomes available, which may cause the estimate of the state to drift away from the real state in between the magnets. Therefore, other sensors will be combined with the magnet reference system in order to obtain a good estimate, also in between the magnets. Possible candidates for these sensors are:

- wheel encoders in combination with steering angle measurements

- gyroscopes

- articulation angle sensors

Although these sensors do not provide direct information about the distance from the vehicle to the path, they improve the kinematic description of the vehicle that will be used in the Kalman filter. Condition of this improvement is
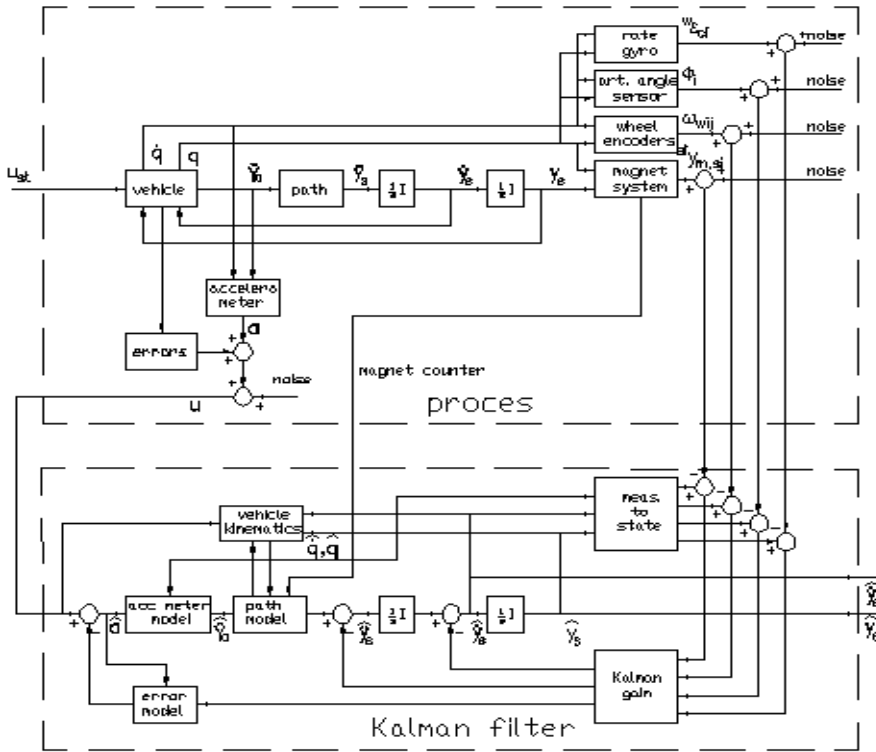
Figure 6.8: Block scheme of feedback linearizing controller

that the sensor outputs are not subjected to unmodeled systematic errors and that the sensor noise is modeled properly. Moreover, adding extra sensors will result in redundancy of the Kalman filter, so that failure of one or more sensors will not result in direct malfunction of the filter, but graceful degradation of the performance will take place. Failure of the sensors can, for example, be detected by comparing redundant sensors on sensor level. Another method is to compare the sensor output with the estimated output of the Kalman filter. It is assumed that all measurements, except the magnet measurements, occur synchronized with the sampling instances k.

In figure 6.8, it is outlined how all measurements are processed in the Kalman filter. The algorithms for this processing will be discussed in the next subsections.

Figure 6.9: Relation between $^{si}y_{m,si}$ and $^{si}y_{p_{si},si}$

6.8.1 Magnet updates

It is assumed that a set of magnetic field sensors is placed at the origin of each coordinate frame. In this chapter, slant of the magnet and vehicle will be neglected. In this way, the frames si can take the place of the frame s as defined in chapter 5 for each set of sensor. Moreover, the frames m and i^1 as defined in the same chapter coincide and are thus interchangeable. Under these assumptions, the vector component $^{i}y_{i,si}$ that is determined from the magnetic field sensor readings can be written as $^{si}y_{m,si}$. This will be done from now on to avoid confusion.

To apply an update to the observer, $^{si}y_{m,si}$ has to be expressed in the tracking errors $^{p_{si}}y_{p_{si},si}$. To allow for inaccurate magnet placement, it will be assumed that the magnets are placed at a known place in the neighborhood of the path to be followed, as shown in figure 6.9. Let the point p_m denote the orthogonal projection of the magnet onto the path. Then the deviation of the magnet from the path is given by $^{m}y_{p_m,m}$. Since, in general, the road curvature is small compared to the distance from the vehicle to the path and the distance from the magnet to the path, the distances $d1$ and $d2$ as defined in figure 6.9 can be neglected, so that the measurement $^{si}y_{m,si}$ can be expressed in the tracking errors with

$$^{si}y_{m,si}(\mathbf{x}) = \frac{^{p_{si}}y_{p_{si},si}(\mathbf{x})}{\cos{^{p_{si}}\epsilon_{si}(\mathbf{x})}} + \frac{^{m}y_{m,p_m}}{\cos{^{p_m}\epsilon_{si}(\mathbf{x})}}, \tag{6.84}$$

---

[1]Note that, with abuse of notation, the symbol i of the frames i denote 'ideal' whereas the symbol i of the frames si denote $0, \ldots, n+1$
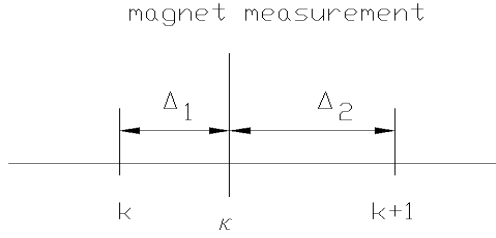
Figure 6.10: Asynchronous character of magnet updates

where $^{p_m}\epsilon_{si}$ denotes the angle between the tangent to the path at point p_m and frame si. A numerical example was worked out to study whether $d1$ and $d2$ can be neglected. With $^{si}y_{m,si} = 0.5\,m$, $^{p_{si}}y_{p_{si},si} = -0.4\,m$ and $^{m}y_{p_m,m} = 0.1\,m$ on a $12\,m$ radius curve, $d1 \approx 13.10^{-6}\,m$ and $d2 \approx 20.10^{-5}\,m$, which illustrates that it is valid to neglect $d1$ and $d2$.

As already discussed in the previous section, the time instance at which one of the vehicle's magnet sensors passes a magnet will, in general, not coincide with a sampling instance at which the prediction equation (6.72) is updated, as illustrated in figure 6.10. If the time instance Δ_2 as illustrated in figure 6.10 is too large, i.e. the deviation measured at $t = k\Delta + \Delta_1$ differs too much from the deviation at $t = (k+1)\Delta$, the asynchronous character has to be brought into account. In [78] a method based on multi-rate Kalman filtering [38] is proposed to deal with this. The same method will be used here. When the time at which magnet sensor i passes a magnet is known in relation to the sampling instances k, the time intervals Δ_1 and Δ_2 as defined in figure 6.10, can be determined. Equation (6.64) can be used then to calculate the prediction till time instance $t = k\Delta + \Delta_1$, assuming $\mathbf{v}(\xi) = \mathbf{0}$, $\mathbf{u}(\xi) = \mathbf{u}_k$, $t = k\Delta$, $\tau = \Delta_1$ and $\mathbf{x} = \hat{\mathbf{x}}_{k,\kappa-1}$, i.e

$$\mathbf{x}_{\kappa,\kappa-1} = e^{\mathbf{A}(\hat{\mathbf{x}}_{k,\kappa-1})\Delta_1} + \int_0^{\Delta_1} e^{\mathbf{A}(\hat{\mathbf{x}}_{k,\kappa-1})\xi}\mathbf{B}(\hat{\mathbf{x}}_{k,\kappa-1})d\xi\mathbf{u}_k. \tag{6.85}$$

The covariance of the estimation error can be propagated till time instant κ with

$$\mathbf{P}_{\kappa,\kappa-1} = \mathbf{A}_p(\hat{\mathbf{x}}_{k,\kappa-1})\mathbf{P}_{k,\kappa-1}\mathbf{A}_p^T(\hat{\mathbf{x}}_{k,\kappa-1}) + \mathbf{V}_k, \tag{6.86}$$

where (6.66), (6.75), (6.82) and (6.83) have to be evaluated at $\Delta = \Delta_1$. Subsequently, the measurement at time instance $t = k\Delta + \Delta_1$ can be utilized to update the state with

$$\hat{\mathbf{x}}_{\kappa,\kappa} = \hat{\mathbf{x}}_{\kappa,\kappa-1} + \mathbf{L}_{y_i}(^{si}y_{m,si} - ^{si}\hat{y}_{m,si}(\hat{\mathbf{x}}_{k,\kappa-1})), \tag{6.87}$$

where

$$\mathbf{C}_{yi} = \left.\frac{\partial^{si}\hat{y}_{m,si}(\mathbf{x})}{\partial\mathbf{x}}\right|_{\mathbf{x}=\hat{\mathbf{x}}_{k,\kappa-1}} \tag{6.88}$$

and

$$\mathbf{L}_{yi} = \mathbf{P}_{\kappa,\kappa-1}\mathbf{C}_{yi}^T(\mathbf{C}_{yi}\mathbf{P}_{\kappa,\kappa-1}\mathbf{C}_{yi}^T + W_{yi})^{-1}, \tag{6.89}$$

with W_{yi} the covariance of the measurement noise, which is assumed to be white and Gaussian with zero mean. The error covariance matrix can be updated with

$$\mathbf{P}_{\kappa,\kappa} = \mathbf{P}_{\kappa,\kappa-1} - \mathbf{L}_{yi}\mathbf{C}_{yi}\mathbf{P}_{\kappa,\kappa-1}. \tag{6.90}$$

Next, the state can be propagated to time instant $k+1$ using equation (6.64) again, but this time with t replaced with $k\Delta + \Delta_1$, $\tau = \Delta_2$ and $\mathbf{x}(t) = \hat{\mathbf{x}}_{\kappa,\kappa}$, so

$$\mathbf{x}_{k+1,\kappa} = e^{\mathbf{A}(\hat{\mathbf{x}}_{\kappa,\kappa})\Delta_2} + \int_0^{\Delta_2} e^{\mathbf{A}(\hat{\mathbf{x}}_{\kappa,\kappa})\xi}\mathbf{B}(\hat{\mathbf{x}}_{\kappa,\kappa})d\xi\mathbf{u}_k. \tag{6.91}$$

The error covariance matrix can be propagated with

$$\mathbf{P}_{k+1,\kappa} = \mathbf{A}_p(\hat{\mathbf{x}}_{\kappa,\kappa})\mathbf{P}_{\kappa,\kappa}\mathbf{A}_p^T(\hat{\mathbf{x}}_{\kappa,\kappa}) + \mathbf{V}_k, \tag{6.92}$$

where (6.66), (6.75), (6.82) and (6.83) have to be evaluated at $\Delta = \Delta_2$.

6.8.2 Wheelencoder updates

Wheel encoders can be used to determine the rotational wheel speed $\omega_{w_{ij}}$. Assuming the wheels do not slide over the road surface, $\omega_{w_{ij}}$ is related to the velocity of the wheel in the direction of the wheel plane $V_{w_{ij}}$ by

$$V_{w_{ij}} = \omega_{w_{ij}}r_{w_{ij}}, \tag{6.93}$$

with $r_{w_{ij}}$ the wheel radius. Note that the same notation has been used as in chapter 3. i.e. j stands for the axle number, with $j = 1$ for the tractor's front axle and $j = n + 1$ for the tractor's rear axle. Furthermore $i = 1$ for the wheels at the left and $i = 2$ for the wheels at the right.

Using the tire model as discussed in chapter 3, $V_{w_{ij}}$ can be expressed in the state vector $\mathbf{x}$ with

$$V_{w_{ij}}(\mathbf{x}) = \cos(\delta_{ij} - \arctan\frac{^{cj}\dot{y}_{w_{ij}}(\mathbf{x})}{^{cj}\dot{x}_{w_{ij}}(\mathbf{x})})\sqrt{^{cj}\dot{x}^2_{w_{ij}}(\mathbf{x}) + {}^{cj}\dot{y}^2_{w_{ij}}(\mathbf{x})}, \tag{6.94}$$

where, with some abuse of notation compared to chapter 3, a distinction has been made between the steering angles at the left and the steering angles at the right, in order to allow for differences in these two due to the steering mechanism.

Using (D.9) and (6.5), $^{cj}\dot{y}_{w_{ij}}$ and $^{cj}\dot{x}_{w_{ij}}$ can be expressed in the state vector $(\mathbf{x})$ with

$$^{cj}\dot{x}_{w_{ij}}(\mathbf{x}) = \mathbf{J}_{\mathrm{long}_{w_{ij}}}\,^{c1}\hat{\mathbf{q}} = \mathbf{J}_{\mathrm{lo}\,_{w_{ij}}}\mathbf{J}_{\mathrm{path}}^{-1}(^{Y}\mathbf{T}_x\mathbf{x} + {}^{Y}\mathbf{T}_{v_x}v_x) \tag{6.95}$$

$$^{cj}\dot{y}_{w_{ij}}(\mathbf{x}) = \mathbf{J}_{\mathrm{lat}\,_{w_{ij}}}\,^{c1}\hat{\mathbf{q}} = \mathbf{J}_{\mathrm{la}\,_{w_{ij}}}\mathbf{J}_{\mathrm{path}}^{-1}(^{Y}\mathbf{T}_x\mathbf{x} + {}^{Y}\mathbf{T}_{v_x}v_x), \tag{6.96}$$

where

$$^{Y}\mathbf{T}_x = \begin{bmatrix} \mathbf{0}^{1\times(n+1)} & \mathbf{0}^{1\times(3(n+1)+5)} \\ \mathbf{I}^{(n+1)\times(n+1)} & \mathbf{0}^{(n+1)\times(3(n+1)+5)} \end{bmatrix} \tag{6.97}$$

$$^{Y}\mathbf{T}_{v_x} = \begin{bmatrix} 1 & \mathbf{0}^{(n+1)\times 1} \end{bmatrix}^{T}. \tag{6.98}$$

Note that in equation (6.95) and (6.96) the longitudinal velocity v_x also has to be measured, since v_x is not part of the observer state. Furthermore

$$\mathbf{J}_{\mathrm{long}\,_{w_{i1}}} = \begin{bmatrix} 1 & 0 & (-1)^i b_1 & 0 & \dots & 0 \end{bmatrix} \tag{6.99}$$

$$\mathbf{J}_{\mathrm{lat}\,_{w_{i1}}} = \begin{bmatrix} 0 & 1 & l_{f1} & 0 & \dots & 0 \end{bmatrix} \tag{6.100}$$

and

$$\mathbf{J}_{\mathrm{long}_{w_{ij}}} = \begin{bmatrix} \cos{}^{c1}\epsilon_{cj} & \sin{}^{c1}\epsilon_{cj} & d_{w_{1j}}\sin{}^{cj}\epsilon_{c1} \dots d_{w_{j-1j}}\sin{}^{cj}\epsilon_{cj-1} & (-1)^i b_j & 0\dots 0 \end{bmatrix}$$

$$\mathbf{J}_{\mathrm{lat}_{w_{ij}}} = \begin{bmatrix} \cos{}^{c1}\epsilon_{cj} & \sin{}^{c1}\epsilon_{cj} & d_{w_{1j}}\sin{}^{cj}\epsilon_{c1} \dots d_{w_{nj}}\sin{}^{cj}\epsilon_{cn} \end{bmatrix}. \tag{6.101}$$

for $j > 1$.

Assuming a measurement of the speed of wheel w_{ij} comes available at time instant $k = \kappa$, the state estimate can be updated with

$$\hat{\mathbf{x}}_{\kappa,\kappa} = \hat{\mathbf{x}}_{\kappa,\kappa-1} + \mathbf{L}_{w_{ij}}(V_{w_{ij}} - \hat{V}_{w_{ij}}(\hat{\mathbf{x}}_{\kappa,\kappa-1})), \tag{6.102}$$

where

$$\mathbf{L}_{w_{ij}} = \mathbf{P}_{\kappa,\kappa-1}\mathbf{C}_{w_{ij}}^{T}(\mathbf{C}_{w_{ij}}\mathbf{P}_{\kappa,\kappa-1}\mathbf{C}_{w_{ij}}^{T} + W_{V\,w_{ij}})^{-1}, \tag{6.103}$$

with

$$\mathbf{C}_{w_{ij}} = \left.\frac{\partial V_{w_{ij}}(\mathbf{x})}{\partial\mathbf{x}}\right|_{\hat{\mathbf{x}}_{\kappa,\kappa-1}}. \tag{6.104}$$

The noise covariance matrix $W_{Vw_{ij}}$ can be calculated with

$$W_{V\,w_{ij}} = W_{\omega w_{ij}}r_{w_{ij}}^{2} + \frac{\partial\hat{V}_{w_{ij}}}{\partial v_x}W_{v_x}\left(\frac{\partial\hat{V}_{w_{ij}}}{\partial v_x}\right)^{T}, \tag{6.105}$$

with $W_{\omega w_{ij}}$ the noise covariance of the wheel speed measurement and W_{v_x} the noise covariance of the velocity measurement. Subsequently, the error covariance matrix can be updated with

$$\mathbf{P}_{\kappa,\kappa} = \mathbf{P}_{\kappa,\kappa-1} - \mathbf{L}_{w_{ij}}\mathbf{C}_{w_{ij}}\mathbf{P}_{\kappa,\kappa-1}. \tag{6.106}$$

6.8.3 Gyroscope updates

A rate gyroscope can be used to measure the yaw-rate of a carriage with respect to the world. The yaw-rate can be expressed in the state vector $\mathbf{x}$

$$^{w}\dot{\epsilon}_{ci}(\mathbf{x}) = {}^{\epsilon_{ci}}\mathbf{T_q}\mathbf{J}_{\text{path}}^{-1}({}^{Y}\mathbf{T}_x\mathbf{x} + {}^{Y}\mathbf{T}_{v_x}v_x). \tag{6.107}$$

Assuming a measurement of $^{w}\dot{\epsilon}_{ci}$ comes available at time instant $k = \kappa$, the state can be updated with

$$\hat{\mathbf{x}}_{\kappa,\kappa} = \hat{\mathbf{x}}_{\kappa,\kappa-1} + \mathbf{L}_{\epsilon_{ci}}({}^{w}\dot{\epsilon}_{ci} - {}^{w}\hat{\dot{\epsilon}}_{ci}(\hat{\mathbf{x}}_{\kappa,\kappa-1})), \tag{6.108}$$

where

$$\mathbf{L}_{\epsilon\,ci} = \mathbf{P}_{\kappa,\kappa-1}\mathbf{C}_{\epsilon_{ci}}^{T} \left[\mathbf{C}_{\epsilon_{ci}}\mathbf{P}_{\kappa,\kappa-1}\mathbf{C}_{\epsilon_{ci}}^{T} + W_{\epsilon_{ci}} + \frac{\partial^{w}\hat{\dot{\epsilon}}_{ci}}{\partial v_x}W_{v_x}\left(\frac{\partial^{w}\hat{\dot{\epsilon}}_{ci}}{\partial v_x}\right)^{T} \right]^{-1}, \tag{6.109}$$

with

$$\mathbf{C}_{\epsilon\,ci} = \left.\frac{\partial^{w}\dot{\epsilon}_{ci}(\mathbf{x})}{\partial \mathbf{x}}\right|_{\hat{\mathbf{x}}_{\kappa,\kappa-1}} \tag{6.110}$$

and $w_{\epsilon\,ci}$ the covariance of the measurement noise of the gyroscope. Subsequently, the covariance matrix can be updated with

$$\mathbf{P}_{\kappa,\kappa} = \mathbf{P}_{\kappa,\kappa-1} - \mathbf{L}_{\epsilon_{ci}}\mathbf{C}_{\epsilon_{ci}}\mathbf{P}_{\kappa,\kappa-1}. \tag{6.111}$$

6.8.4 Articulation angle updates

The articulation angle is one of the quantities that can be measured relatively easily. Therefore, an articulation angle sensor is also a good candidate to be used to update the Kalman filter. A problem with the articulation angle is that it depends on the path to be followed. For example, when the vehicle follows exactly a curve, the articulation angle doesn't equal zero but equals the desired articulation angle $\phi_{i_{\text{des}}} = {}^{w}\epsilon_{ci+1_{\text{des}}} - {}^{w}\epsilon_{ci_{\text{des}}}$, $i = 1..n-1$. Therefore, the shape of the path has to be taken into account with the updates of the filter with articulation angle measurements. In order to do this, the articulation angle relative to the desired articulation angle $\phi_{i_{\text{err}}} = {}^{w}\epsilon_{ci+1_{\text{err}}} - {}^{w}\epsilon_{ci_{\text{err}}}$, $i = 1..n-1$ can be expressed in the states $\mathbf{x}$ with

$$\phi_{i_{\text{err}}} = {}^{\phi_i}\mathbf{T}_{c1_{q'}}{}^{y}\mathbf{T}_{c1_{q'}}^{-1}{}^{y}\mathbf{T}_x\mathbf{x}, \tag{6.112}$$

where the matrix ${}^{\phi_i}\mathbf{T}_{c1_{q'}}$ is an 1 by $n+1$ matrix filled with zeros, except for the $(i+1)$th and the ith component which equal 1 and -1 respectively. Now an estimate of $\hat{\phi}_i$ can be obtained with

$$\hat{\phi}_i = \hat{\phi}_{i_{\text{err}}} + {}^{w}\epsilon_{ci+1_{\text{des}}} - {}^{w}\epsilon_{ci_{\text{des}}} \quad i = 1..n-1 \tag{6.113}$$

Assuming a measurement of ϕ_i comes available at time instant $k = \kappa$, the state can be updated with

$$\hat{\mathbf{x}}_{\kappa,\kappa} = \hat{\mathbf{x}}_{\kappa,\kappa-1} + \mathbf{L}_{\phi_i}(\phi_i - \hat{\phi}_i(\hat{\mathbf{x}}_{\kappa,\kappa-1})), \tag{6.114}$$

where

$$\mathbf{L}_{\phi_i} = \mathbf{P}_{\kappa,\kappa-1}\mathbf{C}_{\phi_i}^T(\mathbf{C}_{\phi_i}\mathbf{P}_{\kappa,\kappa-1}\mathbf{C}_{\phi_i}^T + W_{\phi_i})^{-1}, \tag{6.115}$$

with

$$\mathbf{C}_{\phi_i} = \left.\frac{\partial^w \phi_i(\mathbf{x})}{\partial \mathbf{x}}\right|_{\hat{\mathbf{x}}_{\kappa,\kappa-1}} \tag{6.116}$$

and W_{ϕ_i} the covariance of the measurement noise of the articulation angle measurements. Subsequently, the covariance matrix can be updated with

$$\mathbf{P}_{\kappa,\kappa} = \mathbf{P}_{\kappa,\kappa-1} - \mathbf{L}_{\phi_i}\mathbf{C}_{\phi_i}\mathbf{P}_{\kappa,\kappa-1}. \tag{6.117}$$

6.9 Determination of path orientations and desired orientations

To calculate the articulation angle update of the observer, online information about the desired orientations $^w\epsilon_{ci_{\text{des}}}$ is required. Moreover, the observer depends on the path orientations $^w\epsilon_{p_{si}}$ and their derivatives with respect to time via the matrix $\mathbf{J}_{\text{path}}$ and its time derivative in equation (6.20). How to determine these quantities is topic of this section.

When the path to be followed and the points $\mathbf{s}_i$ are known, the desired orientations $^w\epsilon_{p_{ci_{\text{des}}}}$ can be calculated as function of $\sigma_{p_{s1}}$, and stored in a look-up table which has $\sigma_{p_{s1}}$ as input. Equation (E.8) and (E.8) in combination with equation (3.67) can be used to obtain an online estimate of $\dot{\sigma}_{p_{s1}}$, which can be integrated to obtain an estimate of $\sigma_{p_{s1}}$ that can be used as input for the look-up table.

This integration might be subjected to drift due to for example wrong initial values of the integrator routine. This drift can be corrected for by utilizing the permanent magnets of the magnetic referencing system. A requirement is that the distances from the magnets to the starting point of the path is known (either by placing them at a fixed distance, or by storing the actual distance of each magnet in a look-up table). Each time the magnetic field sensor at the front of the vehicle passes a magnet, the integrator can be reset to the distance of this magnet.

To obtain $^w\epsilon_{p_{si}}$, the same procedure as for the desired orientations can be followed. The orientation of the path can be calculated as function of the distance to the beginning of the path and stored in a look-up table. The look-up table can be read out with $\sigma_{p_{si}}$ as input. $\sigma_{p_{si}}$ can be obtained in a similar way as for $\sigma_{p_{s1}}$.

The rate of change or the path orientation ${}^{w}\dot{\epsilon}_{p_{si}}$, can be obtained by using

$${}^{w}\dot{\epsilon}_{p_{si}} = \frac{d^{w}\epsilon_{p_{si}}}{d\sigma_{p_{si}}}\dot{\sigma}_{p_{si}}, \tag{6.118}$$

By calculating $\frac{d^{w}\epsilon_{p_{si}}}{d\sigma_{p_{si}}}$ off-line as function of $\sigma_{p_{si}}$, and storing the result in a look-up table, ${}^{w}\dot{\epsilon}_{p_{si}}$ can be obtained online by by using the estimate of $\sigma_{p_{si}}$ as input of the table, and multiplying the output of the table by $\dot{\sigma}_{p_{si}}$.

6.10   Simulation results

Simulations have been carried out to investigate the performance of the designed Kalman filter. For these simulations, a model of an all-wheel steered double articulated vehicle has been used. This vehicle was steered along the path to be followed by means of the feedback linearizing controller that will be presented in chapter 8. The true deviation and true velocity with respect to the path were used as input for the controller, so that the observer operates in open loop. The distance between magnets of the magnetic referencing system, as discussed in chapter 5, was set to $4\,m$ in the simulations. Table 6.1 lists the sensor noise covariances as used for the tuning of the Kalman filter and to simulate sensor noise during the simulations.

quantity	covariance	unit
$V_{\alpha_{a i_y}}$	0.2	m^2/s^4
V_{v_x}	0.0004	m^2/s^2
$V_{c1\ddot{x}_{w,c1}}$	0.01	m^2/s^4
$W_{\epsilon_{ci}}$	0.00005	rad^2/s^2
W_{ϕ_i}	0.00002	rad^2
W_{yi}	0.0001	m^2

Table 6.1: Sensor noise covariances

To obtain the noise covariance of the accelerometer readings $\alpha_{a i_y}$ and the gyro readings ${}^{w}\dot{\epsilon}_{ci}$, a test vehicle equipped with accelerometers and a gyroscoop was driven on a straight road. It was assumed that the lateral acceleration and the yaw-rates of the vehicle equal zero for this case. The noise covariances were determined by calculating the mean of the square of the sensor readings minus the mean of the sensor readings, over a finite time interval, i.e.

$$V_{\chi} = \frac{1}{N}\sum_{i=1}^{N}(\chi(i) - \frac{1}{N}\sum_{i=1}^{N}\chi(i))^2, \tag{6.119}$$

where $\chi(i)$ denotes the ith sensor reading, N the total number of samples and V_{χ} the noise covariance. The test vehicle was equipped with a diesel engine

to drive the vehicle. It appeared that the accelerometer noise covariance was influenced by the number of revolutions of the engine. For the tuning of the observer and the simulations, the worst case situation as measured on the test vehicle was considered. The remaining sensor noise covariances are derived from sensor datasheets.

The state disturbance covariances as used to tune the observer are listed in table 6.2. Note that the state disturbances on the derivatives of $^{psi}y_{p_{si},si}$ and on θ were considered to be zero. The state disturbance on $^{psi}\ddot{y}_{p_{si},si}$ were modeled by the noise of the accelerometers.

quantity	covariance	unit
V_y	0	m^2
$V_{o_{ai}}$	0.001	m^2/s^4
$V_{\eta_{ai}}$	0.0005	rad/m
V_Φ	0.1	rad^2
$V_{\dot\theta}$	0.01	rad^2/s^2
V_θ	0.0	rad^2
V_{ζ_1}	0.1	$1/s$
V_{ζ_2}	1	$1/s^2$

Table 6.2: State disturbance covariances

The covariance matrix $\mathbf{P}_{0,0}$ was taken as a diagonal matrix, i.e. the errors in the initial states are considered to be uncorrelated. The diagonal elements of $\mathbf{P}_{0,0}$ are shown in table 6.3. For clarity, the covariances are grouped by the sort of state to which they correspond. The states corresponding with the diagonal elements of $\mathbf{P}_{0,0}$ are listen in the left column of table 6.3. The initial covariances of the lateral velocities $^{psi}\dot{y}_{p_{si},si}$ and the roll velocity $\dot\theta$ are taken equal to zero, since it is assumed that the Kalman filter is switched on when the vehicle starts from standing still.

state	covariance	covariance unit
$^{psi}\dot{y}_{p_{si},si}$	0.00	m^2/s^2
$^{psi}y_{p_{si},si}$	0.1	m^2
o_{ai}	0.04	m^2/s^4
η_{ai}	0.05	rad^2/s^2
Φ	0.01	rad^2
$\dot\theta$	0.0	m^2/s^2
θ	0.01	rad^2
ζ_1	1	$1/s$
ζ_2	10	$1/s^2$

Table 6.3: Diagonal elements of covariance matrix

The left plot in figure 6.11 shows the estimated (dashed lines) and true (continuous lines) tracking errors $^{psi}y_{psi,si}$ for a vehicle entering a curve with $300\,m$ radius at $20\,m/s$ longitudinal speed. The true tracking errors have been calculated with equations 4.4, 4.6 and 4.11. The vehicle enters the curve at $t = 1s$. The right plot in the same figure shows the estimation errors. The maximum estimation error equals about $1\,cm$. The left plot of figure 6.12 shows the true and estimated tracking velocities $^{psi}\dot{y}_{psi,si}$ for the same situation, whereas the right plot of the same figure shows the velocity estimation error. For this situation, the maximum velocity estimation error equals about $0.05\,m/s$. At the beginning of the simulation, the velocity estimation error is a bit larger due to the fact that initial values of the parameters η_i and the sensor offsets o_i were not set correctly. To illustrate this, figure 6.13 shows the estimates of the sensor offsets o_i in the left plot and the estimates of the gains η_i in the right plot. Both figures show that both sets of parameters converge to a steady state value (besides some variations due to noise) after a few seconds. These steady state values do not completely correspond with the true values of the parameters, but as figure 6.11 shows, the mean values of the estimates of the tracking errors still converge to the true tracking errors despite the mismatch between the estimated and true parameters. For completeness, figure 6.14 shows the true and estimated roll angle of the vehicle in the left plot and the true and estimated road banking angle in the right plot. For this simulation, the road banking angle was set to $0\,rad$. As the right plot in figure 6.14 shows, the estimate road banking angle converges to a value close to zero. The left plot of the same figure shows that the estimated vehicle roll angle follows the same trend as the true roll angle. When the vehicle is completely in the curve, the mismatch between the estimated roll angle and the true angle is about $20\,\%$. This is due to the fact that the roll dynamics are not sufficiently excited. Results of closed loop simulations show that in this case the estimate of the roll angle converges better. In closed loop, the roll dynamics are excited by the measurement noise.

With the simulation results as shown so far, the velocity is relatively high, so that the update rate of the magnet measurements also relatively high. To investigate what happens at low speeds, when the update rate of the magnet measurements is low, the same kind of simulation was carried out with a vehicle driving at $6\,m/s$ and entering and exiting a curve with a radius of $20\,m$ at $t = 2.9\,s$ and $t = 13.4\,s$ respectively. With this curve and this speed, the steady state lateral acceleration the vehicle experiences when it is completely in the curve equals $1.8\,m/s^2$, so that there still will be sufficient roll of the vehicle to judge the performance of the observer when the vehicle is subjected to roll.

The left plot of 6.15 shows the true and estimated tracking errors for this situation. The right plot of the same figure shows the estimation error. The estimation error is relatively large at the beginning of the simulation due to a mismatch between the true and estimated accelerometer offsets and the gains of the suspension system, as illustrated in both plots in figure 6.17. Later on
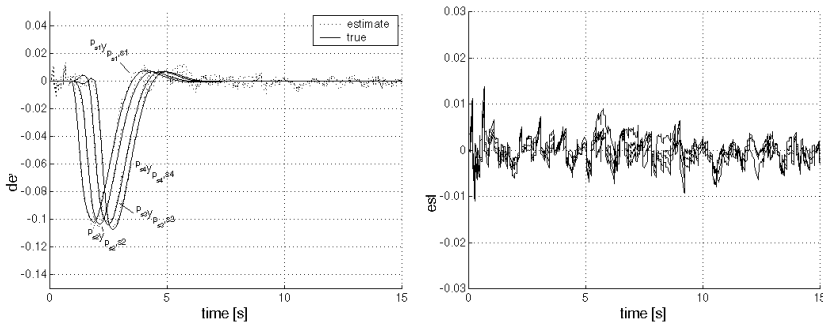
Figure 6.11: True and estimated tracking errors for a vehicle driving at 20 m/s entering a curve with radius of 300 m
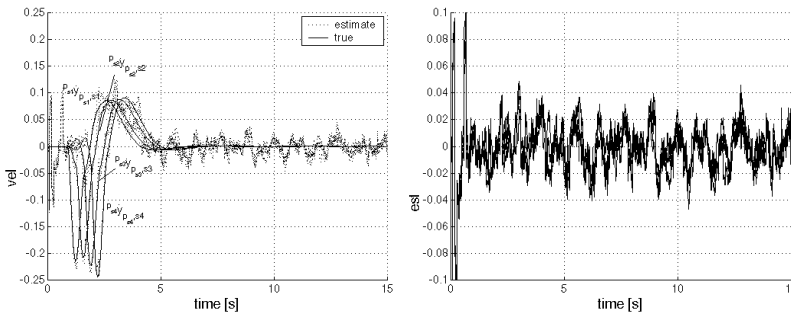

Figure 6.12: True and estimated lateral velocities for a vehicle driving at 20 m/s entering a curve with radius of 300 m

in the simulations, the maximum estimation error is about $3\,cm$. The largest estimation errors mostly take place when the vehicle enters or exits the curve. In steady state in the curve and at the straight road sections, the maximum estimation error is about $1\,cm$. Figure 6.18 shows the true and estimated roll angles of the vehicle as well as the true and estimated road banking angle. The plot of the roll angles show that for this curve, the true roll angles of the carriages are not completely the same anymore, as was assumed with the modeling of the vehicles roll motion in equation (6.27). The difference between the roll angles however is negligibly small. Despite the difference in the true roll angles and the simplifying assumptions that have been made, the estimated roll angle follows the true roll angles reasonably well, especially when the vehicle is completely in the curve. At the entrance of the curve, there is discrepancy between the estimated and the true roll angles. This might be the reason of the somewhat
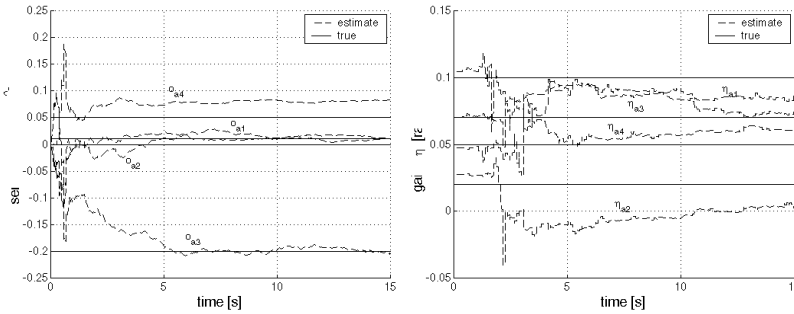
Figure 6.13: True and estimated parameters for a vehicle driving at 20 m/s entering a curve with radius of 300 m
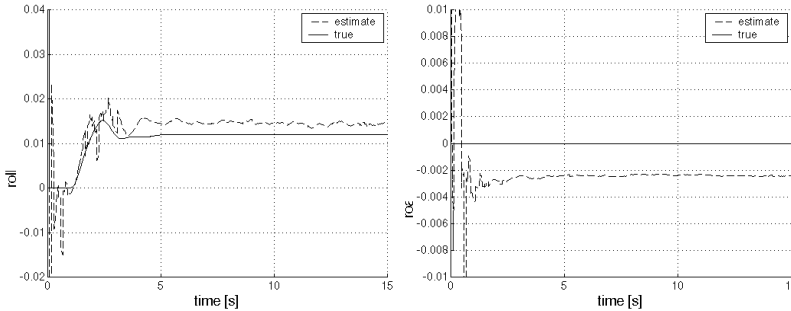

Figure 6.14: True and estimated roll angle (left plot) and road banking angle (right plot) for a vehicle driving at 20 m/s entering a curve with radius of 300 m

larger estimation errors at the entrance of the curve.

In order to show that the designed Kalman filter also performs well when the vehicle is subjected to a wind disturbance, simulations were run with a wind disturbance acting on the vehicle. The vehicle was assumed to drive in between buildings at the beginning of the simulation, so that there is no wind disturbance. After 5 seconds, the vehicle enters the free field where a strong wind is blowing. This simulation was carried out with both a vehicle speed of $5\,m/s$ and a speed of $20\,m/s$. The figures 6.19 and 6.20 show the simulation results for the vehicle driving at $20\,m/s$. These figures show that the maximum error in the estimation of the tracking error is about $1\,cm$ whereas the maximum error in the estimation of the velocity with respect to the path equals about $0.07\,m/s$. At the beginning of the simulation, the estimation errors are somewhat larger due to the mismatch of the estimated gains and sensor offsets as discussed with
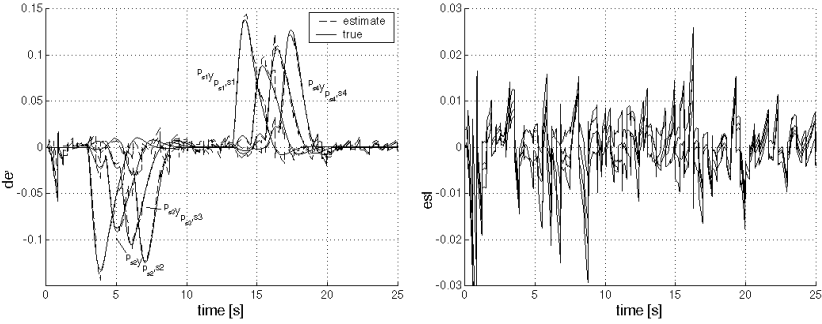
Figure 6.15: True and estimated tracking errors for a vehicle driving at 6 m/s entering a curve with radius of 20 m
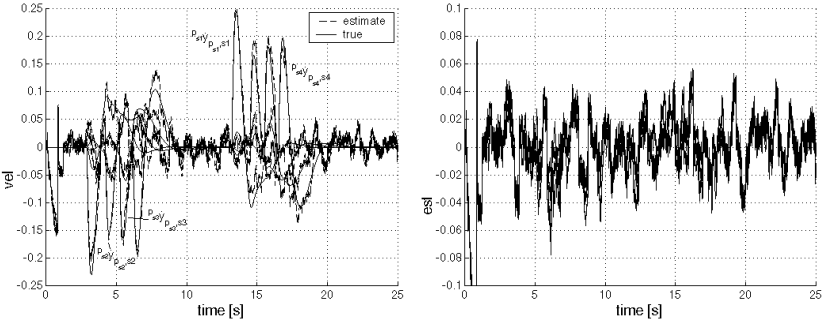

Figure 6.16: True and estimated lateral velocities for a vehicle driving at 6 m/s entering a curve with radius of 20 m
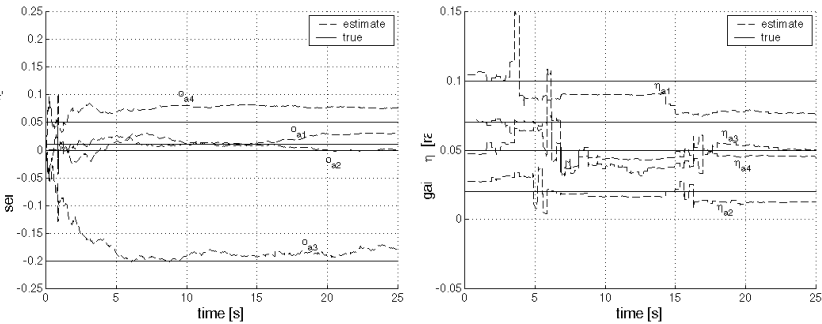

Figure 6.17: True and estimated parameters for a vehicle driving at 6 m/s entering a curve with radius of 20 m
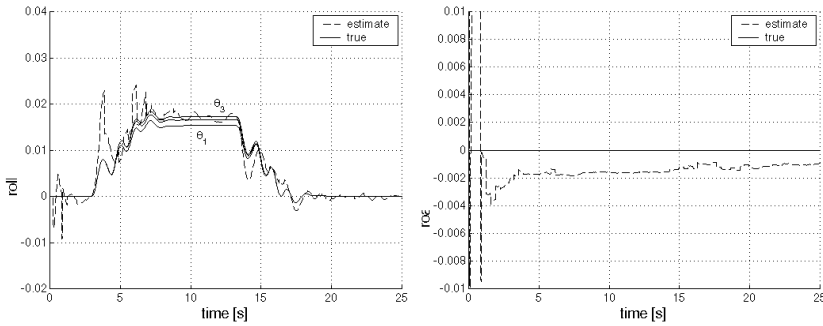
Figure 6.18: True and estimated roll angle (left plot) and road banking angle (right plot) for a vehicle driving at 6 m/s entering a curve with radius of 20 m
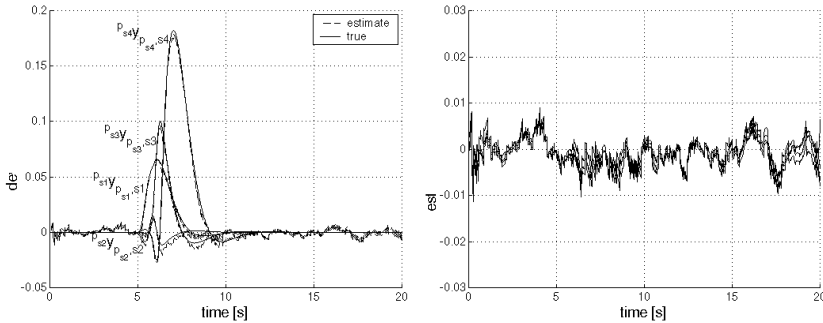

Figure 6.19: True and estimated tracking errors for a vehicle driving at 20 m/s subjected to a wind disturbance

the simulation results for the vehicle entering a curve.

The figures 6.21 and 6.22 show the simulation results for the vehicle driving at $5\,m/s$. In this case, the maximum error in the estimation of the tracking error is about $2\,cm$ whereas the maximum error in the estimation of the velocity with respect to the path equals about $0.08\,m/s$ after the first few second of the simulation. At the beginning of the simulation, the estimation errors are somewhat larger again, as also discussed above. The simulation results show that despite the low update rate of the magnetic referencing system for low speed, the Kalman filter still performs reasonably well.
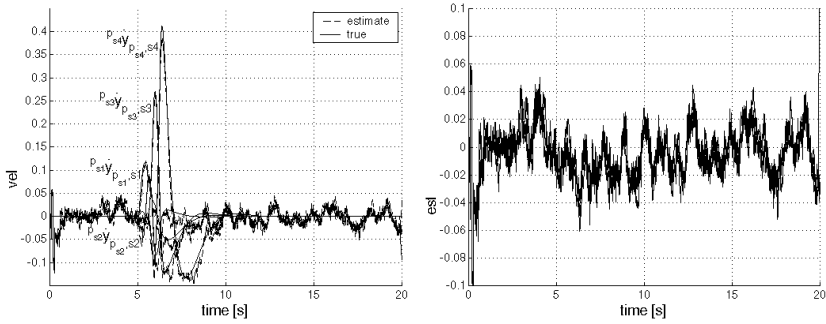
Figure 6.20: True and estimated lateral velocities for a vehicle driving at $20\,\mathrm{m/s}$ subjected to a wind disturbance
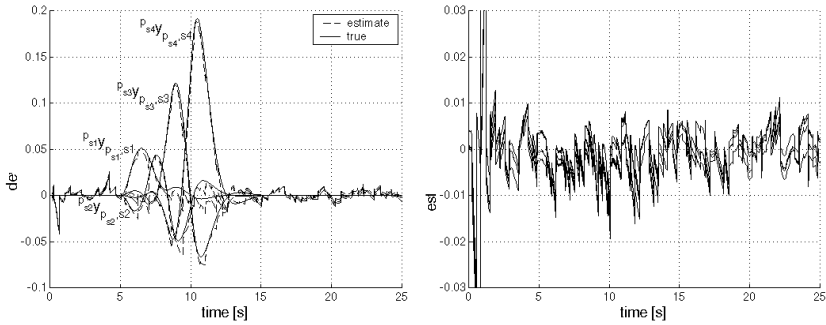

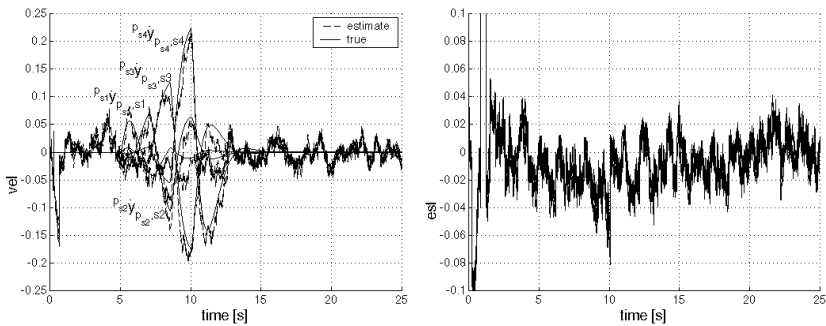Figure 6.21: True and estimated tracking errors for a vehicle driving at 5 m/s subjected to a wind disturbance

Figure 6.22: True and estimated lateral velocities for a vehicle driving at 5 m/s subjected to a wind disturbance

6.11 Summary

An extended multi-rate Kalman filter has been designed to obtain continuous estimates of the tracking errors and tracking velocities. This Kalman filter uses accelerometers as input so that the effects of parameter variations and wind disturbances remain small. To reduce the influence of road banking, vehicle roll and offsets of the accelerometers, these variables are estimated online with the Kalman filter.

The main sensors used to apply updates to the state estimates are the magnetic field sensors as discussed in the previous chapter. To deal with the discrete character of these measurements, these updates are processed asynchronously in time. The use of other sensors like articulation angle sensors, wheel encoders and rate gyro's has been discussed, so that updates to the filter can be applied also in between the magnets. Although these sensors provide no direct information about the distance form the vehicle to the path, they improve the description of the vehicle kinematics that is used in the Kalman filter. In this way, a better estimate can be obtained, and the extra sensors add redundancy to the Kalman filter, which can be useful in case of failure of one or more sensors.

Simulation results show that the Kalman filter performs well both at low and high speed, for a distance of $4\,m$ in between the permanent magnets that are used to mark the path. Although the estimates of the road banking angle, the sensor offsets and vehicle roll do not converge to their true values, estimation errors of less than $2\,cm$ can be achieved under the simulated circumstances.

7

Model analysis for controller design

7.1   Introduction

Before discussing the actual design of controllers, this chapter will be used to address some topics that are important for the controller design. To start with, section 7.2 will be used to consider the locations of the points $\mathbf{s}_i$. Some possible good locations will be discussed and a set of locations will be selected that will be used in the remainder of this thesis. The vehicle model as derived in chapter 3 has the drive torques and steering angles as input. In principle, both type of inputs can be used for steering the vehicle. Section 7.3 will be used to show that the steering inputs are the most beneficial for steering the vehicle. Moreover, it will be derived that the influence of the drive torques on the lateral dynamics of the vehicle can be neglected, so that knowledge of the drive torques is not necessary for the lateral guidance system. The last but one section of this chapter will be used to discuss the advantages of all-wheel steering compared to front-wheel steering. A steady state analysis will be carried out to show the influence of the longitudinal speed on the off-tracking behavior of multiple-articulated vehicles. Finally, the influence of all-wheel steering on the yaw dynamics will be considered, and it will be shown that in order to damp the yaw dynamics, all-wheel steering is recommendable. The conclusions of this chapter will be presented in chapter 7.5

7.2   Selection of outputs

In chapter 2, the outputs to be controlled are defined as the distances between the path to be followed and the points $\mathbf{s}_i$. The exact locations of the points $\mathbf{s}_i$ were left out of consideration till so far. How to choose the location of the points $\mathbf{s}_i$ is topic of this section.
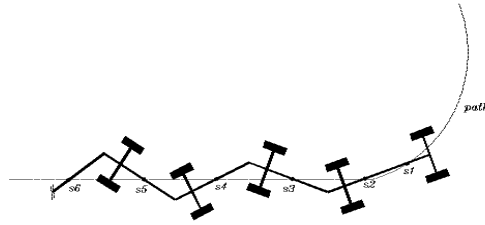
Figure 7.1: Vehicle entering a curve with points **si** chosen to optimize the occupied road space in curved path sections
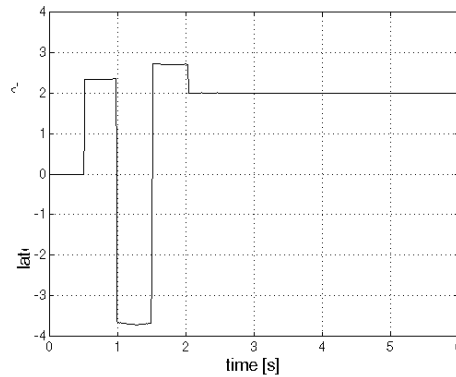

Figure 7.2: Lateral acceleration of rear end of a double articulated vehicle entering a curve with points **si** chosen to optimize the occupied road space when the vehicle is in a curve

Several criteria can be utilized to define the 'optimal' locations for the points $\mathbf{s}_i$. For example, the points $\mathbf{s}_i$ can be chosen to minimize the road space occupied by the vehicle. Another approach is to put the points $\mathbf{s}_i$ in the vicinity of the doors, to minimize the distance between the doors of the busses and the platform at the bus stop. In this way this distance is as small as possible, so that people can board the vehicle very easily. The most obvious approach is to locate the points in the middle of the axles of the vehicle, so that all axles follow the same track, as is the case with railroad vehicles. All these approaches however leave passenger comfort out of consideration.

To illustrate this, figure 7.1 shows a picture of a multiple-articulated vehicle when it enters a curve. The locations of the points $\mathbf{s}_i$ where chosen somewhere in the middle of the semi-trailers for the points $\mathbf{s}_3..\mathbf{s}_{n+1}$ and about 1/4 from each end of the tractor for the points $\mathbf{s}_1$ and $\mathbf{s}_2$. In this way, the occupied road space is minimized, when the vehicle is in a curved path section. As the
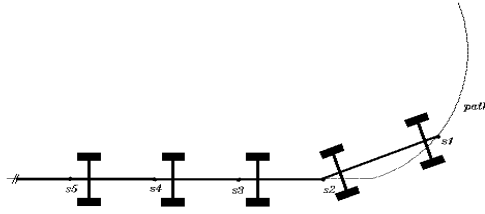
Figure 7.3: Vehicle entering a curve with points **si** chosen for passengers comfort
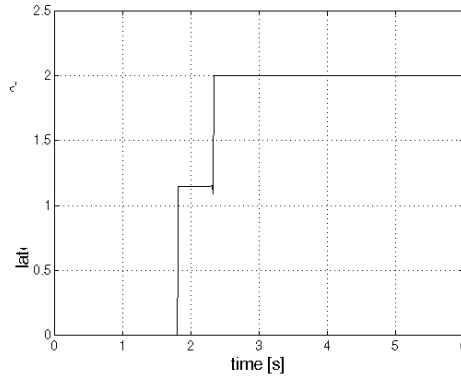

Figure 7.4: Lateral acceleration of rear end of a vehicle entering a curve with points **si** chosen for passengers comfort

figure shows, the rotation that the tractor experiences when it enters the curve is propagated through the succeeding carriages to the last carriage. In this way, passengers in the succeeding carriages already experience a lateral acceleration before the carriage itself enters the curve. Figure 7.2 shows the acceleration profile the passengers in the rear end of the last carriage experience in the lateral direction when a double articulated vehicle enters a curve with zero tracking error. As the figure shows, the passengers experience several changes in lateral acceleration before the last carriage enters the curve. For passenger comfort, this is undesirable.

Figure 7.3 shows the same kind of situation as depicted in figure 7.1, but in this case, the points $\mathbf{s}_i\, i = 2..n$ are placed at the hitching points in between the carriages and the point $\mathbf{s}_{n+1}$ is place at the center of the rear bumper of the vehicle. The point $\mathbf{s}_1$ was placed at the front bumper, but the location of this point is not critical for the following discussion. As the picture illustrates,

there is no premature propagation of rotations to the semi-trailers in this way. Figure 7.4 shows the lateral acceleration of a passenger in the rear end of the last carriage of a double articulated vehicle if the tracking error is zero for this situation. The figure shows this acceleration is unequal to zero only when the last carriage itself is in the curve. This is much more desirable for passenger comfort. For this reason, the points $\mathbf{s}_2, .., \mathbf{s}_{n+1}$ will be located following the last method in the remainder of this thesis. The point $\mathbf{s}_1$ will be located $2\,m$ behind the tractor's front axle, to reduce the road space occupied by the tractor.

7.3   Input selection

The model as described in chapter 3 has $n+1$ steering angles and $2(n+1)$ drive torques as input. The steering angles are meant for steering the vehicle whereas the torques are mainly meant to drive the vehicle. However, applying different torques to the left and right wheel of each axle, the torques can also be used for steering the vehicle. Together with the $n+1$ steering angles, this yields a total of $2(n+1)$ possible inputs for steering the vehicle. Since the model (3.76) only has $n+1$ independent degrees of freedom to be controlled, $n+1$ inputs suffice to control all tracking errors $^{p_{si}}y_{p_{si},si}$. This section will be dedicated to present a method to select those $n+1$ inputs out of the $2(n+1)$ available inputs, which have the largest influence on the tracking errors. As an example, this selection method has been applied to a double articulated vehicle.

The selection method that has been used is based on the singular values of the model of a double-articulated vehicle. The singular values can be considered as the principal gains of a system. To see this, let $\mathbf{G}$ denote a transfer function from input to output of a $l \times m$ system. Then, $\mathbf{G}$ can be decomposed as [80]

$$\mathbf{G} = \mathbf{U}\mathbf{\Sigma}\mathbf{V}^H \qquad (7.1)$$

where $\mathbf{V}^H$ denotes the complex conjugate transpose of $\mathbf{V}$. The matrices $\mathbf{V}$ and $\mathbf{U}$ are unitary matrices. The columns of $\mathbf{V}$ can be considered as the principal input directions, whereas the columns of $\mathbf{U}$ can be viewed as the principal output directions. The matrix $\mathbf{\Sigma}$ is an $l \times m$ matrix with $\Sigma_{[i,i]}$ as the singular values. The remaining elements equal zero. In this way, the ith singular value can be viewed as the gain between the ith principal input and the ith principal output. The larger the singular values are, the more influence the inputs have on the outputs.

To carry out this singular value analysis for one set of inputs, an a priori selection of $n+1$ inputs has to be made. A comparison has to be made between the singular values of, in principle, all possible input combinations. For large values of n, this is quite a lot of work. However, from the physics of the vehicle, it can be concluded beforehand that using both the differential torque and steering angle of the same axle as component of the $n+1$ input vector results in loss of

controllability, since not the whole space spanned by the outputs can be reached in this way. Therefore, for each axle, either the differential torques or steering angles has to be considered. This leaves 2^{n+1} combinations to be checked.

Prior to the analysis as discussed above, the inputs and outputs of the system have to be scaled, such that a scaled input with magnitude one corresponds to the maximum allowed value of the real input and a scaled output value one corresponds to the intended maximum output value. Input scaling is required since different types of inputs are considered with differences in their maximum values. Scaling the outputs is not strictly necessary, but yields an extra screening tool. When the singular values of the input and output scaled system are smaller than 1, the outputs can not be controlled to the intended maximum value.

Let, in order to scale the system, the unscaled system be denoted by

$$\mathbf{y} = \mathbf{H}\mathbf{u} \tag{7.2}$$

Then the transfer function $\mathbf{G}$ from the scaled input

$$\mathbf{u}_{\mathrm{sc}} = \begin{bmatrix} \dfrac{u_{[1]}}{u_{\mathrm{max}_{[1]}}} \\ \vdots \\ \dfrac{u_{[l]}}{u_{\mathrm{max}_{[l]}}} \end{bmatrix}, \tag{7.3}$$

to the scaled output

$$\mathbf{y}_{\mathrm{sc}} = \begin{bmatrix} \dfrac{y_{[1]}}{u_{\mathrm{max}_{[1]}}} \\ \vdots \\ \dfrac{u_{[l]}}{y_{\mathrm{max}_{[l]}}} \end{bmatrix} \tag{7.4}$$

can be written as

$$\mathbf{G} = \begin{bmatrix} \dfrac{H_{[1,1]}u_{\mathrm{max}_{[1]}}}{y_{\mathrm{max}_{[1]}}} & \cdots & \dfrac{H_{[1,n+1]}u_{\mathrm{max}_{[n+1]}}}{y_{\mathrm{max}_{[1]}}} \\ \vdots & \cdots & \vdots \\ \dfrac{H_{[n+1,1]}u_{\mathrm{max}_{[1]}}}{y_{\mathrm{max}_{[n+1]}}} & \cdots & \dfrac{H_{[n+1,n+1]}u_{\mathrm{max}_{[n+1]}}}{y_{\mathrm{max}_{[n+1]}}} \end{bmatrix} \tag{7.5}$$

where $u_{\mathrm{max}_{[i]}}$ denotes the maximum of the absolute value of input $u_{[i]}$ and where $y_{\mathrm{max}_{[i]}}$ denotes the maximum of the absolute value of output $y_{[i]}$.

In order to use the method as described above for selecting the inputs with the largest influence on the tracking errors of the multiple-articulated vehicle, the torque input vector as defined in equation (3.73) has been written as

$$\mathbf{T}_{\mathrm{dr}} = \begin{bmatrix} \mathbf{T}_{\mathrm{dr}m} - \Delta\mathbf{T}_{\mathrm{dr}} \\ \mathbf{T}_{\mathrm{dr}m} + \Delta\mathbf{T}_{\mathrm{dr}} \end{bmatrix}, \tag{7.6}$$

where

$$\mathbf{T}_{\mathrm{dr}m} = \frac{\mathbf{T}_{\mathrm{dr}1} + \mathbf{T}_{\mathrm{dr}2}}{2} \tag{7.7}$$

and

$$\Delta \mathbf{T}_{\mathrm{dr}} = \frac{\mathbf{T}_{\mathrm{dr}_1} - \mathbf{T}_{\mathrm{dr}_1}}{2}. \tag{7.8}$$

So the jth element of the $(n+1)$ vector $\mathbf{T}_{dr_m}$ denotes the mean of the drive torques applied to the wheels on the jth axle and the jth element of the $(n+1)$ vector $\Delta \mathbf{T}_{dr}$ denotes the difference between the torque applied to the right wheel and the torque applied to the left wheel of the jth axle. Substituting equation (7.6) into equation (3.76) yields

$$^y\mathbf{M}(^{c1}\mathbf{q})\ddot{\mathbf{y}}_s + {}^y\mathbf{C}_{\dot{y}}(^{c1}\dot{\mathbf{q}}, {}^{c1}\mathbf{q})\dot{\mathbf{y}}_s + {}^y\mathbf{C}_{v_x}(^{c1}\dot{\mathbf{q}}, {}^{c1}\mathbf{q})v_x + {}^y\mathbf{D}(^{c1}\dot{\mathbf{q}}, {}^{c1}\mathbf{q}) =$$
$$^y\mathbf{B}_{\mathrm{lat}}(^{c1}\dot{\mathbf{q}}, {}^{c1}\mathbf{q}, \Delta\boldsymbol{T}_{\mathrm{dr}}, \boldsymbol{T}_{\mathrm{dr}_m})\boldsymbol{\delta}_t + {}^y\mathbf{B}_{\mathrm{long}}(^{c1}\mathbf{q}) \left(\begin{bmatrix} \mathbf{I} \\ -\mathbf{I} \end{bmatrix} \Delta\boldsymbol{T}_{\mathrm{dr}} + \begin{bmatrix} \mathbf{I} \\ \mathbf{I} \end{bmatrix} \boldsymbol{T}_{\mathrm{dr}_m} \right) \tag{7.9}$$

In order to obtain a linear state space description of the vehicle model, this equation, together with the actuator dynamics (3.78) and (3.79) has been linearized numerically (using Simulink) about a straight track and about $\boldsymbol{T}_{dr_m} = \mathbf{0}$. The mean drive torques have been taken equal to zero to allow for the largest possible differential torque by means of the electric drives. For this linearization, a vehicle with the dimensions of a double articulated bus has been used. The state space description of the linearized model can be written as

$$\begin{aligned} \dot{\mathbf{x}} &= \mathbf{A}\mathbf{x} + \mathbf{B}\mathbf{u}_{\mathrm{sc}} \\ \mathbf{y}_{s_{\mathrm{sc}}} &= \mathbf{C}\mathbf{x}, \end{aligned} \tag{7.10}$$

where the input vector $\mathbf{u}$ is given by

$$\mathbf{u}_{\mathrm{sc}} = \begin{bmatrix} \mathbf{u}_{\mathrm{st}_{\mathrm{sc}}} \\ \mathbf{u}_{\mathrm{dr}_{\mathrm{sc}}} \end{bmatrix} \tag{7.11}$$

and the state vector $\mathbf{x}$ contains the state of the vehicle model (3.76) and the states of the actuator dynamics. The input vector $\mathbf{u}_{\mathrm{st}_{\mathrm{sc}}}$ denotes the scaled steering actuator inputs and $\mathbf{u}_{\mathrm{dr}_{\mathrm{sc}}}$ denotes the scaled differential torques actuator input. Furthermore, $\mathbf{y}_{s_{\mathrm{sc}}}$ denotes the scaled output vector. Prior to the linearization, the steering inputs have been scaled with a scale factor $0.5\,rad$ representing the maximum steering angles. The torque inputs have been scaled with a factor $10.000\,Nm$. Furthermore, time constants of the steering actuators were set to $32\,ms$, representing a bandwidth of about $5\,Hz$, whereas the time constants for the torque actuators were set to $5.3\,ms$, representing a bandwidth of $30\,Hz$. With the state space equation (7.10), the transfer function $\mathbf{G}_{iiii}(j\omega)$ has been calculated as

$$\mathbf{G}_{iiii}(j\omega) = \mathbf{C}(j\omega\mathbf{I} - \mathbf{A})^{-1}\mathbf{B}\mathbf{T}_{iiii}, \tag{7.12}$$

where the $2(n+1) \times (n+1)$ matrix $\mathbf{T}_{iiii}$ denotes a transformation matrix to select the desired input combination. The subscripts *iiii* denotes which input

combination is selected. Each i corresponds to one of the axles, starting with the first i for the front axle and continuing backward for the following $i's$. $i = 1$ corresponds to steering with the steering angles whereas $i = 0$ corresponds to steering with the differential torques.

The figures 7.5 till 7.12 show the plots of the singular values of all input combinations that have to be checked. The singular value plots of the input combinations 0000 till 0011 show only three singular values. The fourth singular value equals zero for these input combinations. This indicates that not the whole output space can be reached by these input combinations. This can also be concluded from observing the physics of the vehicle. With the differential torques as input of the axles of the tractor, only torques can be exerted on the tractor. This means that the tractor only can be rotated. This means that the output directions corresponding to a lateral movement of the tractor can not be reached at all. With the steering angle as input of one of the axles of the tractor, these output directions can be reached, since all singular values corresponding to this type of input combination are larger than zero. For this reasons, the input combinations 0000 till 0011 are not allowed as input combinations.

From the remaining singular value plots, it can be concluded that only for the input combinations 0111, 1011 and 1111 all singular values are large than 1 for some frequency range. This means that only these input combinations can cover the intended output space by the allowed input space for some frequencies. This indicates that at most one axle of the tractor could possibly be actuated by differential torques, but certainly not all axles.

From the input combinations 0111, 1011 and 1111, combination 1111 has the largest singular values. Moreover, the frequency range for which all singular values are larger than 1 is the largest for this combination and ranges from 0 to about $6\,Hz$. This indicates that the steering angles have the most influence on the outputs and that up to $6\,Hz$ steering with the steering angles is completely sufficient. Therefore, the steering angles will be used as control inputs in the remainder of this thesis. It will be assumed that

$$\Delta \mathbf{T}_{\mathrm{dr}} = \mathbf{0} \tag{7.13}$$

Due to this assumption, the width of the vehicle can be neglected.

With the differential torque vector $\Delta \mathbf{T}_{\mathrm{dr}}$ equal to zero, the model (7.9) still depends on the mean drive torque $\mathbf{T}_{\mathrm{dr}_m}$ via the term $^y\mathbf{B}_{\mathrm{long}} \begin{bmatrix} \mathbf{I} & \mathbf{I} \end{bmatrix}^T \mathbf{T}_{dr_m}$ and dependency of the matrix $^y\mathbf{B}_{\mathrm{lat}}$ as equations (3.73) and (3.77e) show. When the drive torque is measured and small enough, the influence of the drive torques on the tracking errors can be compensated for with the controllers to be designed. When the drive torques are too large, complete compensation might be impossible. Therefore, the influence of the drive torques on the tracking errors will be investigated now.

As (3.73) and (3.77e) show, the matrix $^y\mathbf{B}_{\mathrm{lat}}$ is proportional to

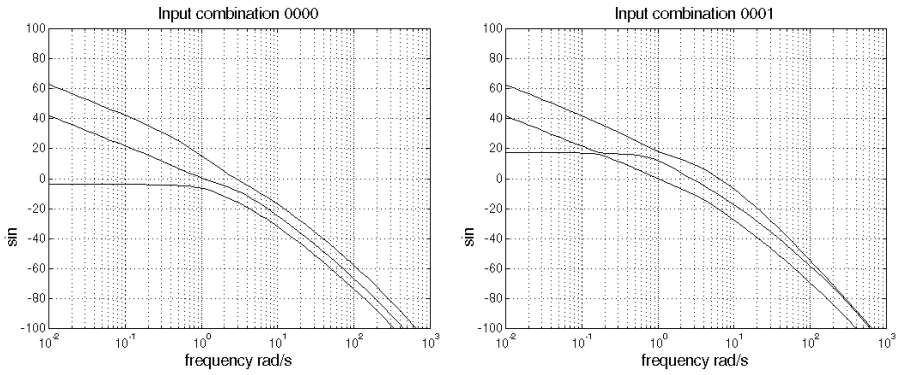$$\boldsymbol{\mathcal{D}}(\mathbf{R}_{wi}\mathbf{T}_{dr_i}) + \mathbf{C}_t, \tag{7.14}$$

Figure 7.5: Plot of singular values for input combinations 0000 and 0001.
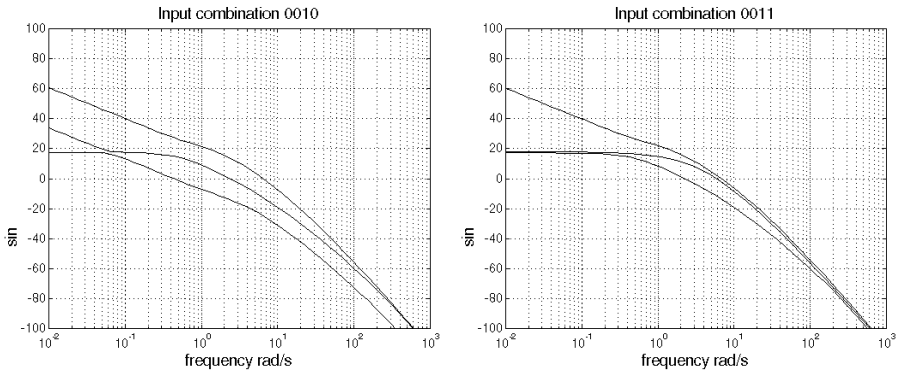

Figure 7.6: Plot of singular values for input combinations 0010 and 0011.
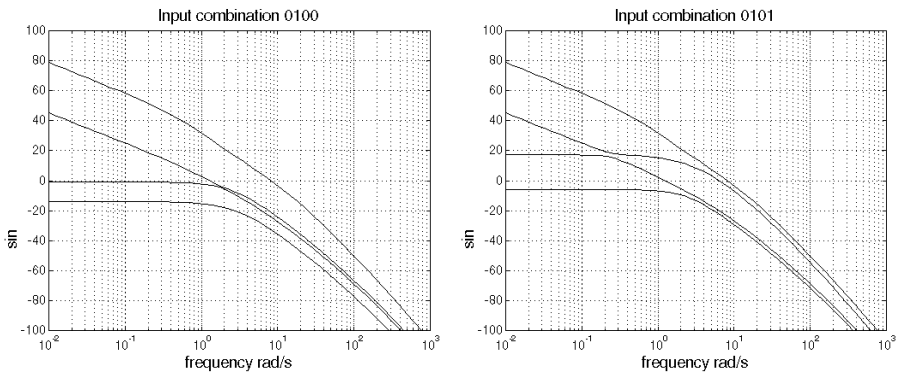

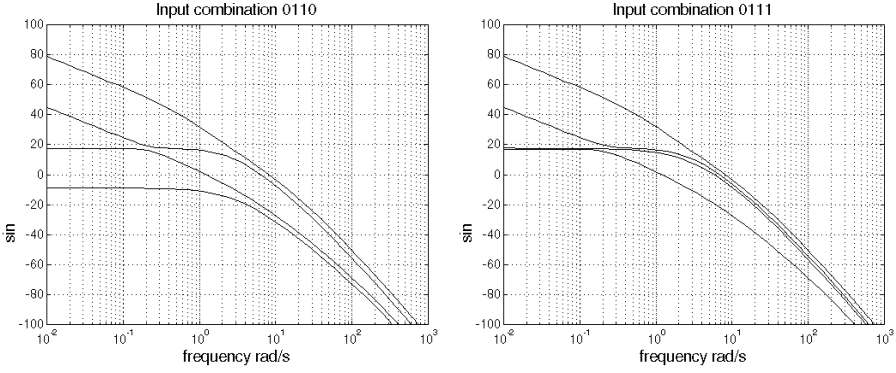Figure 7.7: Plot of singular values for input combinations 0100 and 0101.

Figure 7.8: Plot of singular values for input combinations 0110 and 0111.
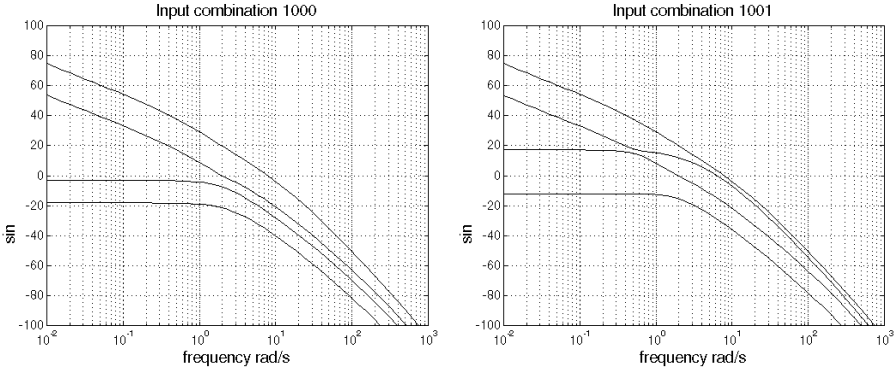

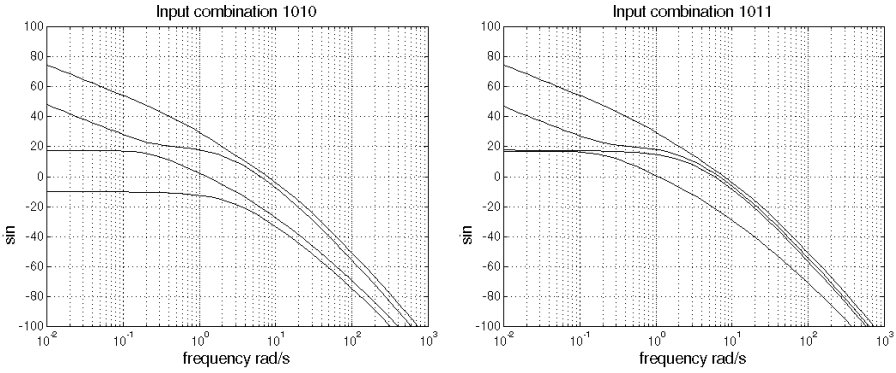Figure 7.9: Plot of singular values for input combinations 1000 and 1001.

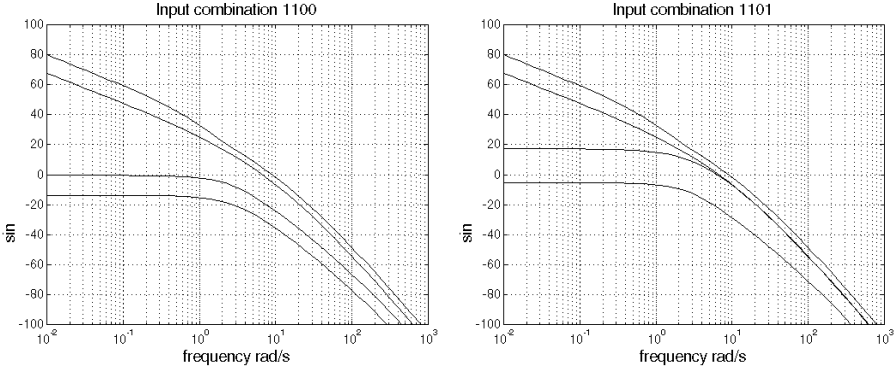Figure 7.10: Plot of singular values for input combinations 1010 and 1011.

Figure 7.11: Plot of singular values for input combinations 1100 and 1101.
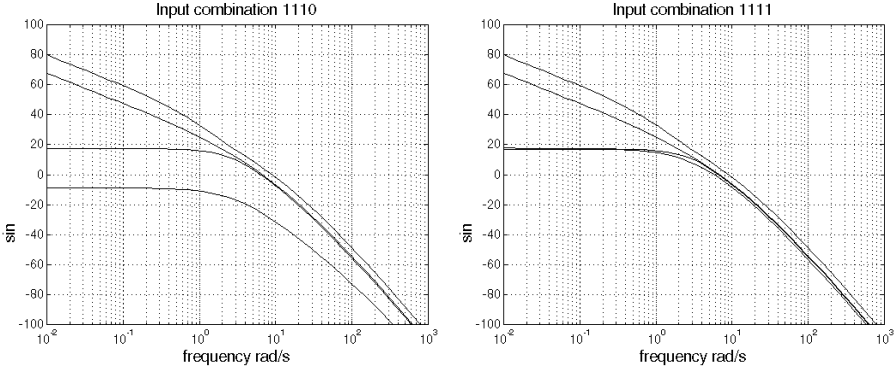
Figure 7.12: Plot of singular values for input combinations 1110 and 1111.

where $\mathbf{R}_{wi}$ is a diagonal matrix with the wheel radii on the diagonal and $\mathbf{C}_t$ is a diagonal matrix with the cornering stiffnesses on the diagonal. For practical vehicle parameters, the jth diagonal element of the product $\boldsymbol{\mathcal{D}}(\mathbf{R}_{wi}\mathbf{T}_{dr_i})$ will be one order of magnitude less than the jth diagonal element of the matrix $\mathbf{C}_t$. Furthermore, as explained in chapter 3, the cornering stiffnesses depend amongst others on factors like load and tire pressure. Therefore, it is difficult to determine the cornering stiffnesses accurately. Moreover, with (unknown) changing load conditions, also the cornering stiffnesses will experience an unknown change. The magnitudes of the diagonal elements of the product $\boldsymbol{\mathcal{D}}(\mathbf{R}_{wi}\mathbf{T}_{dr_i})$ will in general be smaller than the inaccuracy with which the cornering stiffnesses can be determined. Therefore, the influence of the term $\boldsymbol{\mathcal{D}}(\mathbf{R}_{wi}\mathbf{T}_{dr_i})$ can be neglected.

In order to investigate the influence of the dependency of (7.9) on $\mathbf{T}_{\mathrm{dr}_m}$ via

Figure 7.13: Plot of singular values with mean driving torques as inputs

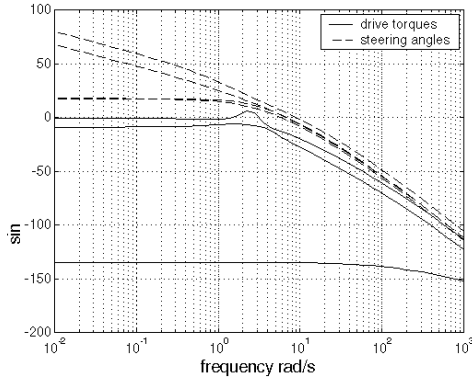the term $^y\mathbf{B}_{\text{long}}(^{c1}\mathbf{q})\begin{bmatrix}\mathbf{I} & \mathbf{I}\end{bmatrix}^T\boldsymbol{T}_{dr_m}$, a same kind of analysis has been carried out as has been done for the differential torques in this section. First the vehicle model was linearized around a straight path and the mean drive torques $\mathbf{T}_{\text{dr}_m}$ were considered as input. For this case, all singular values equal zero. This shows that the drive torques have negligible influence on the tracking errors $^{p_{si}}y_{p_{si},si}$ for this situation. This also can be seen from the vehicle configuration, since with zero articulation angles, the drive torques don't result in forces in the directions of any of the tracking errors $^{p_{si}}y_{p_{si},si}$. This shows that linearizing the model around $\mathbf{T}_{\text{dr}_m} = \mathbf{0}$ during the selection of the inputs is justified.

From the vehicle configuration, it can also be seen that for a sharp curve, i.e. when the articulation angles are large, the influence of the drive torques on the tracking errors is maximal. Therefore, another singular value analysis has been carried out but now for the vehicle model linearized around a sharp curve, such that all articulation angles equal 45 degrees.

Figure 7.13 shows the three nonzero singular values for this situation. The other singular value equals zero, which indicates that not the whole output space is influenced by the drive torques. In the same plot, the singular values of input combination 1111, which are calculated for the same situation, are plotted, in order to make a comparison. As the plot illustrates, the singular values of the drive torques are much smaller at low frequencies than the singular values of the steering angle inputs. This shows that the steering angles can suppress the influence of the drive torques for the vehicle considered here.

The analysis above shows that for the double articulated vehicle considered here, the influence of the drive torques on the lateral dynamics can be suppressed by the steering angles inputs. The situation might change when braking is considered. The braking torque produced by mechanical brakes is larger than the torque that can be produced by electric motors. This means that it might

be impossible to reject the influence of the braking torque completely when the vehicle is in a curve. The same applies when the vehicle is equipped with rear-wheel drive only. In this case, the drive torque delivered by the wheels of the semi-trailers will be larger than considered above, so that it might be impossible to reject the influence of the drive torques on the lateral dynamics completely. Moreover, when a vehicle with more carriages is considered, the influence of the drive torques increases. Also in this case it might be impossible to reject the influence of the drive torques completely.

7.4 All-wheel steering versus front wheel steering

When a controller with integrating action is applied to the all-wheel steered multiple-articulated vehicle, in order to steer the vehicle along the path, all tracking errors $^{p_{si}}y_{p_{si},si}$ can be controlled to zero in steady state, since the whole output space can be reached by the steering angles as has been shown in the previous section. With front wheel steering only, only one of the outputs can be controlled to zero in steady state, since only one input can be used to control the vehicle. Assuming the tracking error $^{p_{s1}}y_{p_{s1},s1}$ will be controlled, steering with the tractor front wheels only might result in large steady state values for the remaining tracking errors, when the vehicle follows a curve or is subjected to lateral disturbance forces like for example wind.

In [86], these steady state tracking errors have been analyzed for a single articulated vehicle following a curve with constant radius $\mathbf{R}$, using a dynamic vehicle model as described in equation (3.55). Neglecting the drive torques $\mathbf{T}_{dr}$, the longitudinal dynamics and second and higher-order terms of the articulation angles and the body slip angles $\beta_{w_{ij}}$, the yaw angles $^{p_{s1}}\epsilon_{si}$ relative to the tangent to the road at the origin of frame p_{s1} can be written as [86]

$$^{p_{s1}}\epsilon_{s2} \quad = \quad -\frac{l_{r1}}{R} + \frac{m_1}{C_{rw1}}\frac{l_{f1}}{l_{f1}+l_{r1}}\frac{v_x^2}{R} \tag{7.15}$$

$$^{p_{s1}}\epsilon_{s3} \quad = \quad -\frac{d_{r1}+d_{f2}+l_{r2}}{R} + \frac{m_2}{C_{rw2}}\frac{d_{f2}}{d_{f2}+l_{r2}}\frac{v_x^2}{R}, \tag{7.16}$$

where R is the radius of the path to be followed. In equation (7.16), the first, mass and velocity independent, term on the right hand side predicts the yaw error for the kinematic case, i.e. when the dynamics of the vehicle can be neglected. The second term on the right hand side is due to the dynamics of the vehicle. Equation (7.16) can be rewritten as

$$C_{rw2}(d_{f2}+l_{r2})(^{p_{s1}}\epsilon_{s3} + \frac{d_{r1}+d_{f2}+l_{r2}}{R}) = m_2 d_{f2}\frac{v_x^2}{R}. \tag{7.17}$$
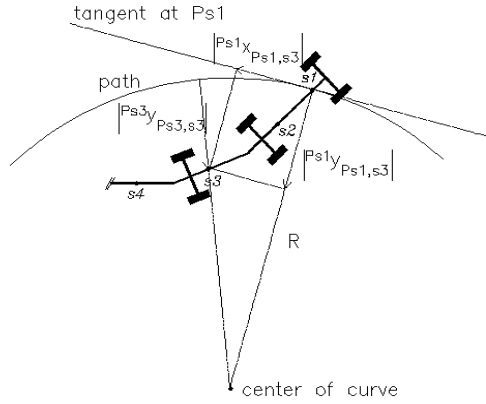
Figure 7.14: Steady state tracking errors with front wheel steering only

This can be viewed as a torque balance around the hitching point in between the tractor and the semi-trailer. The right hand side equals the torque around the hitching point due to the centrifugal acceleration v_x^2/R acting on the center of gravity of the semi-trailer, whereas the left hand side can be viewed as the counter torque exerted on the vehicle by the tires, with the term

$$^{p_{s1}}\epsilon_{s3} + \frac{d_{r1} + d_{f2} + l_{r2}}{R} \tag{7.18}$$

as the tire slip angles. With this insight, equation (7.16) can easily be extended to the multiple-articulated case as

$$^{p_{s1}}\epsilon_{sj+1} = -\frac{\sum_{i=1}^{j} d_{wli}}{R} + \frac{m_j}{C_{rwj}}\frac{d_{fj}}{d_{fj}+l_{rj}}\frac{v_x^2}{R}, \tag{7.19}$$

with $d_{[li]}$ as defined in section 3.4

Given the yaw angles $^{p_{s1}}\epsilon_{sj+1}$, the tracking errors $^{p_{si}}y_{p_{si},si}$, $i > 1$ can be calculated with

$$^{p_{si}}y_{p_{si},si} = R - \sqrt{^{p_{s1}}x_{p_{s1},si}^2 + (R - {}^{p_{s1}}y_{p_{s1},si}^2)^2}, \tag{7.20}$$

$^{p_{s1}}x_{p_{s1},si}$ and $^{p_{s1}}y_{p_{s1},si}$ can be expressed in the yaw angles $^{p_{s1}}\epsilon_{sj+1}$ with

$$^{p_{s1}}x_{p_{s1},si} = (l_{s1} + l_{s2})\cos{}^{p_{s1}}\epsilon_{s2} + \sum_{j=3}^{i} d_{s_{ij-1}}\cos{}^{p_{s1}}\epsilon_{sj} \tag{7.21}$$

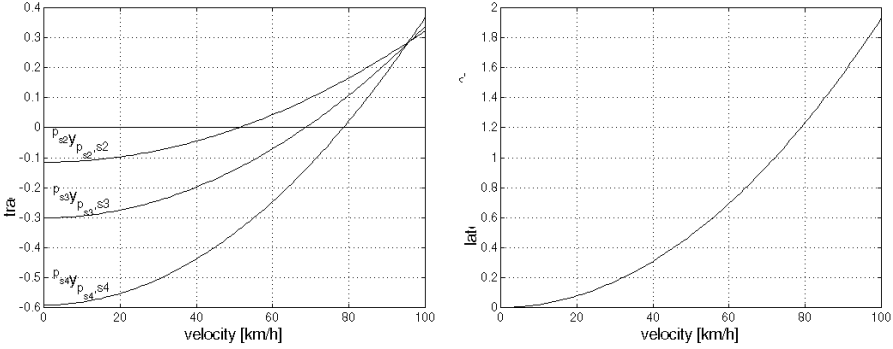Figure 7.15: Tracking errors (left plot) and centrifugal accelerations (right plot) for a double articulated commuter bus following a curve with radius $R = 400\,m$

and

$$
{}^{p_{s1}}y_{p_{s1},si} = (l_{s1} + l_{s2}) \sin {}^{p_{s1}}\epsilon_{s2} + \sum_{j=3}^{i} d_{s_{ij-1}} \sin {}^{p_{s1}}\epsilon_{sj}. \tag{7.22}
$$

with $d_{s_{ij-1}}$ as defined in equation (2.37). One and another is illustrated in figure 7.14.

Equation (7.20) has been used to calculate the tracking errors ${}^{p_{s2}}y_{p_{s2},s2}$, ${}^{p_{s3}}y_{p_{s3},s3}$ and ${}^{p_{s4}}y_{p_{s4},s4}$ for a double articulated commuter bus, while lateral guidance has been applied with front wheel steering only. The left plot in figure 7.15 shows the tracking errors as function of the tractor's longitudinal velocity. For this plot, a curve with a radius R of 400 m has been used. The right plot in the same figure shows the centrifugal accelerations of the centers of gravity of the carriages when the vehicle is completely in the curve. As both plots show, the tracking errors are negative with a relatively large magnitude at low velocity. The negative sign means that the points $\mathbf{s}_2$, $\mathbf{s}_3$ and $\mathbf{s}_4$ are at the inside of the curve. It is clear that certainly at low speed, all-wheel steering can be used to reduce the tracking errors of the points $\mathbf{s}_2$, $\mathbf{s}_3$ and $\mathbf{s}_4$. At increasing speed, the magnitude of the tracking errors decrease. This is due to the dynamic part of the expressions for the yaw angles ${}^{p_{s1}}\epsilon_{p_{si}}$ as given in equation (7.15) and (7.19). At a certain speed, the tracking errors change sign and their magnitudes increase again. The left plot of figure 7.15 shows that at high speed, the magnitude of the tracking errors becomes relatively large again, while the lateral acceleration of the centers of gravity of the carriages is still sufficiently low to guarantee passenger comfort. The positive sign of the tracking errors at high speed indicates that the points $\mathbf{s}_2$, $\mathbf{s}_3$ and $\mathbf{s}_4$ are at the outside of the curve now. This is completely due to the centrifugal forces acting on the carriages.

At a speed of about $95\,km/h$, all tracking errors as shown in the left plot of figure 7.15 are about $29\,cm$ [1]. For accurate path following, this is inadmissibly large. So even at high speed, all-wheel steering can be useful to reduce the tracking errors.

The conclusion drawn above is completely based on a steady state analysis. Also from a dynamical point of view, it is useful to use all-wheels steering. In [42, 69], an analysis has been carried out to study the lateral dynamics of front-wheel steered passenger cars. For this study, a vehicle with a so-called look-down referencing system was considered. With such a system, a lateral displacement sensor is mounted under the vehicle's front bumper. The tracking error is defined as the deviation of this sensor with respect to the path to be followed. The analysis in [42, 69] shows that the transfer function from steering input to lateral displacement of the front bumper consists amongst others of a complex pole-pair and a complex zero-pair. Both the complex zeros and complex poles experience decreased damping for increased velocity. The damping of the zero pair appears to be worse than the damping of the pole pair. When the loop between the lateral displacement sensor and the steering actuator is closed with a controller for steering the vehicle along the path, the complex zero pair attracts the complex pole-pair resulting in a decreased damping for the closed loop pole-pair. For the tracking error dynamics this is not such a problem, since the complex pole-pair and complex zero-pair almost cancel. The transfer function from steering input to yaw movement however, contains the same pole-pair as the closed loop transfer function from steering input to lateral displacement. For the yaw dynamics, this pole-pair is not cancelled by a zero-pair, resulting in oscillatory yaw behaviour at high speed.

To overcome this problem, the authors in [42, 69] propose to use a so called virtual look-ahead referencing scheme instead of a look-down referencing scheme. In a virtual look-ahead scheme for passenger cars, a second displacement is placed under the vehicle's rear bumper. By combining the front and rear displacement sensor, the tracking error of a point at a distance d_s in front of the vehicle can be predicted. Increasing the distance d_s increases the damping of the complex zero-pair in the open loop transfer function from steering input to tracking error, which in turn improves the yaw dynamics. In [47, 86], a same kind of analysis is carried out for a articulated vehicle, and the same conclusions are drawn for this type of vehicle.

Using look-ahead for the vehicle as discussed in this thesis, will increase the steady state tracking errors as predicted by equation (7.20), since the distance l_{s1} increases. By using all-wheel steering, the yaw dynamics will be damped actively, eliminating the need for virtual look-ahead, which in turn avoids the increase of steady state tracking errors. So, also from a dynamical point of view,

---

[1]The tracking errors depend on vehicle parameters like mass and cornering stiffness as shown in equations (7.15) and (7.19), so that the value of the tracking errors will change with changing vehicle parameters. The trend, however, will be the same as shown in figure 7.15

all-wheel steering is advantageous compared with front-wheel steering only.

7.5   Summary

The control model as derived in chapter 3 has been used to analyze the system to be controlled. Some considerations for the locations of the points $\mathbf{s}_i$ have been discussed. For passenger comfort reasons, the points $\mathbf{s}_i, i = 2..n$ have been put on the vertical axes of the hitching mechanisms in between the carriages, and the point $\mathbf{s}_{n+1}$ has been put on the rear bumper of the last carriage. The point $\mathbf{s}_1$ has been put $2.5\,m$ in front of the tractor's center of gravity.

A singular value analysis has been carried out to show that the steering inputs have, compared with differential torque steering, the most influence on the outputs. For this reason, the steering angles have been selected as control inputs of the system. A similar kind of analysis has been carried out to show that the influence of the drive torques on the tracking errors can counteracted by means of the steering angles.

A steady state analysis has been presented to show that both at low and at high speed front-wheel steering only results in large off-tracking of the rear axles. This off-tracking can be reduced by using all-wheel steering. It has been motivated that from a dynamical point of view all wheel steering is useful to damp the yaw-dynamics of the vehicle.

8

Controller design

8.1   Introduction

This chapter is dedicated to discuss the design and simulation results of two controllers for steering an all-wheel steered multiple-articulated vehicle along the path to be followed. Before starting the discussion about controller design, section 8.2 is used to consider the performance requirements on the lateral guidance system that are of importance for the controller design. Section 8.3 discusses the design and simulation results of a feedback linearizing controller. For the design of this controller, the steering actuator dynamics are neglected. Therefore, the controller is extended to a so-called backstepping controller, to be discussed in section 8.4. Concluding remarks about the contents of this chapter are given in section 8.5

8.2   Considerations on performance requirements

For automation of passenger transport, passenger comfort is an important factor to deal with and determines for a great part the performance requirements of a lateral guidance system. One important comfort factor is the frequency contents of the lateral motion of the vehicle. Sudden changes in lateral acceleration may cause that passengers feel uncomfortable. In particular, acceleration components in the $5-10\,Hz$ frequency region can excite internal body resonances, resulting in an uncomfortable feeling [43]. For this reason, the closed-loop bandwidth should certainly be lower than $5\,Hz$. In literature $1.2\,Hz$ is often taken as upperbound for the bandwidth of the lateral guidance system [2].

An other important comfort factor to deal with is the steady state lateral acceleration. The steady state lateral guidance depends on the longitudinal velocity and the curvature of the road. In the vehicle guidance literature, $0.2\,g$

is often used as upperbound for the steady state lateral acceleration [43]. The maximum allowable lateral acceleration for the Dutch roads depends strongly on the longitudinal velocity of the vehicle [74, 75] and ranges from $2.7\,m/s^2$ at low speed to as low as $1\,m/s^2$ at highway speed. For public transport, the maximum allowable lateral acceleration is in general lower than for passenger cars. For the articulated busses in this thesis, a maximum steady state lateral acceleration of $1.5\,m/s^2$ will be assumed for all speeds.

An other important factor for a lateral guidance system is the maximum tracking error. Since the tracking error depends on many factors such as disturbance forces, vehicle parameters, road quality and road shape, it is difficult to give an hard upper bound on the maximum allowable tracking error. Moreover, also limitations on the steering actuators play a major role in reducing the tracking error [1]. For the controller design in this thesis, a trade-off will be made between tracking error on the one hand and passenger comfort and actuator limitations on the other hand, in order to get good tracking behavior for the guided vehicle.

8.3 Feedback linearizing controller

8.3.1 Introduction

The controller that will be presented in this section, is a so-called feedback linearizing controller. This type of controller is extensively discussed in literature [30, 44, 81]. The same kind of controller that will be presented in this section, has also been presented in [19, 22].

Figure 8.1 shows a block scheme of a feedback linearizing controller applied for vehicle guidance. As can be seen, the controller consists of two parts. The first linearizes and decouples the vehicle dynamics, resulting, at least in the ideal case when all vehicle parameters are known, in $n + 1$ decoupled double integrators. In the ideal case, when no disturbances are acting on the vehicle and the model used in the controller describes the dynamics of the vehicle accurately, this linearizing term suffices for steering the vehicle along the path. In practice however, this ideal case can not be achieved. Therefore, a linear controller is used to counteract the effect of disturbances and model uncertainty. This is depicted with the block "linear controller" in figure 8.1. In principle, any stabilizing linear controller can be used for this block. In this thesis, a PID controller will be proposed. The outputs of the Kalman filter, that is presented in the previous chapter, will be used as inputs of the feedback linearizing controller.

8.3.2 Design

To achieve complete linearization and decoupling, it is necessary to incorporate the inverse dynamics of the actuators in the controller. From a practical point
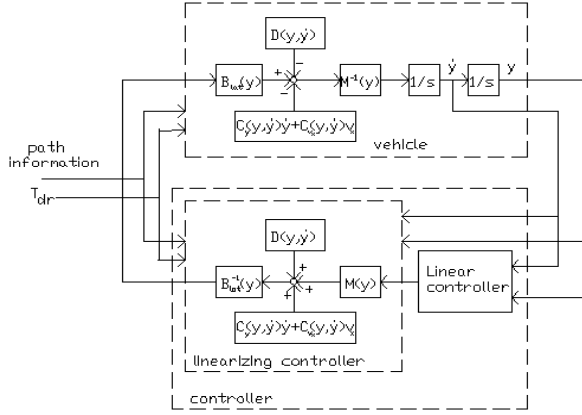
Figure 8.1: Block scheme of feedback linearizing controller

of view, this is undesirable, since this might result in unacceptable wear and oversteering of the steering actuators. For reasons of passenger comfort, the closed loop bandwidth should be less than $1.2\,Hz$ as explained in the previous section. As long as the actuator bandwidth is much larger than the closed loop bandwidth, the actuator dynamics can be neglected, so that

$$\boldsymbol{\delta}_t \approx \mathbf{u}_{st} \qquad (8.1)$$

in equation (3.76). Considering this as an equality, (3.76) can be written as

$${}^y\mathbf{M}\ddot{\mathbf{y}}_s + {}^y\mathbf{C}_{\dot{y}}\dot{\mathbf{y}}_s + {}^y\mathbf{C}_{v_x}v_x + {}^y\mathbf{D} = {}^y\mathbf{B}_{\mathrm{lat}}\boldsymbol{u}_{st} + {}^y\mathbf{B}_{\mathrm{long}}\mathbf{T}_{\mathrm{dr}} + {}^y\boldsymbol{\tau}_{\mathrm{dist}}, \qquad (8.2)$$

where the arguments of the system matrices have been omitted for brevity.

Given this model, the feedback linearizing component of the controller can be written as

$$\boldsymbol{u}_{st} = {}^y\mathbf{B}_{\mathrm{lat}}^{-1}\{{}^y\mathbf{C}_{\dot{y}}\dot{\mathbf{y}}_s + {}^y\mathbf{C}_{v_x}v_x + {}^y\mathbf{D} - {}^y\mathbf{B}_{\mathrm{long}}\mathbf{T}_{\mathrm{dr}} - {}^y\mathbf{M}\mathbf{u}'_{st}\}, \qquad (8.3)$$

where $\mathbf{u}'_{st}$ can be viewed as an artificial input. It is assumed that the influence of the drive torque $\mathbf{T}_{\mathrm{dr}}$ on the lateral dynamics can be suppressed by the steering inputs. Substituting (8.3) in (8.2) yields

$$ {}^y\mathbf{M}\ddot{\mathbf{y}}_s = {}^y\mathbf{M}\mathbf{u}'_{st} + {}^y\boldsymbol{\tau}_{\mathrm{dist}}. \qquad (8.4)$$

Using the fact that the mass matrix is positive definite, this can be written as

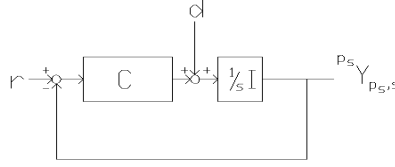$$\ddot{\mathbf{y}}_s = \mathbf{u}'_{st} + \mathbf{d}, \qquad (8.5)$$

Figure 8.2: Simplified block scheme of linearized closed loop system

where $d = {}^y\mathbf{M}^{-1y}\tau_{\text{dist}}$. This equation can be considered as a system formed by $n+1$ double integrators, driven by the artificial input $\mathbf{u}'_{st}$.

The feedback linearized closed loop system can be depicted in simplified form as in 8.2. In this figure $\mathbf{C}$ denotes a linear controller and $\mathbf{r}$ denotes the reference input. For normal track following, $\mathbf{r}$ equals zero, since the outputs of the block scheme are the tracking errors. The shape of the path has been taken care of with the linearizing part of the controller (8.3), so that the only goal of C is to suppress the effect of the disturbance $\mathbf{d}$ and model uncertainty. The disturbance term $\mathbf{d}$ enters the closed loop system just before the double integrator. To suppress steady state disturbances, an integrating action of the controller is required. For this reason, a PID controller will be used, so that

$$\mathbf{u}'_{st} = \mathbf{K}_d\dot{\mathbf{y}}_s + \mathbf{K}_p\mathbf{y}_s + \mathbf{K}_i\mathbf{z}, \tag{8.6}$$

where

$$\dot{\mathbf{z}} = \mathbf{y}_s. \tag{8.7}$$

To obtain similar dynamic behaviour for all tracking errors, the matrices $\mathbf{K}_d$, $\mathbf{K}_p$ and $\mathbf{K}_d$ are taken as $k_d\mathbf{I}$, $k_p\mathbf{I}$ and $k_i\mathbf{I}$ respectively.

To tune the the controller gains a trade-off has been made between passenger comfort tracking error, actuator saturation and bandwidth. Especially the requirements on tracking error on one hand and passenger comfort and actuator saturation on the other hand are conflicting. For accurate track following, high gains are desirable. This however might result in oversteering of the steering actuators. Moreover, since the Kalman filter outputs are influenced by sensor noise, as shown by the simulation results in chapter 6, high controller gains might result in oscillatory behavior of the steering angles, when the controller is not tuned with care.

The transfer function from disturbance $d_{[i]}$ to tracking error ${}^{psi}y_{p_{si},si}$ can be written as

$$^{psi}y_{p_{si},si}(s) = \frac{s}{s^3 + k_d s^2 + k_p s + ki}d_{[i]} = Sd_{[i]}. \tag{8.8}$$

To select k_d, k_p and k_i, the prototype design method [37] has been used. With this design method, the response of a closed loop system is made equal to the

Bode Diagrams

From: U(1)
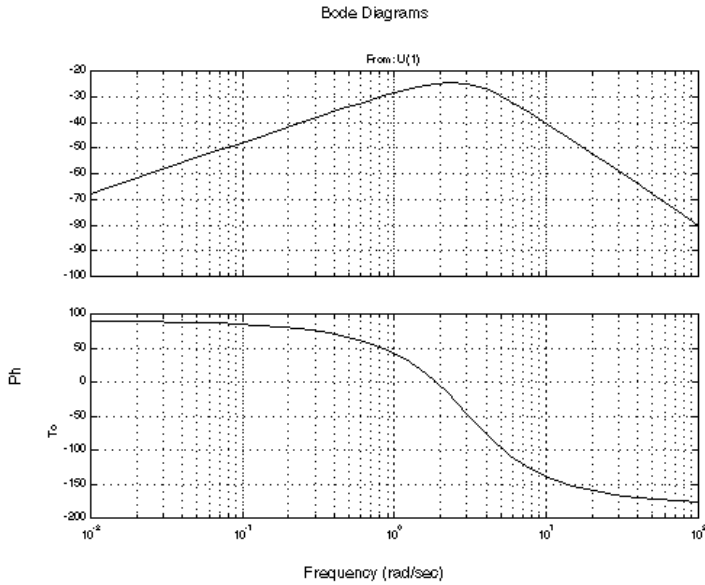
Figure 8.3: Bode plots of the sensitivity function S (see 8.8)

response of a prototype system. For the prototype, a filter

$$\frac{s}{B_3(s)} \tag{8.9}$$

has been used, with $B_3(s)$ a third-order Bessel polynomial

$$B_3(s) = (s/\omega_0 + 0.9420)(s/\omega_0 + 0.7455 + 0.7112j)(s/\omega_0 + 0.7455 - 0.7112j), \tag{8.10}$$

where ω_0 is the bandwidth of the transfer function $\frac{1}{B_3(s)}$. ω_0 was set to $3.2\,rad/s$, which corresponds to a bandwidth of approximately $0.5\,Hz$. The gains k_d, k_p and k_i can be obtained then by equating the coefficients of the denominator polynomial of (8.8) with the coefficients of (8.10). This yields $k_d = 7.75$, $k_p = 25$ and $k_i = 32.4$. Figure (8.3) shows the bode plots of the transfer function (8.8). As this plot shows, the minimal disturbance suppression is about $26\,dB$ at a frequency of $2\,rad/s$.

For the feedback linearizing component of the controller (8.3), it was assumed that all vehicle parameters are exactly known. In practice however, this will not be the case. The model (8.2) depends for example on the masses of the carriages of the vehicle and the cornering stiffnesses of the tires. These parameters may vary during operation of the vehicle due to changing load conditions. The masses

of the carriages can in principle be measured by measuring the load on the axles and the force each semi trailer exerts on its predecessor by means of the hitching mechanism connecting the carriages to each other. This is undesirable since especially measuring the the force of the semi trailers on their predecessors might be costly and difficult to implement. Measuring the tire cornering stiffnesses online might be even more difficult, if not impossible. In literature, several methods are described to estimate the cornering stiffnesses online [70, 73, 79], but most of these methods assume that the vehicle's mass and mass distribution are known, or use difficult to implement measuring equipment, which is still in the research phase [68]. For these reasons, measuring all vehicle parameters online is undesirable, and will not be considered in this thesis.

Since the vehicle parameters will deviate from their nominal values as already explained, the feedback linearizing controller has to be robust against these parameter variations. Proving robustness for feedback linearizing controllers is difficult, and only quite conservative upperbounds on the allowed parameter variations can be found in general [30]. In [30], a conjecture is presented, which states that for robotic manipulators, the controlled system will be stable despite large parameter errors, if a feedback linearizing controller is applied. This conjecture is based on experience obtained from extensive simulations and experimental results. [30] reports that with parameter variations of 50% or even 100% reasonable output behavior can still be obtained. Since the model (8.2) suits a robotic manipulator model very well, and the parameter variations expected for commuter busses due to load variations are less than 50%, it is expected that the feedback linearizing controller will also be robust against parameter variations when applied for lateral vehicle guidance. This expectation is also based on extensively studying the closed loop behavior of the all-wheel steered vehicle controlled by a feedback linearizing controller by means of simulations.

Another possibility to deal with parameter variations in feedback linearizing controllers is to a add a robustifying term to the controller [44], as outlined in appendix F. Problem of this approach is that the robustifying term includes an approximation of a switching element that is multiplied by an upper bound of the parameter variations. Due to this approximation, only boundedness of the tracking errors can be proven. The upper bound on the tracking errors depends on how good the approximation of the switching element is. Simulations showed that for a reasonable approximation of the switching element the robustifying term causes oscillatory behavior of the steering angles, which in turn results in large oscillations of the lateral accelerations. This is very undesirable for passenger comfort. The oscillations can be reduced by using a very smooth approximation of the switching element or by lowering the upper bound for the parameter variations. Using a very smooth approximation of the switching element results in a very high upper bound of the tracking error, which makes the result less usefull. Simulations showed that for a reasonable lateral accel-

eration response and with a reasonable approximation of the switching element the upper bound of the parameter variations has to be made so low, that the incorporation of the robustfying term becomes useless. For these reasons, the robustifying term will not be considered in this thesis.

The feedback linearizing controller presented in this section cancels all non-linearities in the vehicle model (8.3). It is however not always necessary to do this in order to obtain a stable closed loop system. The damping term $^y\mathbf{D}$ in equation (8.3) for example is a dissipating term and need not to be cancelled to obtain a stable closed loop system. However, as mentioned in chapter 3, the damping term due to the tires strongly depends on the vehicle's longitudinal speed. To obtain uniform closed loop behaviour for all longitudinal speeds, it is desirable to cancel at least the damping term due to the tires. Moreover, simulation results with a controller without cancellation of the tire damping term showed worse tracking behavior of the closed loop system, since apparently cancellation of the tire damping term acts as a kind of feed forward in the controller. To obtain better tracking behavior, the controller gains have to increased in this case, resulting in turn in a more oscillatory tracking behavior due to the influence of the sensor noises. In order to obtain uniform behavior for all tracking errors (at least in the theoretical case when all vehicle parameters are known), also the damping term due to the articulation angle dampers has been cancelled. In fact this is waisting energy, since the controller has to counteract the action of the articulation angle dampers. A better approach would be to switch the articulation angle dampers off when the vehicle is under complete lateral guidance. In this case, the yaw dynamics of the semi-trailers will be damped by the lateral guidance system, so that the articulation angle dampers are superfluous.

8.3.3   Simulation results

Extensive simulations were run to investigate the performance of the feedback linearizing controller. For these simulation, the simulation model as described in chapter 4 has been used. The parameters of the simulation model were tuned for a double-articulated commuter bus of $25\,m$ length. To investigate the robustness of the controller against parameter uncertainty, different load conditions were considered during the simulations, ranging from a total vehicle mass of $19000\,kg$ for an empty vehicle to a total mass of $31000\,kg$ for a full vehicle. The linearizing term of the controller was tuned for a bus that is half filled with passengers. Some of the simulations result will be shown here.

To start with, figure 8.4 shows the simulation results of a full double-articulated commuter bus driving a trajectory consisting of a half circle with $20\,m$ radius with straight line segments at the entrance and exit of the circle. fifth-order polynomials were used to connect the straight line segments and the half circle. The length of this polynomial path segments were about $5\,m$. The longitudinal

vehicle speed was $5\,m/s$ for this simulation and the distance between the magnets used for the magnetic referencing system was $4\,m$. For this simulation, a full vehicle was considered.

The vehicle starts entering the curved path section at $t = 1.9\,s$ and starts leaving the curved path segment at $t = 14\,s$, as indicated in the last plot of figure 8.4. The maximum tracking error equals about $4\,cm$ at the entrance of the curve. When the vehicle is completely in the curve or completely on the straight road sections, the maximum tracking error is about $0.6\,cm$. At these sections of the path, the tracking errors still show some oscillations. This is due to the estimation errors of the Kalman filter. The third plot of figure 8.4 shows the lateral accelerations of the accelerometers. These accelerations are representative for the lateral acceleration of the passengers sitting close to the accelerometers. (Note that the accelerations as shown in this plot are without measurement noise.) All accelerations show a peak at the entrance and exit of the curved road section. This is partially due to the polynomial part of the path. Due to this polynomial, the lateral accelerations increase slower at the entrance of the curved road section, compared to the case when an abrupt change between straight and circular part of the path is considered. To end up with the same acceleration when the vehicle is completely in the curve, the accelerations have to peak at the transition from polynomial path segment to circular path segment. The height of the peak can be partially controlled by changing the length of the polynomial path segment. The plot of the lateral accelerations shows some oscillatory behavior. This is due to the fact the estimation errors in the tracking velocities and tracking errors are coupled directly to the steering actuators by the PID controller. Most oscillations are filtered out by the vehicle as the plot of the tracking errors shows.

To show that the controller is robust against a relatively large change in parameters, figure 8.5 shows the simulation results for an empty vehicle. As the plot of the tracking errors shows, the maximum tracking error is slightly smaller at the entrance of the curve compared to the simulation results for the full vehicle. Again, the tracking errors show some oscillations due to the estimation errors.

Some of the closed loop requirements discussed in the previous section are in the frequency domain rather than in the time domain. Most of the 'high' frequency behavior of the closed loop system comes from sensor noise. To investigate the influence of the sensor noise, figure 8.6 shows the frequency spectra of the lateral accelerations of the accelerometers and the the tracking errors, obtained from simulation results of a full vehicle driving at a straight road at $5\,m/s$. Figure 8.7 shows the same spectra for an empty vehicle. As both plots show, the plots of the spectra of the tracking errors show that the main signal contents of the tracking errors are in the region between zero and about $1.2\,Hz$. This fits the requirements reasonably well. Despite this fact, the plots of the lateral acceleration spectra show that the accelerations also contain signals at
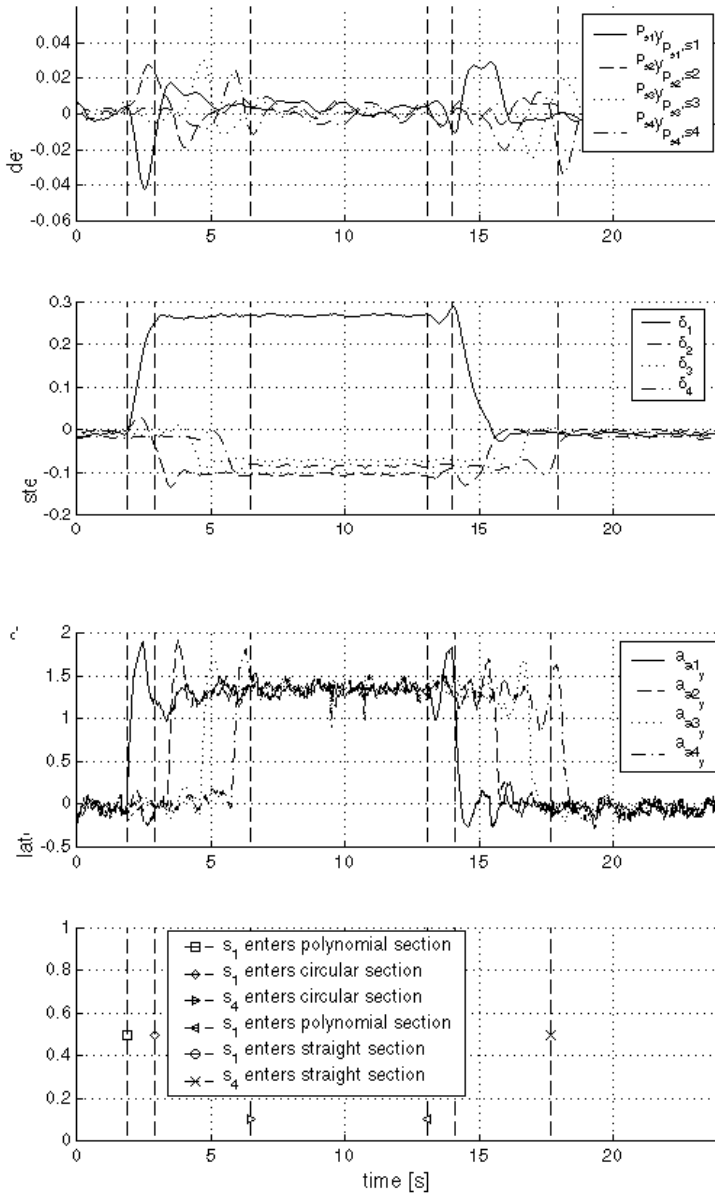
Figure 8.4: Simulation results for a full vehicle driving at $5\,m/s$ entering and leaving a $20\,m$ radius curve

higher frequencies, also above $5\,Hz$. This is due to the fact that the noise in the observer outputs are directly coupled to the steering actuators, as already mentioned. With a PID controller only, as part of the linearizing controller, this cannot be avoided.

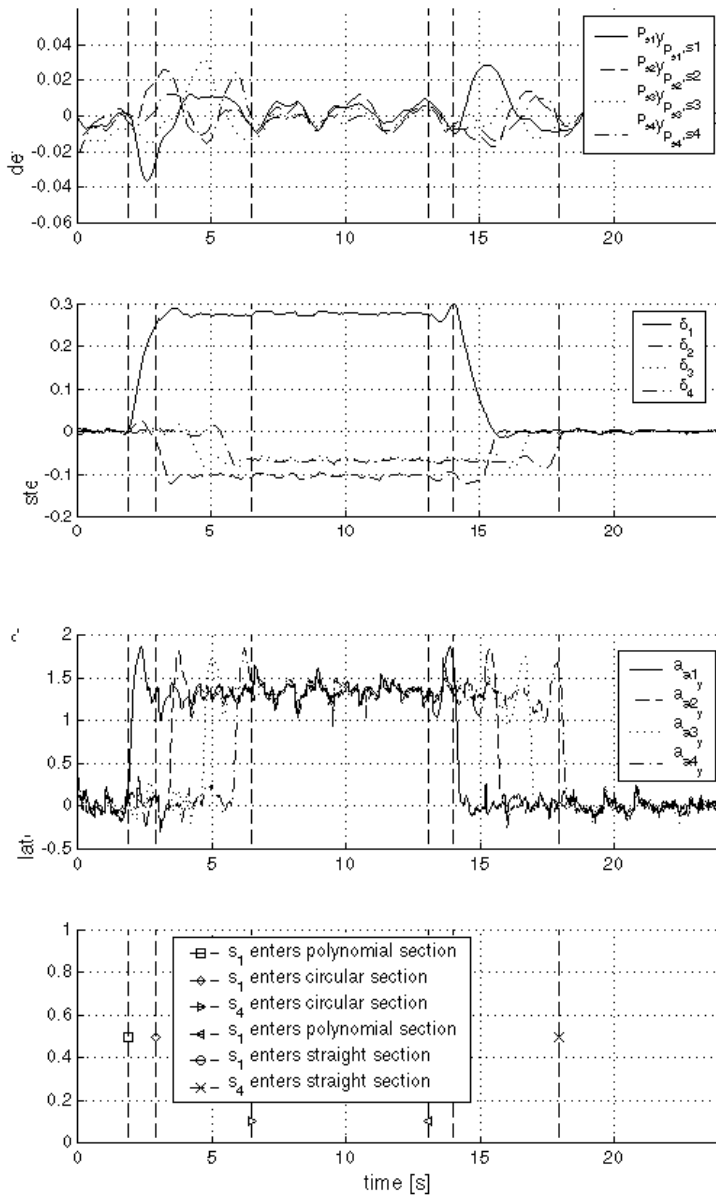Figure 8.5: Simulation results for an empty vehicle driving at $5\,m/s$ entering and leaving a $20\,m$ radius curve
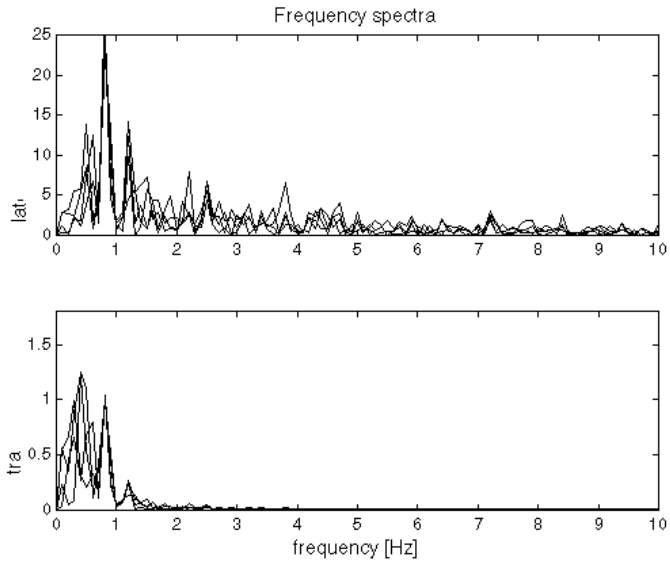
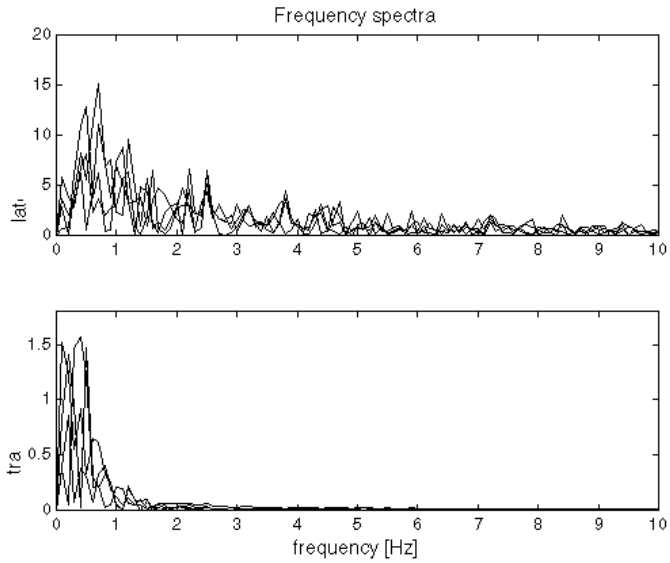Figure 8.6: Frequency spectra for a full vehicle driving at $5\,m/s$

Figure 8.7: Frequency spectra for an empty vehicle driving at $5\,m/s$

To show that the feedback linearizing controller also performs well at high speed, simulations were carried out for a vehicle driving at $20\,m/s$ entering and leaving circular path segment with a radius of $300\,m$. To connect the circular path segment to straight path segments, a fifth-order polynomial was used again. Figure 8.8 shows the simulation results for a full vehicle, whereas figure 8.9 shows the simulation results for an empty vehicle.

In both cases, the vehicle starts entering the curved path section at $t = 2.1\,s$ and leaves the curved path section at about $t = 49\,s$. The maximum tracking error is less than $1.5\,cm$ at the entrance and exit of the curve for both cases. This is just above the tracking error level when the vehicle is completely in the curve or completely at the straight road section. The plots of the steering angles seem to show more noisy behavior of the steering angles than was the case for the low speed. However, it has to be noted that the steering angles necessary to follow a curve with a radius of $300\,m$ are much smaller than is the case for the $20\,m$ radius curve, so that the level of the noise is larger in the relative sense. In the absolute sense, the noise level is about the same. It is interesting to see that the steering angles of the rear axles have an opposite sign compared to the simulation of the $20\,m$ radius curve. This shows that the dynamics of the vehicle do play a role at high speed, as shown in chapter 7.

To show the influence of the measurement noise, the figures 8.10 and 8.11 show plots of the frequency spectra of the lateral accelerations and tracking errors for a full resp. empty vehicle driving at a straight road at $20\,m/s$. To these plots, the same conclusions apply as at low speed.
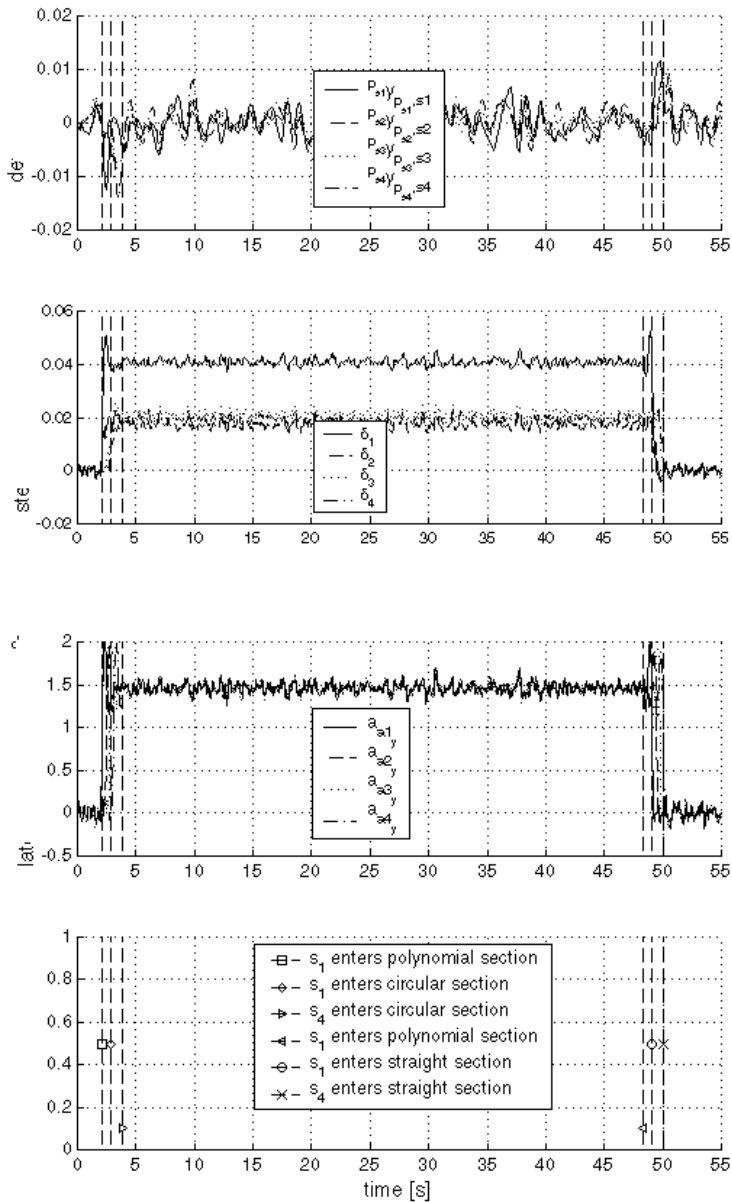
Figure 8.8: Simulation results for a full vehicle driving at $20\,m/s$ entering and leaving a $300\,m$ radius curve
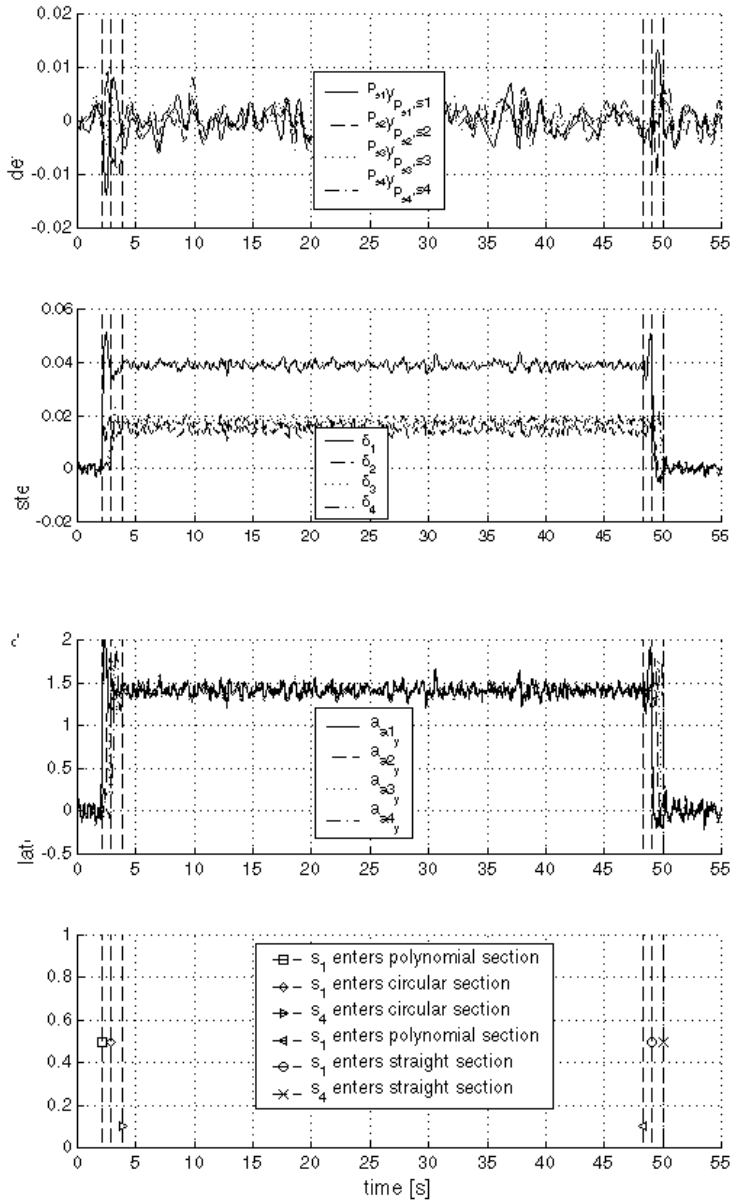
Figure 8.9: Simulation results for an empty vehicle driving at $20\,m/s$ entering and leaving a $300\,m$ radius curve
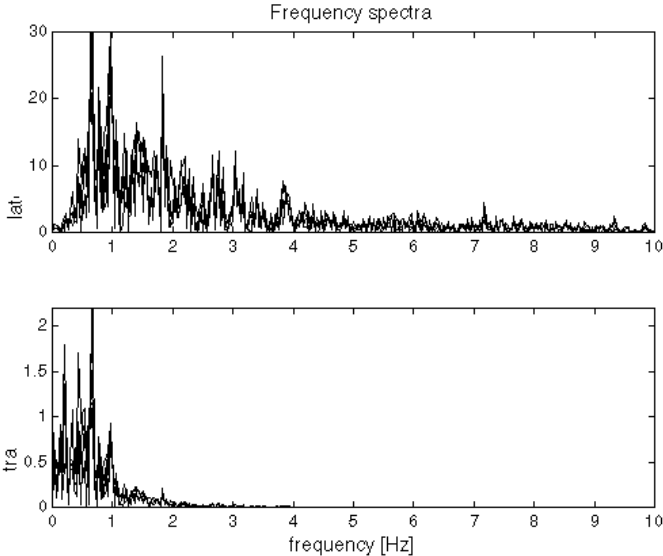
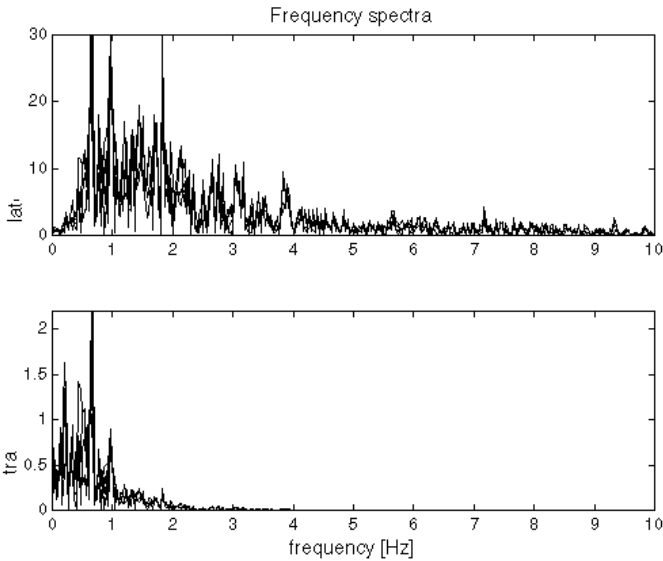Figure 8.10: Frequency spectra for a full vehicle driving at $20\,m/s$

Figure 8.11: Frequency spectra for an empty vehicle driving at $20\,m/s$
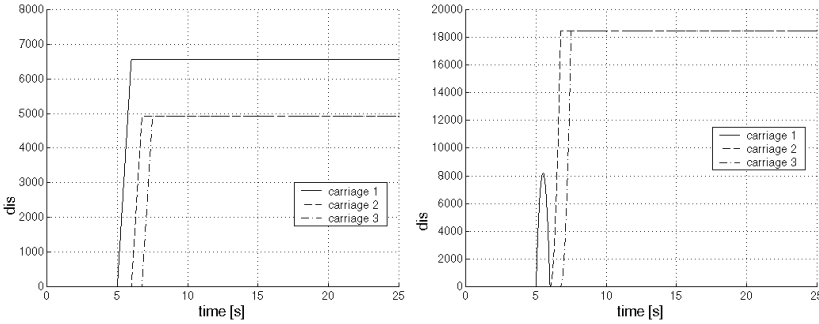
Figure 8.12: Disturbance forces and moments acting on a vehicle driving at 10 m/s

To investigate the performance of the controller when the vehicle is subjected to lateral disturbances, simulations were performed with a wind disturbance acting on the vehicle driving at a speed of $10\,m/s$. For these simulation, an effective lateral wind speed of about $17\,m/s$ was considered. This corresponds to wind force 8 on Beauforts' scale for a vehicle driving at this speed. The vehicle was assumed to drive initially in between buildings, which prevent the wind from blowing against the vehicle, so that no disturbance forces are acting on the vehicle. After a few seconds, the vehicle enters the free field, without buildings to prevent the wind to blow against the vehicle, resulting in disturbance forces. Figure 8.12 shows the disturbance forces and moments acting on a vehicle driving with a speed of $10\,m/s$ in this situation.

Figure 8.13 shows the simulation results for a full vehicle under the influence of the disturbance forces and moments as shown in figure 8.12. The maximum tracking error is about $6\,cm$ for both semi-trailers when they enter the curved section of the path. Due to the integrating action of the controller, the influence of the wind disturbance is almost completely canceled out 5 seconds after the disturbances start. The maximal lateral acceleration due to the wind disturbance is about $0.6\,m/s^2$.

Figure 8.14 shows the same kind of simulation results, but for an empty vehicle in this case. The plots show similar results as for the full vehicles. The maximum tracking errors are about $9\,cm$, which is somewhat larger than for the full vehicle. This is due to the fact that initially the lateral acceleration due to the disturbance forces increases when the mass decreases, as can be shown by applying Newtons law.

Figure 8.13: Simulation results for a full vehicle driving at 10 m/s subjected to a wind disturbance

Figure 8.14: Simulation results for an empty vehicle driving at 10 m/s subjected to a wind disturbance

8.4 Backstepping controller
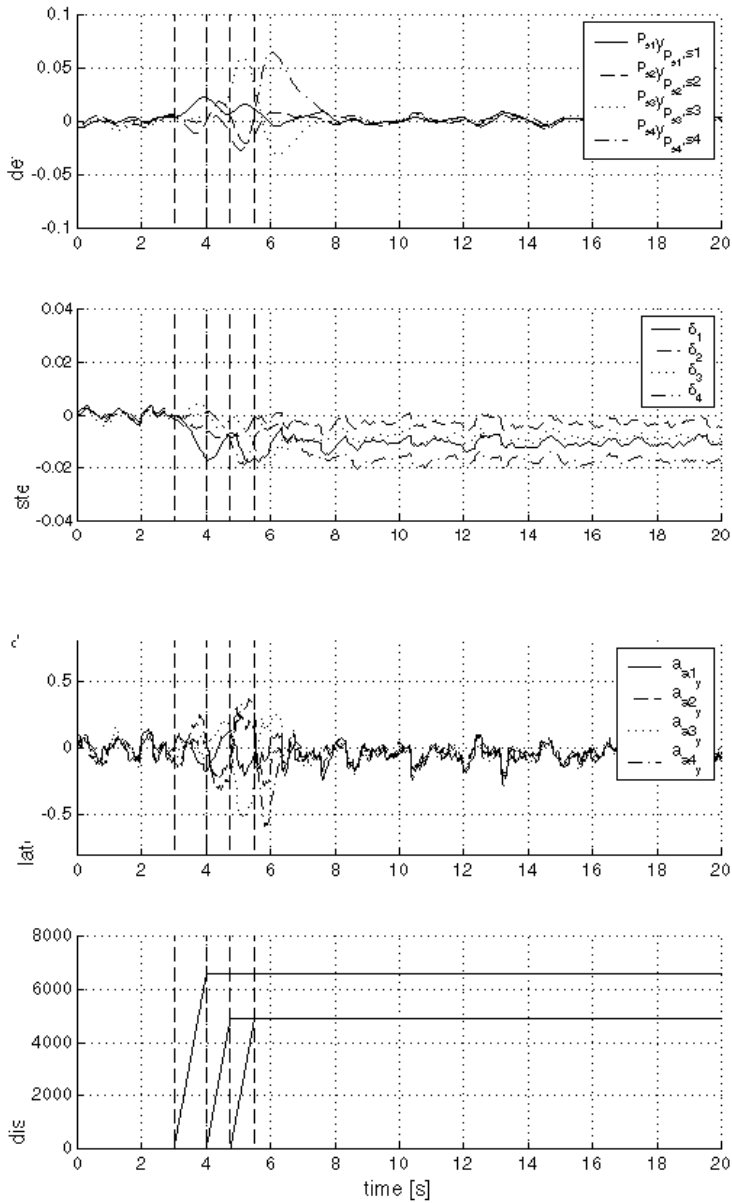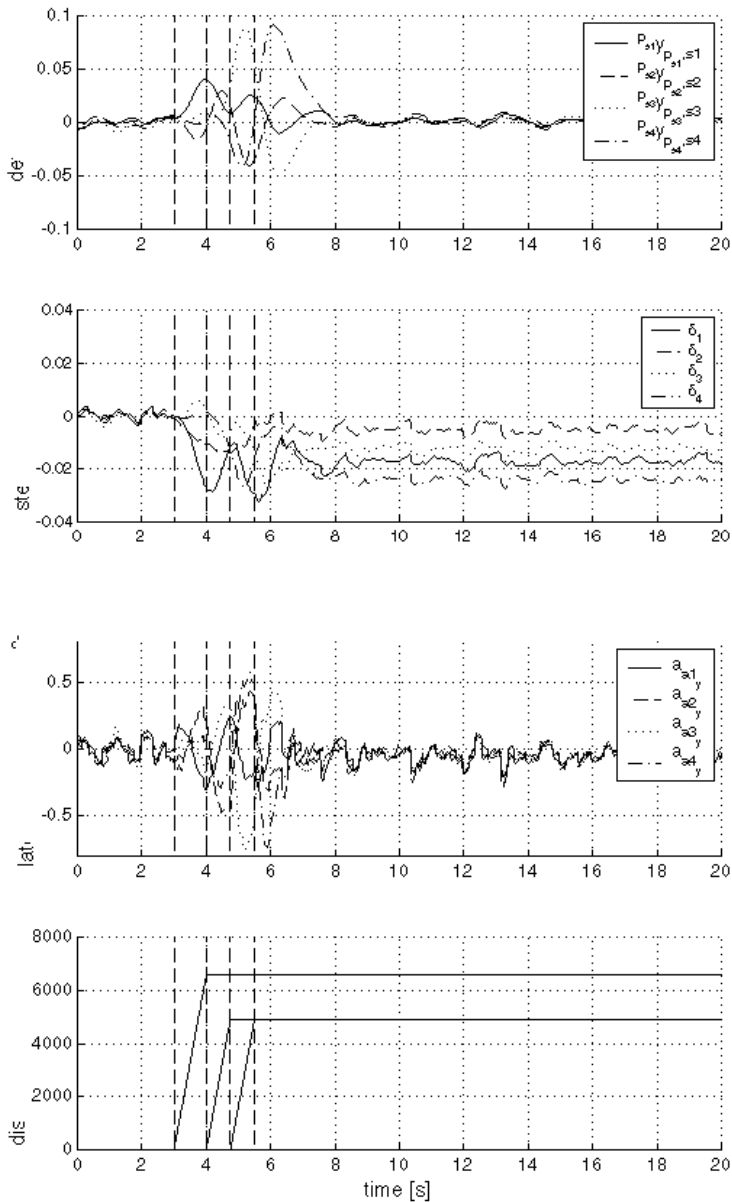
8.4.1 Introduction

In the design of the linearizing controller, the actuator dynamics were completely neglected. In order to take these dynamics into account in a more formal way, a so-called backstepping controller [44, 54] has been designed. The design of such a controller consist of two steps. First, $\boldsymbol{\delta}_t$ is considered as a directly accessible input for the system

$$^{y}\mathbf{M}\ddot{\mathbf{y}}_s + {}^{y}\mathbf{C}_{\dot{y}}\dot{\mathbf{y}}_s + {}^{y}\mathbf{C}_{v_x}v_x + {}^{y}\mathbf{D} = {}^{y}\mathbf{B}_{\text{lat}}\boldsymbol{\delta}_t + {}^{y}\mathbf{B}_{\text{long}}\mathbf{T}_{\text{dr}}, \qquad (8.11)$$

i.e. the steering dynamics are neglected in this step, as in principle has been done with the feedback linearizing controller in the previous section. A stabilizing controller will be designed based on this assumption. The outputs of this controller will be denoted by $\boldsymbol{\delta}_{t_{\text{des}}}$. Subsequently, a suitable Lyapunov function for the system (8.11) with this controller in feedback will be selected.

In the next step, the steering actuators are taken into account and $\boldsymbol{\delta}_t$ is considered as a state of the total system. Therefore the Lyapunov function is augmented with a term depending on the difference between $\boldsymbol{\delta}_t$ and $\boldsymbol{\delta}_{t_{\text{des}}}$. Subsequently, a term is added to the controller that makes the derivative of the resulting Lyapunov function negative definite, so that stability is proved for the system (8.11) including the actuator dynamics (3.78). The outputs of the Kalman filter of the previous chapter will be used as input of the back-stepping controller.

8.4.2 Controller design

step 1
For $\boldsymbol{\delta}_{t_{\text{des}}}$, the feedback linearizing controller as discussed in the previous section will be used, so that

$$\boldsymbol{\delta}_{t_{\text{des}}} = {}^{y}\mathbf{B}_{\text{lat}}^{-1}\{{}^{y}\mathbf{C}_{\dot{y}}\dot{\mathbf{y}}_s + {}^{y}\mathbf{C}_{v_x}v_x - {}^{y}\mathbf{B}_{\text{long}}\mathbf{T}_{\text{dr}} + {}^{y}\mathbf{D} + {}^{y}\mathbf{M}\mathbf{u}'_{\mathbf{st}}\}, \qquad (8.12)$$

where

$$\mathbf{u}'_{\mathbf{st}} = \mathbf{K}_d\dot{\mathbf{y}}_s + \mathbf{K}_p\mathbf{y}_s + \mathbf{K}_i\mathbf{z} \qquad (8.13)$$

and

$$\dot{\mathbf{z}} = \mathbf{y}_s. \qquad (8.14)$$

Assuming that all parameters are exactly known, substitution of $\boldsymbol{\delta}_t = \boldsymbol{\delta}_{t_{\text{des}}}$ into equation (8.11) yields the closed loop dynamics

$$\dddot{\mathbf{z}} + \mathbf{K}_d\ddot{\mathbf{z}} + \mathbf{K}_p\dot{\mathbf{z}} + \mathbf{K}_i\mathbf{z} = \mathbf{0}, \qquad (8.15)$$

This can be written as

$$\dot{\mathbf{x}} = \mathbf{A}\mathbf{x}, \qquad (8.16)$$

where

$$\mathbf{A} = \left[\begin{array}{ccc} -\mathbf{K}_d & -\mathbf{K}_p & -\mathbf{K}_i \\ \mathbf{I} & \mathbf{0} & \mathbf{0} \\ \mathbf{0} & \mathbf{I} & \mathbf{0} \end{array} \right] \tag{8.17}$$

and

$$\mathbf{x} = \left[\begin{array}{c} \ddot{\mathbf{z}} \\ \dot{\mathbf{z}} \\ \mathbf{z} \end{array} \right]. \tag{8.18}$$

Given 8.16, A Lyapunov function

$$V_1 = \mathbf{x}^T \mathbf{P} \mathbf{x}, \tag{8.19}$$

with $\mathbf{P}$ a positive definite constant matrix, can be constructed so that the derivative with respect to time

$$\dot{V}_1 = -\mathbf{x}^T \mathbf{Q} \mathbf{x}, \tag{8.20}$$

with $\mathbf{Q}$ constant and positive definite, is negative. For convenience, the matrix $\mathbf{Q}$ has been selected to be equal to the identity matrix, so that

$$\dot{V}_1 = -\mathbf{x}^T \mathbf{x}, \tag{8.21}$$

step 2

Now $\boldsymbol{\delta}_t$ will be considered as an extra state of the total system. Defining the error variable $\mathbf{w}$ as [1]

$$\mathbf{w} = (\boldsymbol{\delta}_t - \boldsymbol{\delta}_{t_{\mathrm{des}}}), \tag{8.22}$$

the resulting closed loop dynamics can be written as

$$\dddot{\mathbf{z}} + \mathbf{K}_d \ddot{\mathbf{z}} + \mathbf{K}_p \dot{\mathbf{z}} + \mathbf{K}_i \mathbf{z} = {}^y \mathbf{M}^{-1 y} \mathbf{B}_{\mathrm{lat}} \mathbf{w}. \tag{8.23}$$

This yields for the Lyapunov function V_1

$$\dot{V}_1 = -\mathbf{x}^T \mathbf{x} + 2\mathbf{x}^T \mathbf{P} \left[\begin{array}{c} \mathbf{I} \\ \mathbf{0} \\ \mathbf{0} \end{array} \right] {}^y \mathbf{M}^{-1 y} \mathbf{B}_{\mathrm{lat}} \mathbf{w}. \tag{8.24}$$

This is not necessarily negative. Augmenting the Lyapunov function V_1 as

$$V_2 = V_1 + \frac{1}{2} \mathbf{w}^T \boldsymbol{\Gamma} \mathbf{w}, \tag{8.25}$$

with $\boldsymbol{\Gamma}$ a positive definite, symmetric and constant matrix, yields

$$\dot{V}_2 = \dot{V}_1 + \dot{\mathbf{w}}^T \boldsymbol{\Gamma} \mathbf{w}. \tag{8.26}$$

---

[1]Other definitions of $\mathbf{w}$ are possible. The reason to define $\mathbf{w}$ as has been done here is that the controller obtained according to this definition is the simplest.

Using equation (3.78) $\dot{\mathbf{w}}$ can be written as

$$\dot{\mathbf{w}} = \boldsymbol{\tau}_{st}^{-1}(\mathbf{u}_{st} - \boldsymbol{\delta}_t) - \dot{\boldsymbol{\delta}}_{t_{\text{des}}}, \qquad (8.27)$$

so that

$$\dot{V}_2 = -\mathbf{x}^T\mathbf{x} + 2\mathbf{x}^T\mathbf{P}\begin{bmatrix}\mathbf{I}\\\mathbf{0}\\\mathbf{0}\end{bmatrix}{}^y\mathbf{M}^{-1y}\mathbf{B}_{\text{lat}}\mathbf{w} + (\boldsymbol{\tau}_{st}^{-1}(\mathbf{u}_{st} - \boldsymbol{\delta}_t) - \dot{\boldsymbol{\delta}}_{t_{\text{des}}})^T\boldsymbol{\Gamma}\mathbf{w}. \quad (8.28)$$

Taking $\mathbf{u}_{st}$ as

$$\mathbf{u}_{st} = \boldsymbol{\delta}_t + \boldsymbol{\tau}_{st}(\dot{\boldsymbol{\delta}}_{t_{\text{des}}} - 2\boldsymbol{\Gamma}^{-1}(\mathbf{x}^T\mathbf{P}\begin{bmatrix}\mathbf{I}\\\mathbf{0}\\\mathbf{0}\end{bmatrix}{}^y\mathbf{M}^{-1y}\mathbf{B}_{\text{lat}})^T - \boldsymbol{\Gamma}_0\mathbf{w}), \qquad (8.29)$$

with $\boldsymbol{\Gamma}_0$ a positive definite symmetric matrix, such that $\boldsymbol{\Gamma}_0\boldsymbol{\Gamma}$ is positive definite yields

$$\dot{V}_2 = -\mathbf{x}^T\mathbf{x} - \mathbf{w}^T\boldsymbol{\Gamma}_0\boldsymbol{\Gamma}\mathbf{w}, \qquad (8.30)$$

which shows that the system formed by (8.11) and (3.78) in closed loop with (8.29) is asymptotically stable.

To tune the backstepping controller, the same gain matrices $\mathbf{K}_d$, $\mathbf{K}_p$ and $\mathbf{K}_i$ are chosen as for the linearizing controller presented in the previous section. The term $\boldsymbol{\Gamma}_0\mathbf{w}$ tries to make the difference between $\boldsymbol{\delta}_t$ and $\boldsymbol{\delta}_{t_{\text{des}}}$ as small as possible. To tune the gain matrix $\boldsymbol{\Gamma}_0$, a trade off has been made between minimizing the tracking errors and the amount of noise in the lateral accelerations. The final choice for $\boldsymbol{\Gamma}_0$ was $100\mathbf{I}$.

The term including the inverse of the gain matrix $\boldsymbol{\Gamma}$ in equation (8.29) is only necessary to make the derivative of the Lyaponov function negative. The higher the value of $\boldsymbol{\Gamma}$, the less influence the term including the term $\boldsymbol{\Gamma}^{-1}$ has. To make the influence of this term small, $\boldsymbol{\Gamma}$ was set equal to $100\mathbf{I}$.

The backstepping controller (8.29) depends on the derivative of $\boldsymbol{\delta}_{t_{\text{des}}}$. Since $\boldsymbol{\delta}_{t_{\text{des}}}$ depends on $\ddot{\mathbf{z}} = \dot{\mathbf{y}}_s$, the backstepping controller depends on the tracking accelerations $\ddot{\mathbf{y}}_s$. These accelerations can be estimated by using the model (8.11). However, the estimates of $\ddot{\mathbf{y}}_s$ then depend on the parameters of the model (8.11), which depend amongst others strongly on the load of the vehicle, as already explained. Moreover, the effect of lateral disturbances on $\ddot{\mathbf{y}}_s$ is completely neglected in this way. Both effects may result in an biased estimate of $\ddot{\mathbf{y}}_s$.

Another method to obtain $\ddot{\mathbf{y}}_s$ is to extract $\ddot{\mathbf{y}}_s$ from the derivative of the state of the Kalman filter, as calculated with equation (6.35). The advantage of this method is that tracking accelerations obtained in this way are not influenced by model uncertainty and the influence of lateral wind disturbances is also incorporated. The disadvantage of this method is that the measurement noise of the

accelerometers is directly coupled to the actuator inputs. For the simulations, $\ddot{\mathbf{y}}_s$ will be estimated according to this last method.

To make the backstepping controller robust, a robustifying term can be added [28], as outlined in appendix G. For this term, the same approach has to be followed as with the feedback linearizing controller. This means that also in this case, a switching element has to be included in the controller, with the same problems as discussed for the feedback linearizing controller. Also for this type of the controller, simulations showed that the robustifying term causes undesirably high oscillations of the lateral accelerations. For this reason, the robustifying term will not be considered in this thesis. Extensive simulations showed that the backstepping controller is robust without an extra robustifying term.

8.4.3 Simulation results

To investigate the performance of the backstepping controller, extensive simulations were performed under the same conditions as the simulations with the feedback linearizing controller.

To start with, figure 8.15 shows the simulation results for a vehicle driving at $5\,m/s$ entering and leaving a curve with $20\,m$ radius. The vehicle was full during this simulation. The vehicle enters the curve at $t = 1.9\,s$ and leaves the curve at $t = 14\,s$. As the figure shows, the maximum tracking error is about $2\,cm$ at the exit of the curve, which is slightly better compared with the feedback linearizing controller. When the vehicle is completely in the curve or completely at the straight road sections, the maximum tracking error is about $0.5\,cm$. The accelerations of the accelerometers contain more high frequent signals than is the case with the feedback linearizing controller.

To show that the controller is robust against parameter variations, figure 8.16 shows simulation results of the same maneuver but for an empty vehicle. The simulation results are very similar to the simulation results for the empty vehicle.

To investigate the influence of the measurement noise, the figures 8.17 and 8.18 show the spectra of the tracking errors and lateral accelerations for a full and empty vehicle respectively. Compared to the feedback linearizing controller, the spectra of the lateral accelerations show less low frequency signal contents, but more high frequency contents. This is amongst others due to the fact that the accelerometer noise is directly couple to the steering actuators by the controller.
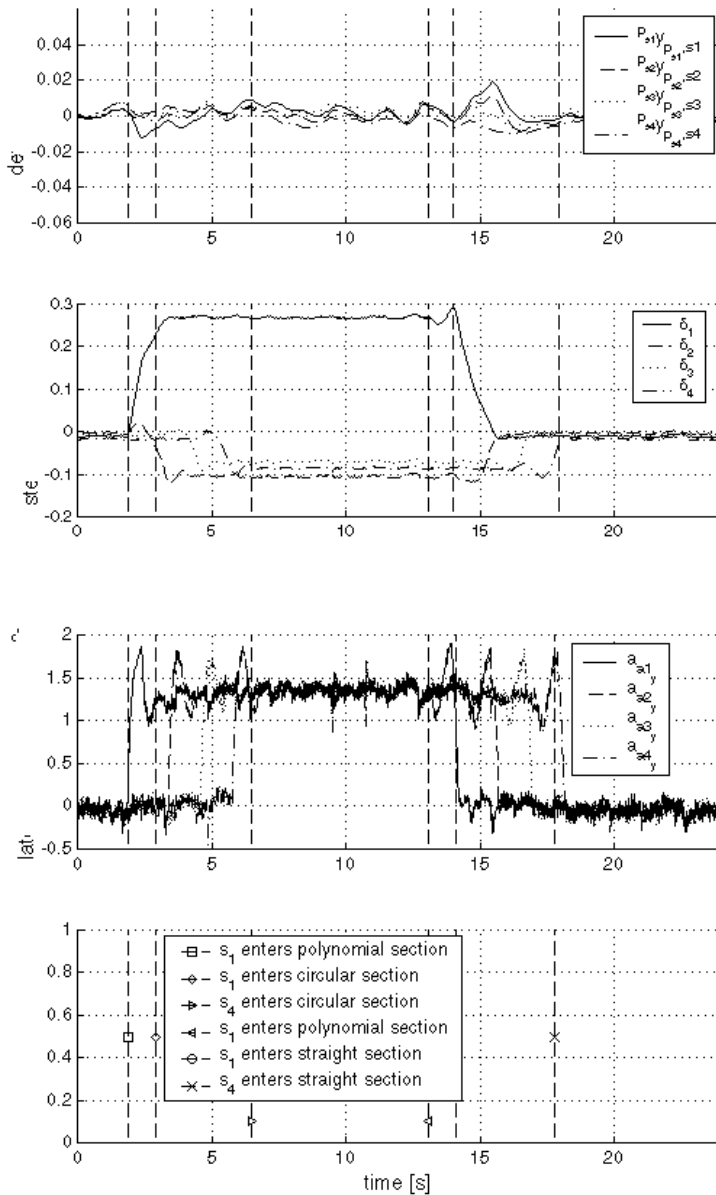
Figure 8.15: Simulation results of a full vehicle driving at $5\,m/s$ entering and leaving a $20\,m$ radius curve
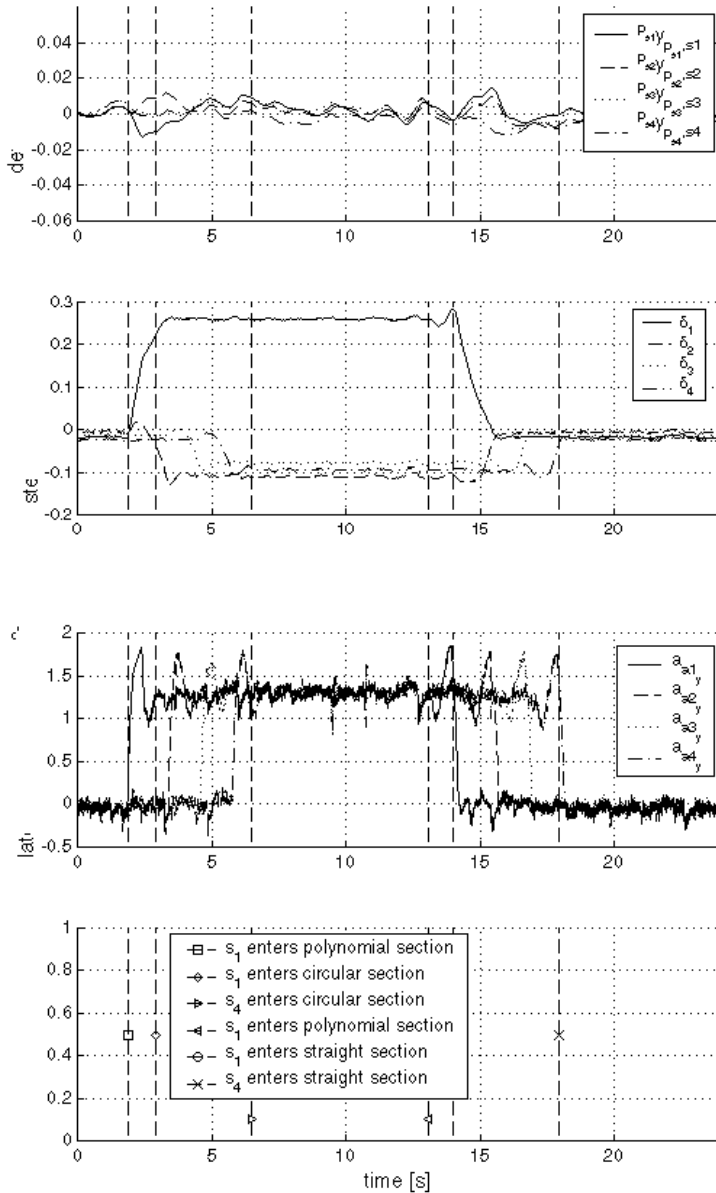
Figure 8.16: Simulation results of an empty vehicle driving at $5\,m/s$ entering and leaving a $20\,m$ radius curve
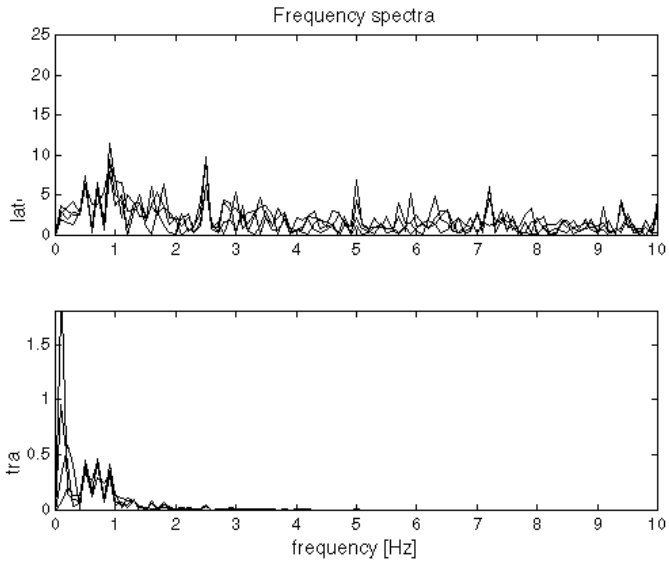
Figure 8.17: Frequency spectra for a full vehicle driving at $5\,m/s$

Figure 8.18: Frequency spectra for an empty vehicle driving at $5\,m/s$

To show that the backstepping controller performs well at high speed, simulations were run for a vehicle driving at $20\,m/s$, following a $300\,m$ radius curve. Figure 8.19 shows the simulation results for a full vehicle, whereas figure 8.20 shows the simulation results for an empty vehicle. Both simulations show that the backstepping controller rejects tracking errors well at high speed. The maximum tracking error is about $0.1\,cm$ for both cases, which is satisfactory.

The figures 8.21 and 8.22 show the spectra of the lateral accelerations and tracking errors for a full resp. empty vehicle driving at $20\,m/s$ at a straight path sections. The spectra of the lateral accelerations show that the lateral accelerations contain too high frequencies. This makes this controller with these gains less suitable from a passenger comfort point of view. A possible way to reduce the high frequency part of the lateral accelerations is to lower the control gain $\mathbf{\Gamma}_0$. This will however go at the cost of larger tracking errors.

To investigate the performance of the backstepping controller under the influence of lateral disturbances, simulations were run for the same disturbance as in the previous section. Figure 8.23 shows the simulation results for a full vehicle. As the plot of the tracking errors shows the maximum tracking error is less than $3.5\,cm$, which is slightly less than was the case with the linearizing controller. The lateral accelerations again are subjected to high frequent behavior, as was also observed with the simulation results of the curved path sections.

Figure 8.24 shows the results for the same kind of simulation for an empty vehicle. Again the controller shows good performance and suppresses this type of disturbance very well. The maximum tracking error is slightly larger than for the full vehicle. This was observed also for the feedback linearizing controller.
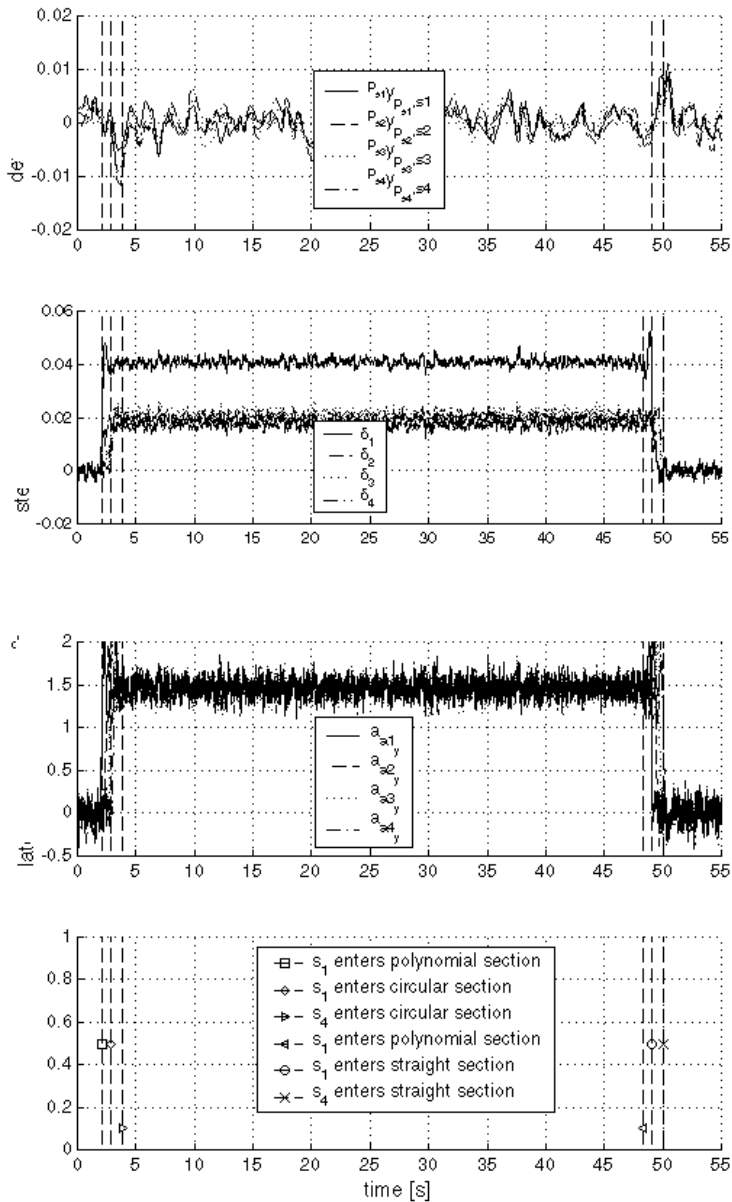
Figure 8.19: Simulation results of a full vehicle driving at $20\,m/s$ entering and leaving a $300\,m$ radius curve
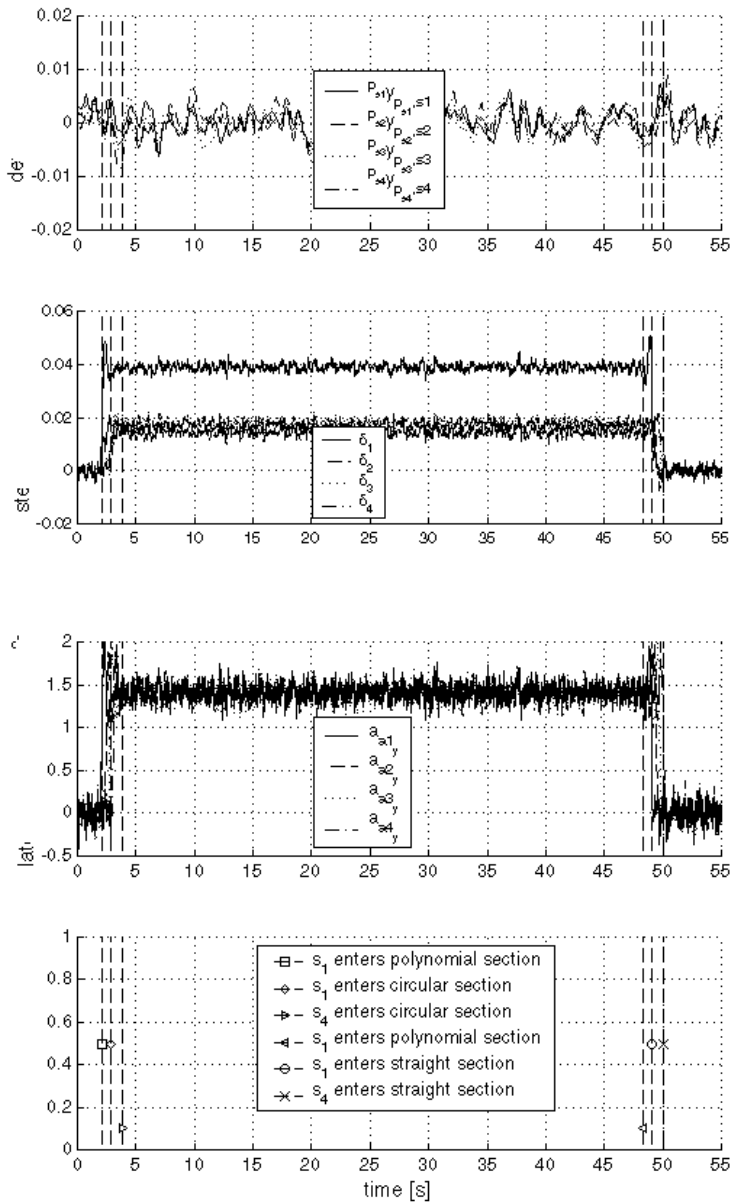
Figure 8.20: Simulation results of an empty vehicle driving at $20\,m/s$ entering and leaving a $300\,m$ radius curve

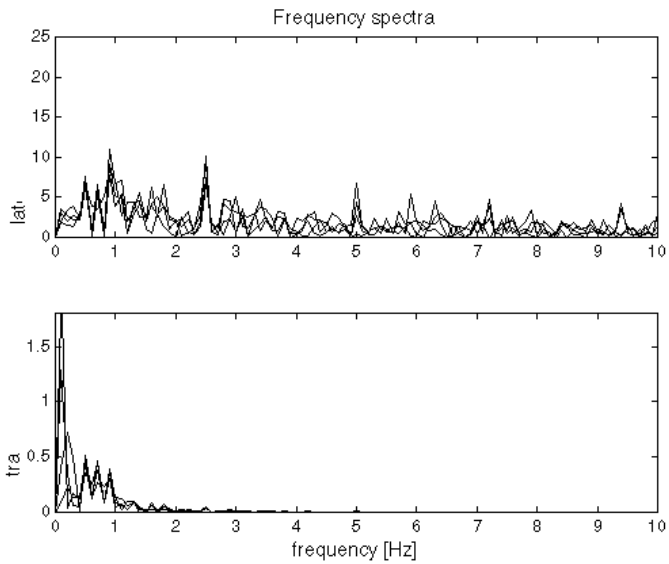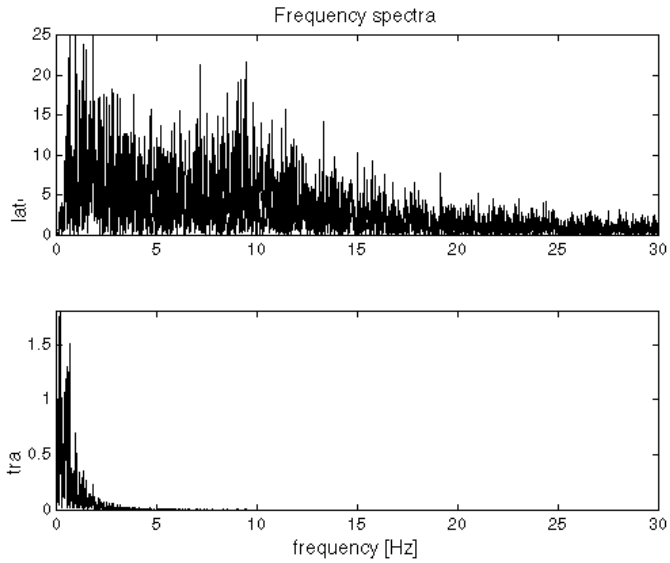Figure 8.21: Frequency spectra for a full vehicle driving at $20\,m/s$
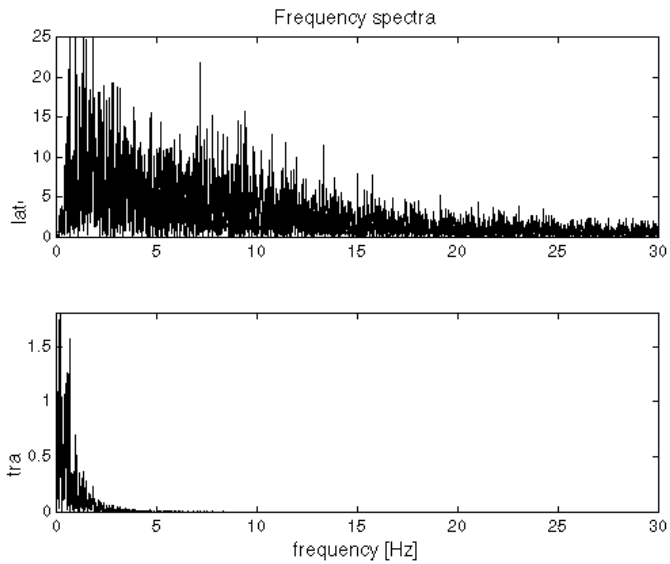
Figure 8.22: Frequency spectra for an empty vehicle driving at $20\,m/s$
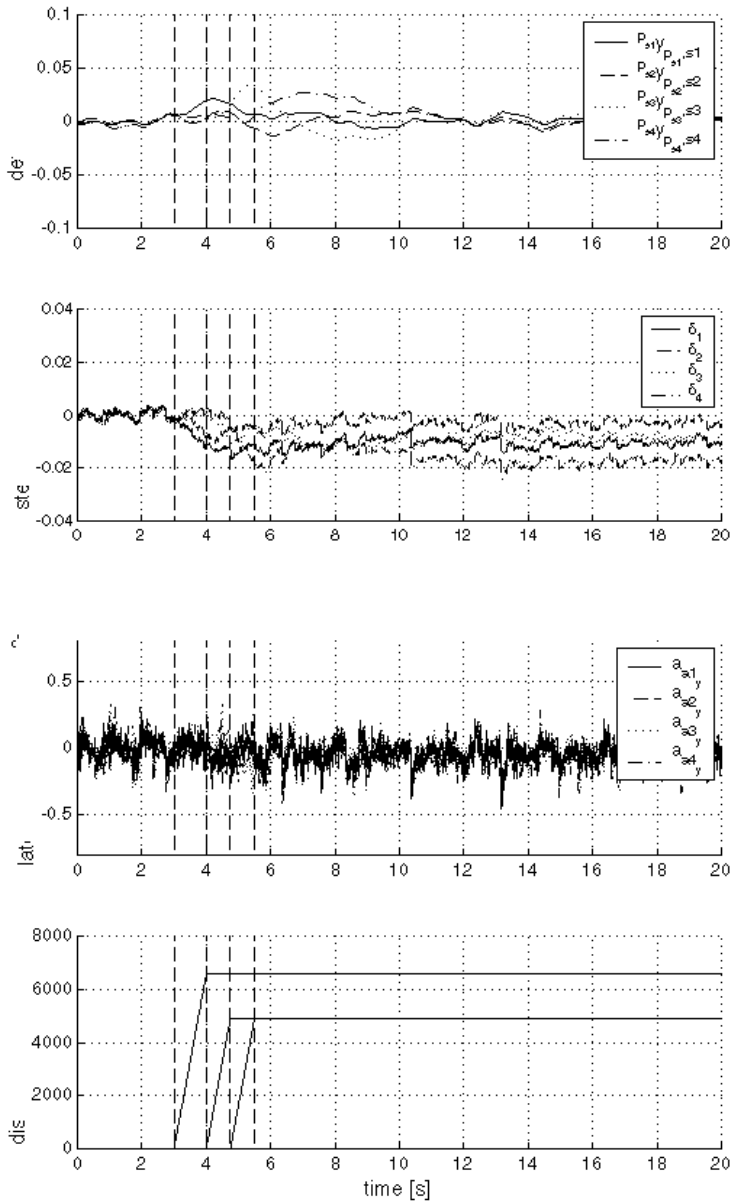
Figure 8.23: Simulation results for a full vehicle driving at 10 m/s subjected to a wind disturbance
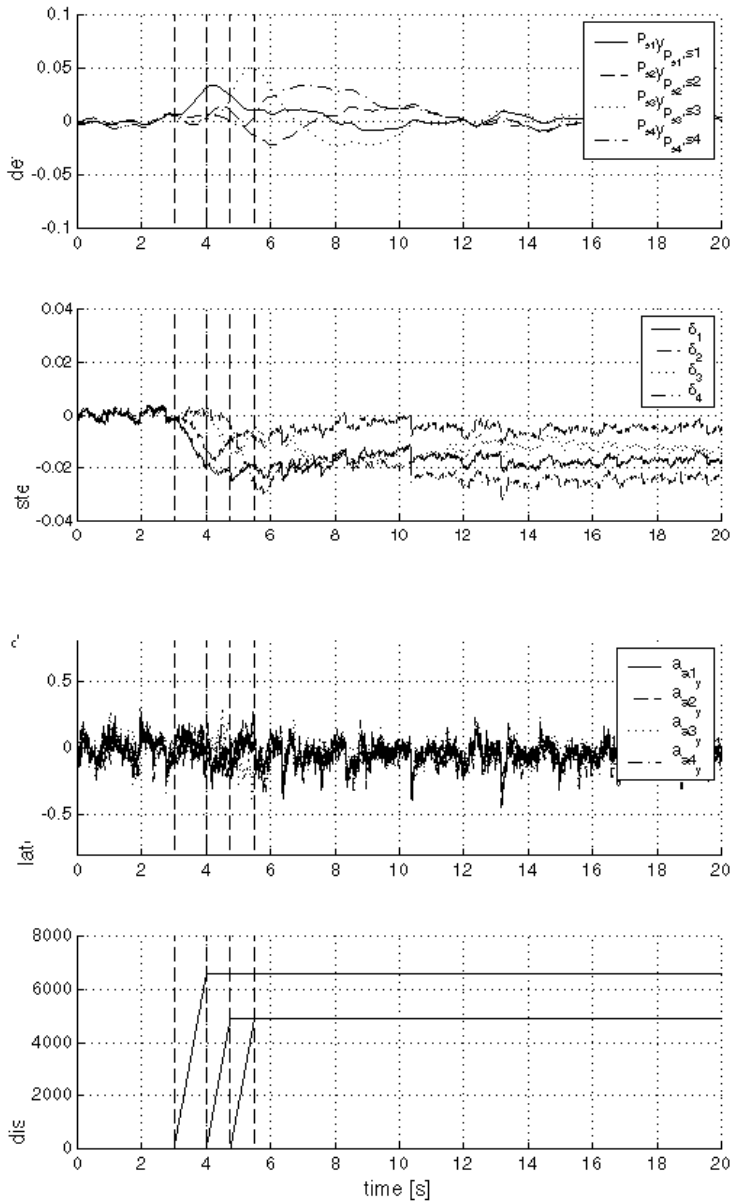
Figure 8.24: Simulation results for an empty vehicle driving at 10 m/s subjected to a wind disturbance

8.5   Summary

A feedback linearizing and a backstepping controller have been designed. The main difference between both controllers is that the linearizing controller neglects the steering actuator dynamics, whereas these dynamics have been accounted for in a more formal way in the backstepping controller. Both controllers use an outer loop consisting of a PID controller.

The linearizing controller shows good tracking performance for both an empty and a full vehicle and it shows robustness against large wind disturbances. The requirements on passenger comfort are fulfilled reasonably well.

Compared to the linearizing controller, the backstepping controller shows improved tracking behavior, sacrificing passenger comfort. To improve passenger comfort the gains of the controller can be reduced. However, this will result in worse tracking behavior.

9

Conclusions and recommendations

9.1   Conclusions

This thesis deals with the design of a lateral guidance system for steering a multiple-articulated vehicle with all-wheel steering along a path. This lateral guidance system forces such a vehicle follow to a path in a 'tram-like' way. This problem statement has been formalized in chapter 2 as controlling the distances of $n + 1$ points to the path, with n the number of carriages, to zero. These distances have been defined as the tracking errors.

9.1.1   Control model

The lateral guidance system is model based. Therefore, a nonlinear dynamic vehicle model has been derived. This model describes the planar motion of an all-wheel steered $n + 1$-carriage vehicle in the horizontal plane. The model has the steering angles and driving torques applied to each wheel as inputs. A linear relationship between tire slip angle and lateral tire force was assumed. The derivation of the model is carried out in an inertial frame. To facilitate the insight into the model, the model has been transformed into vehicle-fixed coordinates. After showing that a dynamic vehicle model is required in order to obtain good closed-loop performance at high speed, another coordinate transformation has been carried out to express the model in the tracking error dynamics.

9.1.2   Simulation model

To investigate the performance of the guidance system, a more complex vehicle model is used. This simulation model describes, apart from the planar motion of the vehicle, also the vertical motion due to the suspension system. Moreover, a more complex tire model has been included in the model. This tire model

includes the load dependency of the cornering stiffness and a nonlinear relationship between tire force and tire slip angle. To simulate the influence of wind disturbance forces, a wind model has been included in the model.

9.1.3 Magnetic referencing system

A measurement method has been developed to measure the distance from the vehicle to the path. This measurement method is based on a magnetic referencing system. This system consists of discrete permanent bar magnets that are buried in the road. By means of measuring the longitudinal and lateral field component of the magnetic field produced by the magnets with a dual-axis magnetic field sensor, the distance of the sensor to the magnets can be determined. In this way, the measurement method is independent of the measurement height and the strength of the magnets that are used. A second dual-axes sensor is added to cancel the influence of slant of the magnets and the vehicle in the longitudinal directions. With the addition of this extra sensor, the measurement method is still sensitive for lateral slant of magnet and vehicle, but the effect of this type of slant is sufficiently small. Measurement results, obtained from a static measurement setup, show a maximum error of about $2\,cm$ in a measurement range of plus and minus $50 cm$ with 9^0 slant of the magnet in both directions.

9.1.4 Observer design

With the help of the magnetic referencing system, the distance to the path can only be obtained at discrete instances. For controlling the distance from the vehicle to the path, continuous information about the distance to the path and the rate of change of this distance is desirable. Therefore, an extended multi-rate Kalman filter has been designed. This Kalman filter uses accelerometers as input. In this way, the filter is almost independent of varying vehicle parameters. Moreover, the effect of lateral disturbances can be predicted directly on the basis of the accelerometer readings. This is desirable, since the influence of this type of disturbance can be measured only by means of the magnetic referencing system, which yields updates only at discrete time instances. When the time till a next magnet is large, this could cause a large drift of the estimates, when the influence of lateral disturbances would not be directly incorporated in the prediction step of the Kalman filter.

To cancel out the effect of slant on the accelerometers, a suspension system model of the vehicle has been incorporated into the Kalman filter. In this way, a good prediction of the roll angle of the vehicle can be obtained. The suspension system parameters are estimated online. Moreover, the road banking angle is also estimated online. In reality, accelerometers are subjected to sensor offsets. An adaptation scheme has been included in the Kalman filter to estimate these

offsets online.

The measurements of the magnetic fields of the magnetic referencing system are incorporated in the Kalman filter to apply a correction to the predictions based on the accelerometer readings. To deal with the asynchronous character of this type of information, this measurement is implemented in a multi-rate fashion. To be able to apply corrections to the estimates of the Kalman filter in between the magnets, rate gyroscopes, wheel encoders and articulation angle sensors are proposed. In this way, redundancy is added to the Kalman filter. This redundancy can be useful when one of the sensors fails. When failure of this sensor is detected, the sensor can be switched off, resulting in a smooth degradation of the performance of the Kalman filter. The performance of the Kalman filter has been investigated by means of simulations. Under the simulated circumstances, the maximum error in the tracking error estimates is about $2\,cm$ when the estimated parameters of the Kalman filter have converged to their final values.

9.1.5 Input and output selection

Since the vehicles considered in this thesis are equipped with independent drives on each wheels, differential braking is an option for steering the vehicles. In chapter 7, an analysis has been carried out to show that the influence of the steering angles on the lateral behavior of the vehicle is much larger than the influence of differential braking. Therefore, differential braking is not considered as input for the controllers that have been designed for steering the vehicles. In the same chapter, an analysis has been carried out to show the advantage of all-wheel steering compared to front-wheel steering. This analysis shows that also at high speed with front-wheel steering, the rear axles might have a large off-tracking. With all-wheel steering, this off-tracking can, at least in theory, be eliminated.

9.1.6 Controller design

For steering the vehicle, two types of controllers have been proposed. The first controller is a feedback linearizing controller. In the ideal case, this controller cancels all nonlinearities in the planar vehicle model and leaves a system consisting of $n+1$ double integrators. To reject the influence of lateral disturbances and model uncertainty, a PID controller has been used. Simulations show this controller performs well for different scenario's and for a large range of parameter variations.

For the design of the feedback linearizing controller, the actuator dynamics have been completely neglected. To incorporate the actuator dynamics in a more formal way in the controller, a backstepping controller has been designed. This backstepping controller utilizes the same PID controller as the feedback

linearizing controller. The same kind of simulations have been carried out to show that the backstepping controller performs well for different scenarios and is robust against a large range of parameter variations

9.2 Recommendations and ideas for further research

9.2.1 Choice of Coordinate systems

The problem statement of this thesis was formalized in the path-fixed coordinate frames p_{si}. As a direct result, the same coordinate frames where used to design the lateral guidance system. In principle, it may not make any difference in which coordinate system the lateral guidance system is expressed. For the implementation, however, one type of coordinate systems might be more favorable than the other, since it differs how the information of the path has to be used in different coordinate systems. Therefore, it might be interesting to investigate if it is advantageous to express the lateral guidance system in an inertial frame. One of the problems that then has to be solved is to calculate the distance to the path online when the Kalman filter is expressed in an inertial frame.

9.2.2 Measurement system

The Kalman filter presented in this thesis uses different types of sensors to apply a correction to the prediction based on accelerometer readings. In this way the Kalman filter still works when one of the sensors fails. The failure of this sensor has to be detected. Detecting this failure was not considered in this thesis. It is therefore an interesting direction to continue research on the lateral guidance system as presented. Possible ways of detecting sensor failures is to compare the sensor outputs of sensors measuring the same type of information. This requires however three different sensors to be able to make a decision. Another method is to compare the sensor readings with the estimates obtained with the Kalman filter. In this way, no extra sensors are required to make a decision.

In the prediction step of the Kalman filter, there is no redundancy in sensors, so that failure of one of the accelerometers means that the filter does not work properly anymore (unless the accelerometers are implemented doubly). To achieve redundancy against failure of one or more of the accelerometers, the accelerometer signals can be predicted by the vehicle model as presented in chapter 3. In case the accelerometers fail, the predicted accelerations can be used as input for the Kalman filter. Since the predicted accelerations depend strongly on varying vehicle parameters such as masses and cornering stiffnesses and since the prediction does not include the influence of lateral disturbances, it has to be investigated how using the predicted accelerations detoriates the performance of the Kalman filter.

9.2.3 Controller design

The closed-loop simulation results show oscillatory behavior of the lateral accelerations of the carriages. For passenger comfort, this is undesirable. A possible way to reduce these oscillations is to use an H_∞/H_2 based controller to replace the PID controllers. In this way, the outputs of the Kalman filter can be pre-filtered, so that the influence of the measurement noise on the lateral accelerations can be reduced.

Trials to prove robustness of the controllers yielded only conservative upper bounds for the allowed parameter variations. Therefore, robustness of the controllers was shown by means of simulations. To get proven robustness of the controller, different design directions of new controllers are possible. One obvious direction is to incorporate robustness in the design of the H_∞ controller as discussed above. Other design directions include robust adaptive controllers as presented in [85]

A

List of frequently used symbols

coordinate frames

ai	vehicle fixed coordinate frame fixed at point $\mathbf{a}_i$
cj	vehicle fixed coordinate frame fixed at the centre of gravity of the jth carriage
si	vehicle fixed coordinate frame fixed at point $\mathbf{s}_i$
p_{c1}	frame moving along the path adjacent to coordinate frame $c1$
p_{si}	frame moving along the path adjacent to coordinate frame si
m	magnet fixed coordinate frame, with z-axis along magnet symmetry axis
p_{ai}	frame moving along the path adjacent to coordinate frame ai
w	world fixed or inertial frame
w_{1j}	frame fixed at the left wheel of the jth axle
w_{2j}	frame fixed at the right wheel of the jth axle

kinematic parameters

$^i\mathbf{q}$	vector with generalized coordinates related to coordinate frame i
$^i\mathbf{x}_{j,k}$	position of point $\mathbf{k}$ with respect to point $\mathbf{j}$ expressed in coordinate frame i
v_x	longitudinal velocity of tractor
v_y	lateral velocity of tractor's center of gravity
$\alpha_{w_{ij}}$	tire slip angle at of wheel w_{ij}
$\beta_{w_{ij}}$	body slip angle at the origin of frame w_{ij}
δ_j	steering angle of wheels on axle j
δ_{1j}	steering angle of left wheel of axle of j
δ_{2j}	steering angle of left wheel of axle of j
$^i\epsilon_j$	orientation of frame j with respect to frame i
ρ_p	curvature of path at point $\mathbf{p}$
σ_p	length of path between fixed reference point and point $\mathbf{p}$

vehicle parameters

b_j	half the distance between the wheels of one axle
C_{w_j}	cornering stiffness of the tires on axle j
D_s	total damping constant of suspension system

d_{rj}	distance between rear articulation point and centre of gravity of jth carriage
d_{fj}	distance between front articulation point and centre of gravity of jth carriage
l_{si}	distance of point $\mathbf{s}_i$ to the center of gravity of the corresponding carriage
l_{ai}	distance of point $\mathbf{a}_i$ to the center of gravity of the corresponding carriage
l_{f1}	distance between centre of gravity and front axle of tractor
l_{rj}	distance between centre of gravity and rear axle of jth carriage
I_{zj}	central moment of inertia of jth carriage around vertical axis
K_s	total spring constant of suspension system
m_j	mass of jth carriage

observer parameters

a_{ai_y}	lateral acceleration in horizontal plane of point $\mathbf{a}_i$
I_x	moment of inertia of jth carriage around longitudinal axis
g	gravitational acceleration
k	sampling moment
o_{ai}	offset of accelerometer at point $\mathbf{a}_i$
α_{ai_y}	accelerometer reading of accelerometer at point $\mathbf{a}_i$
Δ	sampling time
κ	measurement moment
ϕ	road banking angle
θ	vehicle roll angle

B

Proof of shortest distance

This appendix will be used to prove that in two dimensions the shortest distance from a point $\mathbf{s}$ to a curve is measured along a line line through $\mathbf{s}$ that is perpendicular to the tangent to the curve at.

Let $\mathcal{P}$ denote a twice differentiable curve in $\mathbb{R}^2$ and let $\mathbf{s}$ denote a point. Without loss of generality we can define a coordinate frame p_s with its origin $\mathbf{p}_s$ such that the line connecting $\mathbf{s}$ and $\mathbf{p}_s$ is perpendicular to the tangent to $\mathcal{P}$ at $\mathbf{p}_s$. The orientation of p_s is such that its y-axis coincides with this line and the vector component $^{p_s}y_{p_s,s}$ is positive, as illustrated in figure B.1.

Let a point

$$\mathbf{p} = \left[\begin{array}{c} ^{p_s}x_{p_s,p} \\ ^{p_s}y_{p_s,p} \end{array} \right] \tag{B.1}$$

on the curve be locally described by

$$^{p_s}y_{p_s,p} = P(^{p_s}x_{p_s,p}), \tag{B.2}$$

with obviously $P(0) = 0$. Then there is an environment of $\mathbf{p}_s$:

$$\{^{p_s}x_{p_s,p} : |^{p_s}x_{p_s,p}| < \epsilon\}, \tag{B.3}$$

such that

$$(^{p_s}y_{p_s,s} - P(^{p_s}x_{p_s,p}))^2 + {}^{p_s}x_{p_s,p}^2 \geq {}^{p_s}y_{p_s,s}^2, \tag{B.4}$$
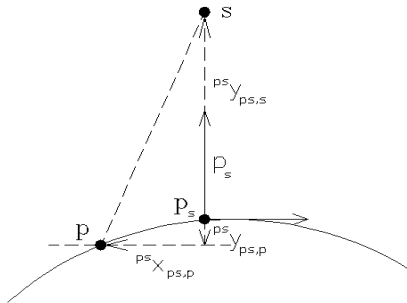
Figure B.1: Definition of points

where the equality sign only applies at $^{p_s}x_{p_s,p} = 0$. This means that the function

$$f(^{p_s}x_{p_s,p}) = (^{p_s}y_{p_s,s} - P(^{p_s}x_{p_s,p}))^2 + {}^{p_s}x_{p_s,p}^2 - {}^{p_s}y_{p_s,s}^2. \qquad (B.5)$$

has a minimum in $^{p_s}x_{p_s,p} = 0$. This implies that

1.
$$\left.\frac{df(^{p_s}x_{p_s,p})}{d^{p_s}x_{p_s,p}}\right|_{^{p_s}x_{p_s,p}=0} = 0 \qquad (B.6)$$

2.
$$\left.\frac{d^2 f(^{p_s}x_{p_s,p})}{d^{p_s}x_{p_s,p}^2}\right|_{^{p_s}x_{p_s,p}=0} \geq 0. \qquad (B.7)$$

The first condition yields

$$\left.\frac{df(^{p_s}x_{p_s,p})}{d^{p_s}x_{p_s,p}}\right|_{^{p_s}x_{p_s,p}=0} = 2^{p_s}y_{p_s,s}\frac{P(^{p_s}x_{p_s,p})}{d^{p_s}x_{p_s,p}} = 0. \qquad (B.8)$$

This indicates that

$$\frac{P(^{p_s}x_{p_s,p})}{d^{p_s}x_{p_s,p}} = 0, \qquad (B.9)$$

which shows that the tangent to the path is parallel to the x-axis of coordinate frame p_s, which in turn shows that indeed, the line connecting **s** and $\mathbf{p}_s$ is perpendicular to this tangent, since the y-axis of coordinate frame p_s coincides with the line $\mathbf{s} - \mathbf{p}_s$.

The second condition yields

$$\left.\frac{d^2 f(^{p_s}x_{p_s,p})}{d^{p_s}x_{p_s,p}^2}\right|_{^{p_s}x_{p_s,p}=0} = -2^{p_s}y_{p_s,s}\frac{d^2 P(^{p_s}x_{p_s,p})}{d^{p_s}x_{p_s,p}^2} + 2 \geq 0, \qquad (B.10)$$

which shows that

$$^{p_s}y_{p_s,s}\frac{d^2 P(^{p_s}x_{p_s,p})}{d^{p_s}x_{p_s,p}^2} \leq 1. \qquad (B.11)$$

For

$$\frac{d^2 P(^{p_s}x_{p_s,p})}{d^{p_s}x_{p_s,p}^2} \leq 0, \qquad (B.12)$$

condition (B.11) is certainly fulfilled. This actually corresponds to the situation as depicted in figure B.1. For positive $\frac{d^2 P(^{p_s}x_{p_s,p})}{d^{p_s}x_{p_s,p}^2}$ (B.11) yields

$$\frac{1}{\frac{d^2 P(^{p_s}x_{p_s,p})}{d^{p_s}x_{p_s,p}^2}} > {}^{p_s}y_{p_s,s}. \qquad (B.13)$$

The turning radius of the curve is given by [40]

$$\frac{(1 + \frac{d\,P(^{p_s}x_{p_s,p})}{d^{p_s}x_{p_s,p}})^{3/2}}{|\frac{d^2\,P(^{p_s}x_{p_s,p})}{d^{p_s}x^2_{p_s,p}}|} \tag{B.14}$$

In $^{p_s}x_{p_s,p} = 0$, this turning radius becomes

$$\frac{1}{|\frac{d^2P(^{p_s}x_{p_s,p})}{d^{p_s}x^2_{p_s,p}}|}. \tag{B.15}$$

So (B.13) is fulfilled when the turning radius of the curve is larger than $^{p_s}y_{p_s,p}$. Under this condition the extremum of $f(^{p_s}x_{p_s,p})$ at $^{p_s}x_{p_s,p} = 0$ is indeed a minimum.

C

Proof of uniqueness of orthogonal projection

This appendix will be used to proof uniqueness of the orthogonal projection of a point onto the path. This proof has been taken from [58]. To prove the orthogonal projection is unique under some conditions, the Voronoï diagram of a curve has to be defined.

Definitio n C.0.1 *Voronoï diagram [58]*

A point $\mathbf{r} \in \mathbb{R}^2$ belongs to the Voronoï diagram $\mathcal{V}$ of a curve $\mathcal{P} \in \mathbb{R}^2$ if and only if there exist and open disc $B_r(p)$, such that

1. $\partial B_r(p) \cap \mathcal{P}$ contains at least 2 points

2. $B_r(p) \cap \mathcal{P} = \emptyset$

In words, this means that the Voronoï diagram $\mathcal{V}$ of a curve $\mathcal{P}$ is the set of centers of circles that are tangent to $\mathcal{P}$ at at least 2 distinct points and have no points of $\mathcal{P}$ inside itself.

Assume that the curvature of $\mathcal{P}$ is bounded by $1/d_{min}$, so that $d(\mathcal{P}, \mathcal{V}) \geq d_{min}$.

Lemma C.0.2 *[58] Let U denote the set $U = \{x \in \mathbb{R}^2 : d(x, \mathcal{P}) < d_{min}\}$. Then every point $x \in \mathbb{R}^2$ has an unique orthogonal projection on $\mathcal{P}$*

Proof: The proof is based on the principle of contradiction. Let $\mathbf{p}_1 \in U$ and suppose that $\mathbf{p}_1$ is projected orthogonaly in $\mathcal{P}$ onto the points $\mathbf{A}$ and $\mathbf{B}$, such that $d(\mathbf{p}_1, \mathcal{P}) = \|\mathbf{p}_1 - \mathbf{A}\|_2 = \|\mathbf{p}_1 - \mathbf{B}\|_2 = r$. Let D represent the open disc $B_r(\mathbf{p}_1)$. It is clear that $D \cap \mathcal{P} = \emptyset$. If there would exist $\mathbf{p}_2 \in D \cap \mathcal{P}$, then $d(\mathbf{p}_2, \mathcal{P}) \leq \|\mathbf{p}_1 - \mathbf{p}_2\|_2 < r$, which contradicts the hypothesis $d(\mathbf{p}_2, \mathcal{P}) = r$. On the other hand, if $\mathbf{A}, \mathbf{B} \in \partial D$, then the center $\mathbf{p}_1$ of D belongs to the Voronoï diagram of $\mathcal{P}$. This is a contradiction since the assumption $d(\mathcal{V}, \mathcal{P}) \geq d_{min}$ means that $U \cap \mathcal{V} = \emptyset$.

D

System matrices

In chapter 3, the mass matrix ${}^{w}\mathbf{M}({}^{w}\mathbf{q})$ has been defined as

$$
{}^{w}\mathbf{M}({}^{w}\mathbf{q}) = \sum_{j=1}^{n} \mathbf{J}_{cj}^{T}({}^{w}\mathbf{q})\mathcal{M}_{j}\mathbf{J}_{cj}({}^{w}\mathbf{q}), \tag{D.1}
$$

where

$$
\mathbf{J}_{cj}({}^{w}\mathbf{q}) = \begin{bmatrix} 1 & 0 & l_{1j}\sin{}^{w}\epsilon_{c1} & \cdots & l_{nj}\sin{}^{w}\epsilon_{cn} \\ 0 & 1 & -l_{1j}\cos{}^{w}\epsilon_{c1} & \cdots & -l_{nj}\cos{}^{w}\epsilon_{cn} \\ 0 & 0 & \delta_{[1j]} & \cdots & \delta_{[1n]} \end{bmatrix}. \tag{D.2}
$$

and

$$
\mathcal{M}_{j} = \begin{bmatrix} m_{j} & 0 & 0 \\ 0 & m_{j} & 0 \\ 0 & 0 & I_{z_{j}} \end{bmatrix}, \tag{D.3}
$$

Elaboration of equation (D.1) yields

$$
{}^{w}M_{[1,1]} = \sum_{j}^{n} m_{j} \tag{D.4a}
$$

$$
{}^{w}M_{[1,2]} = 0 \tag{D.4b}
$$

$$
{}^{w}M_{[2,1]} = 0 \tag{D.4c}
$$

$$
{}^{w}M_{[2,2]} = \sum_{j}^{n} m_{j} \tag{D.4d}
$$

$$
{}^{w}M_{[1,l+2]} = \sum_{j=1}^{n} m_{j}l_{lj}\sin{}^{w}\epsilon_{cl} \tag{D.4e}
$$

$$
{}^{w}M_{[2,l+2]} = \sum_{j=1}^{n} -m_{j}l_{lj}\cos{}^{w}\epsilon_{cl} \tag{D.4f}
$$

$$
{}^{w}M_{[k+2,l+2]} = \sum_{j=1}^{n} m_{j}l_{kj}l_{lj}\cos{}^{ck}\epsilon_{cl} + \delta_{[kl]}I_{z_{l}} \tag{D.4g}
$$

for $1 \leq k,l \leq n$

In chapter 3, the entries of the coriolis and centrifugal matrix ${}^w\mathbf{C}({}^w\dot{\mathbf{q}}, {}^w\mathbf{q})$ have been written as

$$\sum_{k=1}^{n+2}\left\{\frac{\partial^w M_{[i,l]}}{\partial^w q_{[k]}} - \frac{1}{2}\frac{\partial^w M_{[k,l]}}{\partial^w q_{[i]}}\right\} {}^w\dot{q}_{[k]} \tag{D.5}$$

This yields

$$\begin{aligned}
{}^w C_{[1,1]} &= 0 & \text{(D.6a)}\\
{}^w C_{[1,2]} &= 0 & \text{(D.6b)}\\
{}^w C_{[2,1]} &= 0 & \text{(D.6c)}\\
{}^w C_{[2,2]} &= 0 & \text{(D.6d)}\\
{}^w C_{[k+2,1]} &= 0 & \text{(D.6e)}\\
{}^w C_{[k+2,2]} &= 0 & \text{(D.6f)}\\
{}^w C_{[1,l+2]} &= \sum_{j=1}^{n} m_j l_{lj} \cos\left({}^w\epsilon_{cl}\right) {}^w\dot{\epsilon}_{cl} & \text{(D.6g)}\\
{}^w C_{[2,l+2]} &= \sum_{j=1}^{n} m_j l_{lj} \sin\left({}^w\epsilon_{cl}\right) {}^w\dot{\epsilon}_{cl} & \text{(D.6h)}\\
{}^w C_{[k+2,l+2]} &= \sum_{j=1}^{n} -m_j l_{kj} l_{lj} \sin\left({}^{ck}\epsilon_{cl}\right) {}^w\dot{\epsilon}_{cl} & \text{(D.6i)}\\
& & \text{(D.6j)}
\end{aligned}$$

for $1 \leq k, l \leq n$.

In 3.4 of chapter 3, The rows of the matrices ${}^w L_{\text{long}}$ and ${}^w L_{\text{lat}}$ have been defined as

$$
{}^w L_{\text{long}_{i[j,:]}} = \begin{cases} \left(\dfrac{\partial^w \mathbf{x}_{w,w_{i1}}}{\partial^w \mathbf{q}}\right)^T {}^w\mathbf{Rot}_{c1_{[:,1]}} & \text{if } j = 1 \\[2ex] \left(\dfrac{\partial^w \mathbf{x}_{w,w_{ij}}}{\partial^w \mathbf{q}}\right)^T {}^w\mathbf{Rot}_{cj-1_{[:,1]}} & \text{if } j > 1 \end{cases} \tag{D.7}
$$

$$
{}^w L_{\text{lat}_{i[j,:]}} = \begin{cases} \left(\dfrac{\partial^w \mathbf{x}_{w,w_{i1}}}{\partial^w \mathbf{q}}\right)^T {}^w\mathbf{Rot}_{c1_{[:,2]}} & \text{if } j = 1 \\[2ex] \left(\dfrac{\partial^w \mathbf{x}_{w,w_{ij}}}{\partial^w \mathbf{q}}\right)^T {}^w\mathbf{Rot}_{cj-1_{[:,2]}} & \text{if } j > 1 \end{cases}. \tag{D.8}
$$

With

$$
{}^w\mathbf{x}_{w,w_{i1}} = \begin{cases} {}^w\mathbf{x}_{w,c1} - d_{w11}\begin{bmatrix} \cos {}^w\epsilon_{c1} \\ \sin {}^w\epsilon_{c1} \end{bmatrix} + (-1)^i b_j \begin{bmatrix} \sin {}^w\epsilon_{c1} \\ -\cos {}^w\epsilon_{c1} \end{bmatrix} & \text{for } i = 1 \\[3ex] {}^w\mathbf{x}_{w,c1} - \sum_{l=1}^{j-1} d_{wlj}\begin{bmatrix} \cos {}^w\epsilon_{cl} \\ \sin {}^w\epsilon_{cl} \end{bmatrix} + (-1)^i b_j \begin{bmatrix} \sin {}^w\epsilon_{cj} \\ -\cos {}^w\epsilon_{cj} \end{bmatrix} & \text{for } i > 1 \end{cases} \tag{D.9}
$$

$\left(\frac{\partial^w \mathbf{x}_{w,w_{ij}}}{\partial^w \mathbf{q}} \right)$ can be written as

$$\frac{\partial^w \mathbf{x}_{w,w_{ij+1}}}{\partial^w \mathbf{q}} = \begin{bmatrix} 1 & 0 & d_{1j} \sin {}^w\epsilon_{c1} \cdots & d_{jj} \sin {}^w\epsilon_{cj} + (-1)^i \, w_i \cos {}^w\epsilon_{cj} & 0 \cdots 0 \\ 0 & 1 & -d_{1j} \cos {}^w\epsilon_{c1} \cdots & -d_{jj} \cos {}^w\epsilon_{cj} + (-1)^i w_i \sin {}^w\epsilon_{cj} & 0 \cdots 0 \end{bmatrix},$$

(D.10)

for $j > 1$, so that

$$\left(\frac{\partial^w \mathbf{x}_{w,w_{ij+1}}}{\partial^w \mathbf{q}} \right)^T {}^w\mathbf{Rot}_{cj}^T =$$

$$\begin{bmatrix} \cos {}^w\epsilon_{cj} & -\sin {}^w\epsilon_{cj} & d_{1j} \sin {}^{c1}\epsilon_{cj} & \cdots & d_{j-1j} \sin {}^{cj-1}\epsilon_{cj} & (-1)^i b_j & 0 \cdots 0 \\ \sin {}^w\epsilon_{cj} & \cos {}^w\epsilon_{cj} & -d_{1j} \cos {}^{c1}\epsilon_{cj} & \cdots & -d_{j-1j} \cos {}^{cj-1}\epsilon_{cj} & -d_{jj} & 0 \cdots 0 \end{bmatrix}^T.$$

(D.11)

for $j > 1$. In the same way

$$\left(\frac{\partial^w \mathbf{x}_{w,w_{i1}}}{\partial^w \mathbf{q}} \right)^T {}^w\mathbf{Rot}_{c1}^T = \begin{bmatrix} \cos {}^w\epsilon_{c1} & -\sin {}^w\epsilon_{c1} & (-1)^i b_i & 0 & \cdots & 0 \\ \sin {}^w\epsilon_{c1} & \cos {}^w\epsilon_{c1} & l_{f1} & 0 & \cdots & 0 \end{bmatrix}^T.$$

(D.12)

Substitution of (D.12) and (D.11) into equation (D.7) and (D.8) yields

$$
\begin{align}
{}^w L_{\mathrm{long}_i^{[1,1]}} &= 1 \tag{D.13a} \\
{}^w L_{\mathrm{long}_i^{[1,1+l]}} &= \cos {}^w\epsilon_{cl} \tag{D.13b} \\
{}^w L_{\mathrm{long}_i^{[2,1]}} &= \sin {}^w\epsilon_{cl} \tag{D.13c} \\
{}^w L_{\mathrm{long}_i^{[2,1+l]}} &= -\sin {}^w\epsilon_{cl} \tag{D.13d} \\
{}^w L_{\mathrm{long}_i^{[3,1]}} &= (-1)^i b_1 \tag{D.13e} \\
{}^w L_{\mathrm{long}_i^{[2+k,1+l]}} &= d_{w_{k-1l}} \sin {}^{ck}\epsilon_{cl} + (-1)^i b_l \tag{D.13f}
\end{align}
$$

and

$$
\begin{align}
{}^w L_{\mathrm{lat}_i^{[1,1]}} &= 0 \tag{D.14a} \\
{}^w L_{\mathrm{lat}_i^{[1,1+l]}} &= -\sin {}^w\epsilon_{cl} \tag{D.14b} \\
{}^w L_{\mathrm{lat}_i^{[2,1]}} &= \cos {}^w\epsilon_{cl} \tag{D.14c} \\
{}^w L_{\mathrm{lat}_i^{[2,l+1]}} &= \cos {}^w\epsilon_{cl} \tag{D.14d} \\
{}^w L_{\mathrm{lat}_i^{[3,1]}} &= l_{f1} \tag{D.14e} \\
{}^w L_{\mathrm{lat}_i^{[2+k,1+l]}} &= -d_{w_{k+1l}} \cos {}^{ck}\epsilon_{cl} \tag{D.14f}
\end{align}
$$

for $1 \le k, l \le n$.

E

Transformation matrices

In section 3.9, the transformation

$$\dot{\mathbf{Y}}_s = \mathbf{J}_{\text{path}}(^{c1}\mathbf{q})^{c1}\dot{\mathbf{q}}, \tag{E.1}$$

has been introduced. To derive an expression for $\mathbf{J}_{\text{path}}(^{c1}\mathbf{q})$, equation (2.35) will be used.

$$^{w}\mathbf{x}_{w,si} = {}^{w}\mathbf{x}_{w,c1} - \sum_{j=1}^{i} d_{s_{ij}} \begin{bmatrix} \cos {}^{w}\epsilon_{sj} \\ \sin {}^{w}\epsilon_{sj} \end{bmatrix} \tag{E.2}$$

$$\tag{E.3}$$

where

$$d_{s_{ij}} = \begin{cases} -l_{s1} & \text{if } i = 1, j = 1 \\ 0 & \text{if } i > 1, j = 1 \\ l_{si} & \text{if } i > 1, j = i \\ d_{r1} & \text{if } i > 2, j = 2 \\ d_{fj} + d_{rj} & \text{if } i > 2, 1 < j < i \\ 0 & \text{if } j > i \end{cases}, \tag{E.4}$$

Differentiating equation (E.2) with respect to time and using $^{w}\dot{\mathbf{x}}_{w,c1} = {}^{w}\mathbf{Rot}_{c1}{}^{c1}\dot{\mathbf{x}}_{w,c1}$ yields

$$\begin{bmatrix} ^{w}\dot{x}_{w,si} \\ ^{w}\dot{y}_{w,si} \end{bmatrix} = {}^{w}\mathbf{Rot}_{c1} \begin{bmatrix} ^{c1}\dot{x}_{w,c1} \\ ^{c1}\dot{y}_{w,c1} \end{bmatrix} - \sum_{j=1}^{n} d_{s_{ij}} \begin{bmatrix} -\sin {}^{w}\epsilon_{sj} \\ \cos {}^{w}\epsilon_{sj} \end{bmatrix} {}^{w}\dot{\epsilon}_{sj} \tag{E.5}$$

This equation can be written as

$$\begin{bmatrix} ^{w}\dot{x}_{w,s1} \\ ^{w}\dot{y}_{w,s1} \end{bmatrix} = \begin{bmatrix} \cos {}^{w}\epsilon_{c1} & -\sin {}^{w}\epsilon_{c1} & d_{s11}\sin {}^{w}\epsilon_{c1} & 0 \dots 0 \\ \sin {}^{w}\epsilon_{c1} & \cos {}^{w}\epsilon_{c1} & -d_{s11}\cos {}^{w}\epsilon_{c1} & 0 \dots 0 \end{bmatrix} {}^{c1}\dot{\mathbf{q}} \tag{E.6}$$

and

$$\begin{bmatrix} ^{w}\dot{x}_{w,si} \\ ^{w}\dot{y}_{w,si} \end{bmatrix} = \begin{bmatrix} \cos {}^{w}\epsilon_{c1} & -\sin {}^{w}\epsilon_{c1} & d_{s_{i2}}\sin {}^{w}\epsilon_{c1} & \dots & d_{s_{in+1}}\sin {}^{w}\epsilon_{cn} \\ \sin {}^{w}\epsilon_{c1} & \cos {}^{w}\epsilon_{c1} & -d_{s_{i2}}\cos {}^{w}\epsilon_{c1} & \dots & -d_{s_{in+1}}\cos {}^{w}\epsilon_{cn} \end{bmatrix} {}^{c1}\dot{\mathbf{q}} \tag{E.7}$$

for $i > 1$. Using (2.25) yields

$$
\begin{bmatrix} \dot{\sigma}_{p_{s1}} \\ {}^{p_{s1}}\dot{y}_{p_{s1},s1} \end{bmatrix} = \begin{bmatrix} \cos{}^{p_{s1}}\epsilon_{c1} & -\sin{}^{p_{s1}}\epsilon_{c1} & d_{s_{11}}\sin{}^{p_{si}}\epsilon_{c1} & 0 \ldots 0 \\ \sin{}^{p_{s1}}\epsilon_{c1} & \cos{}^{p_{s1}}\epsilon_{c1} & -d_{s_{11}}\cos{}^{p_{si}}\epsilon_{c1} & 0 \ldots 0 \end{bmatrix} {}^{c1}\dot{\mathbf{q}}. \quad (E.8)
$$

and

$$
\begin{bmatrix} \dot{\sigma}_{p_{si}} \\ {}^{p_{si}}\dot{y}_{p_{si},si} \end{bmatrix} = \begin{bmatrix} \cos{}^{p_{si}}\epsilon_{c1} & -\sin{}^{p_{si}}\epsilon_{c1} & d_{s_{i2}}\sin{}^{p_{si}}\epsilon_{c1} & \ldots & d_{s_{in+1}}\sin{}^{p_{si}}\epsilon_{cn} \\ \sin{}^{p_{si}}\epsilon_{c1} & \cos{}^{p_{si}}\epsilon_{c1} & -d_{s_{i2}}\cos{}^{p_{si}}\epsilon_{c1} & \ldots & -d_{s_{in+1}}\cos{}^{p_{si}}\epsilon_{cn} \end{bmatrix} {}^{c1}\dot{\mathbf{q}}
$$
$$(E.9)$$

for $i > 1$.

Stacking v_x and the velocities ${}^{p_{si}}\dot{y}_{p_{si},si}$ together in $\dot{\mathbf{Y}}_s$ yields equation (3.67) with

$$
\mathbf{J}_{\mathrm{path}}({}^{c1}\mathbf{q}) =
$$
$$
\begin{bmatrix}
1 & 0 & 0 & \ldots & 0 \\
\sin{}^{p_{s1}}\epsilon_{c1} & \cos{}^{c1}\epsilon_{p_{s1}} & -d_{s_{11}} & \ldots & d_{s_{1n}} \\
\sin{}^{p_{s2}}\epsilon_{c2} & \cos{}^{c1}\epsilon_{p_{s2}} & -d_{s_{22}}\cos{}^{p_{s2}}\epsilon_{s2} & \ldots & -d_{s_{2n+1}}\cos{}^{p_{s2}}\epsilon_{sn+1} \\
\vdots & \vdots & \vdots & \ddots & \vdots \\
\sin{}^{p_{sn+1}}\epsilon_{cn} & \cos{}^{c1}\epsilon_{p_{sn+1}} & -d_{s_{n+12}}\cos{}^{p_{sn+1}}\epsilon_{s2} & \ldots & -d_{s_{n+1n+1}}\cos{}^{p_{sn+1}}\epsilon_{sn+1}
\end{bmatrix}
$$
$$(E.10)$$

analogous to equation (3.67), the transformations

$$
\dot{\mathbf{Y}}_a = \mathbf{J}_{\mathrm{lat}}({}^{c1}\mathbf{q}){}^{c1}\dot{\mathbf{q}}. \quad (E.11)
$$

and

$$
\mathbf{V}_x = \mathbf{J}_{\mathrm{long}}({}^{c1}\dot{\mathbf{q}}), \quad (E.12)
$$

have been introduced chapter 6. The matrices $\mathbf{J}_{\mathrm{lat}}({}^{c1}\mathbf{q})\,\mathbf{J}_{\mathrm{long}}({}^{c1}\mathbf{q})$ can be derived in a similar way as the matrix $\mathbf{J}_{\mathrm{path}}({}^{c1}\mathbf{q})$. This yields

$$
\mathbf{J}_{\mathrm{lat}}({}^{c1}\mathbf{q}) =
$$
$$
\begin{bmatrix}
1 & 0 & 0 & \ldots & 0 \\
0 & 1 & -d_{a_{11}} & \ldots & d_{a_{1n}} \\
\sin{}^{a2}\epsilon_{c2} & \cos{}^{c1}\epsilon_{a2} & -d_{a_{22}}\cos{}^{a2}\epsilon_{a2} & \ldots & -d_{a_{2n+1}}\cos{}^{a2}\epsilon_{an+1} \\
\vdots & \vdots & \vdots & \ddots & \vdots \\
\sin{}^{an+1}\epsilon_{cn} & \cos{}^{c1}\epsilon_{an+1} & -d_{a_{n+12}}\cos{}^{an+1}\epsilon_{a2} & \ldots & -d_{a_{n+1n+1}}\cos{}^{an+1}\epsilon_{an+1}
\end{bmatrix}
$$
$$(E.13)$$

and

$$
\mathbf{J}_{\mathrm{long}}({}^{c1}\mathbf{q}) =
$$
$$
\begin{bmatrix}
0 & 0 & 0 & \ldots & 0 \\
1 & 0 & 0 & \ldots & d_{a_{1n}} \\
\cos{}^{a2}\epsilon_{c2} & \sin{}^{c1}\epsilon_{a2} & d_{a_{22}}\sin{}^{a2}\epsilon_{a2} & \ldots & d_{a_{2n+1}}\sin{}^{a2}\epsilon_{an+1} \\
\vdots & \vdots & \vdots & \ddots & \vdots \\
\cos{}^{an+1}\epsilon_{cn} & \sin{}^{c1}\epsilon_{an+1} & d_{a_{n+12}}\sin{}^{an+1}\epsilon_{a2} & \ldots & d_{a_{n+1n+1}}\sin{}^{an+1}\epsilon_{an+1}
\end{bmatrix}
$$
$$(E.14)$$
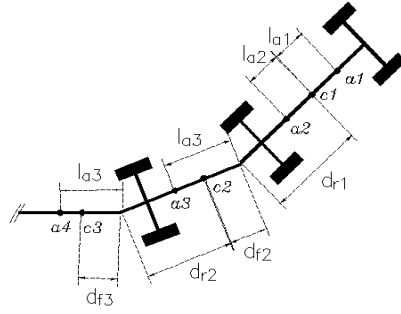
Figure E.1: Definition of distances

with

$$
d_{a_{ij}} = \begin{cases}
-l_{a1} & \text{if } i = 1, j = 1 \\
0 & \text{if } i > 1, j = 1 \\
l_{ai} & \text{if } i > 1, j = i \\
d_{r1} & \text{if } i > 2, j = 2 \\
d_{fj} + d_{rj} & \text{if } i > 2, 1 < j < i \\
0 & \text{if } j > i
\end{cases}
, \tag{E.15}
$$

with l_{ai}, d_{fi} and $d_r i$ as defined in figure E.1.

F

Robust feedback linearization

This appendix will be used to outline the design of a feedback linearizing controller with robustifying term. Let the vehicle be described by

$$^y\mathbf{M}\ddot{\mathbf{y}}_s + {}^y\mathbf{C}_{\dot{y}}\dot{\mathbf{y}}_s + {}^y\mathbf{C}_{v_x}v_x + {}^y\mathbf{D} = {}^y\mathbf{B}_{\text{lat}}\boldsymbol{\delta}_t, \tag{F.1}$$

and suppose $\boldsymbol{\delta}_t$ is directly accessible by the controller. Take this controller as

$$\boldsymbol{\delta}_t = {}^y\hat{\mathbf{B}}_{\text{lat}}^{-1}({}^y\hat{\mathbf{M}}(-\mathbf{K}_d\ddot{\mathbf{z}} - \mathbf{K}_p\dot{\mathbf{z}} - \mathbf{K}_i\mathbf{z}) + {}^y\hat{\mathbf{C}}_{\dot{y}}\dot{\mathbf{y}}_s + {}^y\hat{\mathbf{C}}_{v_x}v_x + {}^y\hat{\mathbf{M}}\mathbf{v}_1), \tag{F.2}$$

where the variables with a hat denote an estimate of the corresponding variables in equation (F.1) and

$$\dot{\mathbf{z}} = \mathbf{y}_s. \tag{F.3}$$

Furthermore, $\mathbf{v}$ denotes an artificial input. Substituting the controller (F.2) into equation (F.1) yields

$$\dddot{\mathbf{z}} + \mathbf{K}_d\ddot{\mathbf{z}} + \mathbf{K}_p\dot{\mathbf{z}} + \mathbf{K}_i\mathbf{z} = \mathbf{v}_1 + \boldsymbol{\Delta}_u. \tag{F.4}$$

In this equation, the uncertainty term $\boldsymbol{\Delta}_u$ is given by

$$
\begin{aligned}
\boldsymbol{\Delta}_u = {}&^y\mathbf{M}^{-1}({}^y\tilde{\mathbf{B}}_{\text{lat}}{}^y\hat{\mathbf{B}}_{\text{lat}}^{-1}{}^y\hat{\mathbf{M}} + {}^y\tilde{\mathbf{M}})\mathbf{v}_1 + {}^y\mathbf{M}^{-1}\{{}^y\tilde{\mathbf{B}}{}^y\hat{\mathbf{B}}_{\text{lat}}^{-1}({}^y\hat{\mathbf{C}}_{\dot{y}}\ddot{\mathbf{z}} + {}^y\hat{\mathbf{C}}_{v_x}v_x) + \\
&+{}^y\tilde{\mathbf{C}}_{\dot{y}}\ddot{\mathbf{z}} + {}^y\tilde{\mathbf{C}}_{v_x}v_x - ({}^y\tilde{\mathbf{B}}_{\text{lat}}{}^y\hat{\mathbf{B}}_{\text{lat}}^{-1}{}^y\hat{\mathbf{M}} + {}^y\tilde{\mathbf{M}})(+\mathbf{K}_d\ddot{\mathbf{z}} + \mathbf{K}_p\dot{\mathbf{z}} + \mathbf{K}_i\mathbf{z})\},
\end{aligned} \tag{F.5}
$$

with

$$^y\tilde{\mathbf{M}} = {}^y\mathbf{M} - {}^y\hat{\mathbf{M}} \tag{F.6a}$$

$$^y\tilde{\mathbf{C}}_{\dot{y}} = {}^y\mathbf{C}_{\dot{y}} - {}^y\hat{\mathbf{C}}_{\dot{y}} \tag{F.6b}$$

$$^y\tilde{\mathbf{C}}_{v_x} = {}^y\mathbf{C}_{v_x} - {}^y\hat{\mathbf{C}}_{v_x} \tag{F.6c}$$

$$^y\tilde{\mathbf{B}}_{\text{lat}} = {}^y\mathbf{B}_{\text{lat}} - {}^y\hat{\mathbf{B}}_{\text{lat}}. \tag{F.6d}$$

Equation (F.4) can be written as

$$\dot{\mathbf{x}} = \mathbf{A}\mathbf{x} + \begin{bmatrix} \mathbf{I} \\ \mathbf{0} \\ \mathbf{0} \end{bmatrix} (\mathbf{v}_1 + \boldsymbol{\Delta}_u), \tag{F.7}$$

where

$$\mathbf{A} = \left[\begin{array}{ccc} -\mathbf{K}_d & -\mathbf{K}_p & -\mathbf{K}_i \\ \mathbf{I} & \mathbf{0} & \mathbf{0} \\ \mathbf{0} & \mathbf{I} & \mathbf{0} \end{array} \right], \tag{F.8}$$

$$\mathbf{x} = \left[\begin{array}{c} \ddot{\mathbf{z}} \\ \dot{\mathbf{z}} \\ \mathbf{z} \end{array} \right]. \tag{F.9}$$

Let

$$V_1 = \mathbf{x}^T \mathbf{P} \mathbf{x}, \tag{F.10}$$

denote a Lyapunov function candidate with $\mathbf{P}$ a positive definite matrix such that

$$\mathbf{A}^T \mathbf{P} + \mathbf{P} \mathbf{A} = -\mathbf{I}. \tag{F.11}$$

Then

$$\begin{array}{rcl} \dot{V}_1 & = & -\mathbf{x}^T \mathbf{x} + \boldsymbol{\chi}(\boldsymbol{\Delta}_u + \mathbf{v}_1) \\ & \leq & -\mathbf{x}^T \mathbf{x} + \boldsymbol{\chi} \mathbf{v}_1 + \|\boldsymbol{\chi}\|_1 \|\boldsymbol{\Delta}_u\|_\infty, \end{array} \tag{F.12}$$

where

$$\boldsymbol{\chi} = 2\mathbf{x}^T \mathbf{P} \left[\begin{array}{c} \mathbf{I} \\ \mathbf{0} \\ \mathbf{0} \end{array} \right] \tag{F.13}$$

Suppose the uncertainties in the parameters are small enough, so that

$$\|\boldsymbol{\Delta}_u\|_\infty \leq h_1(\mathbf{x}) + k_1 \|\mathbf{v}_1\|_\infty, \tag{F.14}$$

with $h_1(\mathbf{x}) \geq 0$ and $0 \leq k_1 < 1$, then

$$\dot{V}_1 \leq -\mathbf{x}^T \mathbf{x} + \boldsymbol{\chi} \mathbf{v}_1 + \|\boldsymbol{\chi}\|_1 (h_1(\mathbf{x}) + k_1 \|\mathbf{v}_1\|_\infty). \tag{F.15}$$

Taking

$$\mathbf{v}_1 = -\frac{h_1(\mathbf{x})}{1 - k_1} \boldsymbol{sgn}(\boldsymbol{\chi}), \tag{F.16}$$

with $\boldsymbol{sgn}(\boldsymbol{\chi})$ a $n + 1$ dimensional vector whose i^{th} component equals $sgn(\chi_{[i]})$, yields

$$\dot{V}_1 = -\mathbf{x}^T \mathbf{x} \leq 0, \tag{F.17}$$

where the identity

$$-\boldsymbol{\chi} \boldsymbol{sgn}(\boldsymbol{\chi}) = \|\boldsymbol{\chi}\|_1 \tag{F.18}$$

has been used. Equation (F.17) shows that the system (F.1) in closed loop with (F.2) is asymptotically stable.

The term including $\mathbf{sgn}(\boldsymbol{\chi})$ causes some practical and theoretical problems [44]. To avoid these problems, the $\mathbf{sgn}(\boldsymbol{\chi})$ function has to be approximated. An useful approximation is an tanh function [1]. In [28], it is shown that

$$0 \leq h(x)x\,\mathrm{sgn}(x) - h(x)x\tanh\left(\frac{0.2785\,h(x)x}{\epsilon}\right) \leq \epsilon, \qquad (\text{F.19})$$

with h a scalar function of the variable x. Taking

$$\mathbf{v}_1 = -\frac{h_1(\mathbf{x})}{1-k_1}\mathbf{tanh}\left(\frac{0.2785\,h_1(\mathbf{x})\boldsymbol{\chi}}{\epsilon_1}\right), \qquad (\text{F.20})$$

with $\mathbf{tanh}\left(\frac{0.2785\,h_1(\mathbf{x})\mathbf{x}}{\epsilon_1}\right)$ an $n+1$ dimensional vector whose i^{th} component equals $\tanh\left(\frac{0.2785\,h_1(\mathbf{x})\chi_{[i]}}{\epsilon_1}\right)$ yields

$$\dot{V}_1 \leq -\mathbf{x}^T\mathbf{x} + (n+1)\epsilon_1, \qquad (\text{F.21})$$

which shows that with the approximated *sgn* function, the solution of the closed-loop system is ultimately bounded with an ultimate bound $(n+1)\epsilon_1$. This, however, means that the the tracking errors of the closed loop systems still can oscillate with an maximum amplitude of $(n+1)\epsilon_1$.

---

[1]Other approximations of the *sgn* function are possible. This one has been used since it is differentiable, which is a requirement for robust backstepping as will be outlined in the next appendix

G

Robust backstepping

This chapter will be used to outline the design of an backstepping controller with an robustifying term. The design follows the same path as the design of a normal backstepping controller. To avoid unnecessary calculations, the some results of the previous appendix and from chapter 8 will be used.

Let the vehicle be described by

$$^y\mathbf{M}\ddot{\mathbf{y}}_s + {}^y\mathbf{C}_{\dot{y}}\dot{\mathbf{y}}_s + {}^y\mathbf{C}_{v_x}v_x + {}^y\mathbf{D} \quad = \quad {}^y\mathbf{B}_{\mathrm{lat}}\boldsymbol{\delta}_t \tag{G.1}$$

$$\dot{\boldsymbol{\delta}}_t \quad = \quad \boldsymbol{\tau}_{st}^{-1}(\mathbf{u}_{st} - \boldsymbol{\delta}_t) \tag{G.2}$$

Describing the desired steering angles $\boldsymbol{\delta}_{t_{\mathrm{des}}}$ by

$$\boldsymbol{\delta}_{t_{\mathrm{des}}} = {}^y\hat{\mathbf{B}}_{\mathrm{lat}}^{-1}({}^y\hat{\mathbf{M}}(-\mathbf{K}_d\ddot{\mathbf{z}} - \mathbf{K}_p\dot{\mathbf{z}} - \mathbf{K}_i\mathbf{z}) + {}^y\hat{\mathbf{C}}_{\dot{y}}\dot{\mathbf{y}}_s + {}^y\hat{\mathbf{C}}_{v_x}v_x + {}^y\hat{\mathbf{M}}\mathbf{v}_1),, \tag{G.3}$$

with $\mathbf{v}_1$ an imaginary input, yields the closed loop-dynamics

$$\dot{\mathbf{x}} = \mathbf{A}\mathbf{x} + \begin{bmatrix} \mathbf{I} \\ \mathbf{0} \\ \mathbf{0} \end{bmatrix} (\mathbf{v}_1 + \boldsymbol{\Delta}_{u2} + {}^y\hat{\mathbf{M}}^{-1y}\hat{\mathbf{B}}_{\mathrm{lat}}\mathbf{w})), \tag{G.4}$$

where

$$\mathbf{w} = \boldsymbol{\delta}_t - \boldsymbol{\delta}_{t_{\mathrm{des}}} \tag{G.5}$$

and

$$\boldsymbol{\Delta}_{u2} = \boldsymbol{\Delta}_{u1} + ({}^y\hat{\mathbf{M}}^{-1y}\tilde{\mathbf{B}}_{\mathrm{lat}} - {}^y\hat{\mathbf{M}}^{-1y}\tilde{\mathbf{M}}(1 + {}^y\hat{\mathbf{M}}^{-1y}\tilde{\mathbf{M}})^{-1y}\hat{\mathbf{M}}^{-1y}\mathbf{B}_{\mathrm{lat}} + {}^y\hat{\mathbf{M}}^{-1y}\tilde{\mathbf{B}}_{\mathrm{lat}})\mathbf{v}_1, \tag{G.6}$$

where $\boldsymbol{\Delta}_{u1}$ is given by equation (F.5). The expression for $\boldsymbol{\Delta}_{u2}$ has been obtained by writing ${}^y\mathbf{M}^{-1y}\mathbf{B}_{\mathrm{lat}}$ as

$$\begin{aligned} {}^y\mathbf{M}^{-1y}\mathbf{B}_{\mathrm{lat}} &= ({}^y\hat{\mathbf{M}} + {}^y\tilde{\mathbf{M}})^{-1}({}^y\tilde{\mathbf{B}}_{\mathrm{lat}} + {}^y\hat{\mathbf{B}}_{\mathrm{lat}}) \\ &= ({}^y\hat{\mathbf{M}}\{1 + {}^y\hat{\mathbf{M}}^{-1y}\tilde{\mathbf{M}}\})^{-1}({}^y\tilde{\mathbf{B}}_{\mathrm{lat}} + {}^y\hat{\mathbf{B}}_{\mathrm{lat}}) \\ &= (1 - {}^y\hat{\mathbf{M}}^{-1y}\tilde{\mathbf{M}}(1 + {}^y\hat{\mathbf{M}}^{-1y}\tilde{\mathbf{M}})^{-1}){}^y\hat{\mathbf{M}}^{-1}({}^y\tilde{\mathbf{B}}_{\mathrm{lat}} + {}^y\hat{\mathbf{B}}_{\mathrm{lat}}) \\ &= {}^y\hat{\mathbf{M}}^{-1}({}^y\tilde{\mathbf{B}}_{\mathrm{lat}} + {}^y\hat{\mathbf{B}}_{\mathrm{lat}}) - {}^y\hat{\mathbf{M}}^{-1y}\tilde{\mathbf{M}}(1 + {}^y\hat{\mathbf{M}}^{-1y}\tilde{\mathbf{M}})^{-1y}\hat{\mathbf{M}}^{-1y}\mathbf{B}_{\mathrm{lat}} \end{aligned} \tag{G.7}$$

Taking a candidate Lyaponuv function (F.10) as

$$V_2 = \mathbf{x}^T\mathbf{P}\mathbf{x} + \frac{1}{2}\mathbf{w}^T\boldsymbol{\Gamma}\mathbf{w} \tag{G.8}$$

with $\boldsymbol{\Gamma}$ positive definite, yields

$$\dot{V}_2 = -\mathbf{x}^T\mathbf{x} + \boldsymbol{\chi}(\boldsymbol{\Delta}_{u2} + \mathbf{v}_1 + {}^y\hat{\mathbf{M}}^{-1}{}^y\hat{\mathbf{B}}_{\text{lat}}\mathbf{w}) + \dot{\mathbf{w}}^T\boldsymbol{\Gamma}\mathbf{w}. \qquad (G.9)$$

Utilizing

$$\dot{\mathbf{w}} = \boldsymbol{\tau}_{st}^{-1}(\mathbf{u}_{st} - \boldsymbol{\delta}_t) - \dot{\boldsymbol{\delta}}_{t_{\text{des}}} \qquad (G.10)$$

with

$$
\begin{aligned}
\dot{\boldsymbol{\delta}}_{t_{\text{des}}} &= \frac{\partial \boldsymbol{\delta}_{t_{\text{des}}}}{\partial \mathbf{x}}\dot{\mathbf{x}} \\
&= \frac{\partial \boldsymbol{\delta}_{t_{\text{des}}}}{\partial \mathbf{x}}\left(\mathbf{A}\mathbf{x} + \begin{bmatrix} \mathbf{I} \\ \mathbf{0} \\ \mathbf{0} \end{bmatrix}(\mathbf{v_1} + \boldsymbol{\Delta}_{u2} + {}^y\hat{\mathbf{M}}^{-1}{}^y\hat{\mathbf{B}}_{\text{lat}}\mathbf{w})\right)
\end{aligned} \qquad (G.11)
$$

this becomes

$$
\begin{aligned}
\dot{V}_2 &= -\mathbf{x}^T\mathbf{x} + \boldsymbol{\chi}(\boldsymbol{\Delta}_{u2} + \mathbf{v}_1 + {}^y\hat{\mathbf{M}}^{-1}{}^y\hat{\mathbf{B}}_{\text{lat}}\mathbf{w}) + \\
&\quad (\boldsymbol{\tau}_{st}^{-1}(\mathbf{u}_{st} - \boldsymbol{\delta}_t) - \frac{\partial \boldsymbol{\delta}_{t_{\text{des}}}}{\partial \mathbf{x}}(\mathbf{A}\mathbf{x} + \begin{bmatrix} \mathbf{I} \\ \mathbf{0} \\ \mathbf{0} \end{bmatrix}(\mathbf{v_1} + \boldsymbol{\Delta}_u + {}^y\hat{\mathbf{M}}^{-1}{}^y\hat{\mathbf{B}}_{\text{lat}}\mathbf{w})))^T\boldsymbol{\Gamma}\mathbf{w}
\end{aligned}
$$
$$(G.12)$$

Taking

$$
\begin{aligned}
\mathbf{u}_{st} &= \boldsymbol{\delta}_t + \boldsymbol{\tau}_{st}(\frac{\partial \boldsymbol{\delta}_{t_{\text{des}}}}{\partial \mathbf{x}}(\mathbf{A}\mathbf{x} + \begin{bmatrix} \mathbf{I} \\ \mathbf{0} \\ \mathbf{0} \end{bmatrix}(\mathbf{v_1} + {}^y\hat{\mathbf{M}}^{-1}{}^y\hat{\mathbf{B}}_{\text{lat}}\mathbf{w}))) + \\
&\quad \boldsymbol{\tau}_{st}(\mathbf{v}_2 - \boldsymbol{\Gamma}(\boldsymbol{\chi}({}^y\hat{\mathbf{M}}^{-1}{}^y\hat{\mathbf{B}}_{\text{lat}}\mathbf{w}))^T - \boldsymbol{\Gamma_0}\mathbf{w})
\end{aligned} \qquad (G.13)
$$

with $\mathbf{v}_2$ an second artificial input and $\boldsymbol{\Gamma}_0$ a positive definite matrix such that $\boldsymbol{\Gamma}_0\boldsymbol{\Gamma}$ is positive definite, yields

$$
\begin{aligned}
\dot{V}_2 &= -\mathbf{x}^T\mathbf{x} + \boldsymbol{\chi}(\boldsymbol{\Delta}_{u2} + \mathbf{v}_1) + (\mathbf{v}_2 - \frac{\partial \boldsymbol{\delta}_{t_{\text{des}}}}{\partial \mathbf{x}}\begin{bmatrix} \mathbf{I} \\ \mathbf{0} \\ \mathbf{0} \end{bmatrix}\boldsymbol{\Delta}_{u2})^T\boldsymbol{\Gamma}\mathbf{w} - \mathbf{w}^T\boldsymbol{\Gamma_0}\boldsymbol{\Gamma}\mathbf{w} \\
&\leq -\mathbf{x}^T\mathbf{x} + \boldsymbol{\chi}\mathbf{v}_1 + \|\boldsymbol{\chi}\|_1\|\boldsymbol{\Delta}_{u2}\|_\infty + \mathbf{w}^T\boldsymbol{\Gamma}\mathbf{v_2} \\
&\quad + \|\mathbf{w}\boldsymbol{\Gamma}\|_1\|\frac{\partial \boldsymbol{\delta}_{t_{\text{des}}}}{\partial \mathbf{x}}\begin{bmatrix} \mathbf{I} \\ \mathbf{0} \\ \mathbf{0} \end{bmatrix}\boldsymbol{\Delta}_{u2}\|_\infty - \mathbf{w}^T\boldsymbol{\Gamma_0}\boldsymbol{\Gamma}\mathbf{w}
\end{aligned}
$$
$$(G.14)$$

Suppose the uncertainties in the parameters are small enough, so that

$$\|\boldsymbol{\Delta}_{u2}\|_\infty \leq h_1(\mathbf{x}, \mathbf{w}) + k_1\|\mathbf{v}_1\|_\infty, \qquad (G.15)$$

with $h_1(\mathbf{x}, \mathbf{w}) \geq 0$ and $0 \leq k_1 < 1$ and

$$\|\frac{\partial \boldsymbol{\delta}_{t_{\text{des}}}}{\partial \mathbf{x}}\begin{bmatrix} \mathbf{I} \\ \mathbf{0} \\ \mathbf{0} \end{bmatrix}\boldsymbol{\Delta}_{u2}\|_\infty \leq h_2(\mathbf{x}, \mathbf{w}), \qquad (G.16)$$

with $h_2(\mathbf{x}, \mathbf{w}) \geq 0$ Taking $\mathbf{v}_1$ and $\mathbf{v}_2$ as

$$\mathbf{v}_1 = -\frac{h_1(\mathbf{x}, \mathbf{w})}{1 - k_1}\mathbf{tanh}\big(\frac{0.2785\,h_1(\mathbf{x}, \mathbf{w})\boldsymbol{\chi}}{\epsilon_1}\big), \tag{G.17}$$

and

$$\mathbf{v}_2 = -h_2(\mathbf{x}, \mathbf{w})\mathbf{tanh}\big(\frac{0.2785\,h_2(\mathbf{x}, \mathbf{w})\boldsymbol{\Gamma}\mathbf{w}}{\epsilon_2}\big), \tag{G.18}$$

yields

$$\dot{V}_2 \leq -\mathbf{x}^T\mathbf{x} + (n+1)\epsilon_1 + (n+1)\epsilon_2 + -\mathbf{w}^T\boldsymbol{\Gamma_0}\boldsymbol{\Gamma}\mathbf{w}, \tag{G.19}$$

which shows that the solution of the closed-loop system is ultimately bounded, with ultimate bound $(n+1)\epsilon_1 + (n+1)\epsilon_2$. This, however, means that the the tracking errors of the closed loop systems still can oscillate with an maximum amplitude of $(n+1)\epsilon_1 + (n+1)\epsilon_2$.

Bibliography

[1] J. Ackermann and T. Bunte. Actuator rate limits in robust car steering control. *Proceedings of the 36th Conference on Decision and Control*, 5:4726–4731, 1997.

[2] J. Ackermann and W. Sienel. Robust control for automatic steering. *Proceedins of the American Control Conference*, 1999.

[3] J. Ackermann. Robust decoupling, ideal steering dynamics and yaw stabilization of 4ws cars. *Automatica*, 30(11):1762–1768, 1994.

[4] B. DePoorter M. Alleyne, A. Williams. A lateral position sensing system for automated vehicle following. *Proceedins of the American Control Conference*, pages 939–943, june 1998.

[5] A. Andrews. Theoretical and emperical analysis of path magnetc lane tracking for the intelligen vehicle higway system. research report UCB-ITS-PRR-92-9, California PATH, Richmond, 1992.

[6] A. Asoake and S. Ueda. An experimental study of a magnetic sensor in an automated higway system. *Proceedings of the 1996 IEEE intelligent vehicle symposium*, pages 373–378, 1996.

[7] S. Bajikar, A. Gorjestani, P. Simpkins, and M. Dotath. Evaluation of in-vehicle gps-based lane position sensing for preventing road departure. *Proceedins of the IEEE conference on Intelligent Transportation Systems*, pages 397–402, November 1997.

[8] R. Balasubramanian. *Continuous time controller design*. Peter Peregrinus Ltd., London, 1 edition, 1989.

[9] Z. Bareket and P. Fancher. Representation of truck tire properties in braking and handlin studies: The influence of pavement and tire conditions on frictional characteristics. Technical Report UMTRI-89-33, The University of Michigan Transportation Research Institute, december 1989.

[10] R. Behringer and M. Maurer. Results on vsiual road recongition for road vehicle guidance. *Proceedings of the IEEE Intelligent Vehicle Symposium*, pages 415–420, 1996.

[11] A. Berghuis. *Model-based Robot Control: from Theory to Practice*. Ph.d thesis, University of Enschede, june 1993.

[12] M. Bertozzi and A. Broggi. Vehision-based vehicle guidance. *Computer Vision*, 30(7):49–55, Juli 1997.

[13] H. Blomenhofer, W. Hein, E. T. Blomenhofer, and W. Werner. Development of a real-time dgps system in the centimeter range. *Proceedins of the IEEE Position Location and Naviation Symposium*, pages 532–539, 1994.

[14] P. Bolzern, R.M. DeSantis, A. Locatelli, and D. Masciocchi. Path-tracking for articulated vehicles with off-axle hitching. *IEEE Transactions on Cotnrol Systems Technology*, 6(4):515–523, 1998.

[15] D. de Bruin and P.P.J. van den Bosch. Lateral control of a four-wheel steering vehicle. *Proceedings of the IFAC workshop on Intelligent Components for VEhicles, ICV*, march 1998.

[16] D. de Bruin and P.P.J. van den Bosch. Measurement of the lateral vehicle position using the longitudinal and lateral field component of the field around a permanent magnet. patent, nr 1008587, 1998.

[17] D. de Bruin and P.P.J. van den Bosch. Measurement of the lateral vehicle position with permanent magnets. *Proceedings of the IFAC workshop on Intelligent Components for VEhicles, ICV*, march 1998.

[18] D. de Bruin and P.P.J. van den Bosch. Modeling a double articulated vehicle with four steerable axles. Internal report, Eindhoven University of Technology, Measurement and Control Group, Eindhoven, the Netherlands, may 1998.

[19] D. de Bruin and P.P.J. van den Bosch. Feedback linearzing control of all-wheel steered articulated vehicles. *proceedings of the ASME International Mechanical Engineering Contress and Exposition*, 67:641–648, november 1999.

[20] D. de Bruin and P.P.J. van den Bosch. Modeling and control of a double articulated vehicle with four steerable axles. *Proceedings of the 1999 American Control Conference*, June 1999.

[21] D. de Bruin, A.A.H. Damen, and P.P.J. van den Bosch. Modeling of the planar motion of all-wheel steered multiple articulated vehicles. internal report 00 I/01, Eindhoven University of Technology, Measurement and Control Group, Eindhoven, the Netherlands, februari 2000.

[22] D. de Bruin, A.A.H. Damen, and P.P.J. van den Bosch. Input-output linearzing control of all-wheel steered multiple articulated vehicles. *sumitted to IEEE transactions on Intelligen Transportation Systems*.

[23] D. de Bruin, A.A.H. Damen, A. Progromsky, and P.P.J. van den Bosch. Backstepping control for lateral guidance of all-wheel steered mulitple articulated vehicles. *Proceedings of teh Intelligent Transportation Conference 2000*, October 2000.

[24] D.J. Chadwick. Applications of the global positioning system to intelligent vheicle highway systems. *Proceedings of the IEEE Telesystems Conference*, pages 139–141, june 1993.

[25] C.Y. Chan, B. Bougler, D. Nelson, P. Kretz, H.S. Tan, and W.B. Zhang. Caracteriztion of magnetic tape and magnetic markers as a position sensing system for vehicle guidance and control. *Proceedins of the American Control Conference*, pages 95–99, 2000.

[26] W. Chee. *Unified approach to vehicle lateral guidance*. Ph.d. thesis, University of California at Berkeley, may 1997.

[27] C. Chen and M. Tomizuka. Passivity-based nonlinear observer for lateral control of tractor-trailer vehicles in automated highway systems. *Proceedins of the 13th triennial IFAC world Congress*, pages 273–278, 1996.

[28] C. Chen. *Backstepping Design of Nonlinear Control Systems and Its Applications to Vehicle Lateral Control in Automated Highway Systems*. PhD thesis, University of California at Berkeley, Fall 1996.

[29] S.B. Choi. The design of a look-down feedback adaptive controller for the lateral control of front-wheel steered autonomous higway vehicles. *Proceedings of the American Control Conference*, pages 1603–1607, 1997.

[30] J.J. Craig. *Adaptive Control of Mechanical Manipulators*. Addison-Wesley Publishing Company, 1 edition, 1988.

[31] M. Dominicus. Lateral positioning measurement using magnetic sensors. Master's thesis, Eindhoven University of Technology, august 2000.

[32] Y. Du, B. Schiller, C. Krantz, and M. Donath. Alx: Autonomous vehicle guidance for roadway following and obstacle avoidance. *Proceedings of the IEEE Conference on Systems, Man and Cybernetics*, 1:364–370, 1995.

[33] J.R. Ellis. *Vehicle handling dynamics*. Mechanical Engineering Publications, London, 1 edition, 1994.

[34] J. Farrelly and P. Wellstead. Estimation of vehicle lateral velocity. *Proceedings of the IEEE international conference on control applications*, pages 552–557, 1997.

[35] R.E. Fenton, G.C. Melocik, and K.W. Olson. On the steering of automated vehicles:theory and experiment. *IEEE Trans.*, AC-21:306, 1976.

[36] R.F. Fenton, G.C. Molocik, and K.W. Olson. On the steerign of auto-
mated vehicles: Theory and experiment. *IEEE transactions on Automatec
Control*, AC-21(3):306–315, June 1976.

[37] G.F. Franklin, J.D. Powell, and A. Emami-Naeini. *Feedback Control of
Dynamic Systems*. Adisson Wesley, 1994.

[38] B Friedland. *Advanced Control System Design*. Prentice Hall, Englewood
Cliffs, New Jersey, 1 edition, 1996.

[39] M. Gérardin and D. Rixen. *Mechanical vibrations: Theory and applica-
tions to structural dynamics*. Wiley, Chichester, 1 edition, 1994.

[40] A.W. Grootendorst and B. Meulenbeld. *Analyse: deel2, Functies met twee
of meer variabelen*. Delfste Uitgevers Maatschappij, Delft, The Nether-
lands, 7 edition, 1989.

[41] J. Guldner, W. Sienel, J. Ackermann, S. Pathwardhan, H.S. Tan, and
T. Bunte. Robust control design for automatic steering based on feedback
of front and tail lateral displacement. *Proceedings of the 4th European
Control Conference*, 1997.

[42] J. Guldner, H.S. Tan, and S. Patwardhan. Analysis of automatic steer-
ing cotnrol for highway vehicles with look-down lateral reference system.
Vehicle System Dynamics, 26(4):243–269, oct 1996.

[43] J. Guldner, H.S. Tan, and S Patwardhan. On fundamental issues of vehicle
steering control for higway automation, institution =. Technical report.

[44] H.K. Halil. *Nonlinear Systems*. Prencice Hall, Upper Saddle River, NJ,
USA, 2 edition, 1996.

[45] M. Heller and M. Huie. Vehicle lateral guidance using vision, passive wire
and radar sensor. *Vehicle Navigation and Information Systems Confer-
ence*, pages 505–508, 1993.

[46] P. Hingwe and M. Tomizuka. Experimental evaluation of a chatter free
sliding mode control for lateral control in ahs. , 1997.

[47] P. Hingwe, J.Y. Wang, M. Tai, and M. Tomizuka. Lateral control of
heavy duty vehicles for automated highway system: Experimental study
on a tractor semi-trailer. PATH Working paper UCB-ITS- PWP-2000-1,
California PATH, 2000.

[48] P. Hingwe. *Robustness and Performance issues in the Lateral Control
of Vehicles in Automated Highway Systems*. PhD thesis, University of
California at Berkeley, 1997.

[49] M. Ito, T.and Furumata, F. Harashima, H. Inaba, and S. Matsumoto. An automatic driving system of automobiles by guidance cables. *Proceedings of the International Automotive Engineering Congres, SAE paper 730127,* 1993.

[50] B. Jiang, Z. Liu, X. Q, and S. Zhang. Nonlinear feedback and robust tracking control of articulated vehicles. *Proceedings of the third IEEE Conference on Control Applications,* 1-3:373–378, 1994.

[51] A.R. Johnston, T. Assefi, and J.Y. Lai. Automated vehicle guidance using discrete reference makrers. *IEEE Transactions on Vehicular Tecnology,* 28(1):95–105, februari 1979.

[52] B.J. Kerhof. *Wegenbouw.* Uitgevers-Maatschappij Kosmos, Amsterdam, 5 edition, 1946.

[53] U. Kiencke and A. Daiss. Observation of lateral vehicle dynamics. *Control Engineering Practice,* 5(8):1145–1150, august 1997.

[54] M. Krstic, I. Kanellkopoulos, and P.V. Kokotovic. *Nonlinear and adaptive control design.* Wiley-interscience, New York, 1995.

[55] H. Kwakernaak and R. Sivan. *Linear Optimal Control Systems.* Wiley-interscience, London, 1 edition, 1972.

[56] A. Lee and M. Donath. Differential gps based control of a heavy vehicle. *Proceedings of the IEEE Conference on Intelligent Transportation Systems,* pages 662–667, 1999.

[57] C.F. Lin and A.G. Ulsoy. Vehicle dynamics and external disturbance estimation for future vehicle path prediction. *Proceedins of the American Control Conference,* 1:155–159, 1996.

[58] D.A. Lizarraga-Navarro. *Contributions a la stabilisation de systemes non-lineaires et a la commande de vehicles sur roues.* Ph.d. thesis, Institut National Polytechnique de grenoble, , april 2000.

[59] Palkovics L. Effect of the controller parameters on the steerability of the four wheel car. *Vehicle System Dynamics,* 21:109–128, 1992.

[60] S.S. Mahil. On the application of lagrange's method the distribution of dynamic systems. *IEEE Transactions on Systems, Man, Cybernetics,* SMC-12(6):877–888, November/December 1982. .

[61] W.F. Milliken and D.L. Milliken. *Race car vehicle dynamics.* Warendale: SAE international, 1995.

[62] V. Morellas, T. Morris, L. Alexander, and M. Donath. Preview based control of a tractor trailer using dgps for preventing road departure accidents. *Proceedins of the IEEE conference on Intelligent Transportation Systems*, pages 797–805, November 1997.

[63] Liand Z. Murray, R.M. and S.S. Sastry. *mathematical introduction to robotic manipulation*. CRC Press, London, 1 edition, 1994.

[64] M. Nakamura, A. Arai, M.P. Bedett, R.W. Goudy, Y. Suzuki, and H. Kusunoki. Vehicle lateral control system using laser radar. *Proceedings of the SPIE*, 3244:267–277, 1994.

[65] T. M. Nguyen, J. W. Sinko, and R.C. Galijan. Using differential carrier phase gps to ctonrol automated vehicles. *Proceedings of the 40th Midwest Symposium on Circuist and Systems*, 1:493–496, August 1997.

[66] K.W. Olson. wire reference configurations in vehicle lateral control. *IEEE Transactions on Vehicular Technology*, 26:161, 1977.

[67] R. Ortega, A. Loria, P.J. Nicklasson, and Sira-Ramirez H. *Passivity-based Control of Euler-Lagrange Systems*. Springer, Berlin, 1 edition, 1998.

[68] W.R. Pasterkamp. *TheTyre as Sensor*. Ph.d thesis, Delft University of Technology, Delft, the Netherlands, december 1997.

[69] S. Pathwardhan, H.S. Tan, and Guldner J. A general framework for automatic steering control: System analysis. *Proceedings of the 1997 American Control Conference*, 1-6:1598–1602, 1997.

[70] H. Peng and M. Tomizuka. Vehicle lateral control for highway automation. *Proceedings of the American Control Conference*, pages 3090–3095, 1990.

[71] H. Peng and M. Tomizuka. Preview control for vehicle lateral guidance in highway automation. *Journal of Dynamic Systems, Measurement and Control*, 115:679-686, December 1993.

[72] H.A. Pham and J.K. Hedrick. A robust optimal lateral vehicle control strategy. *Proceedings of the 1996 IEEE International Conference on Control Applications*, pages 361–366, september 1996.

[73] L.R. Ray. Nonlinear state and tire force estimation for advanced vehicle control. *IEEE Transactions on Control Systems Technology*, 3(1):117–124, march 1995.

[74] rijkswaterstaat. *Richtlijnen voor het ontwerpen van autosnelwegen*. SDU, Den Haag, 1990.

[75] rijkswaterstaat. *Richtlijnen voor het ontwerpen van niet autosnelwegen (RONA)*. SDU, Den Haag, 1992.

[76] R. Roest. *Inleiding Mechanica*. Delfste Uitgevers Maatschappij, Delft, 3 edition, 1990.

[77] M. Sampei, T. Tamura, T. Kobayashi, and N. Shibui. Arbitrary path trackin control of articulated vehicles using nonlinear control theory. *IEEE Transactions on Control Systems Technology*, 3(1), march 1995.

[78] S. Saraf and M. Tomizuka. Slip angle estimation for vehicles on automated higways. *Proceedings of the 1997 American Control Conference*, 1-6, 1997.

[79] W. Sienel. Estimation of the tire cornering stiffness and its application to active car steering. *Proceedings of the 36th Conference on Decision and Control*, pages 4744–4748, december 1997.

[80] S. Skogestad and I. Postlethwaite. *Multivariable Feedback Control: analysis and design*. Wiley, Chichester, 1 edition, 1996.

[81] M.W. Spong and M. Vidyasagar. *Robot dynamics and control*. Wiley, Chichester, 1 edition, 1989.

[82] S. Stauffer, B. Barett, N. Demma, and T. Dahlin. Magnetic lateral guidance sensors for automated higways. *Proceedings o fthe spie*, 2592:138–149.

[83] D Stinton. *The Design of the Airoplane*. Granada, London, 4 edition, 1983.

[84] M. Tai and M. Tomizuka. Dynamic modeling of multi-unit heavy-vehicles. *ASME symposium on Transportation Systems*, November 1998.

[85] M. Tai and M. Tomizuka. Robust lateral control of heavy vehicles for ahs. *Proceedins of the 14th IFAC World Congress*, 1999.

[86] M. Tai, J. Wang, P. Hingwe, C. Chen, and Tomizuka M. Lateral control of heavy duty vehicles for automated highway systems. research report UCB-ITS- PRR-98-8, California PATH, Richmond CA, 1998.

[87] D.H. Titterton and J.L. Weston. *Strapdown inertial navigation technology*. IEE Radar, Sonar Naviation and Avionics Series. Peter Peregrinus Ltd, on behalf of IEE, London, 1 edition, 1997.

[88] M. Tomizuka, M. Tai, J.Y. Wang, and P. Hingwe. Automated lange guidance of commercial vehicles. *Proceedings of the 1999 IEEE International Conference on Control Applications*, 2:1359–1364, 1999.

[89] P.J.Th. Venhovens and K. Naab. Vehicle dynamics estimation using kalman filters. *Vehicle System Dynamics*, 32:171–184, 1999.

[90] J.Y Wang and M. Tomizuka. Robust h_∞ lateral control of heavy-duty vehicles in automated highway systems. *Proceedins of the 1999 American Control Conference*, pages 3671–3675, 1999.

[91] L.C. Westhphal. *Sourcebook of Control Systems Engineering*. Chapman and Hall, 2-6 Boundary row, London, 1 edition, 1995.

[92] C.C. de Wit, B Siciliano, and G Bastin. *Theory of Robot Control*. Communications and Control Engineering. Springer-Verlag, London, 2 edition, 1997.

[93] J.Y. Wong. *Theory of ground vehicles*. Wiley, New York, 2 edition, 1993.

[94] D. Yanakiev, J. Eyre, and I. Kanellakopoulos. Longitudinal control of heavy vehicles with air brake actuation delays. *Proceedings of the American Control Conference*, 1997.

[95] Y. Yang, J Farrel, and M. Barth. High-accuracy, high-frequency differential carrier phase gps aided low-cost ins. *IEEE proceedins of the Position Location and Navigation Symposium*, pages 148–155, 2000.

[96] O. Yaniv. Robustness to speed of 4ws vehicles for yaw and lateral dynamics. *Vehicle System Dynamics*, 27:221–234, 1997.

[97] K.I. Yoshimoto, H. Ogawa, and H. Kubota. Course tracking control algorithm using visual information. *Vehicle System Dynamics*, 28, 1997.

[98] W. Zhang and R.E. Parson. An intelligent road reference system for vehicle lateral. *Proceedings of the American Control Conference*, pages 281–286, 1991.

[99] W. Zhang. A roadway information system for vehicle guidance/control. *Vehicle Naviation and Information Systems Conference Proceedings*, 2:1111–1116, 1991.

[100] Y. Zhao. *Vehicle Location and Naviation Systems*. The Artech House ITS Series. Artech House, Inc, Norwood, USA, 1997.

Samenvatting

Vandaag de dag zorgen verkeersopstoppingen voor een steeds groter wordend probleem, dat zorgt voor toenemende economische verliezen als gevolg van de resulterende vertragingen. Dit probleem kan gereduceerd worden door meer mensen gebruik te laten maken van het openbaar vervoer. Om dit te bereiken, dient het openbaar vervoer verbeterd te worden. De kwaliteit van het openbaar vervoer kan worden verbeterd door de voordelen van railvoertuigen en stadsbussen te combineren in een nieuw type voertuig. Dit type voertuig zou een multi-gelede bus kunnen zijn, met onafhankelijke besturing op alle assen.

In Eindhoven zal in het jaar 2003 een nieuw openbaar vervoersysteem in gebruik worden genomen, wat is gebaseerd op het gebruik van zulke voertuigen. Om hetzelfde rijgedrag als trams te krijgen, worden deze voertuigen uitgerust met een lateraal geleidingssysteem dat het voertuig langs een van tevoren bekende vrije busbaan moet sturen.

Dit proefschrift behandelt het ontwerp van zo'n geleidingssysteem. Om een goed spoor volgend gedrag te krijgen dient dit geleidingssysteem rekening te houden met de planaire dynamica van het voertuig. Daarom is er een voertuigmodel afgeleid. Dit model geeft een beschrijving van de niet lineaire planaire dynamica van een multi-gelede bus met een instelbaar aantal aanhangers. Om te laten zien dat dit model het planaire voertuig gedrag voldoende goed beschrijft, is het vergeleken met een 3-D multi-body model van een dubbel geleden bus dat 125 graden van vrijheid beschrijft. Verder is met een analyse aangetoond dat voor een goedspoor volgend gedrag een dynamisch voertuigmodel nodig is.

Om de positie van het voertuig ten opzichte van de te volgen baan te bepalen, is een nieuwe meetmethode ontwikkeld. Deze meetmethode maakt gebruik van rotatie symmetrische staafmagneten, die op een bekende plaats onder het wegdek zijn geplaatst. Door gebruik te maken van de rotatie-symmetrie van de magneetvelden rondom de magneten, kan de positie van de magneet ten opzichte van een op het voertuig geplaatste magneetveld sensor worden bepaald, onafhankelijk van de meethoogte en sterkte van de magneet. In principe is 1 dubbel-assige magneet veld sensor voor deze meting voldoende. Analyse laat echter zien dat deze methode, bij gebruikmaking van 1 dubbel-assige sensor gevoelig is voor scheefstand van magneet en/of voertuig. Deze gevoeligheid kan worden gereduceerd door gebruik te maken van een tweede dubbel-assige sensor. Meetresultaten laten zien dat de afstand tussen magneet sensor en de magneet kan worden bepaald met ongeveer $2\,cm$ nauwkeurigheid.

De permanente magneten geven alleen positie-informatie op discrete momenten. Voor het ontwerp van een regelaar is het gewenst om de totale (planaire) toestand van het voertuig ter beschikking te hebben. Om deze toestand te schatten is een extended Kalman filter ontworpen. Versnellingsopnemers zijn gebruikt

als ingangen van het Kalman filter om tot een voorspelling van de afstand tot het pad te komen. Op deze manier is de invloed van variërende voertuigparameters klein. Om correcties toe te passen op deze voorspelling, zijn geledingshoek sensoren, wiel encoders, rate-gyro's en de permanente magneten gebruikt. Voordeel van het gebruiken van meerdere sensoren is dat op deze manier redundantie van sensoren in het Kalman filter gebracht wordt. Deze redundantie kan worden gebruikt om het filter robuust te maken tegen uitval van een of meerdere sensoren. Het a-synchrone karakter van de permanente magneten is in rekening gebracht door de magneetsensor signalen als multi-rate signalen te behandelen.

De voertuigen die in Eindhoven gebruikt zullen gaan worden, hebben naast onafhankelijke besturing op alle assen ook onafhankelijke aandrijving op alle achterwielen. Deze onafhankelijke aandrijvingen kunnen in principe ook gebruikt worden om het voertuig te sturen. Een singuliere waarde analyse is uitgevoerd om aan te tonen dat de normale stuuringangen meer invloed uit oefenen op de uitgangen dan de aandrijfkoppels. Verder is aangetoond dat met onafhankelijke besturing op alle assen, off-tracking van de achterassen kan worden gereduceerd, en dat de gierdynamica van alle voertuigsegmenten beter onder controle kan worden gehouden.

Twee verschillende regelaars zijn ontworpen om het voertuig langs de te volgen baan te sturen. De eerste regelaar is een zogenaamde feedback lineairiserende regelaar. Deze bestaat in principe uit een binnenlus en een buitenlus. De binnenlus lineairiseert de planaire voertuig dynamica, onder de aanname dat de dynamica van de stuursystemen kan worden verwaarloosd. De buitenlus dient om de gevolgen van verstoringen en model onzekerheid te onderdrukken. Voor deze buiten lus is een PID-regelaar gebruikt. De tweede regelaar is een zogenaamde backstepping regelaar. Bij deze regelaar is de dynamica van de stuuractuatoren op een formele manier in rekening gebracht.

Om het totale geleidingssysteem te simuleren, is een 3-D voertuigmodel in software geïmplementeerd. Dit model beschrijft naast de planaire dynamica ook het veersysteem van een multi-gelede bus. Verder is in dit model een niet lineair band model opgenomen, dat ook de load afhankelijkheid en saturatie van de laterale bandkracht karakteristiek in rekening brengt.

Simulaties met dit 3-D simulatiemodel laten een goed spoorvolgend gedrag zien voor de feedback lineairiserende en backstepping regelaar. Vergeleken met de lineairiserende regelaar is het spoorvolgende gedrag van de backstepping regelaar beter. Dit gaat evenwel ten koste van toenemend hoog frequent gedrag van de laterale versnellingen,wat minder gewenst is voor passagierscomfort.

Dankwoord

Graag wil ik deze voorlaatste bladzijde van mijn proefschrift gebruiken om een aantal mensen te bedanken die tijdens mijn promotie van belang zijn geweest.

In de eerste plaats wil ik Sandra bedanken voor haar mentale ondersteuning en omdat ze mij vaak heeft moeten missen, doordat ik weer zonodig tot in de kleine uurtjes of in het weekend aan mijn promotie moest werken. Daar dit soms ten koste ging van mijn goede humeur, denk ik dat zij het meeste onder dit werk te leiden heeft gehad.

Ook Paul van den Bosch wil ik hier vermelden. Zonder zijn medewerking zou dit onderzoek niet van de grond zijn gekomen. Ad Damen ben ik veel dank verschuldigd voor zijn inzet als copromotor tijdens de laatste anderhalf jaar van mijn promotie. Tweede promotor en lid van de STW gebruikerscommissie Joop Pauwelussen ben ik dankbaar voor zijn waardevolle discussies tijdens de gebruikerscommissiebijeenkomsten en voor het nauwkeurig lezen van mijn proefschrift. Voor deze laatste reden ben ik ook de kern commissieleden Frans Veldpaus en Maarten Steinbuch erkentelijk.

My visit to the University of Berkeley has been of essential importance for my research. Therefore, I would like to thank Prof. Tomizuka for making this visit possible. I also would like to thank Pushkar Hingwe, Frederick Bonnay, Meihua Tai, Jeng-Yu Wang and Craig Smith for the valuable discussions and the nice trips and evenings.

Dank ben ik ook verschuldigd aan APTS en de mensen van Nedcar en FROG Navigation Systems die aan het Phileas- project werken. Zonder deze mensen zou mijn onderzoek een stuk minder waarde hebben.

De afstudeerders Peter Chao, Peter Engelaar, Erol Enkur, Henri Visser en Marco Dominicus ben ik erkentelijk voor hun bijdrage aan mijn onderzoek. Uiteraard wil ik ook Willem-Jan Kok niet vergeten, die zijn TU-Delft stage op de TU in Eindhoven heeft willen uitvoeren om simpele voertuigmodellen met complexe Adams modellen te vergelijken.

Bijzondere dank ben ik verschuldigd aan mijn (ex)collega's. Met name de collega AIO's Vick, Mario, Bart, Patrick, Leo, Patricia, Hardy, Andreï en Diederik voor de gezellig lunches en lol die we gehad hebben. Leon en Maurice wil ik bedanken voor het beschikbaar stellen van 'hun' style file, hun hulp daarbij en de leuke 'voetbal' avonden. Udo wil ik natuurlijk niet vergeten voor zijn computerondersteuning en leuke 'modelbouw' uitjes. Barbara wil ik bij deze bedanken voor haar correcties op mijn engels en Paul Borghouts voor de administratieve ondersteuning van mijn onderzoeks project. Will, Remi en Ton ben ik erkentelijk voor hun hulp bij de experimenten die helaas te laat kwamen om op een goede manier in dit proefschrift op te nemen.

Tot slot wil ik natuurlijk mijn familie en vrienden niet vergeten, die ook op deze bladzij een plaats verdienen.

Curriculum Vitae

Dik de Bruin was born in Geldermalsen in The Netherlands on December 12 in 1971. In 1992 he started a study in electrical engineering on the Eindhoven University of Technology, in Eindhoven, The Netherlands. He carried out his practical trainings and master thesis project in the field of semiconductor materials and devices. In August 1996 he obtained his master thesis on his work on modeling of MOSFET transistors.

In september 1996, he started a postgraduate study in the field of mechatronics on the Eindhoven University of Technology. In march 1997, he was employed as Ph.D. student at the same university at the measurement and control group of the Electrical Engineering department.

Dik de Bruin is currently employed by Philips Research in the Netherlands, where he is working on plasma displays.